Remote sensing, geological mapping and sampling in stream sediments for the exploration of Lithium (Li) and associated minerals

César Alexandre Almeida Carvalho

Mestrado em Geologia

Departamento de Geociências, Ambiente e Ordenamento do Território

2022

Orientador

Alexandre Martins Campos de Lima, Professor Associado, Faculdade de Ciências da Universidade do Porto

Coorientadores

Ana Cláudia Moreira Teodoro, Professora associada com agregação, Faculdade de Ciências da Universidade do Porto

Joana Maria Cardoso Fernandes, Investigadora Doutorada de Nível Inicial, Faculdade de Ciências da Universidade do Porto



Fortescue Portugal

U.PORTO

FACULDADE DE CIÊNCIAS
UNIVERSIDADE DO PORTO

Sworn Statement

I, César Alexandre Almeida Carvalho, enrolled in the Master Degree in Geology at the Faculty of Sciences of the University of Porto hereby declare, in accordance with the provisions of paragraph a) of Article 14 of the Code of Ethical Conduct of the University of Porto, that the content of this internship report reflects perspectives, research work and my own interpretations at the time of its submission.

By submitting this internship report, I also declare that it contains the results of my own research work and contributions that have not been previously submitted to this or any other institution.

I further declare that all references to other authors fully comply with the rules of attribution and are referenced in the text by citation and identified in the bibliographic references section. This internship report does not include any content whose reproduction is protected by copyright laws.

I am aware that the practice of plagiarism and self-plagiarism constitute a form of academic offense.

César Alexandre Almeida Carvalho

FCUP, 05/12/2022

Agradecimentos

I would like to thank Fortescue Portugal (Fortescue Metals Group Lda.) to give me the opportunity to work in this project and providing all the information and equipments needed, and particularly to Romeu Vieira for the opportunity to join the team.

Thanks must also go to ESA and USGS for providing the Sentinel-2 and Landsat-9 data used to apply remote sensing techniques.

My thanks to Prof. Dr. Alexandre Lima and Prof. Dr. Ana Claudia Teodoro for the invitation and trust to carry out this project.

To Joana Cardoso Fernandes for teaching me all the methods used in this study, helping with the writing of the report and for always support me in the last days of the report submission.

To the Faculty of Science of the University of Porto and all the teaching and nonteaching staff of the Department of Geosciences, Environment and Spatial Planning.

This work could not be done without the help of all the members of Fortescue Portugal exploration team. Thank you Rui Frutuoso, Ana Gonçalves and Cátia Dias for helping me with everything i needed and for passing on so much knowledge.

Thanks to all the other members of Fortescue Portugal Eduarda Silva, Francisco Loureiro and Sara Oliveira.

And a special thanks to my parents and grandparents for all the effort, sacrifice, and support.

Abstract

A study was carried out in the Circo concesssion area, in Northern Portugal, with the objective of supporting exploration activities for Lithium (Li) minerals. This study was divided into three components: (i) remote sensing (using Sentinel-2 and Landsat-9 images), (ii) geological mapping (at a scale of 1:25 000), and (iii) stream sediments analysis (low density, < 1 sample/km^2).

The exploration and prospection concession for the study area was obtained by Fortescue Portugal Unipessoal Lda. (subsidiary of Fortescue Metals Group Ltd.), for the exploration of Li and associated minerals. This license covers three municipalities: Macedo de Cavaleiros, Vinhais and Mirandela, in a total area of 254.5 Km^2. Geologically, the area is located in the Galicia Trás-os-Montes Zone (GTMZ), with the presence of peraluminous Variscan granites, Silurian metasediments, and the occurrence of mineralizations with tin (Sn) and tungsten (W).

Several remote sensing techniques were used, such as band ratios, RGB combinations, principal component analysis (PCA), and image classification algorithms for geological mapping, in order to define target areas for exploration. The geological mapping was intended to update the knowledge of the area and the stream sediments analysis aimed to determine the lithological background for each catchment basin.

The targets identified by remote sensing were subject to field visits, where samples were collected and then submitted to XRF and LIBS analysis. This samples are described throughout the report. Steps for a good practice of geological mapping are also described, and a geological map at scale 1:95 000 is presented. Anomalous basins were detected by the box-plot method on the basis of XRF analysis results of the stream sediments.

Keywords: Remote sensing, Geological mapping, Stream sediments, Lithium, Prospection, Research

Resumo

Foi realizado um estudo na concessão de Circo, no Norte de Portugal, com o objetivo de suportar as atividades de prospeção e pesquisa de minerais de Lítio (Li). Este estudo dividiu-se em três componentes: (i) deteção remota (com recurso a imagens Sentinel-2 e Landsat-9), (ii) cartografia geológica (à escala de 1:25 000) e (iii) análise de sedimentos de corrente (de baixa densidade, < 1 amostra/km^2).

A concessão de prospeção e pesquisa da zona de estudo foi obtida pela empresa Fortescue Portugal Unipessoal Lda. (subsidiária de Fortescue Metals Group Ltd.), para a prospeção de lítio e minerais associados. Esta licença abrange três municípios: Macedo de Cavaleiros, Vinhais e Mirandela, numa área total de 254,5 Km^2. Geologicamente, a área localiza-se na Zona Galiza Trás-os-Montes (ZGTM), e carateriza-se pela presença de granitos Variscos peraluminosos, metasedimentos silúricos, e mineralizações de estanho (Sn) e tungsténio (W).

Foram utilizadas diversas metodologias de deteção remota, como, rácios de bandas, combinações RGB, análise de componentes principais (PCA) e classificação de imagem para cartografia geológica, com o objetivo de definir áreas alvo. A cartografia geológica tem o propósito de atualizar a cartografia da área e a análise de sedimentos de corrente pretende determinar o *background* litológico para cada bacia de drenagem.

Os alvos identificados por deteção remota foram alvo de visitas de campo, onde foram recolhidas amostras, sendo depois submetidas à análise de XRF e LIBS. Estas amostras estão descritas ao longo do relatório. São também descritos os passos para uma boa prática de cartografia geológica, e é apresentado um mapa geológico à escala 1:95 000. Foram definidas bacias anómalas pelo método box-plot com base nos resultados da análise de XRF nos sedimentos de corrente.

Palavras-chave: Deteção remota, Cartografia Geológica, Sedimentos de corrente, Lítio, prospeção, pesquisa

List of figures

Figure 1. The eletromagnetic spectrum (adapted from: JARS, 1993). 20

Figure 2. Landsat missions` timeline (NASA, 2021). 22

Figure 3. Comparison between Landsat-8/9 and Sentinel-2 bands (adapted from: USGS Landsat program, 2017). 24

Figure 4. Geological map 1:50 000 of Mirandela, Portugal (7-C sheet); the red area represents the southern part of Circo area (LNEG, 2010). 27

Figure 5. Location of Circo area on the Portuguese geological maps. a) Portugal divison at scale 1:500 000; b) Portugal division at scale 1:200 000; c) Portugal division at scale 1:50 000 (adapted from: LNEG). 28

Figure 6. Main stages of geological mapping (Fortescue, 2021). 29

Figure 7. Catchment basins (green) generated for Barroso/Alvão area, stream sediments sampling sites (red points) and the blue lines are the water streams (adapted from: Dias, 2016) 31

Figure 8. Study area (orange area), Circo (adapted from: Google Earth, 2015). 32

Figure 9. Digital elevation model and water streams within the Circo area. 33

Figure 10. Circo area limits and polygon coordinates, contract code: MNPP00121 (DGEG, 2021). 34

Figure 11. Mineral occurrences in the Circo area, on top of the 1:200 000 Portuguese geological map; black line represents the shearing zone that connects Ervedosa, Agrochão and Murçós. 36

Figure 12. Subdivision of the Iberian Massif in geotectonic zones (according to Lotze, 1945 *in* Pérez-Estaún *et al*., 2004), Julivert *et al*. (1972;1974) and Farias *et al.* (1987) (adapted from: Pérez-Estaún *et al*., 2004). 38

Figure 13. Simplified geological map of the Central Iberian Zone (CIZ) and the Galiza-Trás-os-Montes Zone (GTMZ), in Portugal and Spain, showing the location of Li mineralization (Roda-Robles *et al.*, 2018). 40

Figure 14. Geological setting of the Circo area (extracted from annual Circo Exploration Program, 2021). 42

Figure 15. Overlap of Landsat-9 and Sentinel-2 bands to the spectral curves of Li-bearing minerals (adapted from: Cardoso-Fernandes et al, 2019a). 49

Figure 16. Overlap of Landsat-9 and Sentinel-2 bands to the spectral curves of petalite alteration minerals and other associated minerals and other associated minerals (adapted from: Cardoso-Fernandes et al, 2019a). 49

Figure 15. a) Specac Manual Hydraulic Press; b) sampling device used to create the pellets; c) 100 µm sieve; d) some produced pellets. 54

Figure 16. CRM pellets for LIBS analysis; AMIS 0683 and AMIS 0577. 55

Figure 17. LIBS analysis; a) SciAps Z-300 device ; b) SciAps Z-300 menu; c) SciAps Z-300 testing ; d) SciAps Z-300 up to temperature; e) analysis results; f) and d) device being cleaned up. 56

Figure 18. Psammite outcrop from the Circo area. 59

Figure 19. Folded quartz veins in the psammite outcrop. 60

Figure 20. Psammite foliation. 61

Figure 21. Dip-dip direction measure and "right hand rule" (Sanuja, 2013). 62

Figure 22. Measuring structures in the psammite outcrop. 62

Figure 23. Sampling the rock using the geological hammer. 63

Figure 24. Collected sample from the psammite outcrop. 64

Figure 25. One hundred and eighty points generated from stream sediments sampling. 66

Figure 26. a) Picture of the water stream (dry); b) selected sampling site by the team. 67

Figure 27. a) Cleaning the surface layer of the ground to open a hole; b) collecting the sediment sample; c) picture of the sampling bag along the sampling site; d) cover the sampling hole. ... 68

Figure 28. Used tools for the stream sediments washing process (pan – black tool; sieve – green tool). 69

Figure 29. a) and b) Sieving the sample with the hand; c) washing the sample in the river with stream flow; d) putting the washed sample back in the sapling bag; e) washing the tools before moving into another sample. 70

Figure 30. a) XRF Vanta (Olympus); b) and c) CRM pellets measurements. 71

Figure 31. a) Elements that each XRF beam measures; b) Stream sediments samples drying. 72

Figure 32. a) XRF analysing a sample; b) and c) cleaning the device after a measure with a cloth and compressed air; d) returning the sample back to the sampling bag; e) weighing the sample; f) cleanning the tools to not contaminate the next sample. 73

Figure 33. Vanta periodic table (Olympus) with the respective LODs. 74

Figure 34. RGB combination (4-3-2); natural color images: a) Landsat-9; b) Sentinel-2. Coordinate System: UTM29N WGS84. 78

Figure 35. RGB combinations that identify iron oxides and clay minerals: a) RGB 2-5-7 for Landsat-9; b) RGB 2-5-7 with a vegetation mask; c) RGB 2-8-12 for Sentinel-2; d) RGB 2-8-12 with a vegetation mask. Blue and white areas show the highest iron oxide content. Some white

spots in “Palão” quarry and Rebordelo exploration could indicate a simultaneous presence of iron oxides and clay minerals. Coordinate System: UTM29N WGS84. 80

Figure 36. RGB combinations that identify hydrothermally altered rocks: a) RGB 5-7-3 for Landsat-9; b) RGB 5-7-3 with a vegetation mask; c) RGB 8-12-3 for Sentinel-2; d) RGB 8-12-3 with a vegetation mask. Light green represents the granites while blue color represents the metasediments. Hydrothermally altered rocks show to be discriminated in deep green and deep blue colors. Coordinate System: UTM29N WGS84. 82

Figure 37. RGB combination 7-3-11 for Landsat-9 to discriminate Li-bearing minerals. Granites appear in purple and metasediments in blue. “Palão” quarry, Rebordelo exploration and Ervedosa mine appear in a yellowish green. Coordinate System: UTM29N WGS84. 83

Figure 38. RGB combination 7-3-11 with a vegetation mask for Landsat-9 to discriminate Li-bearing minerals. Coordinate System: UTM29N WGS84. 84

Figure 39. RGB combinations that identify Li-bearing minerals: a) RGB 3-2-11 for Landsat-9; b) RGB 3-2-11 with a vegetation mask; c) RGB 3-2-12 for Sentinel-2; d) RGB 3-2-12 with a vegetation mask. In Landsat-9 images its impossible to distinguish granites from metasediments and marked areas appear in bright yellow. In Sentinel-2 images, marked aras are also in bright yellow and granites (bluish grey) and metasediments (yellow) can be distinguished. Coordinate System: UTM29N WGS84. 85

Figure 40. RGB combination (6-7-4) that identify lithological contrasts in Landsat-9. Coordinate System: UTM29N WGS84. 86

Figure 41. RGB combination (11-4-12) that identify lithological contrasts in Sentinel-2. Coordinate System: UTM29N WGS84. 87

Figure 42. Iron oxides ratios: a) Sentinel-2’s ratio 4/2 image with density slice (high ratio values shown in red); b) Sentinel-2’s ratio 4/2 image; c) histogram for Sentinel-2’s 4/2 image; d) Landsat-9’s ratio 4/2 image with density slice (high ratio values shown in red); e) Landsat-9’s ratio 4/2 image; f) histogram for Landsat-9’s 4/2 image. 88

Figure 43. Ferric iron ratios: a) Sentinel-2’s ratio 4/3 image with density slice (high ratio values shown in red); b) Sentinel-2’s ratio 4/3 image; c) histogram for Sentinel-2’s 4/3 image; d) Landsat-9’s ratio 4/3 image with density slice (high ratio values shown in red); e) Landsat-9’s ratio 4/3 image; f) histogram for Landsat-9’s 4/3 image. 90

Figure 44. Ferrous minerals ratios: a) Sentinel-2’s ratio 11/8 image with density slice (high ratio values shown in red); b) Sentinel-2’s ratio 11/8 image; c) histogram for Sentinel-2’ 11/8 image; d) Landsat-9’s ratio 6/5 image with density slice (high ratio values shown in red); e) Landsat-9’s ratio 6/5 image; f) histogram for Landsat-9’s 6/5 image. 91

Figure 45. Alunite and clay minerals ratios: a) Sentinel-2’s ratio 11/12 image with density slice (high ratio values shown in red); b) Sentinel-2’s ratio 11/12 image; c) histogram for Sentinel-2’s

11/12 image; d) Landsat-9's ratio 6/7 image with density slice (high ratio values shown in red); e) Landsat-9's ratio 6/7 image; f) histogram for Landsat-9's 6/7 image..... 93

Figure 46. Spodumene ratios: a) Sentinel-2's ratio 3/8 image with density slice (high ratio values shown in red); b) Sentinel-2's ratio 3/8 image; c) histogram for Sentinel-2's 3/8 image; d) Landsat-9's ratio 3/5 image with density slice (high ratio values shown in red); e) Landsat-9's ratio 3/5 image; f) histogram for Landsat-9's 3/5 image. 95

Figure 47. Lepidolite ratios: a) Sentinel-2's ratio 4/12 image with density slice (high ratio values shown in red); b) Sentinel-2's ratio 4/12 image; c) histogram for Sentinel-2's 4/12 image; d) Landsat-9's ratio 4/7 image with density slice (high ratio values shown in red); e) Landsat-9's ratio 4/7 image; f) histogram for Landsat-9's 4/7 image. 97

Figure 48. RGB combination of PC1, -PC4 and -PC5 for Sentinel-2. Granites appear in a green color and metasediments in blue; vegetation is discriminated in pink; high contents of iron oxides are presented in intense blue and hydroxyl minerals in light blue. The "Palão" quarry, Rebordelo exploration and Ervedosa mine, all appear in green. All burned areas appear in aan intense red color..... 99

Figure 49. RGB combination of PC1, PC6 and -PC4 for Landsat-9. Granites appear in a blue color and metasediments in green to blue; vegetation is discriminated in pink; high contents of iron oxides are presented in intense blue and hydroxyl minerals in light blue. The "Palão" quarry, Rebordelo exploration and Ervedosa mine, all appear in dark blue. All burned areas appear in a greenish yellow.....101

Figure 50. RGB combination of PC1, PC2 and PC3 of Landsat-9.....102

Figure 51. Selective PCA on 4 bands to highlight ferric iron: a) PC4 from Sentinel-2 subset; b) Selective F band (-PC4) from the Sentinel-2 subset; c) PC4 from Landsat-9 subset; d) Selective F band (-PC4) from the Landsat-9 subset. 104

Figure 52. Selective PCA on 4 bands to highlight hydroxyl minerals: Selective H band (PC4) from the Sentinel-2 subset. 106

Figure 53. Selective PCA on 4 bands to highlight hydroxyl minerals: Selective H band (PC4) from the Landsat-9 subset.....106

Figure 54. Selective PCA on 4 bands to highlight Li-bearing minerals: a) Selective Li bearing band (PC2) from Sentinel-2 subset; b) PC3 from Landsat-9 subset; c) Selective Li band (-PC3) from Landsat-9 subset.....108

Figure 55. RGB combination of Selective H band, Selective H band + Selective F band and Selective F band for Sentinel-2. This combination maps hydrothermal alteration areas. 109

Figure 56. RGB combination of Selective H band, Selective H band + Selective F band and Selective F band for Landsat-9. This combination maps hydrothermal alteration areas. 110

Figure 57. SAM classification result, using the Rebordelo exploration as the input spectral feature for training. The red polygon represents the Circo area. 111

Figure 58. SAM classification result, using the Ervedosa mine as the input spectral feature for training. The red polygon represents the Circo area. 111

Figure 59. Both SAM analysis overlapped, over a satellite image; some of the selected remote sensing targets area represented in the blue areas. The red polygon represents the Circo area. 112

Figure 60. Extracted lineaments over a hillshade image (with 135º of azimuth of the light). Green and red lines correspond to geological faults, and blue lines are probable faults.....113

Figure 61. Rose diagram where the trends of the extracted lineaments were plotted. Two main directions are visible: the first around N22ºE, and the second, N112ºE. 114

Figure 62. All the remote sensing targets considered initially, over the Portuguese geological map 1:200 000. 115

Figure 63. Remote sensing targets with field validation; numbered from T1 to T39, over the Portuguese geological map 1:200 000. 116

Figure 64. a) Target 2 soil; b) target 2 sample bag.....118

Figure 65. Target 3 sample bag. 118

Figure 66. a) and b) T4 deitailed images; c) T4 outcrop ; d) T4 sample bag. 119

Figure 67. a) T5 outcrop; b) and c) a portion of T5`s sample; d) T5 sample bag. 120

Figure 68. a) Soil found in T7; b) T7 sample bag. 120

Figure 69. a) Outcrop found in T10; b) and c) a portion of T10 sample; d) soil found in T10; e) detailed picture of T10 soil. 121

Figure 70. Distance picture that shows the different between T13 (granites zone) and T14 (metasediments zone) soil color. 122

Figure 71. a) and b) Highly weathered granite outcrop in T13. 122

Figure 72. a) T14 terrain with planted vineyards; b) a portion of T14 sample (banded (mica)-schist); c) T14 sample bag. 123

Figure 73. a) T20 terrain; b) T20 sample bag. 123

Figure 74. Quartzite outcrop in T22 zone. 124

Figure 75. a) T24 terrain; b) T24 sampling site.....124

Figure 76. a) T26 terrain; b) T26 soil; c) T26 sampling site. 125

Figure 77. a) T31/32 terrain; b) T31/32 sampling site.....126

Figure 78. a) and b) T33 terrain; c) T33 sampling site.....126

Figure 79. a) T35 terrain; b) detailed picture of T35 soil; c) T35 sampling site. 127

Figure 80. Geological map produced at 1:95 000 scale. Stars represent locations where samples were collected. 130

Figure 81. a) Detailed picture showing the most relevant features displayed by the two-mica granite. b) Picture of Sample 1 bag. 131

Figure 82. a) Quaternary deposit outcrop; b) intercalation of levels composed of coarse-grained elements and levels containing fine-grained elements. 132

Figure 83. T4 sample bag. 133

Figure 84. General features observed in the field; a), b) and c) general overview of pelite outcrop; d) detailed picture showing the most relevant features; e) detailed picture of Sample 2 bag. 134

Figure 85. Quartzite outcrop. 135

Figure 86. General features observed in the field; a) and b) general overview of quartz-phyllite outcrop; c) detailed picture showing the most relevant features; d) detailed picture of sample 3 bag. 136

Figure 87. Basic statistics for each lithology, generated by ioGAS (pink color represents granite; bue color represents granite+schist; green color represents schist; yellow rows represent the values that were used for the IQR standardization (IQR and Tukey upper outlier threshold). ..139

Figure 90. Al graphics and map: a) boxplot; b) histogram; c) Q-Q plot; d) Split Q-Q plot; e) variable map; (images -a to -d discriminate the difference between the lithologies (green – schist; pink – granite; blue – granite+schist), image -e presents a map where the large dots and warmer colors represent higher Al contents). 140

Figure 91. K graphics and map: a) boxplot; b) histogram; c) Q-Q plot; d) Split Q-Q plot; e) variable map; (images -a to -d discriminate the difference between the lithologies (green – schist; pink – granite; blue – granite+schist), image -e presents a map where the large dots and warmer colors represent higher K contents). 141

Figure 92. Mn graphics and map: a) boxplot; b) histogram; c) Q-Q plot; d) Split Q-Q plot; e) variable map; (images -a to -d discriminate the difference between the lithologies (green – schist; pink – granite; blue – granite+schist), image -e presents a map where the large dots and warmer colors represent higher Mn contents). 142

Figure 93. Nb graphics and map: a) boxplot; b) histogram; c) Q-Q plot; d) Split Q-Q plot; e) variable map; (images -a to -d discriminate the difference between the lithologies (green – schist; pink – granite; blue – granite+schist), image -e presents a map where the large dots and warmer colors represent higher Nb contents).....142

Figure 94. Rb graphics and map: a) boxplot; b) histogram; c) Q-Q plot; d) Split Q-Q plot; e) variable map; (images -a to -d discriminate the difference between the lithologies (green – schist; pink – granite; blue – granite+schist), image -e presents a map where the large dots and warmer colors represent higher Rb contents).....143

Figure 95. Sn graphics and map: a) boxplot; b) histogram; c) Q-Q plot; d) Split Q-Q plot; e) variable map; (images -a to -d discriminate the difference between the lithologies (green – schist; pink – granite; blue – granite+schist), image -e presents a map where the large dots and warmer colors represent higher Sn contents).....144

Figure 96. Th graphics and map: a) boxplot; b) histogram; c) Q-Q plot; d) Split Q-Q plot; e) variable map; (images -a to -d discriminate the difference between the lithologies (green – schist; pink – granite; blue – granite+schist), image -e presents a map where the large dots and warmer colors represent higher Th contents).....145

Figure 97. W graphics and map: a) boxplot; b) histogram; c) Q-Q plot; d) Split Q-Q plot; e) variable map; (images -a to -d discriminate the difference between the lithologies (green – schist; pink – granite; blue – granite+schist), image -e presents map where the large dots and warmer colors represent higher W contents).....145

Figure 98. Biplot projecting components RQ1 and RQ4; PCA of group "PATH1". 147

Figure 99. Biplot projecting components RQ1 and RQ3; PCA of group "PATH1". 148

Figure 100. 3D biplot of PCA; group "PATH1".....149

Figure 101. Biplot projecting components RQ1 and RQ2; PCA of group "PATH2". 150

Figure 102. Biplot projecting components RQ2 and RQ4; PCA of group "PATH2". 151

Figure 103. 3D biplot of PCA; group "PATH2".....152

Figure 104. Biplot projecting components RQ1 and RQ3; PCA of group "PATH3". 153

Figure 105. Biplot projecting components RQ1 and RQ2; PCA of group "PATH3". 154

Figure 106. 3D biplot of PCA; group "PATH3".....155

Figure 107. Biplot projecting components RQ1 and RQ2; PCA of group "PATH4". 156

Figure 108. Biplot projecting components RQ2 and RQ4; PCA of group "PATH4". 157

Figure 109. 3D biplot of PCA; group "PATH4".....158

Figure 110. a) Thematic map based on the Tukey values of Al; b) thematic map based on standardized Tukey values of Al.....159

Figure 111. a) Thematic map based on the Tukey values of K; b) thematic map based on standardized Tukey values of K. 160

Figure 112. a) Thematic map based on the Tukey values of Mn; b) thematic map based on standardized Tukey values of Mn. 161

Figure 113. a) Thematic map based on the Tukey values of Nb; b) thematic map based on standardized Tukey values of Nb. 161

Figure 114. a) Thematic map based on the Tukey values of Rb; b) thematic map based on standardized Tukey values of Rb. 162

Figure 115. a) Thematic map based on the Tukey values of Sn; b) thematic map based on standardized Tukey values of Sn. 163

Figure 116. a) Thematic map based on the Tukey values of Th; b) thematic map based on standardized Tukey values of Th. 164

Figure 117. Thematic map based on the Tukey values of W. 164

List of tables

Table 1. Landsat-9 OLI-2 and TIRS-2 Bands (adapted from: Landsat-9 Data Users Handbook, 2022). 23

Table 2. Sentinel-2A bands' characteristics (adapted from: ESA, 2018c). 25

Table 3. RGB combinations tested for the Landsat-9 and Sentinel-2 imagery. 50

Table 4. Band ratios tested for Landsat-9 and Sentinel-2 imagery. 51

Table 5. Chosen subsets to the application of selective PCA and respective target mineral information 52

Table 6. PCA on 6 Sentinel-2 bands: Eigenvector and eigenvalues matrix. 98

Table 7. PCA on 6 Landsat-9 bands: Eigenvector and eigenvalues matrix. 100

Table 8. Selective PCA for ferric iron mapping (four Sentinel-2 bands): Eigenvector and eigenvalues matrix. 103

Table 9. Selective PCA for ferric iron mapping (four Landsat-9 bands): Eigenvector and eigenvalues matrix. 103

Table 10. Selective PCA for hydroxyl minerals mapping (four Sentinel-2 bands): Eigenvector and eigenvalues matrix. 105

Table 11. Selective PCA for hydroxyl minerals mapping (four Landsat-9 bands): Eigenvector and eigenvalues matrix. 105

Table 12. Selective PCA for Li-bearing minerals mapping (four Sentinel-2 bands): Eigenvector and eigenvalues matrix. 107

Table 13. Selective PCA for Li-bearing minerals mapping (four Landsat-9 bands): Eigenvector and eigenvalues matrix. 107

Table 14. XRF and LIBS analysis results (T2 sample). 118

Table 15. XRF and LIBS analysis results (T3 sample). 118

Table 16. XRF and LIBS analysis results (T4 sample). 119

Table 17. XRF and LIBS analysis results (T5 sample). 120

Table 18. XRF and LIBS analysis results (T7 sample). 121

Table 19. XRF and LIBS analysis results (T10 sample). 122

Table 20. XRF and LIBS analysis results (T13 sample). 122

Table 21. XRF and LIBS analysis results (T14 sample). 123

Table 22. XRF and LIBS analysis results (T20 sample). 124

Table 23. XRF and LIBS analysis results (T22 sample). 124

Table 24. XRF and LIBS analysis results (T24 sample). 125

Table 25. XRF and LIBS analysis results (T26 sample). 125

Table 26. XRF and LIBS analysis results (T31/32 sample). 126

Table 27. XRF and LIBS analysis results (T33 sample). 127

Table 28. XRF and LIBS analysis results (T35 sample). 127

Table 29. XRF and LIBS analysis results (T39 samples). 128

Table. 30 Main features related to Sample 1.....131

Table. 31 Main features related to Sample T4.....132

Table. 32 Main features related to Sample 2.....133

Table 33. Main features related to Sample T22.....134

Table. 34 Main features related to Sample 3.....135

Table of contents

1. Introduction 18

1.1. Remote sensing 20

1.2. Geological mapping 26

1.3. Stream sediments analysis 30

2. General description 32

2.1. Location 32

2.2. Physiography 33

2.3. Description of the Tenement 34

2.4. Historical background 35

3. Geological Setting 37

3.1. Regional Geology 37

3.2. Local Geology 41

3.3. Circo Prospectivity Support 43

4. Methodology 44

4.1. Remote sensing 44

4.1.1. Data 44
4.1.2. GIS Software 44
4.1.3. Image Processing 44
4.1.3.1. Pre-processing 45
4.1.3.2. Image processing methods 47
4.1.4. Targets analysis 53

4.2. Geological mapping 57

4.2.1. Planning 57
4.2.2. Data collection 58
4.2.3. Reporting (database) 65

4.3. Stream sediments analysis 66

4.3.1. Generation of water streams, catchment basins and outlets 66
4.3.2. Stream sediments sampling and washing 67
4.3.3. XRF analysis 71
4.3.4. Detection of anomalous catchment basins 74

5. Results 77

5.1. Remote sensing 77

5.1.1. RGB combinations 77
5.1.2. Band ratios 87
5.1.3. Principal Component Analysis (PCA) 98
5.1.4. Spectral Angle Mapper (SAM) 111
5.1.5. Lineament extraction 113
5.1.6. Remote sensing targets 115
5.2. Geological Mapping 130
5.3. Stream sediment analysis 138
5.3.1 Exploratory data analysis (EDA) 138
5.3.2. Anomalies determination and creation of thematic maps 159
6. Discussion 166
6.1. Remote Sensing 166
6.2. Geological mapping 169
6.3. Stream sediments analysis 170
7. Conclusions 173
8. References 174
Appendices 185
Appendix A – XRF results of the stream sediment samples 185
Appendix B – Graphics and maps of all elements (stream sediments) 188
Appendix C – Basic statistics of all stream sediment samples 201
Appendix D – PCA applied to the stream sediment samples 202
Appendix E – Pearson correlation matrices for the stream sediment samples 227
Appendix F – Tukey values (Anomaly Assessment Tool for the stream sediment samples) 230
Appendix G – Standardized Tukey values for stream sediment anomaly definition ... 232

1. Introduction

Lithium (Li) has always been an element with several applications, especially in the ceramic and glass industries, and has become a strategic metal due to its physical and chemical properties, being the lightest solid element and an excellent conductor of heat and electricity (Gourcerol *et al.*, 2019). Over the last decade, the increased demand for more environmentally friendly technologies and energies has led to an increase in demand for this element. This increased interest stems from the need to produce rechargeable batteries (European Commission: DG Internal Market Industry Entrepreneurship and SMEs, 2020), which allow for greater energy storage, helping the construction of electric vehicles that require less environmental expenditure than a fuel car, and the need to stop high emissions of greenhouse gases, since Li, when it is used, has zero greenhouse gas emissions. In 2020, the European Commission added Li to the Critical Raw Materials (CRM) list. As stated by the European Commission President von der Leyen, “Lithium and rare earths will soon be more important than oil and gas”.

The remote sensing analysis has proved itself an important tool to locate mineral deposits by recognizing processes of mineralization through spectral anomalies (Sabins, 1999; Rajesh, 2004; Cardoso-Fernandes, et al. 2021). It is a powerful technique for identifying hydrothermally altered rocks, structures, geological lineaments, oxidation products, morphology, lithological units, vegetation anomalies, and other valuable information to geologists (Sabins, 1999; Goetz et al., 1982; Drury, 2001; Frutuoso, et al. 2021).

The combination of remote sensing with other geological exploration techniques can be useful to create mineral potential maps defining exploration targets (Köhler *et al.*, 2021). In this study, remote sensing techniques were complemented by geological mapping and stream sediments analysis to create a “well-supported project” which can guide future exploration campaigns. The objective of this study is to create target areas, and visit them on the field, evaluating their potential for Li exploration.

The work described in this report was developed during an internship with Fortescue Portugal Unipessoal Lda. (Fortescue) (subsidiary of Fortescue Metals Group Ltd.). Fortescue holds several applications for prospection in Portugal with the main focus on Li exploration. The company acquired the Circo License from Direcção Geral de Energia e Geologia (DGEG) in October 2021. This license covers three municipalities: Macedo de Cavaleiros, Vinhais and Mirandela, in a total area of 254,5 Km^2.

Geologically, the area is located in the Galicia Trás-os-Montes Zone (GTMZ), with the presence of peraluminous Variscan granites, Silurian metasediments, and tin (Sn)-bearing pegmatites.

There is a record of old tin (Sn) and tungsten (W) mining around the licensed area, namely in Ervedosa, Murçós and Agrochão, but the region has never been studied in terms of Li potential. Some geological mapping is not published in the area (07-A and 07-B sheets of Portugal's geological map at scale 1:50 000), and this work tries to fill this gap.

The Circo area has never been targeted for Li before, so, there is a weak understanding of the occurrence of Li mineralizations in this region, thus constituting a classical greenfield area for exploration. In order to identify possible areas with Li mineralization, a remote sensing approach was applied using Landsat-9 and Sentinel-2 multispectral imagery. The satellite imagery was analyzed in a Geographic Information System (GIS) environment by applying different image processing techniques to identify iron oxides, hydroxyls, and Li-bearing minerals. The results were interpreted and spatial analysis tools were used to define new target areas.

The geological mapping and a stream sediments campaign were made simultaneously with the remote sensing work. During the geological mapping work, some samples were collected and analyzed, and combining with the other techniques a geological map was produced. Stream sediments samples were collected and analyzed with XRF (X-ray fluorescence spectroscopy), and then the objective was to identify pathfinders that correlate with Li, since XRF does not obtain the Li values. Histograms, boxplots and Q-Q plots were produced in ioGAS software, along with the basic statistics. Then, IQR (interquartile range) standardization by lithologies was also made. After that, the determination of anomalies was carried out using the boxplots method, in order to create thematic maps and find the anomalous basins.

1.1. Remote sensing

Remote sensing is the analysis of data obtained by sensors in satellites or more recently portable, that allow to obtain, process and interpret information from the interaction between between matter and electromagnetic energy at a distance (Sabins, 1997). Remote sensing applied to geology consist on differences in the chemical and physical properties of rocks, thus different rock types emit electromagnetic energy at different wavelengths of the electromagnetic spectrum (Figure 1) that will be unique to that rock (Bachri et al., 2019), thus allowing for lithological and mineral mapping.

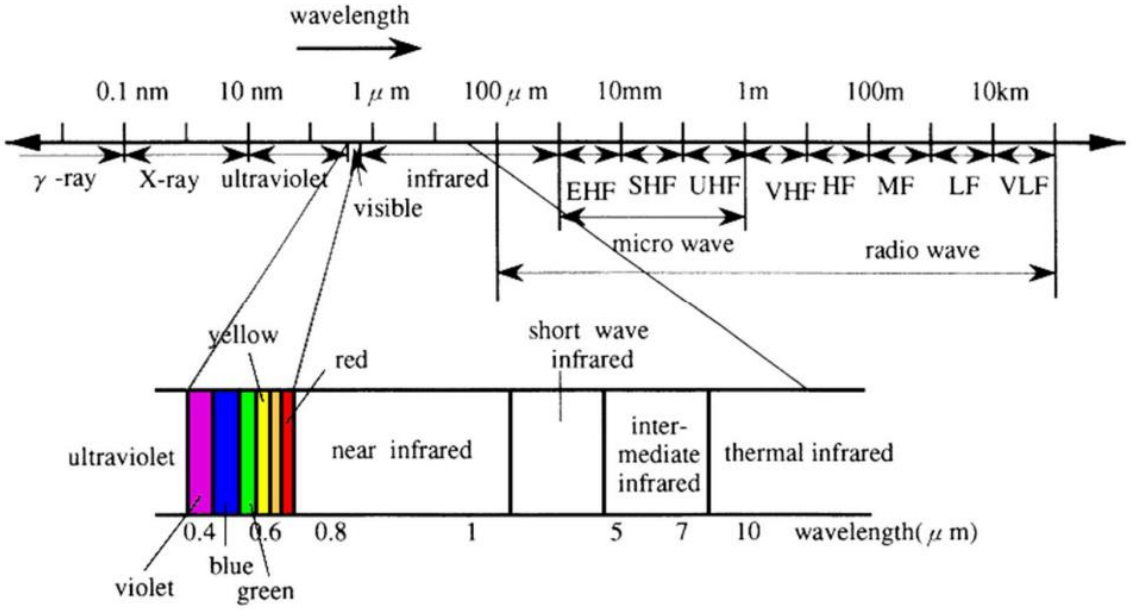


Figure 1. The eletromagnetic spectrum (adapted from: JARS, 1993).

Depending on how the energy is used and detected, two forms of remote sensing could be defined: if the source of energy is the sun, then it is called passive remote sensing; if the energy is emitted by the sensor, then it is called active remote sensing (JARS, 1993; Richards & Jia, 2006).Minerals have important absorption features in the regions of visible, NIR (Near Infrared), SWIR (Short Wave Infrared) and TIR (Thermal Infrared) which is why passive sensors are the most used in the field of geology.

The sensors can be on board aircrafts, satellites and, more recently, drones, measuring the electromagnetic radiation at specific wavelength ranges (frequently called bands). The sensors measure a physical parameter named radiance, which corresponds to the brightness in a given direction toward the sensor. Another important parameter is the reflectance, that is, the ratio of reflected versus total power energy.

The measures are quantized and converted to a digital image, called a raster, composed of a bi-dimensional matrix of picture elements (pixels). The intensity of each pixel corresponds to a discrete numerical value – a Digital Number (DN) (NASA, 2021; Richards & Jia, 2006).

In the last decades, geological remote sensing has proved to be a great tool in mineral exploration. Many ore deposits have been recognized using satellite imagery (Sabins, 1999; van der Meer *et al.*, 2012; Gao *et al.*, 2020; Pour & Hashim, 2015). Geologists developed techniques and analysis methods to digitally process satellite images and recognize hydrothermal alteration areas. This is possible because each mineral or rock has a unique spectral signature, and therefore these signatures can be used for geological classification and mapping. The identification of the mineral assemblage resulting from hydrothermal alteration can allow the recognition of mineralized areas (Sabins, 1999; Rajesh, 2004; Moradi *et al.*, 2014). Typical applications of hydrothermal alteration mapping include the prediction of the occurrence of iron oxides and clay minerals.

The application of remote sensing to discover pegmatite deposits have been studied by several authors (Santos, et al., 2022; Gao, et al., 2020; Rossi, et al., 2020; Cardoso-Fernandes et. al., 2022). For example, Gao, et al., 2020, prove that combining geological mapping, geochemistry and remote sensing it is possible to find Li-bearing pegmatites.

It is also important to mention the history and characteristics of the different remote sensing satellite missions used in this work.

The Landsat program represents the world's longest continuously acquired collection of space-based land remote sensing data with a moderate multispectral resolution (USGS, 2017b). Since 1972, in a joint effort of the United States Geological Survey (USGS) and the National Aeronautics and Space Administration (NASA), the Landsat series of Earth Observation (EO) satellites have continuously acquired images of the Earth’s surface, providing data to help research areas focused on land applications such as geology, hydrology, geography, among others. The Landsat missions have sent eight satellites to space. The last one was Landsat-9 on September 27th, 2021 (NASA, 2021).

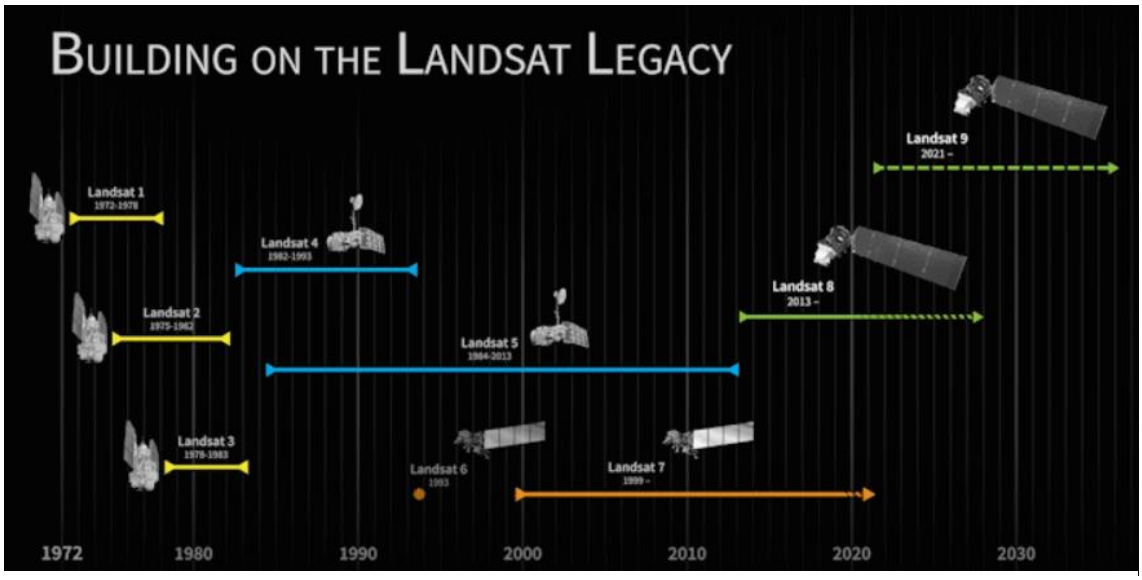


Figure 2. Landsat missions` timeline (NASA, 2021).

Landsat-9 carries two instruments: the Operational Land Imager 2 (OLI-2) and the Thermal Infrared Sensor 2 (TIRS-2). Each Landsat-9 (Level 1) scene contains a grayscale image file for each band (nine for OLI-2 and two for TIRS-2), along with two QA (Quality Assessment) bands, two metadata files, and five files related to Angle Coefficients (USGS, 2022). Of these eleven bands, eight of them have a spatial resolution of 30 meters (bands 1, 2, 3, 4, 5, 6, 7 and 9). Band 8 (panchromatic) has a 15 meters spatial resolution and bands 10 and 11 (thermal bands) have a 100 meters spatial resolution (these two bands are acquired at 100 meters resolution but are resampled to 30 meters).

Bands 1 (ultra-blue) and 9 (cirrus) are useful for coastal and aerosol studies, and for cirrus cloud detection, respectively. Bands 2, 3 and 4 correspond to the visible (red, green, blue (RGB)), band 5 corresponds to the Near-infrared (NIR), and bands 6 and 7 correspond to the Shortwave infrared (SWIR). The Thermal Infrared bands (TIRS) (10 and 11) provide more accurate surface temperatures. Table 1 show all these aspects.

Table 1. Landsat-9 OLI-2 and TIRS-2 Bands (adapted from: Landsat-9 Data Users Handbook, 2022).

Landsat-9 Operational Land Imager 2 (OLI-2) and Thermal Infrared Sensor 2 (TIRS-2)		
Band Number/ description	**Band Range (nm)**	**Spatial resolution (m)**
OLI-2 Sensors		
Band 1 – Coastal / Aerosol	**435-451**	**30**
Band 2 – Blue	**452-512**	**30**
Band 3 – Green	**533-590**	**30**
Band 4 – Red	**636-673**	**30**
Band 5 – Near infrared (NIR)	**851-879**	**30**
Band 6 – Shortwave infrared (SWIR) 1	**1566-1651**	**30**
Band 7 - Shortwave infrared (SWIR) 2	**2107-2294**	**30**
Band 8 - Panchromatic	**503-676**	**15**
Band 9 - Cirrus	**1363-1384**	**30**
TIRS-2 Sensors		
Band 10 – Thermal infrared Sensor 1	**10600-11190**	**100 (30)**
Band 11 – Thermal infrared Sensor 2	**11500-12510**	**100 (30)**

Sentinel-2 is a medium- to high-resolution, multispectral imaging mission developed by the European Space Agency (ESA) in the frame of Copernicus land monitoring services (ESA, 2018a, b). The full Sentinel-2 mission comprises twin polar-orbiting satellites in the same orbit, phased at 180° to each other, to ensure a high revisiting frequency of 5 days at the Equator (ESA, 2018b). Sentinel-2A was launched on 23 June 2015, while Sentinel-2B was launched on 7 March 2017.

The acquired data, mission coverage and high revisit frequency allow the generation of geoinformation at local, regional, national and international scales. All the data acquired by Sentinel-2 is supposed to be modified and adapted, in order to be used in several different areas such as: spatial planning, agro-environmental monitoring, water monitoring, forest and vegetation monitoring, land carbon, natural resource monitoring and global crop monitoring (ESA, 2012).

Sentinel-2 is capable of sampling in 13 spectral bands (Table 2): four bands at 10 m (bands 2, 3, 4 and 8), six bands at 20 m (bands 5, 6, 7, 8a, 11 and 12) and three bands at 60 m (bands 1, 9 and 10) spatial resolution (ESA, 2018a, b). The orbital swath width (or scene size) is 290 km. As in Landsat-9, band 1 of Sentinel-2 is also used for coastal and aerosol studies. The visible and near-infrared (VNIR) are represented by bands 2, 3, 4, 5, 6, 7, 8 and 8a. Bands 9 to 12 correspond to the SWIR. Figure 3 compares Landsat 8/9 and Sentinel-2 bands.

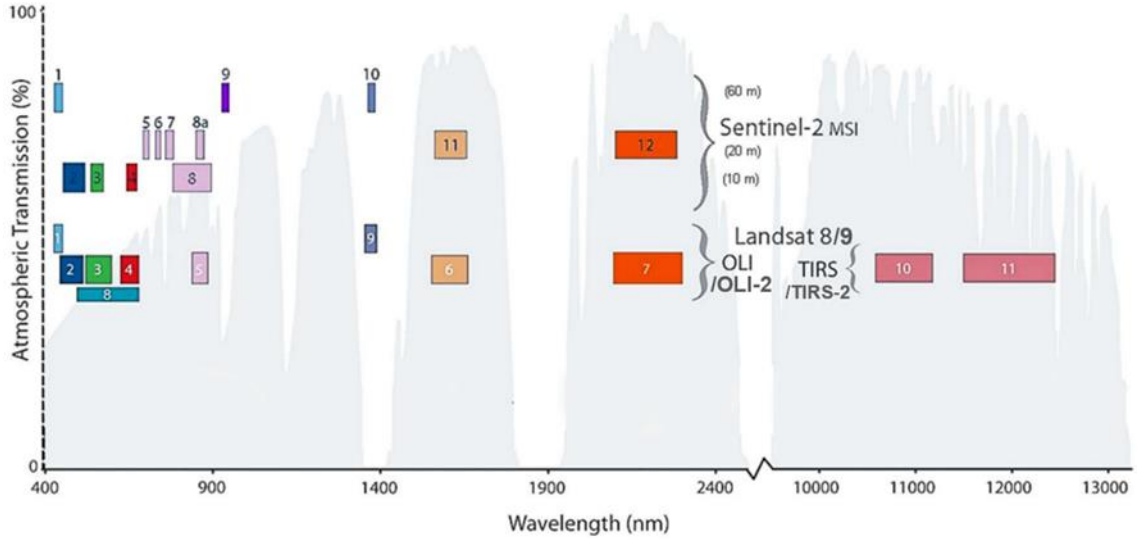


Figure 3. Comparison between Landsat-8/9 and Sentinel-2 bands (adapted from: USGS Landsat program, 2017).

Table 2. Sentinel-2A bands' characteristics (adapted from: ESA, 2018c).

Sentinel-2A			
Band number/ description	**Central wavelength (nm)**	**Bandwidth (nm)**	**Spatial Resolution (m)**
Band 1 – Coastal / Aerosol	**443.9**	**27**	**60**
Band 2 – Blue	**496.6**	**98**	**10**
Band 3 – Green	**560.0**	**45**	**10**
Band 4 – Red	**664.5**	**38**	**10**
Band 5 – Visible and Near Infrared (VNIR)	**703.9**	**19**	**20**
Band 6 - Visible and Near Infrared (VNIR)	**740.2**	**18**	**20**
Band 7 - Visible and Near Infrared (VNIR)	**782.5**	**28**	**20**
Band 8 - Visible and Near Infrared (VNIR)	**835.1**	**145**	**10**
Band 8a - Visible and Near Infrared (VNIR)	**864.8**	**33**	**20**
Band 9 - Shortwave infrared (SWIR)	**945.0**	**26**	**60**
Band 10 - Shortwave infrared (SWIR)	**1373.5**	**75**	**60**
Band 11 - Shortwave infrared (SWIR)	**1613.7**	**143**	**20**
Band 12 - Shortwave infrared (SWIR)	**2202.4**	**242**	**20**

1.2. Geological mapping

Geologic mapping is a highly interpretive, scientific process that can produce a range of map products for many different uses, including assessing ground-water quality and contamination risks; predicting earthquake, volcano, and landslide hazards; characterizing energy and mineral resources and their extraction costs; waste repository siting; land management and land-use planning; and general education (USGS, 2004).

The geological map is a scientific and technical document that graphically represents synthetically, on an appropriate topographic background, information relating to the rocky materials that outcrop on the surface of the Earth's crust and the phenomena that affected them in the past, some of which persist today. It contains abundant information on the nature and spatial distribution of the different rocks, both on the surface and at depth, their position, attitude, relative or absolute age and the tectonic movements that have occurred during geological time, as well as the occurrence of mineral substances and the location of fossil deposits, natural water springs, wells, quarries, among others (Bolton, 1989). In a more traditional conception, the geological map is presented in analogical format (Figure 4), accompanied by the respective explanatory notes.

The geologic mapping activity is fundamental for understanding the composition and structure of geologic materials at the Earth's surface and at depth, and to represent observations and interpretations on maps using specific symbols and colors. Therefore, proper geological maps with high accuracy and all details are crucial for the mineral exploration process, otherwise, the exploration cannot be carried out.

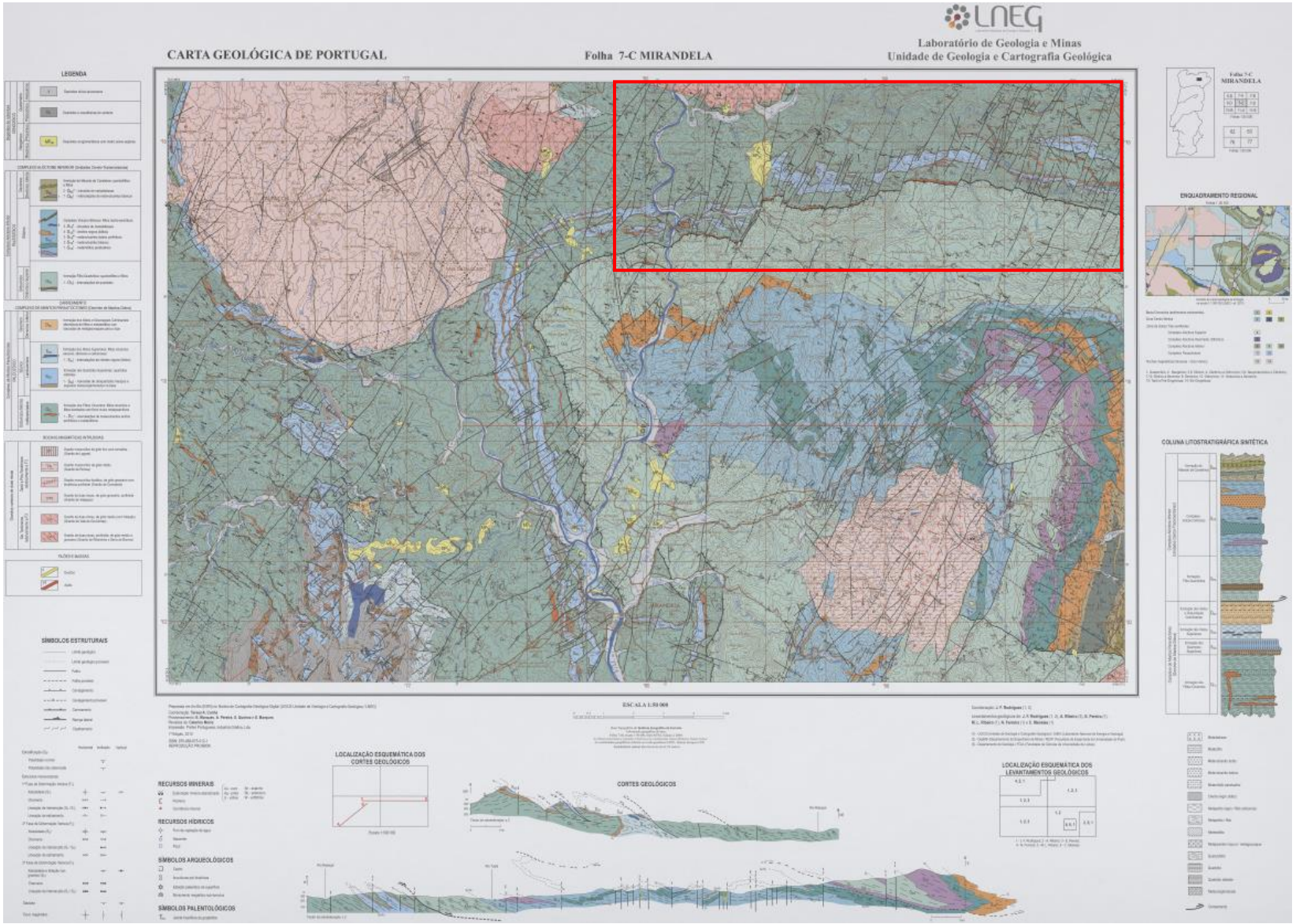


Figure 4. Geological map 1:50 000 of Mirandela, Portugal (7-C sheet); the red area represents the southern part of Circo area (LNEG, 2010).

The geological maps of Portugal are published in different scales, namely: 1:50 000, 1:200 000, 1:500 000 and 1:1 000 000. Maps with the better resolution are the ones with a higher ratio, i.e., a 1:25 000 map has better resolution than a 1:50 000 one. Scaled map 1:1 000 000 (LNEG, 2010), presents Portugal in one sheet; 1:500 000 (LNEG) in two sheets (North and South, Figure 5-a); 1:200 000 (LNEG) in eight sheets (where sheets 3 and 5 are not published, Figure 5-b); and 1:50 000 (LNEG) in 177 sheets (Figure 5-c).

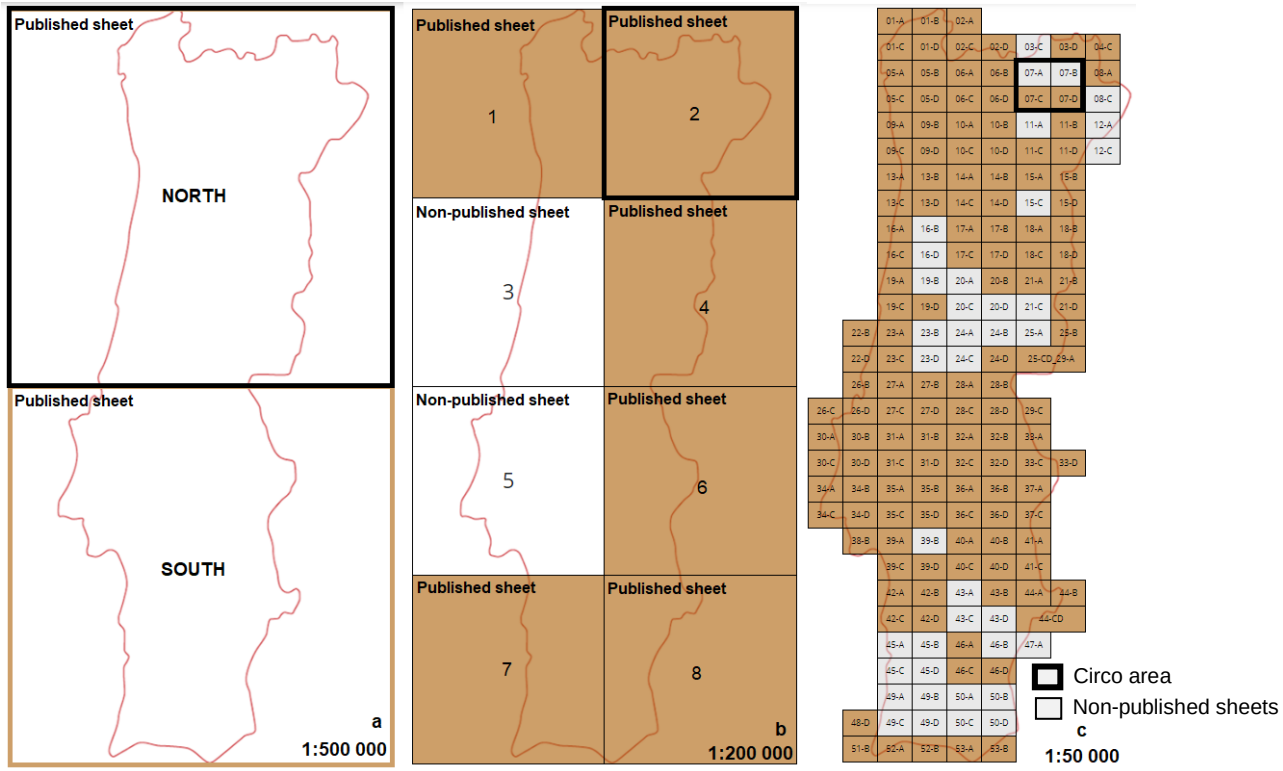


Figure 5. Location of Circo area on the Portuguese geological maps. a) Portugal divison at scale 1:500 000; b) Portugal division at scale 1:200 000; c) Portugal division at scale 1:50 000 (adapted from: LNEG).

As can be seen in Figure 5-c, sheets 7-A and 7-B from the map (corresponding to part of the Circo area) are not published, so mapping that part of the map is an objective of this work (at the scale of 1:25 000).

Within the past 10 to 20 years, geographic information system (GIS) technology has begun to change aspects of geologic mapping by providing software tools that permit the geometry and characteristics of rock bodies and other geologic features (such as faults) to be digitally stored, displayed, queried, and analyzed in conjunction with a seemingly infinite variety of other data types (USGS, 2004).

GIS allows to integrate all types of information (like lithology, mineral occurrences, structures, roads, districts, cities, topography, water streams, etc.) that can be stored in

a computer software and it greatly facilitates the analysis and, as a result, offers to geologists the opportunity to provide geo-referenced information in map form that is easily interpreted and used by others.

Currently, geological maps are presented as a set of data from different scientific areas, organized into different levels of information, which allows the use of increasingly sophisticated modeling techniques and even the representation of three-dimensional underground space in computer models in three dimensions (3D).

Geological field mapping is part of the creation of a geological map and a database with all the data collected in the field. A map showing the occurrence of structural features across a region, the distribution of rock units, and their type and age relationship is termed a geological map. Geological field mapping is the process of selecting an area of interest and identifying all the geological aspects of that area to prepare a detailed geological report which must include a map (Njue, 2013). A successful geological mapping campaign should be executed in three phases: planning, data collection and reporting. Certain parameters must be considered when mapping geology, geological landforms, structures and geothermal manifestations the most important being detail, accuracy and precision. Figure 6 presents the main stages of geological mapping.

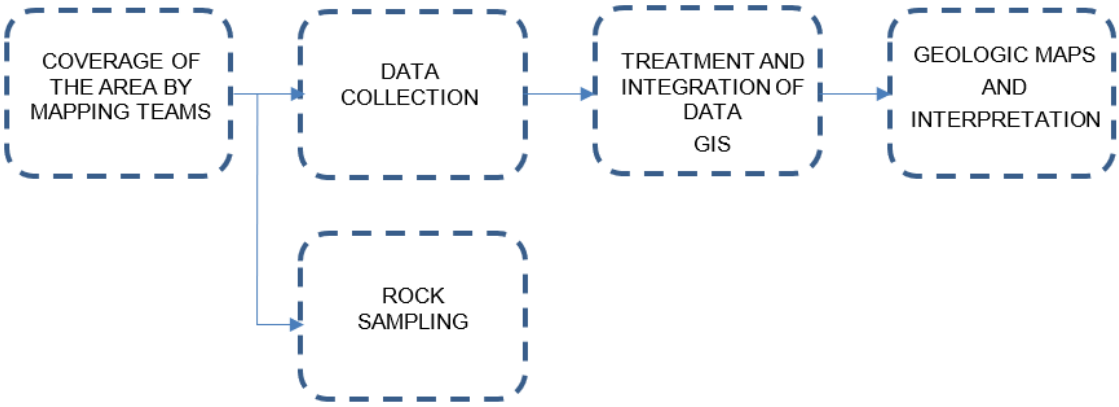


Figure 6. Main stages of geological mapping (Fortescue, 2021).

1.3. Stream sediments analysis

Stream sediment analysis has been widely used in mineral exploration (Fyzollahhi *et al.*, 2018). Stream sediments reflect the geology of upstream catchment basins (Figure 7) and therefore can imply the presence of several lithological groupings in one sample (Hale and Plant, 1994).

In licensed areas with sufficient rivers and streams, sampling stream sediments is a well-accepted tool and may be favored for early-stage mineral exploration, especially to target metallic mineral occurrences, namely gold (Au) and copper (Cu), where the pathfinder elements and their mobility are well-known (Hawkes, 1976; Cheng *et al.*, 1994; Carranza & Hale, 1997; Zuo, 2011; Mokhtari & Garousi Nezhad, 2015; Shahrestani & Mokhtari, 2017; Ghezelbash & Maghsoudi, 2018). They represent, at any point along drainage systems, composite materials derived from the weathering and erosion of one or more sources upstream. It follows the premise that uni-element concentrations in stream sediments are derived from multiple (mostly background and rarely anomalous) sources. In most cases, a major proportion of variation in stream sediment uni-element concentrations is due to lithologic units underlying the areas upstream of sample points. Elevations in the metal concentration of samples might be attributed to background differences between catchment basins or to potential mineralization occurrences inside the basin(s).

Analysis of stream sediment geochemical data alone can therefore be insufficient for the recognition of significant anomalies. Effective interpretation of stream sediment geochemical data requires the integration of every available piece of spatial information pertinent to the zone of influence of every stream sediment sample location – its catchment basin (Carranza, 2009).

Stream sediment sampling allows the delineation of target areas and reduces the number of favorable regions to conduct more detailed studies in the subsequent exploration stages (Carranza & Hale, 1997; Mokhtari & Garousi Nezhad, 2015).

Some recent articles have been proving that stream sediment campaigns can be a good technique for Li exploration. For example, the work of Cardoso-Fernandes *et al.* (2022), where one pegmatite containing Li mineralization and three others with possible Li mineralization were detected, in the Douro region. Some approaches as the ones followed in this report, basic statistics analysis, graphics, Pearson correlations, PCA and IQR standardization were used.

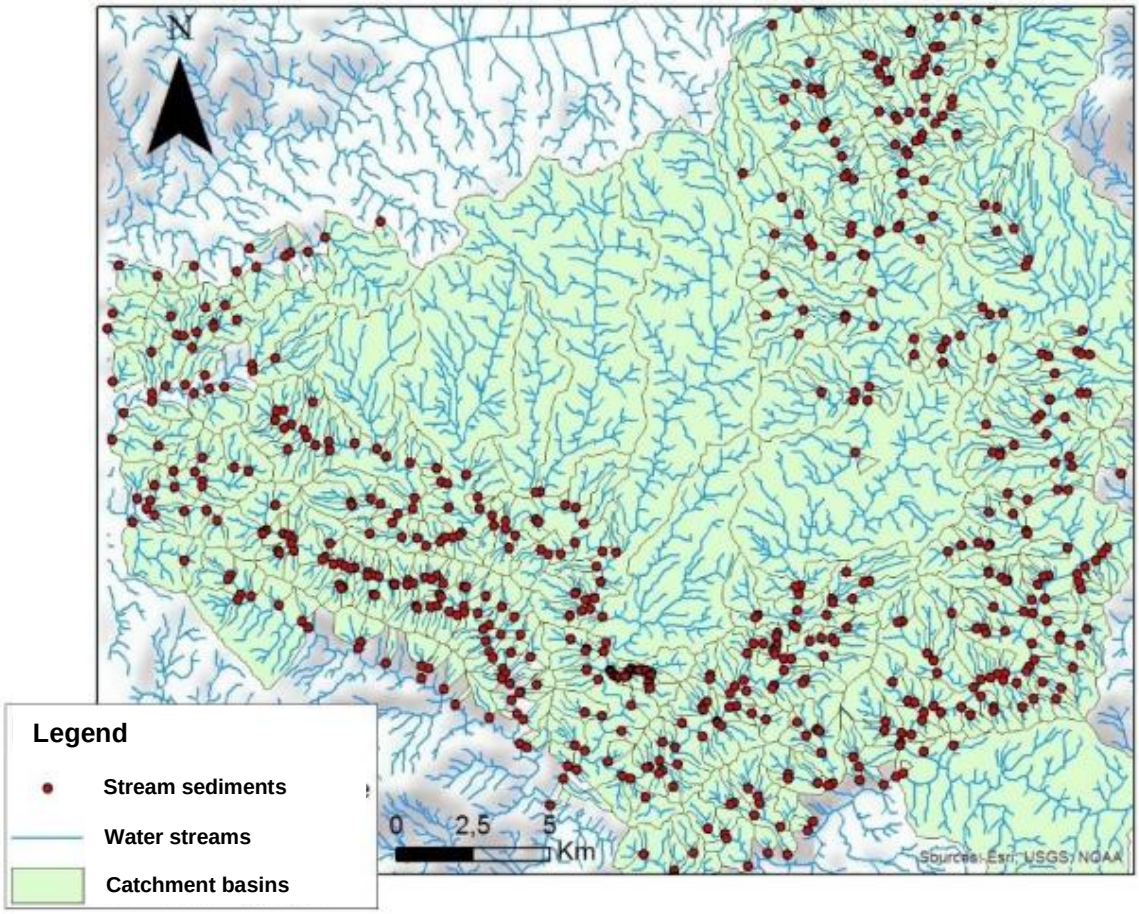


Figure 7. Catchment basins (green) generated for Barroso/Alvão area, stream sediments sampling sites (red points) and the blue lines are the water streams (adapted from: Dias, 2016)

2. General description

2.1. Location

The Circo area under study is situated in Northern Portugal, in the Trás-os-Montes region, in the Bragança district, approximately 180 km northeast of Porto and includes the municipalities of Vinhais, Mirandela and Macedo de Cavaleiros (Figure 8).

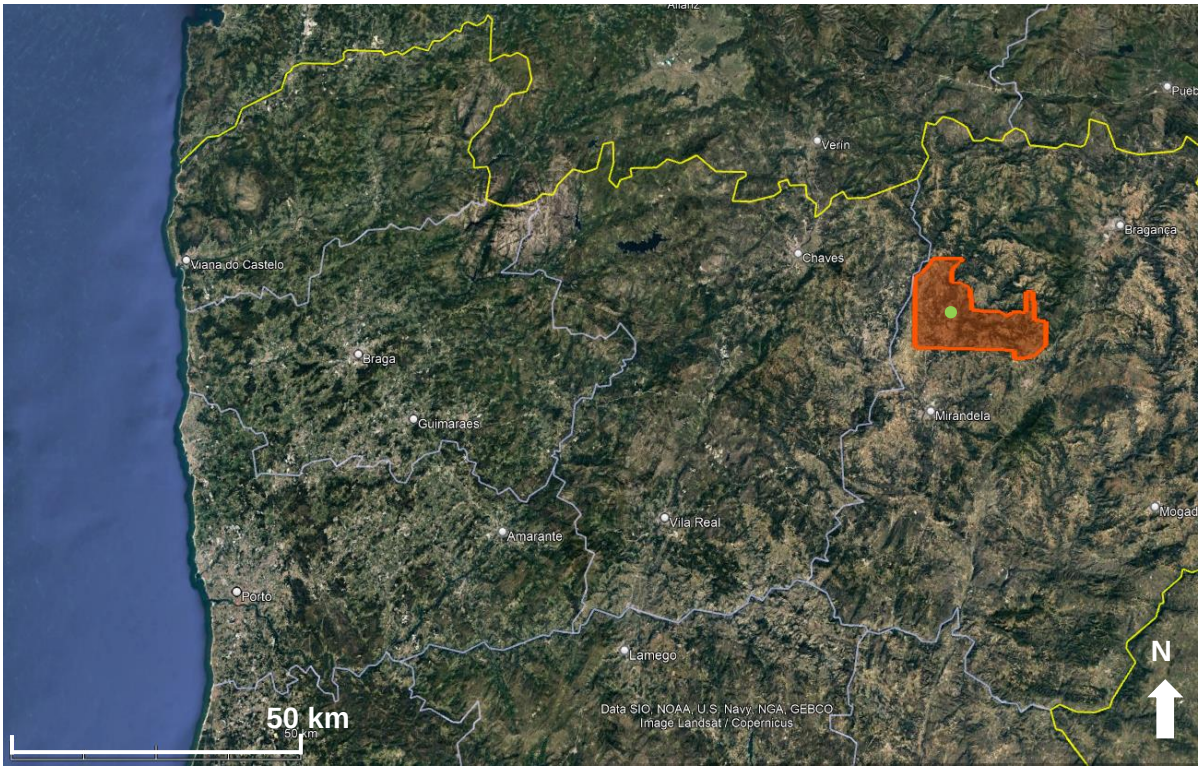


Figure 8. Study area (orange area), Circo (adapted from: Google Earth, 2015).

Theexploration team of Fortescue Portugal is based in Torre de Dona Chama (represented as a green point in Figure 8), a village in the municipality of Mirandela.

The local economy is strongly based on agricultural practices, and the demography indicates an aging population. Most of the local population and administration are supportive of resource development and exploration programs.

Historical mining works in the area are a great expression of the “Romans and Phoenicians” presence in this region, like Ervedosa, Murçós and Agrochão (Gomes, 1996). These works were open pits and their principal products were Sn and As (in the case of Ervedosa) and W and Sn (in the case of Murçós and Agrochão).

2.2. Physiography

The climate in this region is temperate with considerable thermal amplitude. The winter season is cold with high precipitation and in the summer temperatures can reach 40ºC.

As seen in Figure 9, the topography is mountainous with deep valleys on the east side of the area and the altitude range between 240 m, at the Tuela river (west side, Mirandela and Vinhais region, blue/green/yellow areas) and 800 m, in Macedo de Cavaleiros (east side of the concession, dark orange/black areas). The Tuela river runs through the area following the regional orientation of N30ºE. It is a subsequent water stream, controlled by tectonic structures, with steep valleys (Gomes, 1996).

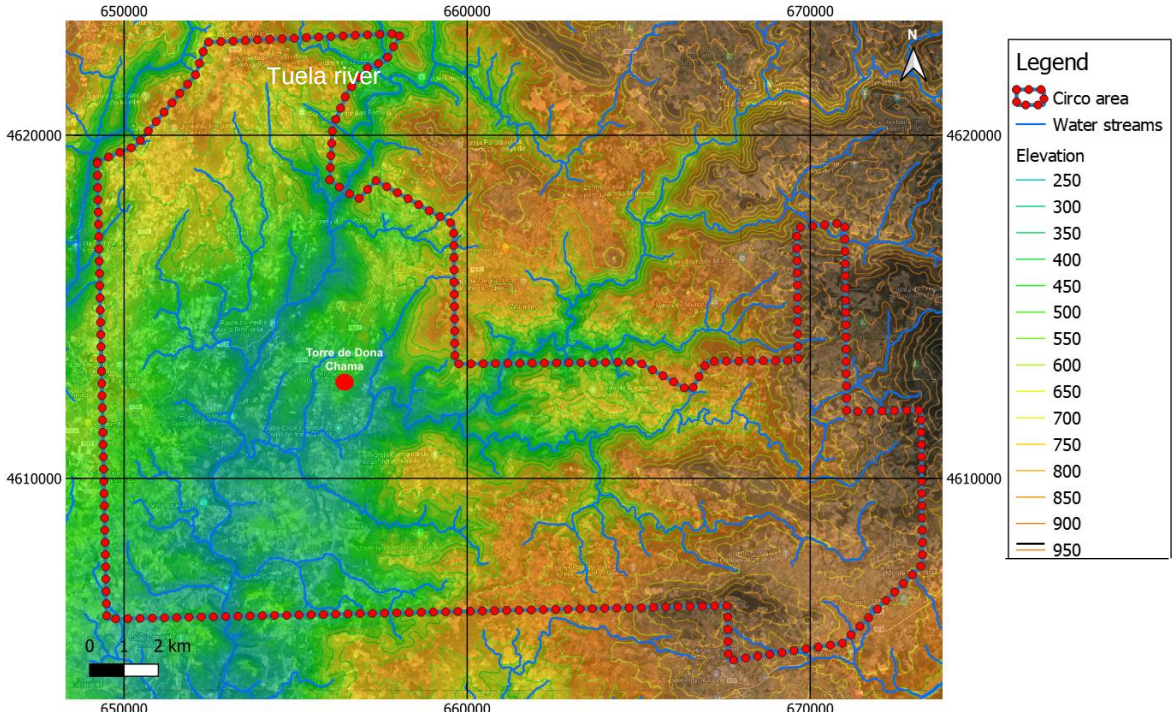


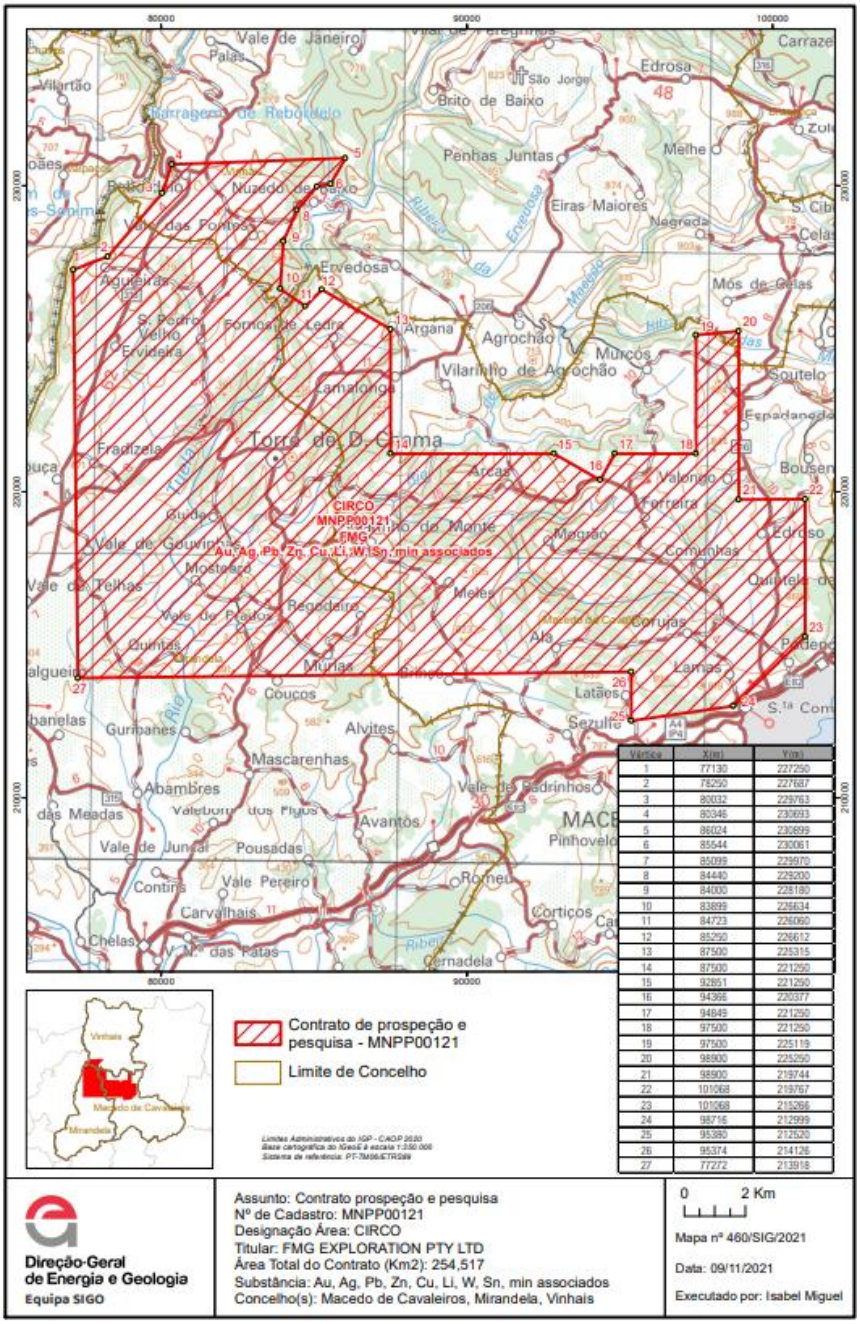
Figure 9. Digital elevation model and water streams within the Circo area.

Considering the topography of the area, higher difficulty in the stream sediments was to be expected in the eastern part of the area, due to the steep relief.

The concession area is covered by the E20N20 Digital Elevation Map (DEM), with a resolution of 25 m, provided by Copernicus Land Monitoring Service (EU-DEM v1.1). Using this DEM, it is possible to notice an orientation of the elevations with an NNE-SSW trend (same orientation as the rivers), possibly related to a strong structural and lithological control on the geomorphology of this region.

2.3. Description of the Tenement

Fortescue acquired the Circo area license from the Direção-Geral de Energia e Geologia (DGEG) of Portugal in October 2021. This concession covers an area of 254,5 km^2 delineated by a polygon with coordinates ETRS89/PT-TM06 (European Terrestrial Reference System 1989), showed in Figure 10:



Vértice	X(m)	Y(m)
1	77130	227250
2	78250	227687
3	80032	229763
4	80346	230693
5	86024	230899
6	85644	230061
7	85099	229970
8	84440	229200
9	84000	228180
10	83899	226634
11	84723	226060
12	85290	226612
13	87500	225315
14	87500	221250
15	92851	221250
16	94366	220377
17	94649	221250
18	97500	221250
19	97500	225119
20	98900	225250
21	98900	219744
22	101068	219767
23	101068	215266
24	98716	212999
25	95380	212520
26	95374	214126
27	77272	213918

Figure 10. Circo area limits and polygon coordinates, contract code: MNPP00121 (DGEG, 2021).

2.4. Historical background

The Circo area is classified as a greenfield in terms of Li potential, and a brownfield in terms of Sn and W. In Circo and its surroundings, old mining operations for W and Sn are known, belonging to Tin-Tungsten Province (Thadeu, 1951). The oldest mining works are reported at the end of the 19th century, in the Ervedosa mining area (Sn and As). However, in the 1950s and 1960s, a greater number of Sn mining concessions were registered (for example, Murçós and Agrochão), forming an NW-SE alignment, from Rebordelo to Murçós immediately north of the licensed area, in the same geological setting. The mineralization is mainly hosted in pegmatites and quartz veins (Gomes, 1996).

In Ervedosa, according to Gomes, 1996, a quartz vein ("Balbiani", with an N40ºE orientation and a large thickness) was mined for Sn and As. This vein was poorly mineralized, but a swarm of other veins with an irregular form, create a stockwork deposit (economically profitable). The mineralization of economic interest occurred in the form of cassiterite. Ervedosa started as an underground mining work in 1909, then later became an open pit. After 1959, there was an impoverishment of the mineralization. For some periods cassiterite was also mined in alluvial deposits of the Tuela river. The Ervedosa mine was abandoned in 1969, leaving noticeable marks on the landscape.

In Murçós, according to Gomes, et al., 2011, exists a stockwork-type W-Sn mineralization in Silurian schists intruded by a Variscan biotite granite. The mineralization of economic interest is formed by cassiterite and scheelite. The deposit was mined in four open pits as well as underground. Overall production reached 335 tons of W and 150 tons of Sn. The abandoned works originated three lakes and ruined infrastructures, intervened by the Empresa de Desenvolvimento Mineiro (EDM) for environmental remediation between 2005 and 2007.

In Agrochão, according to Gomes, et al., 2008, dense swarms of quartz veins (with orientations between N20ºE and N50ºE), mineralized in scheelite and with low cassiterite were mined. The mineralization of economic interest occurred therefore in the form of cassiterite and scheelite, but also occurred in the form of secondary minerals such as arsenopyrite, pyrite and tourmaline. This mine was granted a concession license in 1948 and was mined until around 1970, using underground mining, but mostly open pit mining.

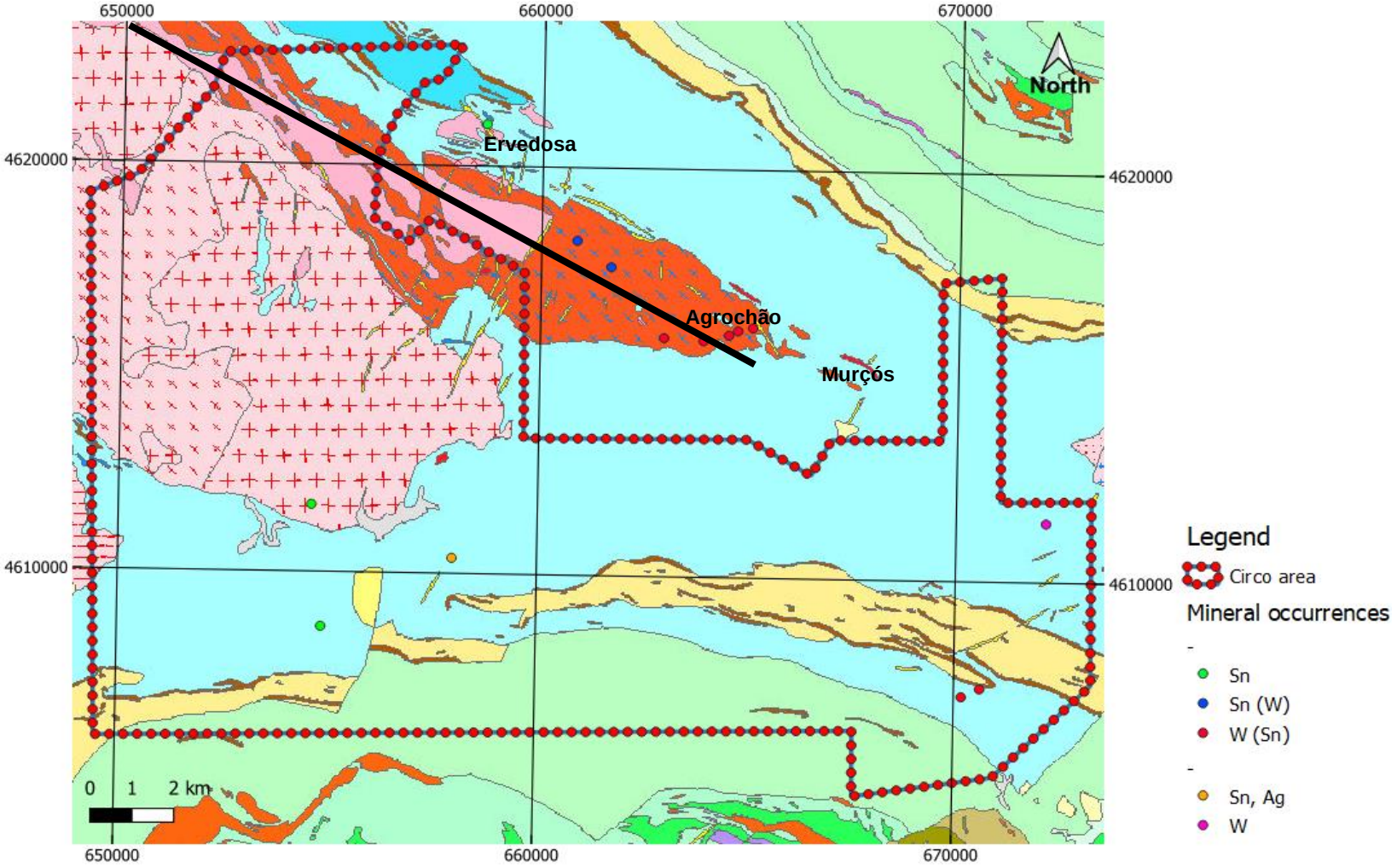


Figure 11. Mineral occurrences in the Circo area, on top of the 1:200 000 Portuguese geological map; black line represents the shearing zone that connects Ervedosa, Agrochão and Murçós.

3. Geological Setting

3.1. Regional Geology

During the long diverse history of the Earth, different orogenies have sculpted the geological structure visible today. The Variscan orogeny (380-280 Ma) consists of an important geological mountain-building event that was the result of the collision between Laurasia and Gondwana (closure of the Rheic ocean), which affected what is now Europe including the Iberian Peninsula. This orogeny produced a deformed belt called the Ibero-Armorican arc (Martínez Catalán *et al.*, 2014; Matte, 1986, 1991; Ribeiro et al., 2007; Vigneresse, 1999; Dias et al., 1995) during Devonian (390 Ma) to Carbonic (290/280 Ma) period (Dias and Ribeiro, 1993, 1995; Ribeiro et al., 1995; Matte, 1986, 1998, 2001; Fernández et al., 2003).

The Iberian Massif is limited in the west by the Atlantic Ocean whereas the east is covered by Mesozoic and Paleogene/Neogene terranes. The Biscay gulf is situated northwards from the Iberian Massif and the Alpine belt lies SE with segments of the Iberian Massif containing a complex structure that develops with a WNW-ESE orientation (Vigneresse, 1999; Fernández et al., 2003).

The Iberian Massif was divided into different geotectonic zones with different paleogeographic, tectonic, metamorphic and plutonic characteristics parallel to the structural alignments of the Variscan orogeny (Lotze, 1945). Julivert (1972) based on the work of Lotze, reevaluated these geotectonic zones to establish the newly-accepted zones (Figure 12). These zones are denominated as: Cantabrian zone (CZ), West Asturian-Leonese zone (WALZ), Central Iberian Zone (CIZ), Ossa Morena Zone (OMZ), and South Portuguese Zone (SPZ). Later Farias et al (1987) define a new Zone, the Galícia Trás-os-Montes Zone (GTMZ).

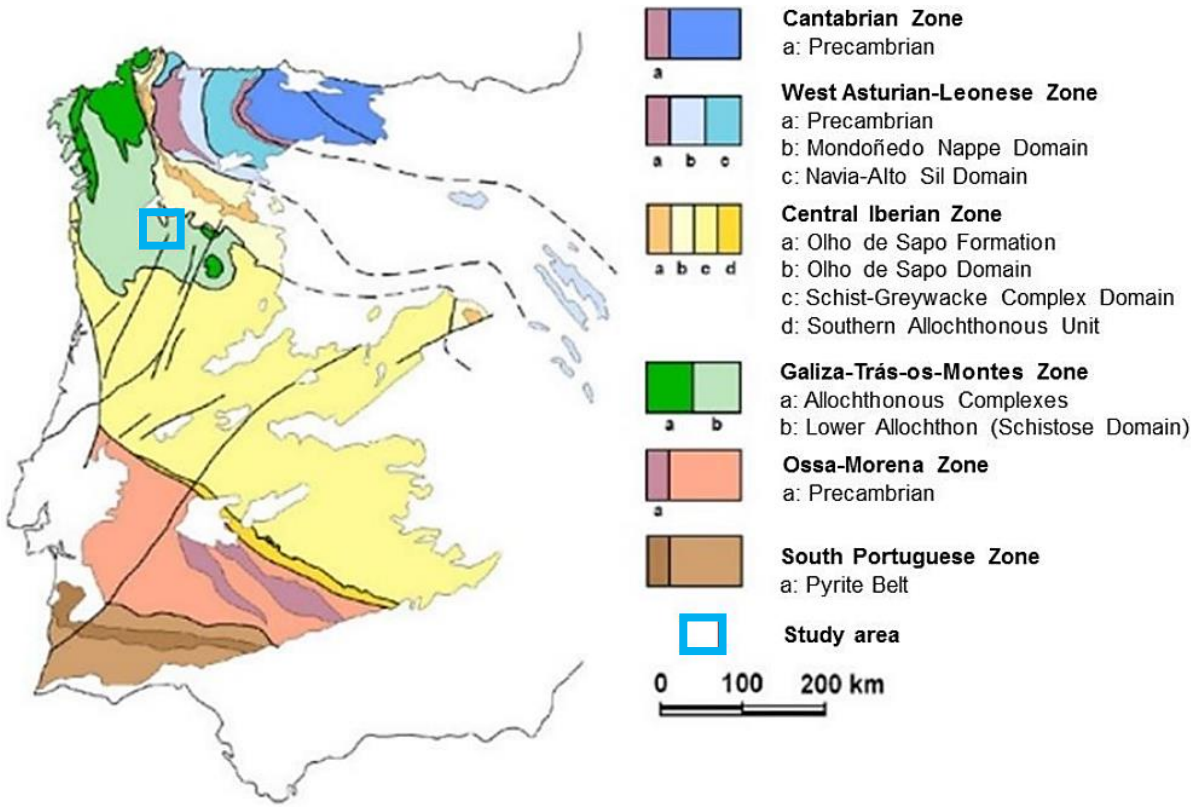


Figure 12. Subdivision of the Iberian Massif in geotectonic zones (according to Lotze, 1945 *in* Pérez-Estaún *et al*., 2004), Julivert *et al*. (1972;1974) and Farias *et al.* (1987) (adapted from: Pérez-Estaún *et al*., 2004).

This geotectonic organization results from three main ductile deformation phases (D1, D2 and D3) that acted during the Variscan orogeny and several post-D3 phases (Noronha *et al.*, 1979; Dias e Ribeiro, 1995; Noronha et al., 2006). These three phases are responsible for the foliations in the deformed rocks.

The D1 phase (~ 330 Ma) is characterized by the formation of large folds with different vergence and orientations in autochthonous, allochthonous and parautochthonous terranes. These folds present an NW-SE trending orientation with a sub-vertical axial plane in autochthonous (CIZ) and slightly vergent in the parautochthonous (Noronha et al., 2006). Stratigraphical and geochronological data allowed dating the first Variscan stage as medium Devonian (Ferreira et al. 1998). The D2 phase (~ 320 Ma) accentuates the vergence to SE, forming overturned folds with a short inverse limb and a subhorizontal shear cleavage. This stage is represented principally in the allochthonous and parautochthonous (Noronha et al., 2006). The D3 (less than 310 Ma) is present in all of the terranes (autochthonous, allochthonous and parautochthonous). The D3 developed large open folds with sub-vertical axial planes

and a WNW-ESE orientation associated with a sub-vertical cleavage of crenulation (Pereira et al., 1993; Noronha et al., 2006).

Post-D3 late phases developed a ductile-brittle and brittle regime, responsible for two conjugates fractures NNE-SSW, with sinistral movement, and NNW-SSE with dextral (Noronha et al., 2006). These fractures controlled the emplacement of the post-tectonic Variscan granites. In that way, different granite types are distributed along alignments coincident in most cases with D3 shear zones (syn- to late-tectonic granites) or along alignments coincident with post-D3 fragile fractures (Ferreira et al., 1987; Noronha et al., 2006).

The Variscan granites can be divided into two groups (Ferreira et al., 1987; Noronha et al., 2006; Dias et al., 2010): two mica granites, with dominant muscovite and resultant from the crystallization of peraluminous wet magmas formed through the partial melting of metasedimentary rocks at mesocrustal levels; and biotitic granites, with a calc-alkaline character and related to dry magmas formed in a deep crustal level. The first type of granites is syn-tectonic (Sin-D3, 315-310 Ma) and is associated with ductile shear zones inside elongated D3 regional antiforms. The emplacement of the second type of granites was conditioned by the shear zones and fractures with N-S and NNE-SSW orientations and can be either syn- to late-D3, or post-D3.

The biotitic granites are typically highly fractionated, and the two mica granites are spatially related to LCT (Lithium-Cesium-Tantalum) pegmatites. Magmatic fluids associated with the granites locally produced pegmatite swarms, especially in specific structural corridors, both within and marginal to the granites and also greisenised cupolas of the granites (Figure 13) (Roda-Robles *et al.*, 2016).

Variscan pegmatites have historically been mined since at least Roman times as a source of Sn for the manufacture of bronze. More recently some have also been mined for tantalum (as a sub-product of tin mining). It has been recognized that some also contain Li minerals including spodumene, petalite and lepidolite with some small-scale mining occurring in the last few decades targeting Li minerals for the ceramic industry, especially in central and northern Portugal (Roda-Robles *et al.*, 2016).

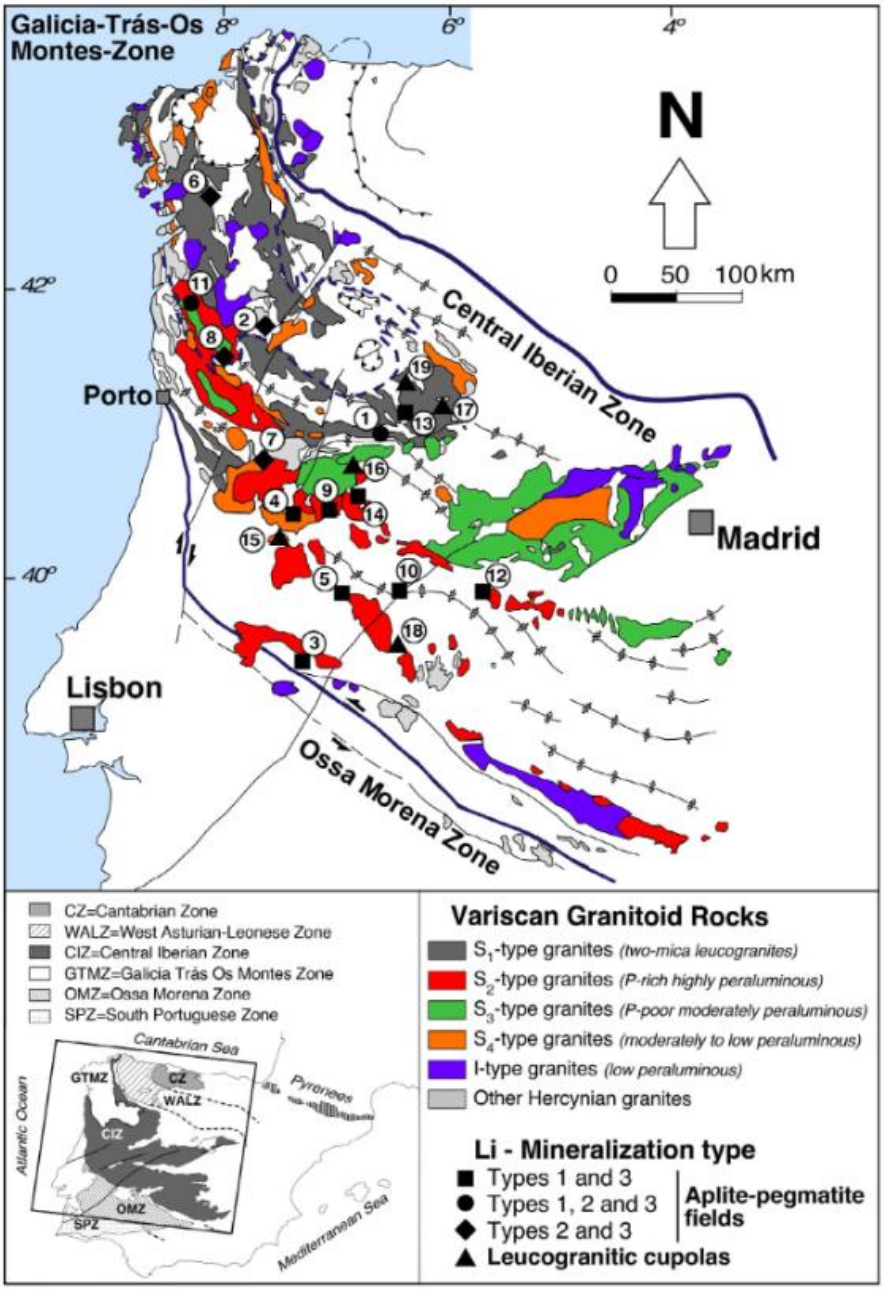


Figure 13. Simplified geological map of the Central Iberian Zone (CIZ) and the Galiza-Trás-os-Montes Zone (GTMZ), in Portugal and Spain, showing the location of Li mineralization (Roda-Robles *et al.*, 2018).

The Circo area lies within GTMZ which is related to a nappe emplacement over the CIZ, with two Variscan deformation phases associated (D1 and D2) (Ballévre, et al, 2014). This emplacement developed a sub-horizontal foliation (S2). This geotectonic zone is characterized by allochthonous mafic and ultramafic complexes, surrounded by parautochthonous (Ordovician – Lower-Devonian in age) metasedimentary sequences (Schistose Domain). The Schistose Domain represents a continental margin of Gondwana whereas the mafic-ultramafic complexes are ophiolitic units with an exotic

origin. The parautochthonous terrane consists of early-Palaeozoic metasedimentary sequences constituted by phyllites, micaschists and quartz greywackes with rare calc silicate rocks. These metasedimentary sequences were intruded by different granitoids with distinct ages. The installation of post-tectonic granites was controlled by the NNW-SSE trending Régua-Verín regional fault, a major late-D3 shear structure with a polyphasic reactivation.

3.2. Local Geology

The study area is covered by sheets 7-A (Rebordelo), 7-B (Bragança), 7-C (Mirandela) and 7-D (Macedo de Cavaleiros), of the Portuguese geological map at scale 1:50 000.

The Circo area is mainly covered by the parautochthonous Silurian metasedimentary sequence of grey-shales and alternating pelites, psammites, greywackes and volcanic tuffs, intruded by Variscan syn-tectonic two-mica granites with greisen and pegmatites spatially associated (Gomes, 1996). The two-mica granites vary from medium-grained to coarse-grained and from equigranular to porphyritic. In the south side of the area, it is possible to find lithologies from the Lower Allochthonous unit, namely phyllites, quartzphyllites and quartzites, considered from Ordovician to Silurian periods. Greisen cupolas and pegmatites hosting Sn-W mineralisations are also known, indicating a high degree of crustal-melt fractionation (Gomes, 1996).

Two different types of granites are identified in the Circo area: (i) a syn-tectonic two-mica granite (most abundant) elongated along an NW-SE strike, which intruded the metasediments during the D3 phase, being fractured and hydrothermally modified, due to late-D3 processes; and (ii) a syn-tectonic biotitic granodiorite (less abundant) located more in the north side of the area, with an elongated NW-SE shape body.

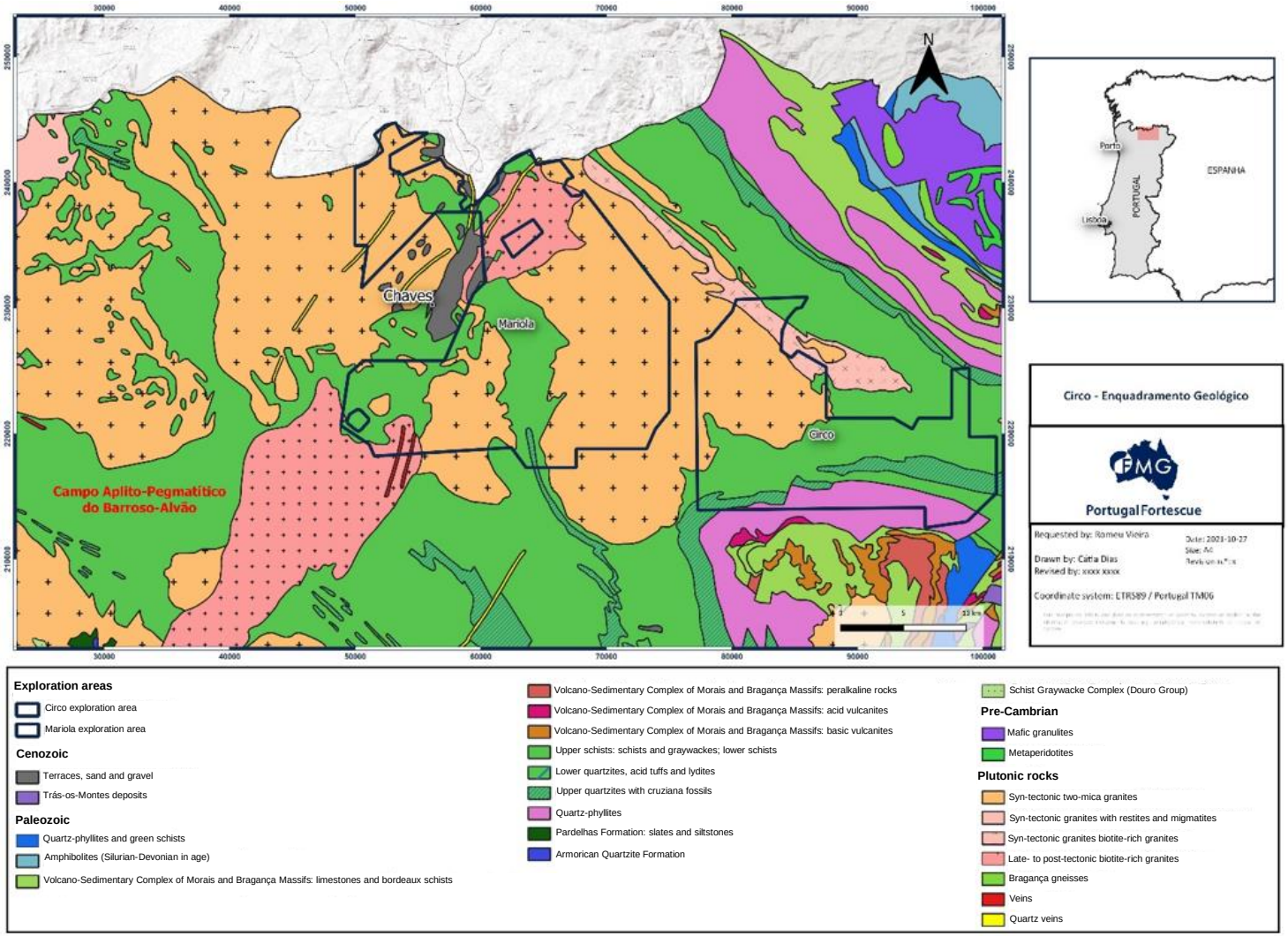


Figure 14. Geological setting of the Circo area (extracted from annual Circo Exploration Program, 2021).

3.3. Circo Prospectivity Support

The Circo area was requested based on a couple of conceptual features that support the potential prospectivity of Circo.

First, the geological framework of the Circo region encompasses the (i) presence of Variscan peraluminous two mica granites, (ii) Silurian metasediments, and (iii) Sn occurrences, mined in the past, similar factors observed in the geological setting of the Barroso-Alvão aplite-pegmatite field, located west of this concession, where Li bearing aplite-pegmatites are well known (Lima, 2000).

Second, the existence of greisen cupolas and quartz veins with Sn-W mineralisations exploited in the past (Gomes, 1996) indicates a high degree of crustal-melt fractionation. This may indicate the presence of highly fractionated pegmatites, which are prospective for Li minerals.

Third, there is a possibility that metasediments have some mineralizations in their aplite-pegmatite dykes, because the hydrothermal fluids created mineralizations in quartz veins, which are hosted in the metasediments (for example in Ervedosa).

Fourth, there is an important shearing zone (Figure 11, presented as a black line), connecting Ervedosa (quartz with tin and arsenic), Murçós (quartz with tin and tungsten) and Agrochão (quartz with tin and tungsten) that goes across the Circo area and could also be an important source for hydrothermal fluid circulation, potentially carrying Li mineralisation.

4. Methodology

The materials and data used, and the methodology followed in this work are described in this chapter.

4.1. Remote sensing

4.1.1. Data

For digital image processing and interpretation, Landsat-9 OLI-2 and Sentinel-2 MSI multispectral images were used. In particular, images with a cloud cover of less than 10% were downloaded.

The Landsat-9 OLI-2 (Level 1) images were acquired from USGS's "Earth Explorer" on 23/07/2022 (path 204, row 31), and Sentinel-2 MSI (Level 2A) from ESA "Copernicus Open Acess Hub" on 08/07/2022 (tile number T29TPG). All the images cover the entire study area. The images' map projection is Universal Transverse Mercator zone 29 N, WGS84 datum. Both products come with a metadata file (MTL file for Landsat-9 and MTD file for Sentinel-2), containing important information about the images.

4.1.2. GIS Software

GIS (Geographic Information Systems) software was employed for preprocessing and enhancement, to classify remote sense imagery, and to extract spatial information. This is an effective tool for the integration and analysis of a large amount of georeferenced spatial data with different formats and attributes. Within the GIS environment, QGIS 3.26.1 (Buenos Aires) with the SCP (Semi-Automatic Classification Plugin) (Congedo, 2016) was used. SNAP 9.0.0 was also used in this work for image processing.

The data collected (geochemical data, geological data (lithological and structural), satellite data, topographical data (DEM), mineral occurrence data, and ground survey data) acquired in this study was spatially analyzed to generate a final target exploration map.

4.1.3. Image Processing

The main image processing objective is to extract qualitative and/or quantitative information relevant to the chosen application (Lillesand et al., 2015). This process is

summarized in three steps: (i) pre-processing; (ii) processing stage *sensu stricto*, which involves image transformation and extraction; and (iii) post-processing.

By trial and error, it was attempted to establish a spectral analysis methodology capable of detecting structures (veins, e.g.), rocks (pegmatites, e.g.), or some indicator that could give a connection to Li mineralization.

Red-Green-Blue (RGB) combinations, Band Ratios, Selective Principal Component Analysis (PCA) and Supervised Classification (in this case, Spectral Angle Mapper method), which are among the classical methodologies for remote sensing (Cardoso-Fernandes et al., 2019a), were employed in this work. These methods allowed the extraction of spatial and spectral information related to lithology, structures, hydrothermal alteration, and others.

4.1.3.1. Pre-processing

Before analyzing the images, the satellite images need to be pre-processed. The goal of pre-processing is to eliminate different distortions in the images and to prepare them for the image processing methods.

- **Sub-setting**

The multispectral images acquired have a high spatial coverage (of several square kilometers), so a clip of the images, to the study zone, was made (in both products, Landsat-9 and Sentinel-2). The images were not clipped by the study area itself. Instead, a rectangular image was obtained, in order to consider the surroundings of the Circo area. The clipped rectangular area was delineated to cover some old mines like Murçós and Ervedosa, both important because they can provide more spectral information for the images' analysis.

For mineral exploration mapping, the most appropriated bands are located in the visible, NIR and SWIR regions, so some bands were excluded to facilitate the application of the image processing algorithms. In Landsat-9, bands 1 (coastal/aerosol), 8 (panchromatic) and 9 (cirrus) were excluded from the band set. In the case of Sentinel-2, band 1 (coastal/aerosol), band 5 (VNIR), band 6 (VNIR), band 7 (VNIR), band 9 (SWIR) and band 10 (cirrus) were also excluded (Cardoso-Fernandes et al., 2019a).

- **Atmospheric correction and surface reflectance conversion**

To minimize scattering and atmospheric absorption effects, Landsat-9 digital numbers (DNs) were converted to top-of-the-atmosphere (TOA) reflectance. This conversion

used the information contained in the metadata files. Sentinel-2 images are already provided in scaled TOA reflectance.

SCP does the conversion of Landsat-9 images to TOA reflectance (ρ_P) by applying the equation:

$$\rho_P = \frac{\pi \times L_\lambda \times d^2}{ESUN_\lambda \times \cos\theta_S}$$

where: $L\lambda$ represents the spectral radiance at the sensor's aperture (at-satellite radiance), d the Earth-Sun distance in astronomical units (provided in the metadata files), $ESUN\lambda$ the mean solar exo-atmospheric irradiances, θs the solar zenith angle in degrees, which is equal to $\theta_S = 90° - \theta_e$ (where θe is the Sun elevation)

A DOS1 (Dark Object Subtraction 1) atmospheric correction (Chavez, 1996) was applied, which is a process that converts TOA reflectance into surface reflectance. Thermal bands are not included in this correction. The DOS1 correction is an image-based correction where the algorithm identifies the dark regions in the image. Theoretically, the pixel values of these dark regions should be around zero, but these pixel values are higher due to the interaction with the atmosphere (scattering phenomena). The difference between the expected value (zero) and the measured one is calculated by the algorithm. Then, the difference is subtracted for all image pixels. DOS1 atmospheric correction is only applicable if the images contain dark zones, for example, water bodies, in the NIR band.

In the case of the Sentinel-2, the conversion of TOA reflectance to surface reflectance in SCP does an automatic rescale of the images: pixels of 20 m bands are split into 4 pixels of 10 m whose values are the same as the original 20 m pixel.

- **Pan-sharpening**

Pan-sharpening is the combination of the spectral information of multispectral bands (MS), which have a lower spatial resolution, with the spatial resolution of a panchromatic band (PAN), which for Landsat-9 is 15 meters (band 8). The final product is composed of multispectral bands 2, 3 and 4 with a 15 m resolution. To convert the remaining bands to this resolution a resampling and a rescale were performed. SCP elaborates pan-sharpening automatically, applying a Brovey Transform, where the pan-sharpened values of each multispectral band are calculated as follows (Johnson, Tateishi and Hoan, 2012):

$$MS\,pan = \frac{MS \text{ x } PAN}{I}$$

where: *MS* represents the multispectral band; *PAN* the panchromatic band and I the Intensity, which is a function of multispectral bands.

The following weights for I are defined, based on several tests performed using the SCP. For Landsat-9, I is calculated as:

$$I = \frac{0.42 \text{ x } Blue + 0.98 \text{ x } Green + 0.6 \text{ x } Red}{2}$$

- **Masking**

A vegetation mask was created to reduce spectral variability, using the information resulting from Normalized Difference Vegetation Index (NDVI) computation. For Sentinel-2 images, the considered threshold for vegetation was 0.3 (0.2 is the value that indicates the presence of vegetation according to Weier & Herring, 2000), because in this case study a lower value would mask a big part of the image. On the other hand, for Landsat-9, the considered threshold was 0.50.

NDVI is calculated using the red and NIR bands, according to the equation (Tucker, 1979):

$$NDVI = \frac{NIR - RED}{NIR + RED}$$

A mask for water (Normalized Difference Vegetation Index, NDWI) was also tried, but the results were not satisfactory, since both satellites, Landsat-9 and Sentinel-2, do not have enough special resolution to detect the water streams inside the study area (which are small), so there was reason to keep the water masks.

The Land use Land cover map – COS 2018 – was also used for masking urban territory and plowed fields. This spatial dataset was produced by DGT (Direção-Geral do Território) and has information about the land occupation. Before masking, the file was clipped to the Circo area.

4.1.3.2. Image processing methods

Image processing methods transform the multispectral satellite data into images that enhance geological features in contrast with the *background* (Lillesand et al., 2015).

As stated by Pour & Hashim (2015), discriminating between hydrothermally altered rocks and unaltered rocks is essential in mineral exploration. The image processing methods presented in this section allow to achieve the same goal. In this study, enhancements techniques, such as RGB combinations, Band Ratios and Principal Component Analysis (PCA) were applied which allowed the extraction of spatial and spectral information related to lithology, structures, hydrothermal alteration, and others. These techniques allowed the definition of some target areas so that later they could be verified in the field validation.

- **RGB combinations**

All satellite images are composed of grey-scale images correspondent to spectral bands, and when three bands (multispectra or thermal) are combined, it is possible to obtain a colorful multispectral image, which can be of true color (where only visible bands are used) or false color (where visible and infrared bands or only infrared bands are used). Then, it is possible to select which band corresponds to Red, Green and Blue channels.

Depending on which bands are selected, it produces an image that identifies a specific characteristic. There are several simple band combinations to discriminate vegetation, water bodies, among others. In addition to these, there are also more specific combinations to identify relevant features for mineral exploration, such as hydrothermally altered rocks, iron oxides, and Li-bearing minerals for example (combinations used in this work).

The laboratory spectra of Li-bearing minerals and minerals related to hydrothermal alteration show which bands should be used for the image processing stage (Figure 15 and Figure 16). For example, according to Sabins (1999), minerals like alunite and clay minerals (illite, kaolinite, and montmorillonite) have low reflectance features at SWIR-2 and low absorption at SWIR-1 bands. Silicate minerals have high absorption in the region between 10.30 and 11.70 µm. Iron oxides and sulfate minerals have a high reflectance near red and low reflectance in the blue band (Sabins, 1999; van der Meer *et al.*, 2012; Ali & Pour, 2014; Pour and Hashim 2015). In general, Li-bearing minerals have absorption features around 2.2 µm and lepidolite, apart from those absorptions, also has another between 0.5 and 0.6 µm (Cardoso-Fernandes et al., 2019a). Using the bands that contain these specific mineral absorption and reflectance features, it should be possible to obtain an RGB combination capable of showing the minerals in question.

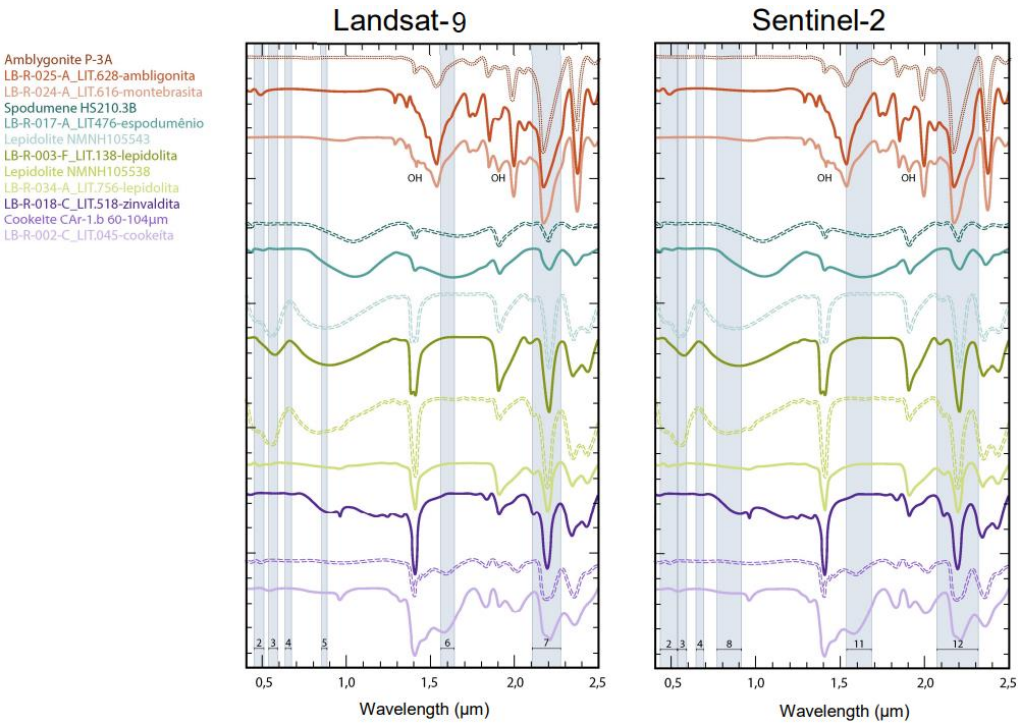


Figure 15. Overlap of Landsat-9 and Sentinel-2 bands to the spectral curves of Li-bearing minerals (adapted from: Cardoso-Fernandes et al, 2019a).

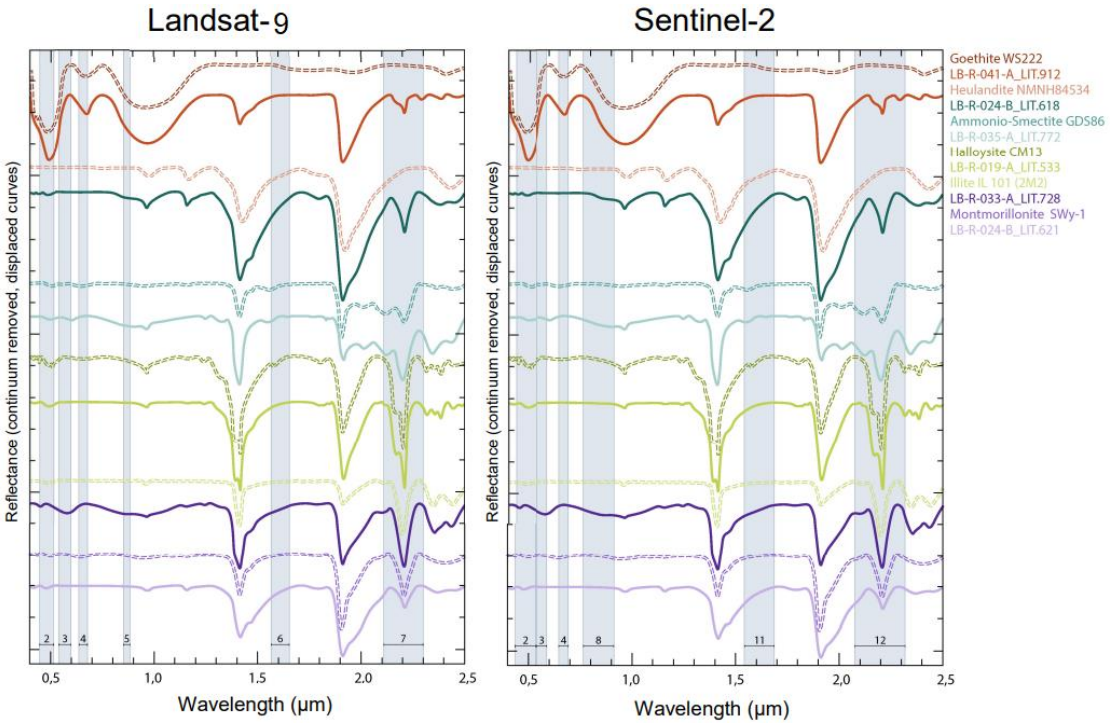


Figure 16. Overlap of Landsat-9 and Sentinel-2 bands to the spectral curves of petalite alteration minerals and other associated minerals and other associated minerals (adapted from: Cardoso-Fernandes et al, 2019a).

According to certain authors, different types of combinations were tested, for both Landsat-9 and Sentinel-2 imagery (Table 3). All Landsat-9 combinations were self-proposed based on literature of Landsat-8 imagery.

Table 3. RGB combinations tested for the Landsat-9 and Sentinel-2 imagery.

RGB combination		Feature	Author(s)
Landsat-9	Sentinel-2		
2-5-7 (S.P)	2-8-12	Iron oxides and clay minerals	Ali & Pour, 2014
5-7-3 (S.P)	8-12-3	Hydrothermally altered rocks	Mia & Fujimitsu, 2012
6-7-4 (S.P)	11-4-12	Lithological contrasts	Mwaniki et al., 2015
7-3-11 (S.P)	-	Li-bearing minerals	Cardoso-Fernandes et al., 2019
3-2-11 (S.P)	3-2-12	Li-bearing minerals	Cardoso-Fernandes et al., 2019

* S.P. – self-proposed based on the author(s)

- **Band ratios**

Band rationing is a technique where digital numbers (brightness values) of one band are divided by that of another band. These correspond to the peaks (high reflectance) and absorption features (low reflectance) of a spectral curve (Vincent and Thompson, 1972; Goetz et al., 1975, Pour et al., 2015). Usually, the band with higher reflectance is divided by a band with low reflectance.

Band ratios allow analyzing of certain features that cannot be seen in raw bands (Sabins, 1997; Inzana *et al.*, 2003; Ali & Pour, 2014) and eliminate shadowing and topographic effects, helping the analysis of complex terrains (Mwaniki *et al.*, 2015). Band ratios should not be used for quantitative applications, for example, mapping (Han & Nelson, 2015).

According to Sabins (1999), there are two groups of minerals associated with hydrothermally altered rocks: (i) alunite and clay minerals like illite, kaolinite, and montmorillonite, and (ii) iron oxides and sulfates. Taking this into account, band ratios that discriminate these minerals should highlight hydrothermally altered zones as bright pixels.

Some known ratios from the literature were tested during this work, to identify iron oxides, clay minerals, alunite, and Li-bearing minerals (Table 4). The selection of bands was related to the spectral reflectance and position of the absorption bands of

the mineral or assemblage of minerals to be mapped. All Landsat-9 band ratios were self-proposed based on literature of Landsat-8 imagery.

Table 4. Band ratios tested for Landsat-9 and Sentinel-2 imagery.

Band ratio		Feature	Author(s)
Landsat-9	Sentinel-2		
3/5 (S.P)	3/8	Spodumene	Cardoso-Fernandes et al., 2019
4/2 (S.P)	4/2	Iron oxides	Ali & Pour 2014; Sabins, 1999
4/3 (S.P)	4/3	Ferric iron	Cardoso-Fernandes et al., 2019
4/7 (S.P)	4/12	Lepidolite (cookeite, amblygonite; montebrasite)	Cardoso-Fernandes et al., 2019
6/5 (S.P)	11/8	Ferrous minerals	Ali & Pour 2014; Mia & Fujimitsu, 2012
6/7 (S.P)	11/12	Alunite and clay minerals	Ali & Pour 2014; Pour & Hashim 2015; Sabins, 1999

* S.P. – self-proposed based on the author(s)

- **Principal Component Analysis (PCA)**

The Principal Components Analysis (PCA) is a technique used to enhance and separate certain spectral signatures from the background (Gabr et al., 2010; Moradi 2015). This technique reduces the redundancy of correlated data by applying a linear transformation and can also be used for dimensionality reduction (Ali & Pour 2014; Mia & Fujimitsu, 2012). The PCA analysis consists of a multivariate statistical technique that selects uncorrelated linear combinations (eigenvector loadings) of variables in such a way that each successively extracted linear combination, or Principal Component (PC), has a lower variance (Singh and Harrison, 1985; Mia and Fujimitsu, 2012).

The first Principal Component (PC1) contains most of the data variability, highlighting features common to all input bands and often displaying important structural information. PC1 corresponds to a vector in the direction of the maximum variance of pixels in the scene. The second PC (PC2) contains the second most data variability. It is orthogonal to PC1 in the n-directional space and highlights the spectral differences between visible and infrared spectral bands. The third PC (PC3) includes the third most variability and is orthogonal to the other two PCs. The other PCs have less variability (Vincent, 1997; Gabr et al., 2010; Moradi, 2015). The number of output PCs depends on how many spectral bands are used in the input of the PCA.

In this work, two main approaches were applied: (i) the first involved the application of PCA to all visible, NIR and SWIR bands; (ii) the second approach consisted of a selective PCA, in which PCA was applied to a selected subsets of the satellites' bands.

The selective PCA corresponds to the application of the "Crosta technique" (Loughlin, 1991), in which the PCA is applied to a subset of four bands (Table 5).

Table 5. Chosen subsets to the application of selective PCA and respective target mineral information.

Subset		Target mineral Information	Author(s)
Landsat-9	Sentinel-2		
2, 4, 5, 6 (S.P)	2, 4, 8, 11	Ferric iron	Loughlin, 1991
2, 5, 6, 7 (S.P)	2, 8, 11, 12	Hydroxyl minerals	Loughlin, 1991
2, 3, 5, 11 (S.P)	2, 3, 8, 11	Li-bearing minerals	Cardoso-Fernandes et al., 2019

* S.P. – self-proposed based on the author(s)

Using the images obtained in these selective PCA subsets (Selective H band and Selective F band, bands that discriminate hydroxyls and ferric iron, respectively), an RGB combination was created by merging the Selective H band and Selective F band (Crosta technique), for both sensors (Red - Selective H band; Green - Selective H band plus Selective F band; Blue - Selective F band).

- **Spectral Angle Mapper (SAM)**

Spectral Angle Mapper or SAM is a physically-based spectral classification that uses an n-D angle to match pixels to reference spectra. The algorithm determines the spectral similarity between two spectra by calculating the angle between the spectra and treating them as vectors in a space with dimensionality equal to the number of bands (Kruse et. al., 1993). SAM compares the angle between the endmember spectrum vector and each pixel vector in n-D space. Smaller angles represent closer matches to the reference spectrum. Pixels further away than the specified maximum angle threshold in radians are not classified. SAM classification considers reflectance values.

Using this supervised classification algorithm, correlations to the Ervedosa mine and Rebordelo exploration were made, based on pixel spectral information. One pixel was chosen from the Rebordelo exploration and another from the Ervedosa mine. Different thresholds were tested to enhance the best result (find the balance between having almost no correlatable pixels and having too many correlatable pixels). SAM was employed using the software SNAP version 9.0.0.

- **Lineament Extraction**

As aforementioned, the Circo area is affected by the regional structures, thus a structural map was made based on the manual extraction of linear features.

Structural discontinuities and features can result in morphological lineaments such as fault scarps, joints, and fold axis (Ramsay & Huber, 1987). According to Hung *et al.* (2005), such structural features can manifest through different types of lineaments: (i) straight streams and valleys; (ii) aligned surface depressions; (iii) soil tonal changes; (iv) alignments in vegetation; (v) vegetation type and height changes; and (vi) abrupt topographic changes.

The aforementioned lineaments are formed by edges, which can be marked by pronounced differences in brightness in satellite images, or, by subtle brightness differences in the image and may be difficult to recognize (Sabins, 1997). Edge enhancement techniques are then applied to overcome this problem.

To map the lineaments, the delineation was supported with some processing tools such as the creation of four hillshade images (each with a different azimuth of the light, being considered 0º, 45º, 90º and 135º degrees) based on the EU-DEM-v1.1-E20N20, with the resolution of 20 meters, downloaded from the Copernicus platform. Hillshade images with different azimuths allow the extraction of lineaments with different orientations (e.g. using azimuth 0º it is possible to extract lineaments with the orientation E-W, that is, perpendicular lineaments to the defined azimuth; this is just a general rule, lineaments with other orientations can also be extracted). The lineaments were manually digitized over the hillshade images in a GIS environment (QGIS software).

4.1.4. Targets analysis

Selected remote sensing targets were submitted to X-ray fluorescence (XRF) and Laser Induced Breakdown Spectroscopy (LIBS) analyses. This section describes the methodology employed for LIBS analysis. The methodological procedures concerning the XRF analysis are described in section 4.3.3.

- **Pellet production**

Before starting the LIBS analysis, pellets of the target's sediment/soil samples were produced using the Specac Manual Hydraulic Press (Figure 15-a). The maximum load used for the pellets production was 10 tons, and two duplicate pellets were created at a time. Previously, the samples were sieved to a granulometry of 100 µm (Figure 17-c).



Figure 15. a) Specac Manual Hydraulic Press; b) sampling device used to create the pellets; c) 100 µm sieve; d) some produced pellets.

- **LIBS analysis**

The first step is to turn on the LIBS device (in this case, SciAps Z-300 LIBS, Figure 16-a) and choose the calibration method. In this case, a calibration curve created by the Fortescue Portugal team was used. Then, some analysis of other samples was done to warm up the equipment. The device must be at a temperature between 30ºC and 42ºC. All the samples must be dry before being submitted to LIBS analysis. LIBS measures light elements, such as Li, unlike XRF.

Before and after each samples batch analysis, a Certified Reference Materials (CRM) analysis must be performed. Standards AMIS 0683 (Li fusion pellets with approximately 2023 ppm of Li) and AMIS 0577 (Blank Silica powder) were used (Figure 16). The LIBS results of these pellets are established and must always be checked beforehand.

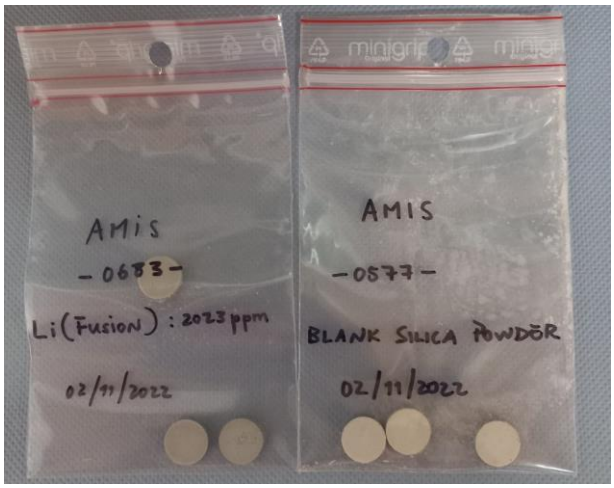


Figure 16. CRM pellets for LIBS analysis; AMIS 0683 and AMIS 0577.

After that verification, sample measurements can begin. Two measurements were made in pellets, and five in rock samples, due to rock heterogeneity. In XRF, two measures were made for each soil target sample (rock samples were not analyzed). It is always important to describe/take note of the date and the analysis number (for example, analysis #XXX) to be able to identify the measurements after exporting the results to the computer. Figure 17-c to -g, shows all the steps to be followed when measuring the samples. LIBS uses a laser that turns the sample into powder, which is then analyzed, so whenever a measurement of a sample has been completed, the device must be cleaned using paper and compressed air (Figure 17-f and -g).



Figure 17. LIBS analysis; a) SciAps Z-300 device ; b) SciAps Z-300 menu; c) SciAps Z-300 testing ; d) SciAps Z-300 up to temperature; e) analysis results; f) and d) device being cleaned up.

4.2. Geological mapping

The geological mapping was carried out in this area following three main pahses: planning, data collection and reporting.

4.2.1. Planning

The planning phase was mostly carried out in the office. Once the area for mapping was identified, geological information was compiled and consolidated to carry out a successful field work campaign. A field campaign is a step-by-step guide that outlines the time to be spent in the field and the objectives of each day, thus ensuring successful and satisfactory results. The following steps were outlined:

- Compilation of all available and relevant data – to avoid duplication of work and most importantly simplify the field work, all possible geological reports and data, including aerial and satellite photographs, maps whether topographical, base maps, legislative boundary maps (etc.) were obtained. The most important document, however, is the official approval by a government office and/or a local community. A bibliographic collection about the Circo area was also an important contribution to this step.
- Area division – a square grid (each square with 1 Km^2) was generated, dividing the Circo area into a total of 304 (numbered from C1 to C304) in order to maintain the rhythm of geological mapping and also for security reasons of the exploration team.
- Remote sensing studies – a first approach to the area was made using some remote sensing techniques (RGB combinations and others) in the software SNAP, to discriminate the lithologies of the area and monitor environmental aspects such as water and vegetation.
- Field mapping plan – in this case, the activities to be developed in the fieldwork were defined as follows: (i) observation and characterization of geological features, such as lithologies and geological structures, (ii) recognition of old mining works and other aspects considered relevant, that can be found within the exploration area. Locally and occasionally, a small rock sample (up to 2 Kg) could be collected for a correct lithology identification or chemical assay. Hammer, compass, eye lens, notebook, camera, maps, notepads, sampling bags and GPS were the materials chosen to be used during the geological mapping. Portable geochemical analyzers (XRF and LIBS) were also available

to identify element contents in the collected samples. All the data from the field ought to be noted (in the field notebook), with a photographic record (using a cellphone, for example) and coordinates acquisition (GPS). The treatment and integration of all data allowed the creation of a GIS database with the final production of geological maps, at different scales.

4.2.2. Data collection

This phase is crucial in any geological field mapping and was carried out in the field for the sole purpose of gathering new information about the study area. This section describes the steps to be followed for a good geological mapping practice, with an example of a psammite outcrop found in the area.

- Identify the lithology and basic features – in this step we identify the lithology of the found outcrop. It does not mean that we will know, certainly, which rock we are seeing, and that is why rock samples are collected, so they can be analyzed later in the laboratory. Basic features (visible to the “naked eye”) like color, mineralogy, weathering, deformation, among others, should also be taken into consideration. In Figure 18 is represented a greyish psammite, slightly weathered and poorly fractured.



Figure 18. Psammite outcrop from the Circo area.



Figure 19. Folded quartz veins in the psammite outcrop.

- Analyze structures and other features - in this stage, were measured any possible structures (folds, joints, veins, faults, bedding, foliation, fractures) and other features such as predominant minerals, texture, enclaves, and fabric of the rock. We assess the outcrop to find the best place to do the structural analysis because the rock can be affected by other structures around it. Additionally, those structures are also measured to understand the rock's geological history. In this psammite (Figure 18), we found quartz veins with thicknesses from 1 mm to 5 cm (some of them folded) and two joint families (one perpendicular to the foliation and the other parallel) (Figure 19).



Figure 20. Psammite foliation.

- Measure structures – all aforementioned structures should be measured (if they exist) using the compass (Figure 22). In order to standardize the measurements and later to use in GIS softwares, the right-hand rule (explained in Figure 21) was considered, by Fortescue, to record Dip-Dip direction values. Dip-Dip direction format is: for example, 10º - N230º (10º being the plane inclination and N230º plane inclination direction. Measurements must be performed meticulously and, if necessary, more than once for confirmation purposes. The psammite's foliation is 45º - N230º, and the fold axis of the quartz vein represented in Figure 19 is 18º - N120º.

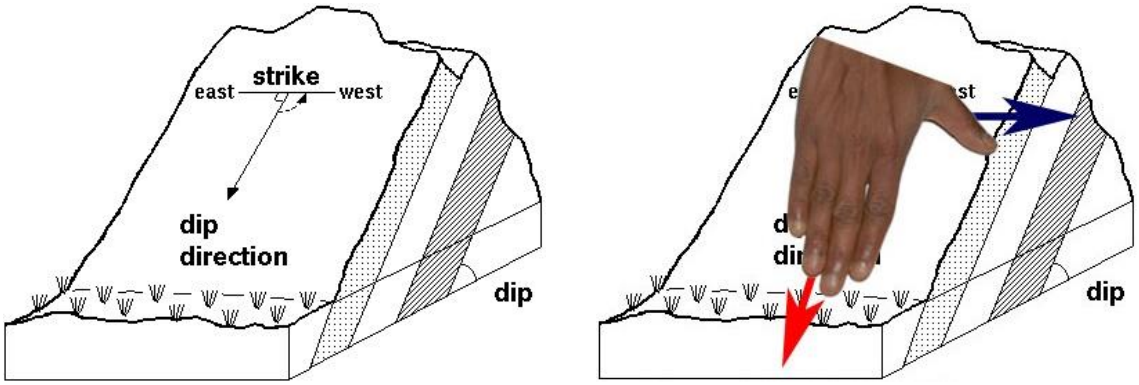


Figure 21. Dip-dip direction measure and "right hand rule" (Sanuja, 2013).



Figure 22. Measuring structures in the psammite outcrop.

- Collect rock samples – as stated in the first step, a rock sample should be collected to analyze it later (using geochemical analyzers like XRF and LIBS, for example) or to be analyzed in a certified laboratory. The basic tool to collect rock samples is the geological hammer. Additionally, the person who is sampling, should always wear work glasses and gloves, and look for fresh samples, ensuring that the sample is not weathered. An eye lens can also be used to analyze the rock on a larger scale (ideally, searching for a fresh rock surface). The rock sample must be kept in a sample bag and properly identified Figure 24).



Figure 23. Sampling the rock using the geological hammer.



Figure 24. Collected sample from the psammite outcrop.

- Take notes and photographs – while doing every step, all the rock features, measures, sample collection (etc.) must be written down in the field notebook. Other than those parameters, it is also important to include the date, sample ID, WGS84 coordinates, location name, grid number, etc. Some photographs should also be taken, to complement the database. Once in the field, it is also important to be as detailed as possible in all descriptions and to be keen and observant.

4.2.3. Reporting (database)

When all possible available data has been collected it is taken back to the office or laboratory for sorting, interpretation, and analysis. This phase is the most challenging of all three as wrong analysis or misinterpretation of data can lead to an inaccurate report and consequently misinformation. It is always a good practice if the data collectors are part of this process (in the Fortescue Portugal case, all the geologists from the exploration team are the same ones who did the data interpretation).

The objective of the reporting phase is to create a database with all the data collected in the field. The Fortescue Portugal exploration team is working together to create the database. As a result of the database, a geological map should be elaborated in the end, with detail level in conformity with map scale.

All the rock samples were prepared in “batches” and weighed, before being shipped to ALS Spain (a certified laboratory) for detailed geochemical analysis.

4.3. Stream sediments analysis

The stream sediments analysis is divided into four steps: (i) generation of water streams, catchment basins and outlets; (ii) stream sediments sampling and washing; (iii) XRF analysis of the collected samples; and (iv) detection of anomalous catchment basins.

4.3.1. Generation of water streams, catchment basins and outlets

This process was made by the Fortescue Portugal Exploration team in the office using QGIS software. Water streams, catchment basins and outlets were provided by the team for this study.

It was defined that sediment sampling would be done in streams from 1st to 4th order and the sampling points would be located 50 meters above the confluence of water streams. The map in Figure 25 shows the sampling points and water streams over a satellite image. One hundred and eighty points were determined for stream sediment sampling.

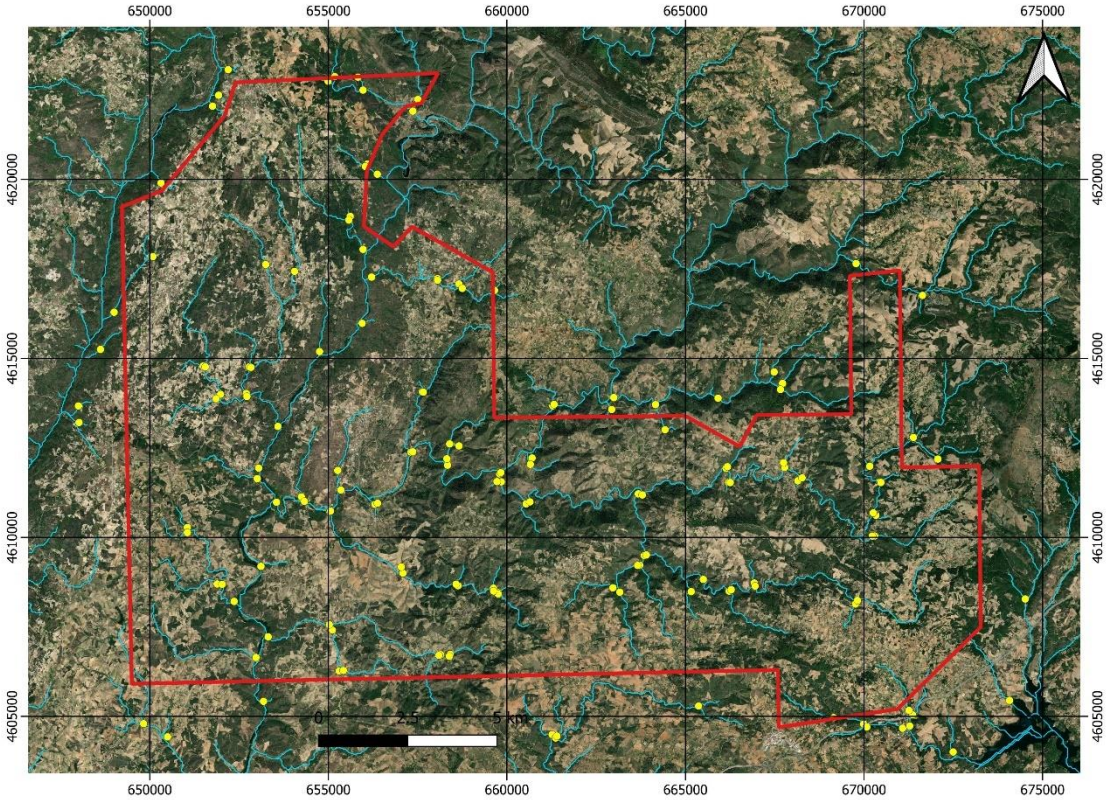


Figure 25. One hundred and eighty points planned to execute the stream sediments campaign.

4.3.2. Stream sediments sampling and washing

This phase was carried out in the field. The stream sediment sampling campaign lasted from June to September 2022 (from the one hundred and eighty planned points, one hundred and fifty-seven were collected). In the next pages are described the steps to be followed for a good stream sediments sampling practice.

- Find the best sampling site and collect a sample – after reaching the water stream and being close to the planned point for sampling, it is time to find a good sampling site. In this work, the team searched for a natural sediment traps, for example bolder traps, or stream margins favoring sediment deposition. Also, the team should evaluate the presence and, if present, the type and the level of possible contaminations. Then, pictures of the area around the sampling site and the sampling bag (properly identified) in the site (Figure 26-a and -b) were taken. After removing the surface layer, a small hole was opened to collect 1 to 2 kg of sample (Figure 27-a). After that, a picture of the sample bag near the sampling site was taken and the team finished by covering the opened hole in the ground. It is crucial to assess the sediment and see if it is better to collect a large quantity of sample, avoiding the need for resampling later.



Figure 26. a) Picture of the water stream (dry); b) selected sampling site by the team.



Figure 27. a) Cleaning the surface layer of the ground to open a hole; b) collecting the sediment sample; c) picture of the sampling bag along the sampling site; d) cover the sampling hole.

- Take notes about relevant features to create the stream sediments database – every feature about the sampling site, the sediment, etc, should be registered by a team member. These are the features that Fortescue Portugal planned to take note: coordinates obtained through GNSS/GPS, general physiography, bulk site, bank types, stream source, water color, water clarity, contaminations, stream sediments sample color, stream sediments composition, surface expression, type of vegetation, site rating, bedrock exposure, drainage pattern, site drainage, stream type, stream flow, pebble lithologies, and other comments.
- Wash the sample – if the stream has water flowing, the washing process would be performed on site after collecting the sample, otherwise, the sediment washing must be done in a river (with a low stream flow). This procedure uses three tools: a pan, a sieve (80 mesh), and a shovel (Figure 28). First, the pan was filled with water, and the sieve was placed on top. Then the sample was poured into the sieve and washing of the sample started with hand movements. After making sure that all the sediments smaller than 80 mesh went through the sieve and into the pan, the remaining sediments stuck in the sieve were discarded and the process was repeated with other portions of the sample. After washing the whole sample, an area of the river with some stream flow was found to place the pan slightly under water so that the less dense sediments and organic matter were separated from the denser sediments. Then, using the hand scoop, the washed sample was transfered into the washed sampling bag again (Figure 29). Before moving to another sample, every tool was cleaned.



Figure 28. Used tools for the stream sediments washing process (pan – black tool; sieve – green tool).



Figure 29. a) and b) Sieving the sample with the hand; c) washing the sample in the river with stream flow; d) putting the washed sample back in the sapling bag; e) washing the tools before moving into another sample.

4.3.3. XRF analysis

The XRF device used for the analysis was Vanta (Olympus, M Series). XRF uses X-rays to analyze the sediments in a non-destructive way. The calibration selected for the XRF equipment was the Geochem3-extra.

Similarly to LIBS analysis procedure, before starting the sample analysis and at the end, certified materials pellets must be analyzed, for Quality Assurance and Quality Control (QAQC) purposes. CRM 2711a (high trace element concentrate) and BLANK (Si + light elements concentrate) were used (Figure 30-b and -c).

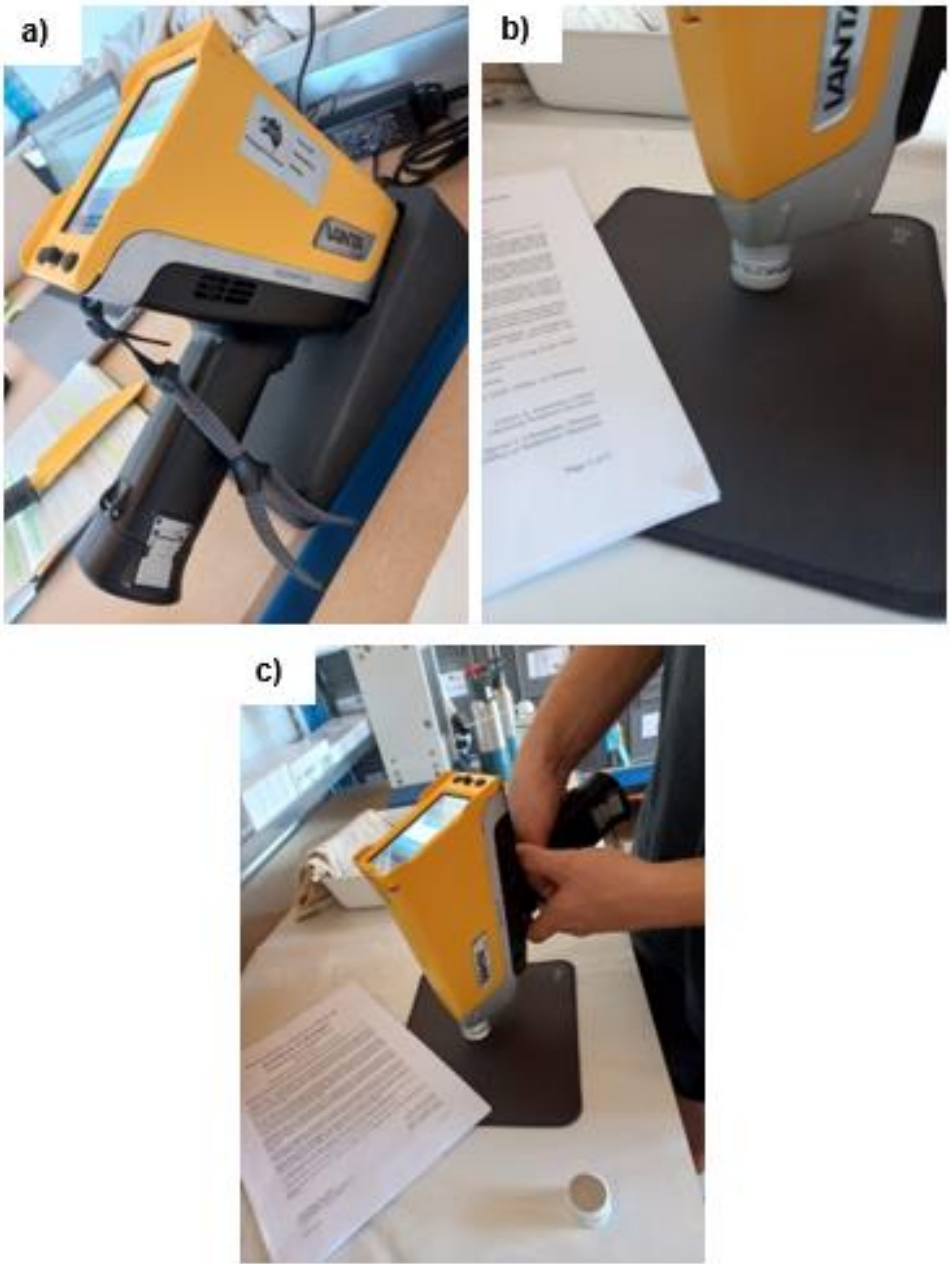


Figure 30. a) XRF Vanta (Olympus); b) and c) CRM pellets measurements.

The XRF device divides the analysis into three beams: Beam 1, Beam 2 and Beam 3. All the elements measured in each of the three beams are represented in Figure 31-a. XRF does not measure the contents of elements with lower atomic number than Mg (12) (H, He, Li, Be, B, C, N, O, F, Ne and Na). The samples should be well-dried before the XRF analysis (Figure 31-b).

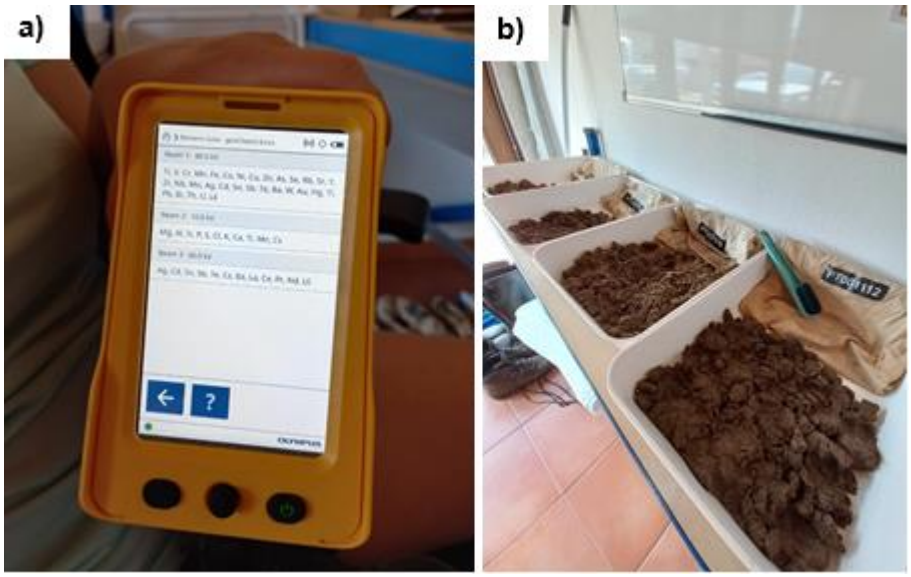


Figure 31. a) Elements that each XRF beam measures; b) Stream sediments samples drying.

Three measurements were made for each sample. It is always important to write down the date and the analysis number to be able to identify the measurements after exporting the results to the computer. Cleaning procedures in between samples are also crucial to avoid cross contamination. Figure 32-a to -f, shows all the steps to be followed when measuring the samples.

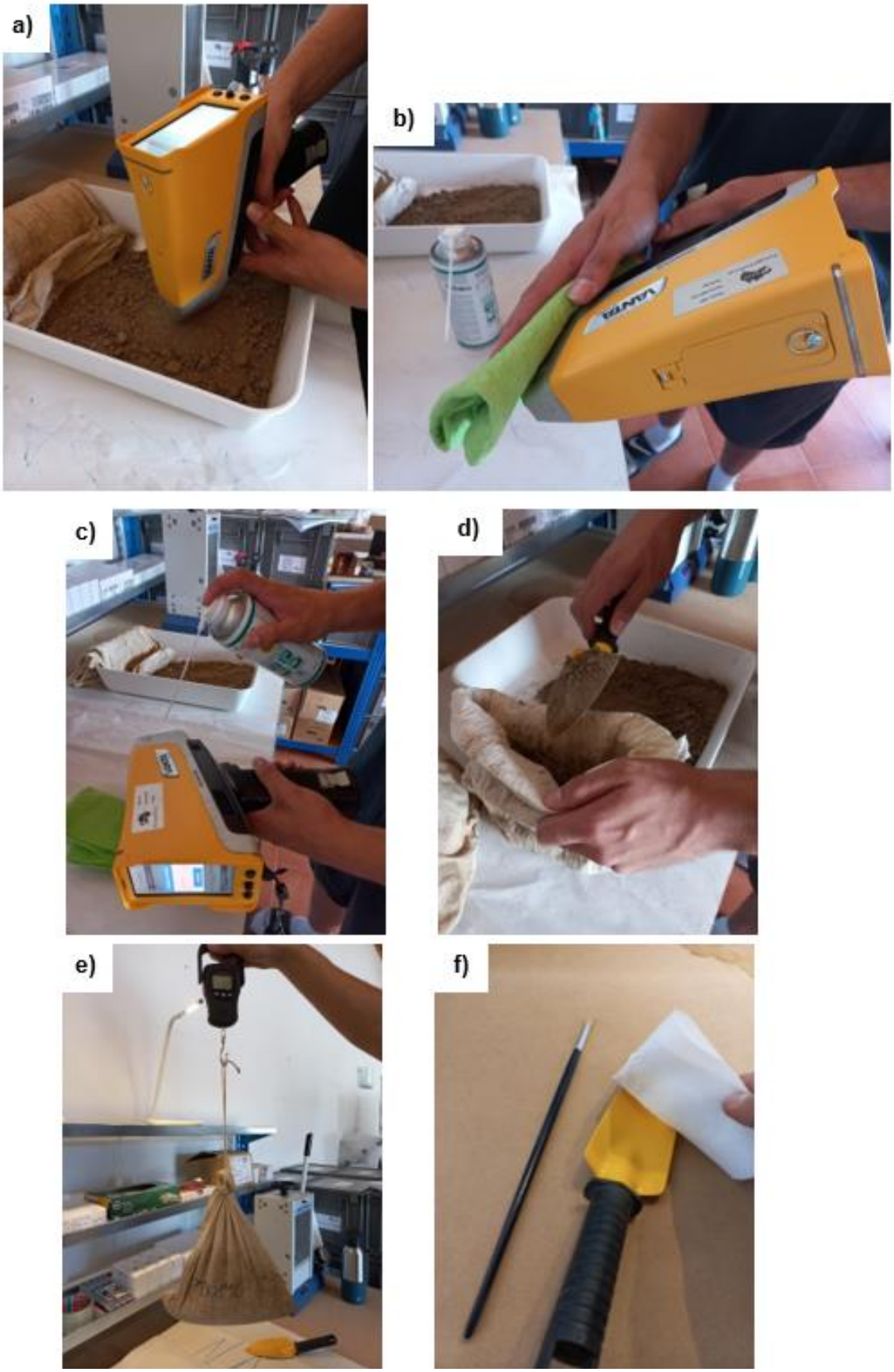


Figure 32. a) XRF analysing a sample; b) and c) cleaning the device after a measure with a cloth and compressed air; d) returning the sample back to the sampling bag; e) weighing the sample; f) cleanning the tools to not contaminate the next sample.

4.3.4. Detection of anomalous catchment basins

With the XRF results, the methodology to find the anomalous catchment basins was divided into two steps: (i) exploratory data analysis (EDA) and (ii) anomaly determination and creation of thematic maps.

- **Exploratory data analysis (EDA)**

Exploratory data analysis consists of processing the XRF analysis data/results using graphics, maps, PCA, etc. For this analysis, software IMDEX ioGAS was used, which is a leading exploratory data analysis software application developed specifically for the resources industry (Index Limited, 2021).

Firstly, a total of 157 stream sediments samples were separated by lithology (according to the pebbles found in the sampling site) into (i) granite, (ii) schist and (iii) granite+schist, and all the values represented as "< LOD" (i.e., below the Limit Of Detection of the XRF equipment) were converted to half of the LOD established for each element according to the "Vanta periodic table" (Figure 33) (Curie, 1978). This was the methodology employed by the Fortescue Portugal exploration team.

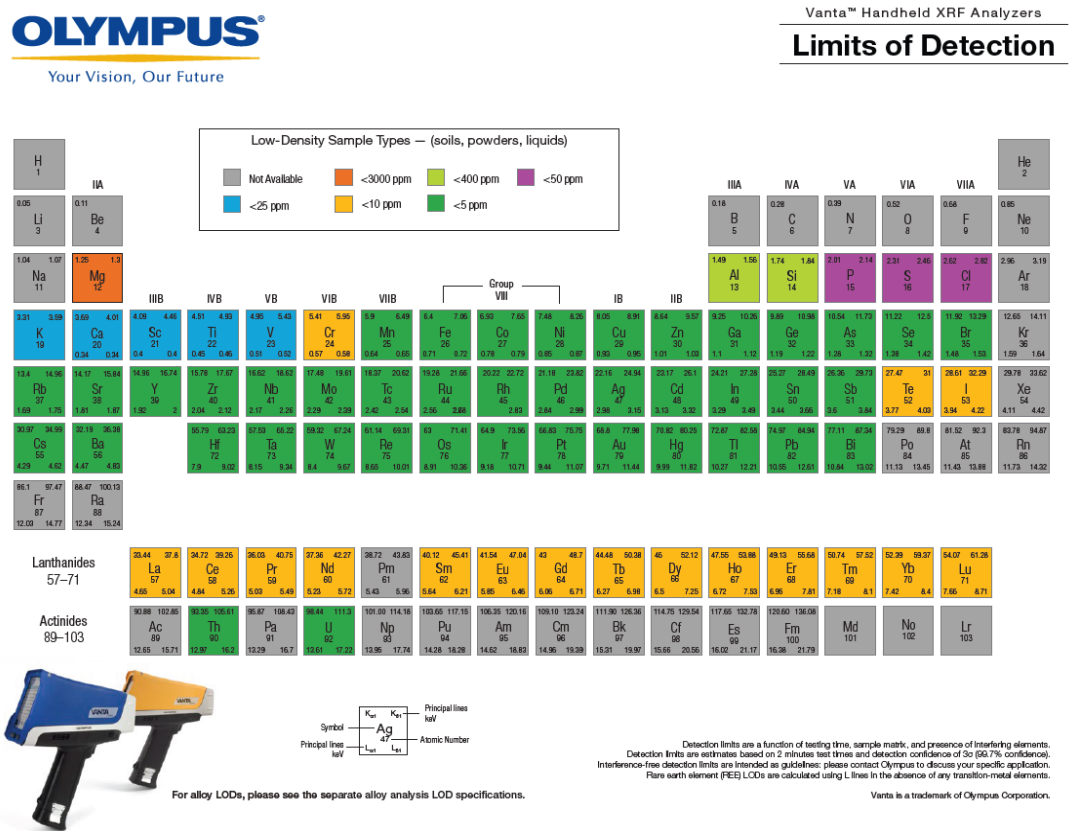


Figure 33. Vanta periodic table (Olympus) with the respective LODs.

Then, all the data exported from XRF (.csv file) was organized to be inserted in ioGAS. In the first approach, different types of graphics and maps were created for all the variables/elements, such as histograms, boxplots, Tukey plots, Q-Q plots, split Q-Q plots, dispersion graphics, variable maps, and attribute maps.

The software ioGAS, automatically, does the basic statistics and allows the determination of statistical parameters such as median, interquartile range (IQR), percentiles, minimum, maximum, etc. Basic statistics were determined for all the samples, and each lithological group.

In a second approach, a classical PCA approach was made using all the variables. Thirty PCs were generated (corresponding to all the elements measured by XRF). After analyzing the Scree plot that ioGAS generates, it was concluded that PCs above PC7, did not have statistically relevant information. So, a subset of some PCs was made (PC1 to PC7 were used) for data dimensionality reduction. By performing PCA in ioGas, it automatically generates 2D biplots (X, Y graphics), attaching one PC to the X axis and another to the Y axis, and all the selected variables appear as vectors. All the possible combinations from PC1 to PC4 were shown in a total of six graphics. It also generates one 3D biplot. All the PCA information (such as eigenvectors, eigenvalues, and explained variance) was registered and saved in an Excel file.

Four Pearson correlation matrices (one for all variables and one for each lithology) were also created using ioGAS, allowing the evaluation of linear correlations between elements. The objective was to find pathfinders that correlate with Li. The thresholds employed to find correlations were the ones based on Mukaka (2012) ($0.5 \leq$ Pearson r < 0.7 or Pearson r ≥ 0.7). Based on Pearson's correlation, four groups of pathfinders were created, and PCA was again employed for each group.

- **Anomaly determination and creation of thematic maps**

The ioGAS's Anomaly Assessment tool was used for the identification of outliers or atypical samples within domain-classified data using a combination of univariate tests (Tukey plots) to isolate near and/or far outlier samples and multivariate test (robust variant of Mahalanobis Distance) to examine variable correlations within each domain (Index Limited, 2019). The aforementioned tool allowed the identification of positive anomalous samples (outliers) for each analyzed element considering the entire dataset.

Moreover, when calculating the basic statistics in ioGAS, it was possible to automatically retrieve the upper outlier threshold based on the Tukey plots for each

lithological subset. This means that for the three previously defined lithological classes, a different anomaly threshold was obtained.

Next, all data was standardized using the IQR to compare the anomalies associated with each different population/lithology in the geochemical data set and find the uni-elemental anomalies. The standardization was done following the equation (Carranza, 2009):

$$Z_{ij} = \frac{X_{ij} - Threshold_j}{IQR_j}$$

Where, Z_{ij} represents the standardized data values for population j; X_{ij} is the original value i in the population j, $Threshold_j$ corresponds to the box-plot defined threshold for population j (Tukey upper outlier threshold), and IQR_j is the defined interquartile range for population j.

This standardization allows the determination of the anomalies based on the boxplot information of each lithology thus reducing the lithological background/influence of lithologies in the anomaly definition.

After the last step, two Excel files were imported to QGIS, one containing the Tukey values (obtained with the Anomaly Assessment Tool) and the standardized Tukey/Z values (after IQR standardization), for each sample. These files had coordinates (X and Y), allowing the conversion into shapefiles (.shp).

Then, the points were intersected with the previously generated catchment basins, joining the attributes by location. This resulted in two polygon shapefiles where each basin has the Tukey values and the Z values associated in the respective attributes table. A few points had to be rearranged because in some cases the sampling points did not correspond exactly to the same coordinates of the planned points.

The last step was to change the symbology of each polygon shapefile, to create two types of maps: (i) thematic maps based on the Tukey values and (ii) thematic maps based on the Z values. These two maps were produced for each pathfinder previously defined.

5. Results

5.1. Remote sensing

In this chapter, the results obtained from remote sensing imagery processing techniques of the study area are presented. These results were analyzed, compared and combined with the geological data. The combination of the extracted information allowed the definition of new targets within the Circo area.

5.1.1. RGB combinations

RGB combinations were applied as a first approach, to analyze the study area and visually interpret the multispectral imagery. Using Landsat-9 bands (2, 3, 4, 5, 6 and 7) and Sentinel-2 bands (2, 3, 4, 8, 11 and 12) was possible to produce different band combinations, some of them enhancing relevant features for mineral exploration.

First, a natural color image was produced for both sensors (Figure 34-a and -b), using the RGB combination 4-3-2. With this band combination, it is possible to do an exploratory analysis of the area, identifying rock exposure areas, vegetated areas, water bodies, and urbanized areas. In addition, some structural features such as faults and fractures were identified.

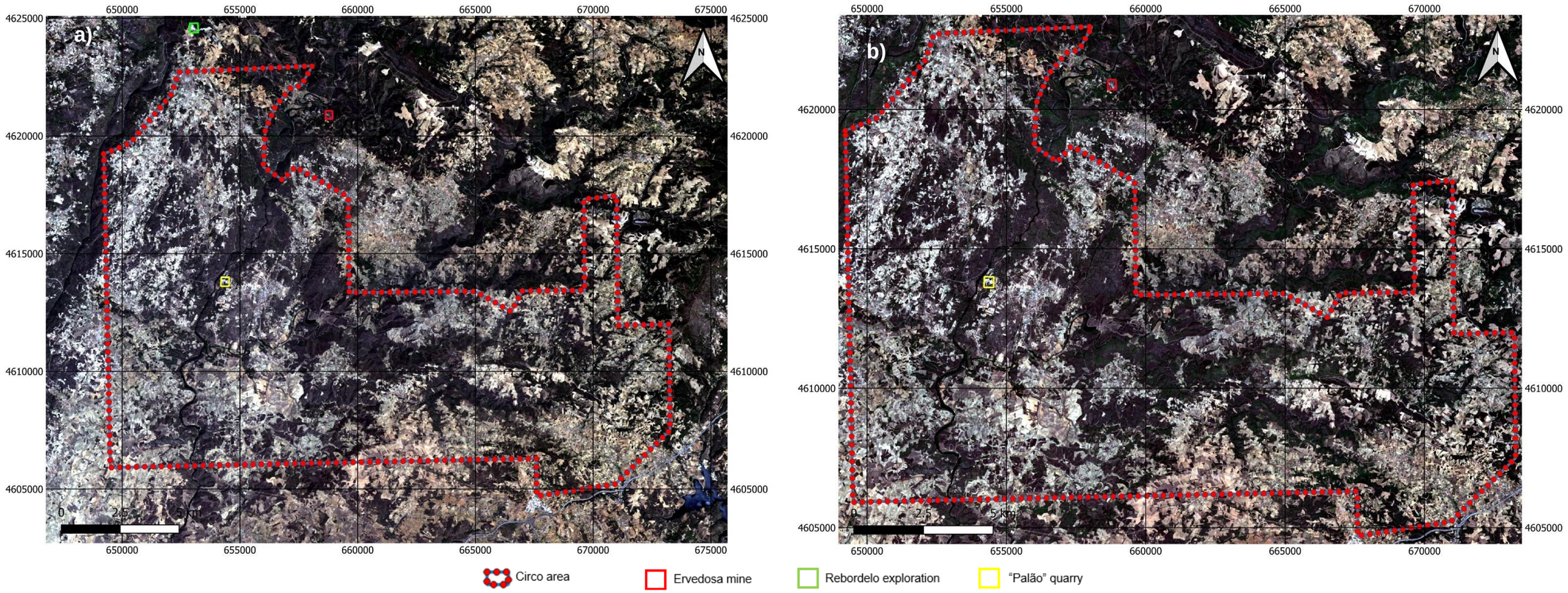


Figure 34. RGB combination (4-3-2); natural color images: a) Landsat-9; b) Sentinel-2. Coordinate System: UTM29N WGS84.

In order to map and distinguish iron oxides and clay minerals, RGB combinations 2-5-7 and 2-8-12 (Figure 35-a, -b, -c and -d) were used, for Landsat-9 and Sentinel-2, respectively.

In both sensors, bright white color pixels represents urbanized areas and plowed fields, black shows water streams/bodies and the green represents vegetation. Vegetation is fully masked in Figure 35– a and -c.

Also, there is a good distinction between the granites and the metasediments in both sensors. Granites appear in a bright purple to blue color (north side of the area) and metasediments in a pink to blue color (south).

Ervedosa and Rebordelo explorations (red and green squares, respectively) and the "Palão" quarry (yellow square, this is a granite quarry operating in Torre de Dona Chama) are good spots to see the spectral response, and then see if it is possible to find any other sites with a similar response (described later on chapter 5.1.5). Comparing the "Palão" quarry and Rebordelo exploration in both sensors, it appears in light pink in the Sentinel-2 image and bright pink in the Landsat-9 image. White spots in these zones could also indicate the presence of iron minerals and clay minerals because the white color is due to high reflectance in the three bands (Cardoso-Fernandes *et al.*,2019).

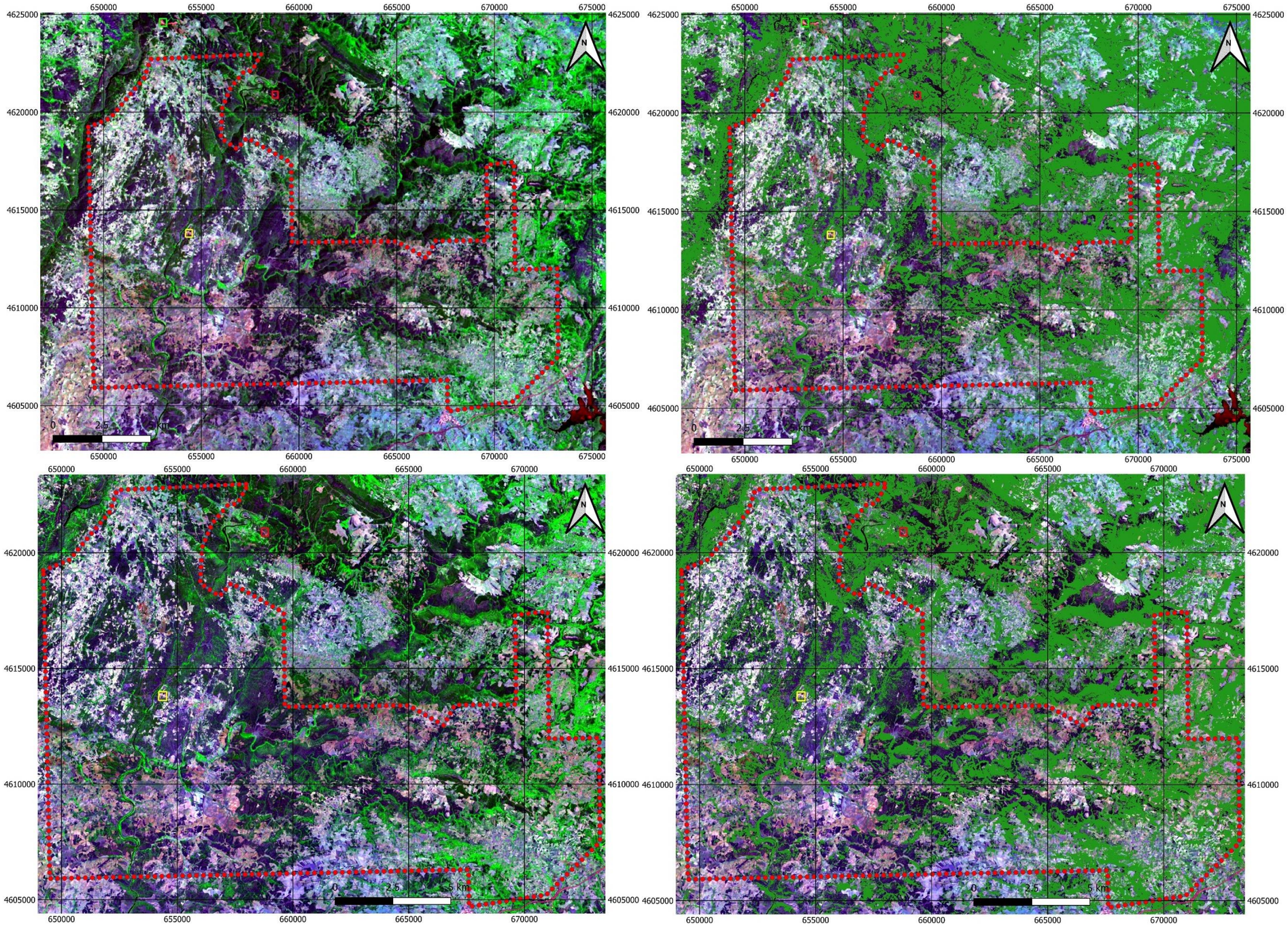


Figure 35. RGB combinations that identify iron oxides and clay minerals: a) RGB 2-5-7 for Landsat-9; b) RGB 2-5-7 with a vegetation mask; c) RGB 2-8-12 for Sentinel-2; d) RGB 2-8-12 with a vegetation mask. Blue and white areas show the highest iron oxide content. Some white spots in "Palão" quarry and Rebordelo exploration could indicate a simultaneous presence of iron oxides and clay minerals. Coordinate System: UTM29N WGS84.

The RGB combinations that best identified hydrothermally altered rocks were 5-7-3 (for Landsat-9 imagery) and 8-12-3 (for Sentinel-2). These combinations contain a NIR band in the red channel, a SWIR band in the green, and a visible band in the blue channel. These RGB combinations are also very good at enhancing geological structures like geological faults (Cardoso-Fernandes *et al.*, 2019).

Both in Landsat-9 and Sentinel-2 sensors, urbanized areas and plowed fields are presented in a bright white color, with water bodies in black and vegetation in red. Vegetation is fully masked in Figure 36-a and -c.

Just like iron oxides and clay minerals RGB, it is possible to see a distinction between the granites and the metasediments, granites being presented in a light to medium green color, and the metasediments in a blue to purple color (for both sensors).

The three spots marked on the map (“Palão” quarry, Rebordelo exploration and Ervedosa mine) appear in a bluish tint (probably indicating some hydrothermal alteration), but beyond that, the “Palão” quarry is presented more in white than blue in Sentinel-2, comparing to Landsat-9, probably due to Sentinel-2 having a better spatial resolution.

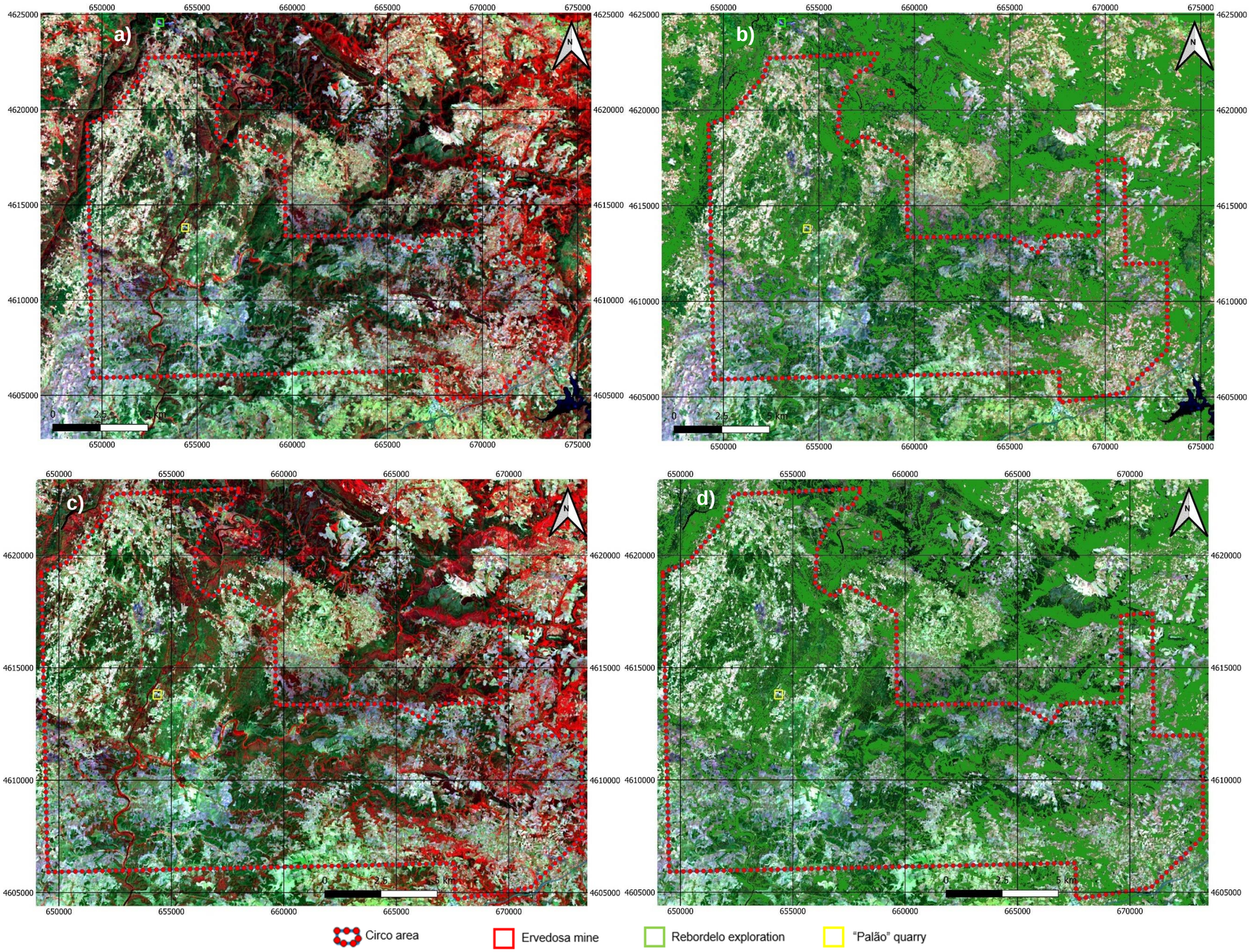


Figure 36. RGB combinations that identify hydrothermally altered rocks: a) RGB 5-7-3 for Landsat-9; b) RGB 5-7-3 with a vegetation mask; c) RGB 8-12-3 for Sentinel-2; d) RGB 8-12-3 with a vegetation mask. Light green represents the granites while blue color represents the metasediments. Hydrothermally altered rocks show to be discriminated in deep green and deep blue colors. Coordinate System: UTM29N WGS84.

According to Cardoso-Fernandes et al. (2019), the best RGB combinations to highlight Li-mineralizations are divided into two sets. The first set (where a SWIR band is used in the red channel, a visible band in the green one, and a thermal band in the blue one) includes the RGB combination 7-3-11 for Landsat-9; and the second set (which uses two visible bands (in red and green) and a thermal band (in blue), in case of Landsat-9 and two visible bands and a SWIR band (in case of Sentinel-2) is composed by 3-2-11 and 3-2-12 combinations, for Landsat-9 and Sentinel-2, respectively.

In the first set, the combination 7-3-11 represents urban areas and plowed fields in bright white to yellow color, water bodies in black, and the vegetation is not distinguished. Again, there is a difference between granites (presented in purple) and metasediments (presented in a bluish color).

Mineralized zones where Li-bearing pegmatites outcrop were supposed to appear in a yellowish-green or green color, which happens in “Palão quarry”, Rebordelo exploration and Ervedosa mine, so there is something in those spots giving the same response of Li-bearing pegmatites. Also, some other areas can be seen in the same colors and, for this reason, they were considered good targets for field validation.

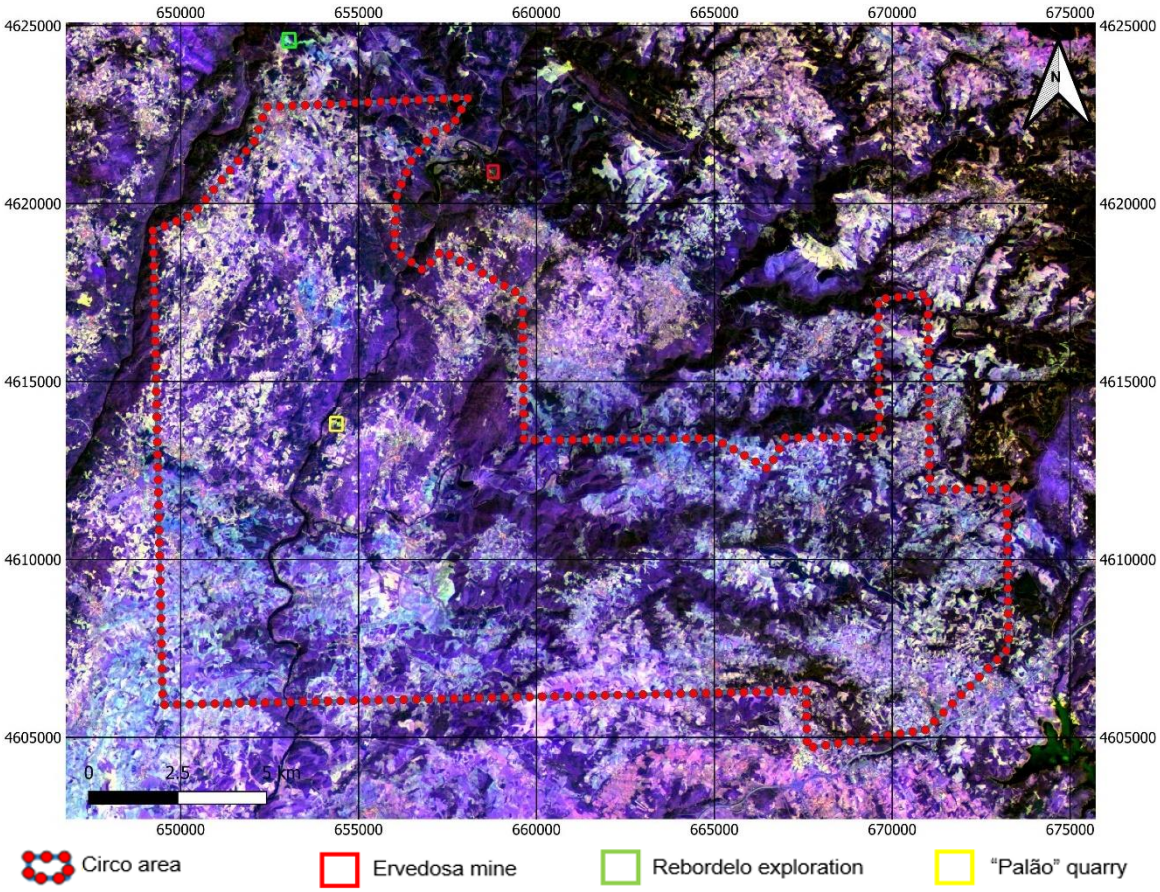


Figure 37. RGB combination 7-3-11 for Landsat-9 to discriminate Li-bearing minerals. Granites appear in purple and metasediments in blue. “Palão” quarry, Rebordelo exploration and Ervedosa mine appear in a yellowish green. Coordinate System: UTM29N WGS84.

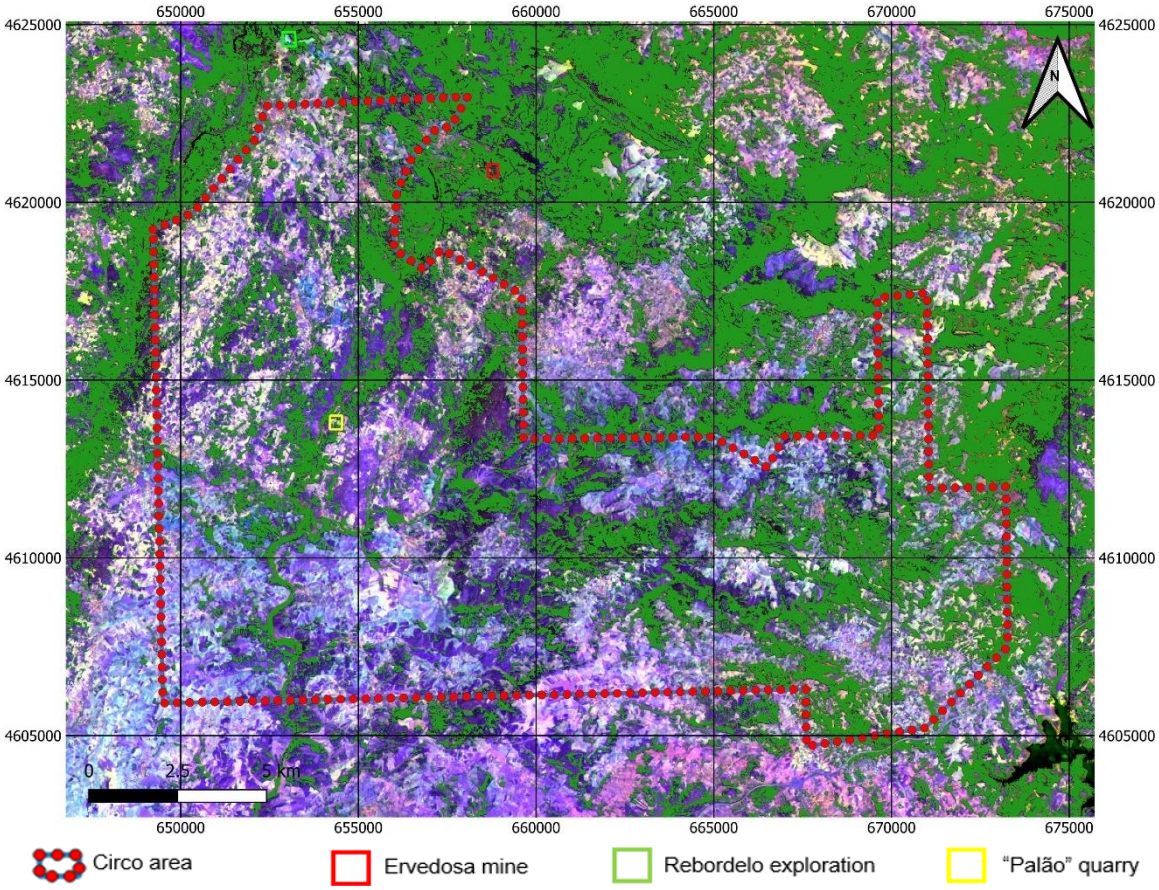


Figure 38. RGB combination 7-3-11 with a vegetation mask for Landsat-9 to discriminate Li-bearing minerals. Coordinate System: UTM29N WGS84.

The second set includes RGB combinations 3-2-11 (for Landsat-9) and 3-2-12 (for Sentinel-2). In the RGB combination 3-2-11, bright yellow/yellowish white color represents urban areas and plowed fields, black color represents water bodies and there is no possible distinction between granites and metasediments. The "Palão" quarry, Rebordelo exploration and Ervedosa mine appear in bright yellow. In the case of Sentinel-2 images, urbanized areas and plowed fields present a bright white color, vegetation and granites present a blue/bluish grey color and the metasediments present a yellow color. The "Palão" quarry, Rebordelo exploration and Ervedosa mine have a bright yellow color.

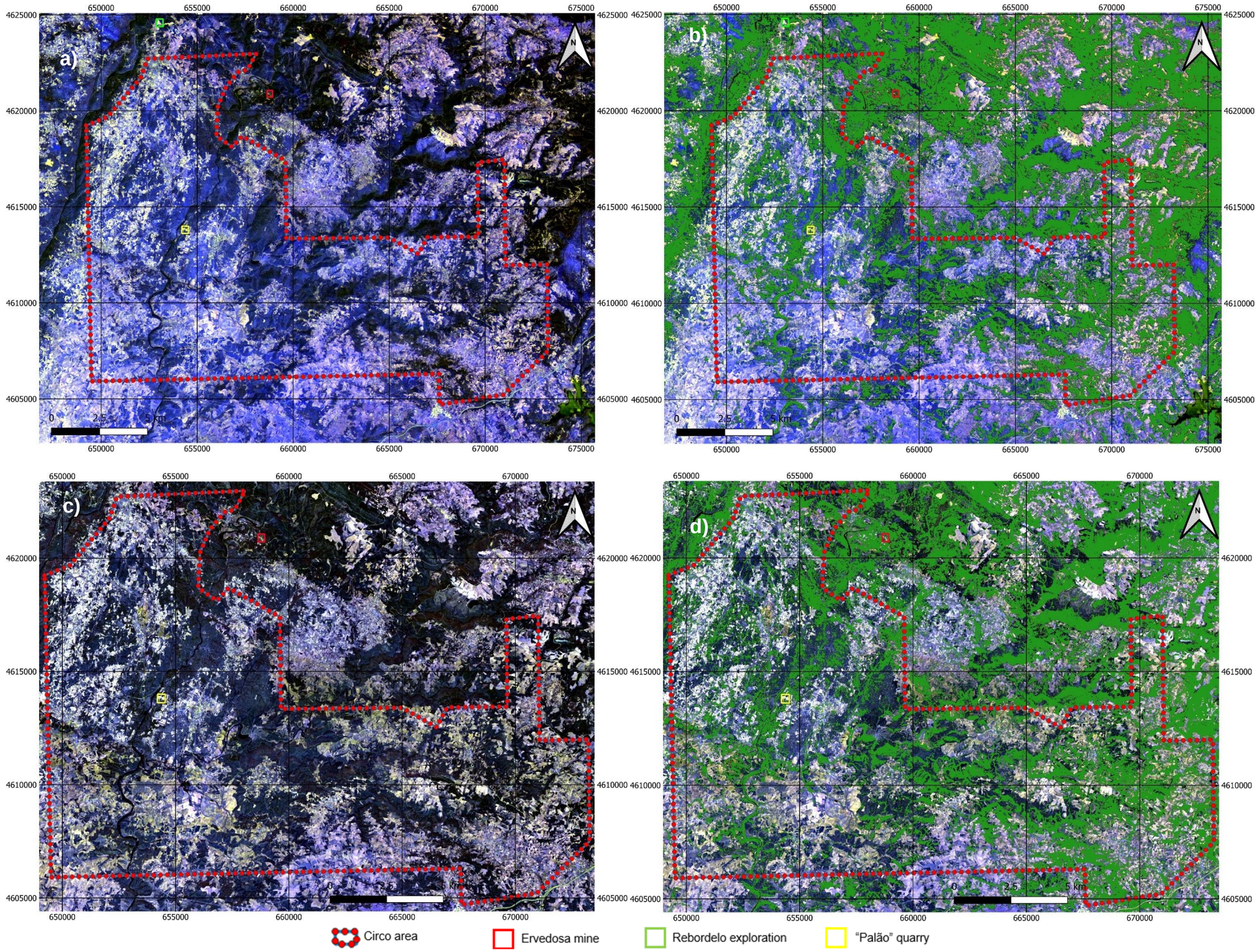


Figure 39. RGB combinations that identify Li-bearing minerals: a) RGB 3-2-11 for Landsat-9; b) RGB 3-2-11 with a vegetation mask; c) RGB 3-2-12 for Sentinel-2; d) RGB 3-2-12 with a vegetation mask. In Landsat-9 images its impossible to distinguish granites from metasediments and marked areas appear in bright yellow. In Sentinel-2 images, marked aras are also in bright yellow and granites (bluish grey) and metasediments (yellow) can be distinguished. Coordinate System: UTM29N WGS84.

To aid geological mapping, some RGB combinations were made for lithological contrasts, namely: 6-7-4 for Landsat-9 imagery and 11-4-12 for Sentinel-2 imagery. For both sensors, two SWIR bands and one visible band were used.

Using the RGB combination 6-7-4, vegetation appears in green, urban areas and plowed fields in white, water bodies in black, granites in yellow, and metasediments in blue. The “Palão” quarry, Rebordelo exploration and Ervedosa mine are not highlighted zones, but that is not the objective of this set of RGB combinations.

For Sentinel-2 (RGB combination 11-4-12), vegetation is presented in a pink color, water bodies in black color, urban areas and plowed fields in white color, granites in pink color, and metasediments in green color.

After seeing these combinations, a linear correlation with regional mapping was made. Both combinations correlate perfectly with the geological maps of the concession (at a large scale). Some outcrops cannot be highlighted in the area because there is not enough resolution to detect them through remote sensing, but this shortcoming will be overcome by the geological mapping done during the fieldwork.

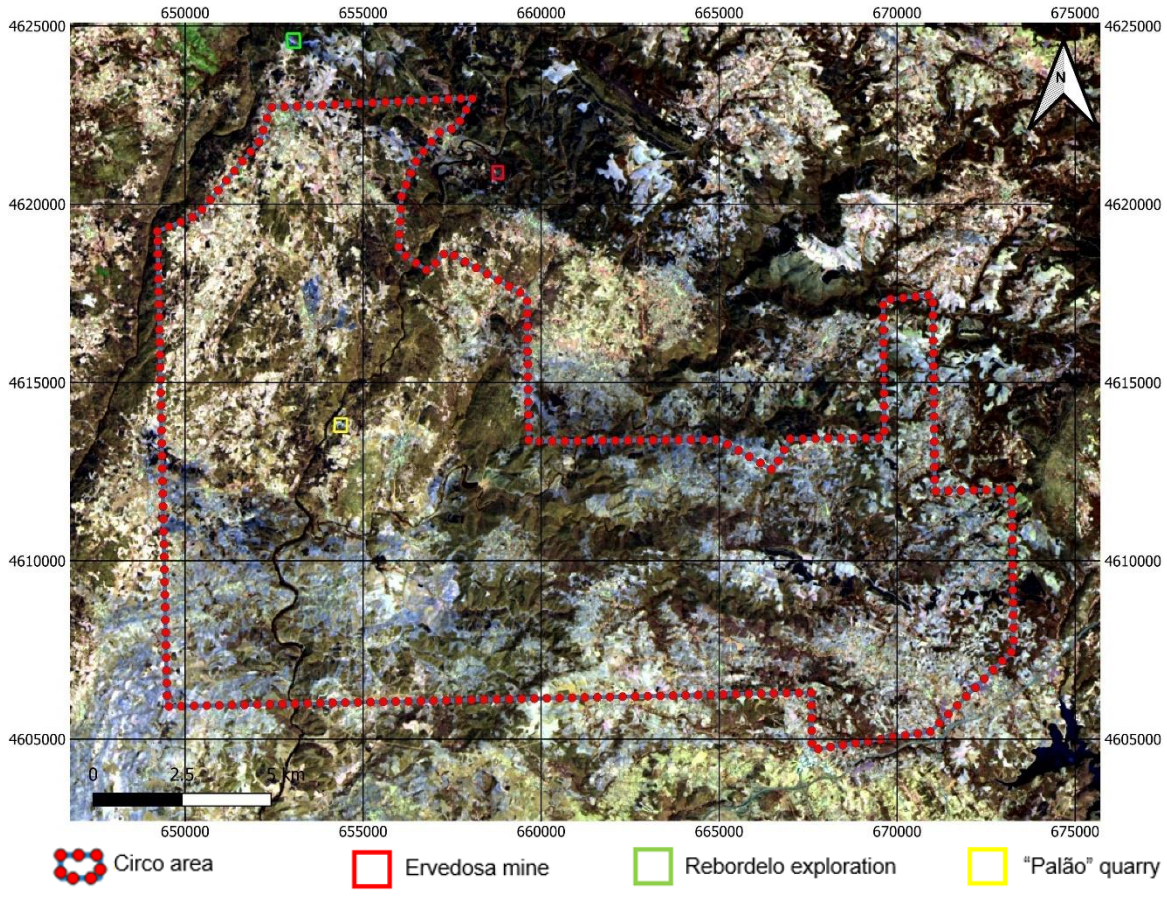


Figure 40. RGB combination (6-7-4) that identify lithological contrasts in Landsat-9. Coordinate System: UTM29N WGS84.

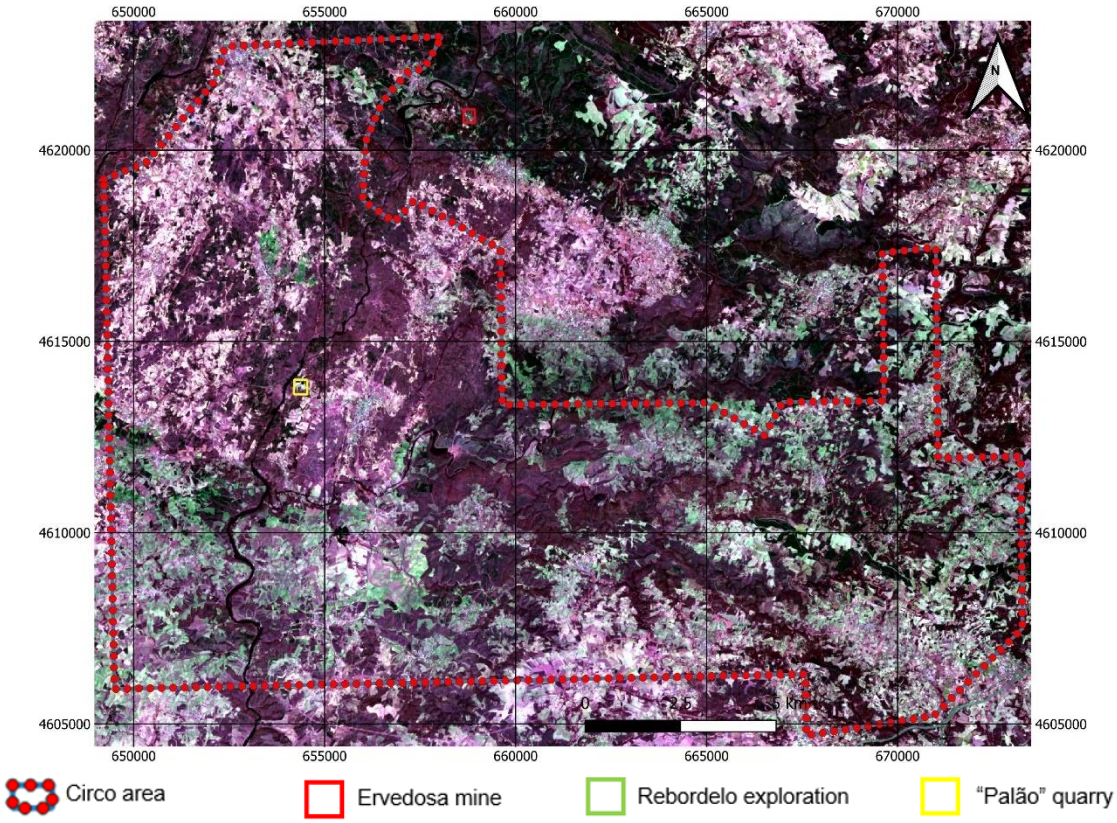


Figure 41. RGB combination (11-4-12) that identify lithological contrasts in Sentinel-2. Coordinate System: UTM29N WGS84.

5.1.2. Band ratios

In this section are presented the best band ratios found to map: iron oxides, ferric iron, ferrous minerals, alunite and clay minerals, spodumene and lepidolite, for both sensors (Sentinel-2-and Landsat-9). The resulting images presented different surface reflectance values which hinders a direct comparison between images, despite atmospheric correction. The same bands employed in the RGB combinations were used for this method.

Iron oxides, such as hematite and magnetite, were mapped using the ratio 4/2, either for Sentinel-2 or Landsat-9. Iron oxides are discriminated in bright pixels because iron minerals have low reflectance in blue and high reflectance in red.

Figure 42-a represents a colored density slice version of Sentinel-2's 4/2 band ratio (Figure 42-b), and the respective histogram is presented in Figure 42-c. Yellow and red areas correspond to the highest surface reflectance values (yellow ≈ 1.47; red ≥ 1.75) and therefore should also correlate with altered rocks. In the case of Landsat-9 (Figure 42-d, -e, -f), reflectance values change a little, but yellow and red areas (yellow ≈ 2.04; red ≥ 2.8) also correlate with altered rocks.

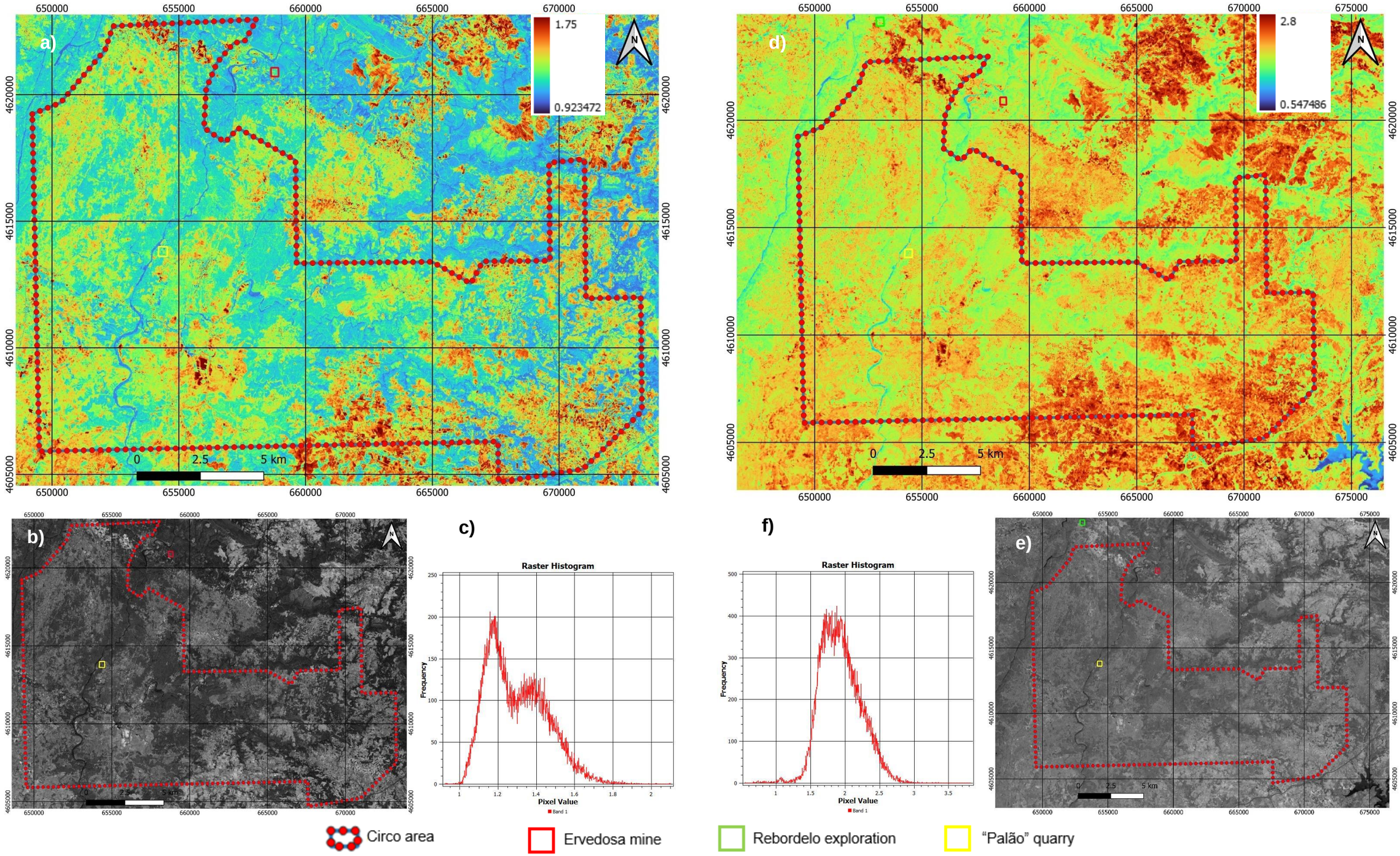


Figure 42. Iron oxides ratios: a) Sentinel-2's ratio 4/2 image with density slice (high ratio values shown in red); b) Sentinel-2's ratio 4/2 image; c) histogram for Sentinel-2's 4/2 image; d) Landsat-9's ratio 4/2 image with density slice (high ratio values shown in red); e) Landsat-9's ratio 4/2 image; f) histogram for Landsat-9's 4/2 image.

In both sensors, the highest contents of iron oxides appear mainly in the metasediments, including the phyllite and quartzite formations in the southern part of the area. The “Palão” quarry, Rebordelo exploration and Ervedosa mine present low to medium ratio values indicating low predominance in iron oxides, and the lowest values appear in vegetation zones (blue areas).

Ferric iron ratio 4/3 was also applied for both sensors (Figure 43), and the result is very similar to the iron oxides mapped, presenting the highest values in the same areas (urbanized areas also appear in red, yellow ≈ 1.14, red ≥ 1.35 for Sentinel-2 and yellow ≈ 1.33, red ≥ 1.7 for Landsat-9).

To map ferrous minerals, the ratios 11/8 (Sentinel-2) and 6/5 (Landsat-9) were applied. High reflectance values appear in granites and metasediments equally (there is not a big difference like with the iron oxide ratio).

Figure 44-a represents a colored density slice version of Sentinel-2’s 11/8 band ratio (Figure 44-b), and the respective histogram is presented in Figure 44-c. Yellow and red areas correspond to the highest surface reflectance values (yellow ≈ 1.19; red ≥ 1.6).

Figure 44-d represents a colored density slice version of Landsat-9’s 6/5 band ratio (Figure 44-e), and the histogram is presented in Figure 44-f. Yellow and red areas correspond to the highest surface reflectance values (yellow ≈ 1.2; red ≥ 1.8).

Comparing these ratios to the iron oxide, just a few areas with low reflectance in ferrous minerals can be seen. The “Palão” quarry, Rebordelo exploration and Ervedosa mine present medium reflectance for ferrous minerals.

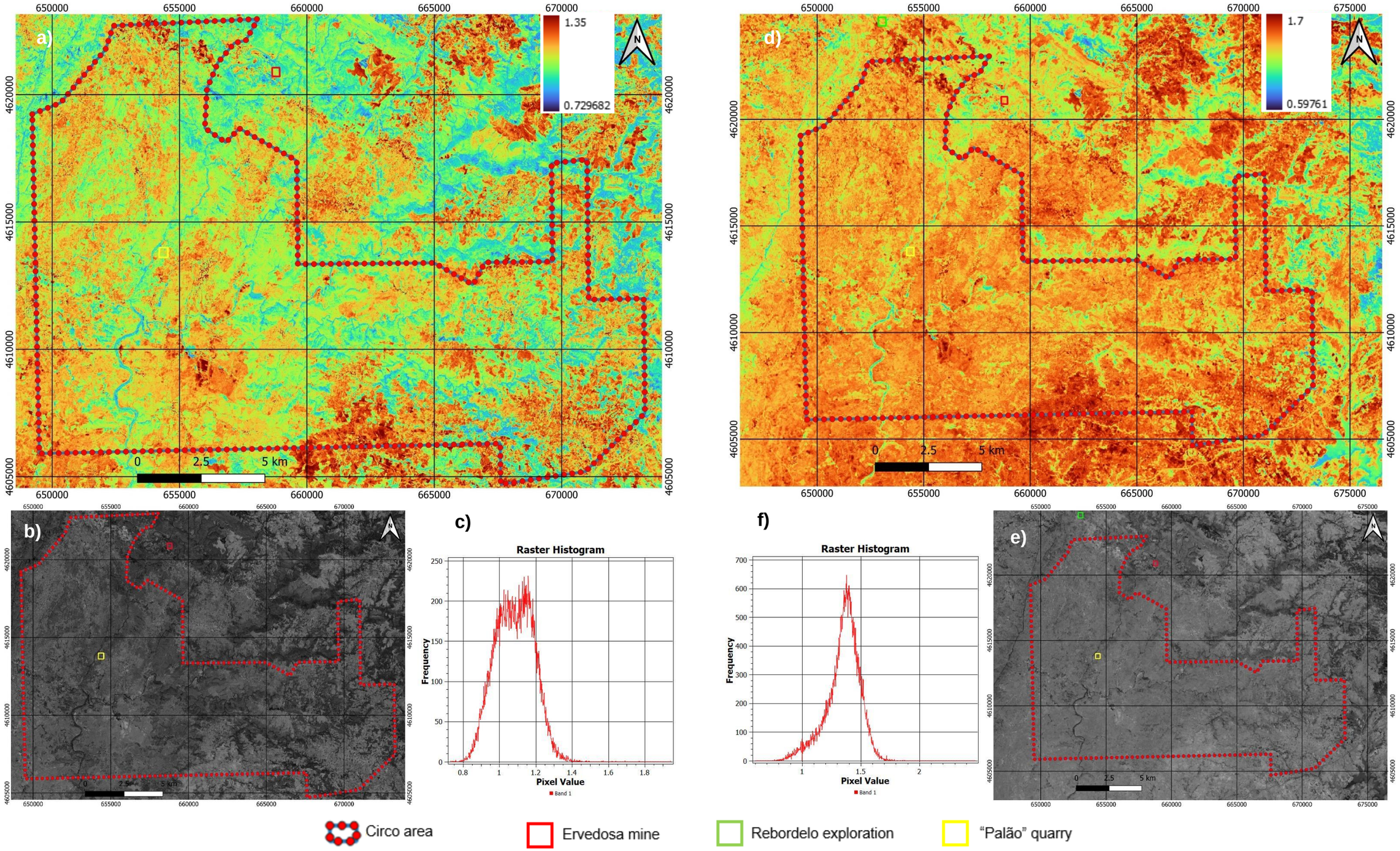


Figure 43. Ferric iron ratios: a) Sentinel-2's ratio 4/3 image with density slice (high ratio values shown in red); b) Sentinel-2's ratio 4/3 image; c) histogram for Sentinel-2's 4/3 image; d) Landsat-9's ratio 4/3 image with density slice (high ratio values shown in red); e) Landsat-9's ratio 4/3 image; f) histogram for Landsat-9's 4/3 image.

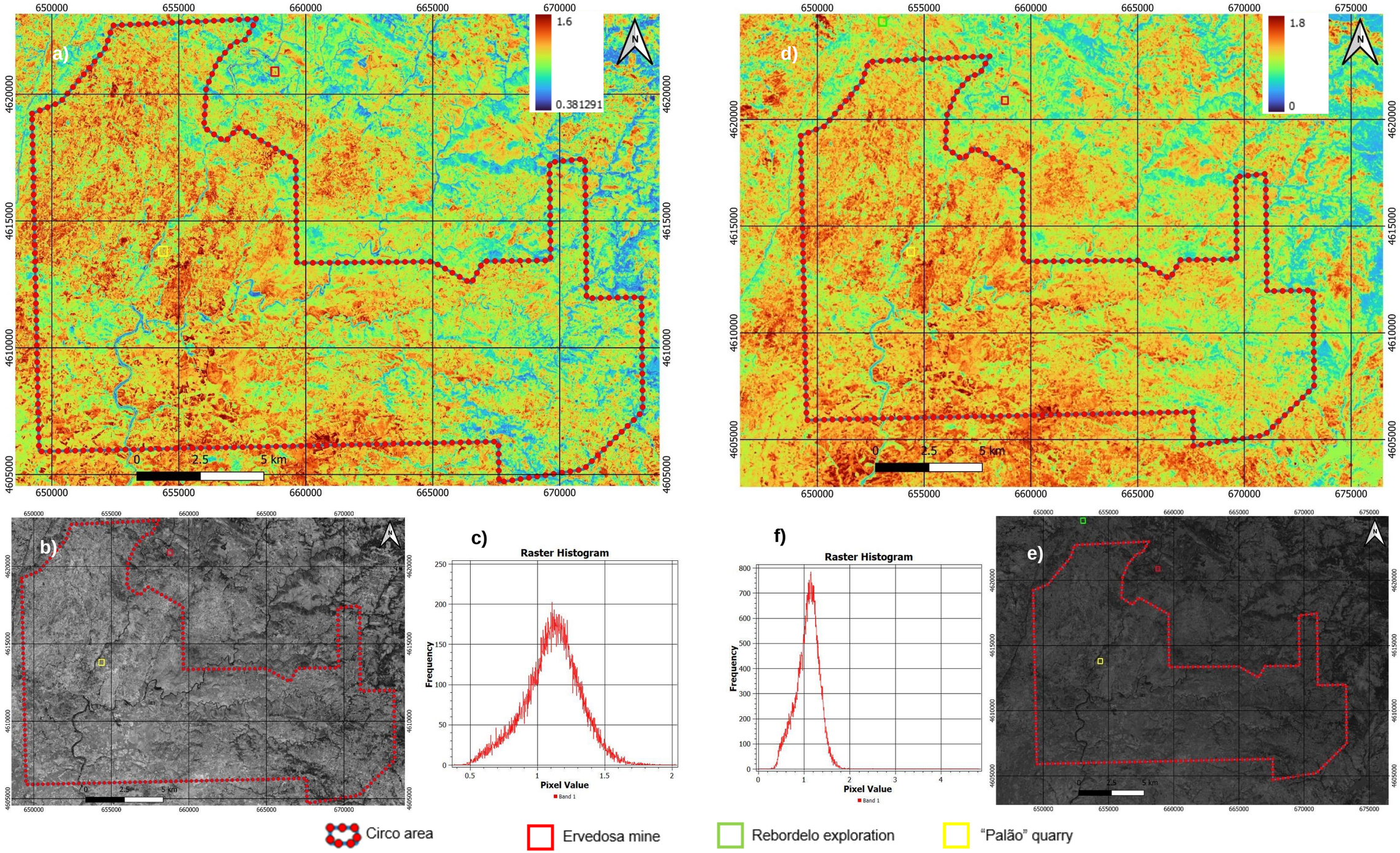


Figure 44. Ferrous minerals ratios: a) Sentinel-2's ratio 11/8 image with density slice (high ratio values shown in red); b) Sentinel-2's ratio 11/8 image; c) histogram for Sentinel-2' 11/8 image; d) Landsat-9's ratio 6/5 image with density slice (high ratio values shown in red); e) Landsat-9's ratio 6/5 image; f) histogram for Landsat-9's 6/5 image.

Other minerals frequently associated with hydrothermal alterations are alunite and/or clays such as kaolinite, montmorillonite, and illite, among others. To represent these minerals, the band ratio 11/12 was applied to Sentinel-2 images and a 6/7 ratio to Landsat-9.

Figure 45-a represents a colored density slice of Sentinel-2's 11/12 band ratio (Figure 45-b), and the respective histogram is presented in Figure 45-c. Yellow and red areas correspond to the highest surface reflectance values (yellow ≈ 1.34; red ≥ 1.55).

Figure 45-d represents a colored density slice of Landsat-9's 6/7 band ratio (Figure 45-e), and the respective histogram is presented in Figure 45-f. Yellow and red areas correspond to the highest surface reflectance values (yellow ≈ 1.6; red ≥ 2.4).

As expected, the highest reflectance in alunite and/or clays appear near the water streams. It is possible to see slightly higher reflectance in the metasediments compared to the granites. The "Palão" quarry, Rebordelo exploration and Ervedosa mine present low to medium reflectance in alunite and clay minerals.

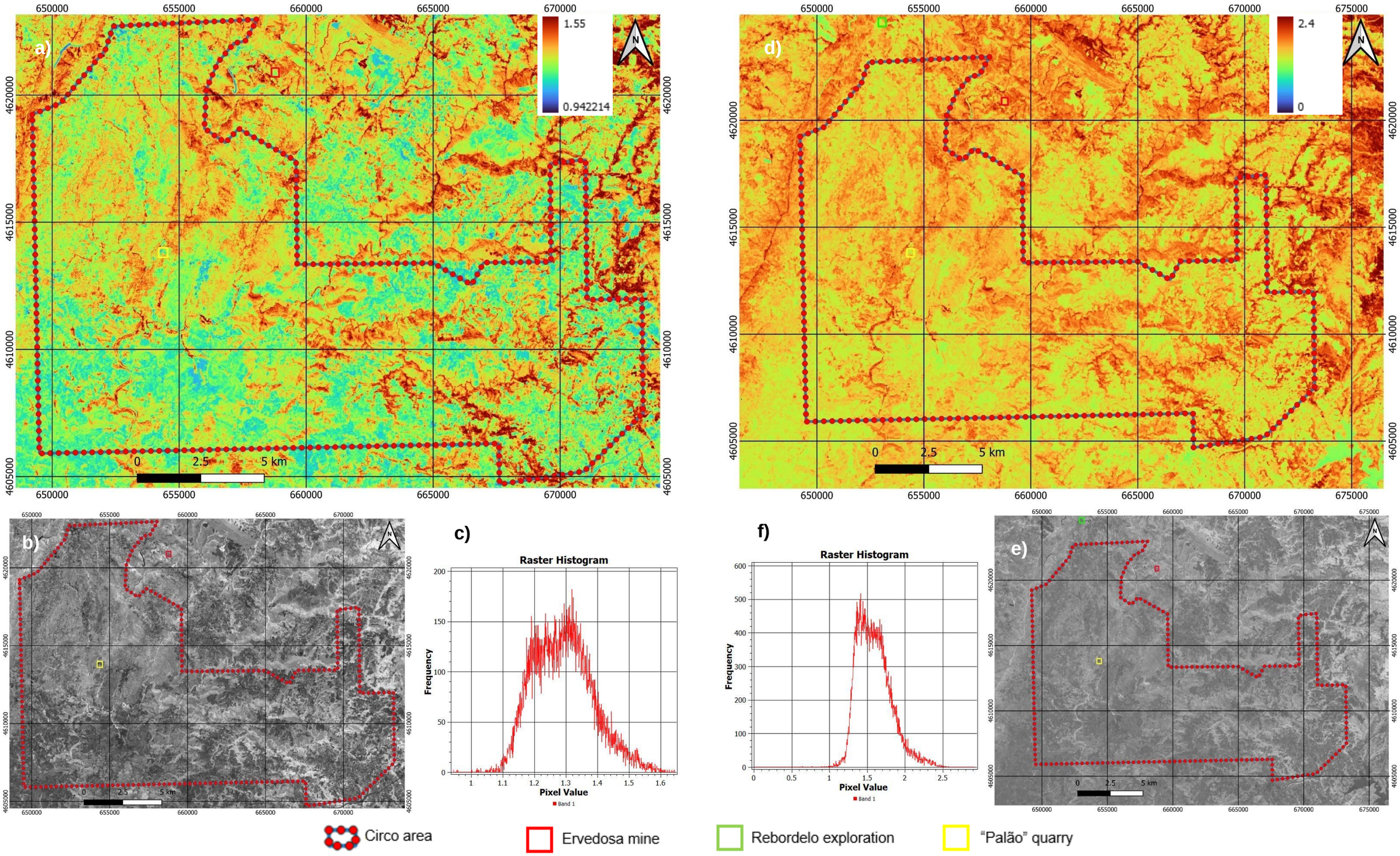


Figure 45. Alunite and clay minerals ratios: a) Sentinel-2's ratio 11/12 image with density slice (high ratio values shown in red); b) Sentinel-2's ratio 11/12 image; c) histogram for Sentinel-2's 11/12 image; d) Landsat-9's ratio 6/7 image with density slice (high ratio values shown in red); e) Landsat-9's ratio 6/7 image; f) histogram for Landsat-9's 6/7 image.

According to the work of Cardoso-Fernandes *et al.* (2019), some ratios to discriminate Li-mineralizations were tested (based on the spectral behavior of spodumene). Ratio 3/8 for Sentinel-2 (Figure 46-a, -b, -c), and ratio 3/5 for Landsat-9 (Figure 46-d, -e, -f).

Both colored density slice versions (Figure 46-a and -d) show very high reflectance (red ≥ 0.75 (Sentinel-2) and red ≥ 0.65 (Landsat-9)) in spodumene in the “Palão” quarry, Rebordelo exploration and Ervedosa mine and some other areas. Therefore, it is impossible to conclude that those areas represent Li-bearing rocks (due to the unknown lithologies of the area), but according to the ratios, they can be considered good remote sensing targets to discriminate in fieldwork.

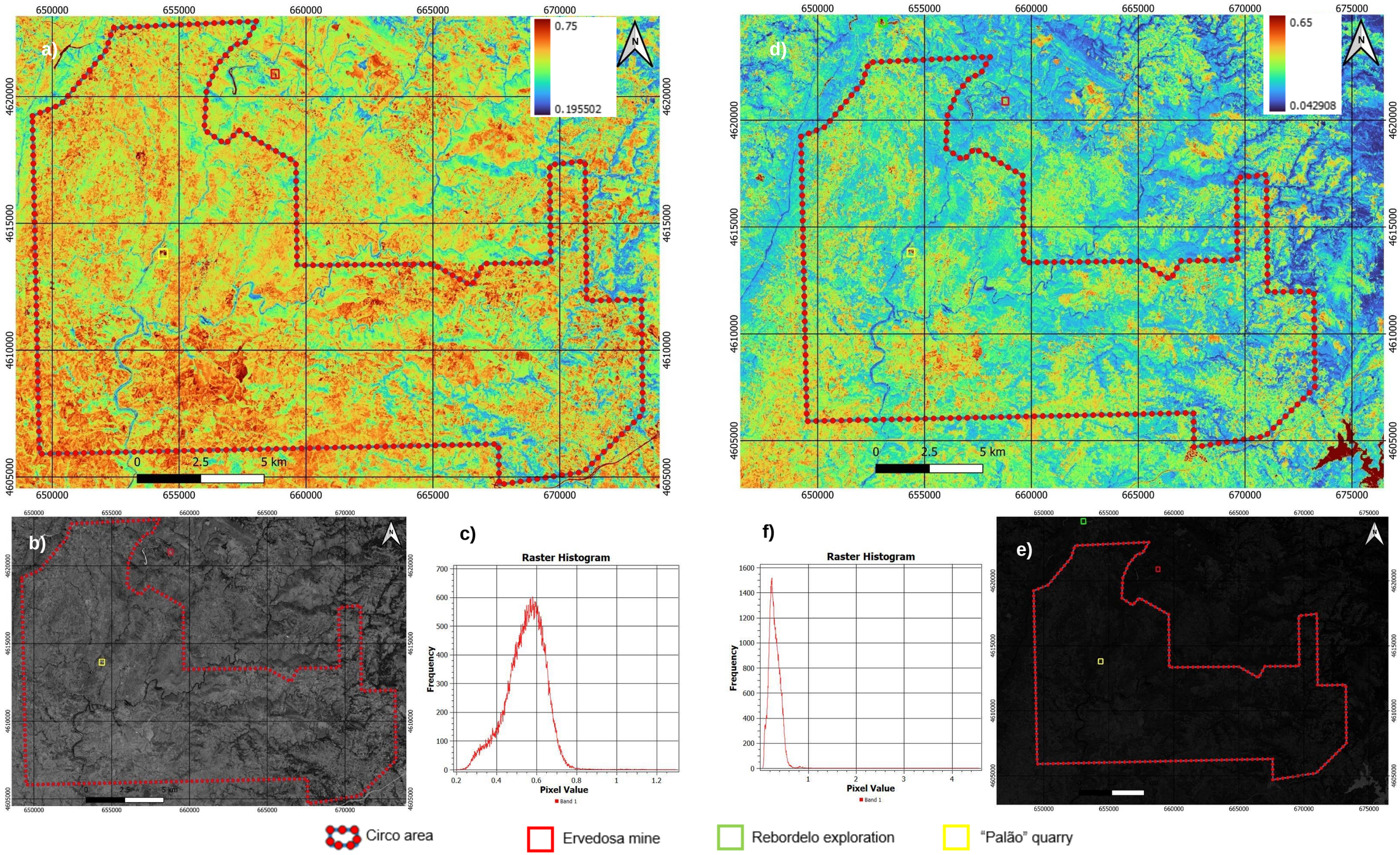


Figure 46. Spodumene ratios: a) Sentinel-2's ratio 3/8 image with density slice (high ratio values shown in red); b) Sentinel-2's ratio 3/8 image; c) histogram for Sentinel-2's 3/8 image; d) Landsat-9's ratio 3/5 image with density slice (high ratio values shown in red); e) Landsat-9's ratio 3/5 image; f) histogram for Landsat-9's 3/5 image.

Two more ratios were used, based on the lepidolite spectral curve: 4/12 for Sentinel-2 and 4/7 for Landsat-9.

Figure 47-a represents a colored density slice of Sentinel-2's 4/12 band ratio (Figure 47-b), and the respective histogram is presented in Figure 47-c. Yellow and red areas correspond to the highest surface reflectance values (yellow ≈ 0.74; red ≥ 1).

Figure 47-d represents a colored density slice of Landsat-9's 4/7 band ratio (Figure 47-e), and the respective histogram is presented in Figure 47-f. Yellow and red areas correspond to the highest surface reflectance values (yellow ≈ 0.76; red ≥ 1.1).

In both sensors, there is a clear difference between the granites and the metasediments which present higher ratio values. The "Palão" quarry, Rebordelo exploration and Ervedosa mine present medium to high ratio values.

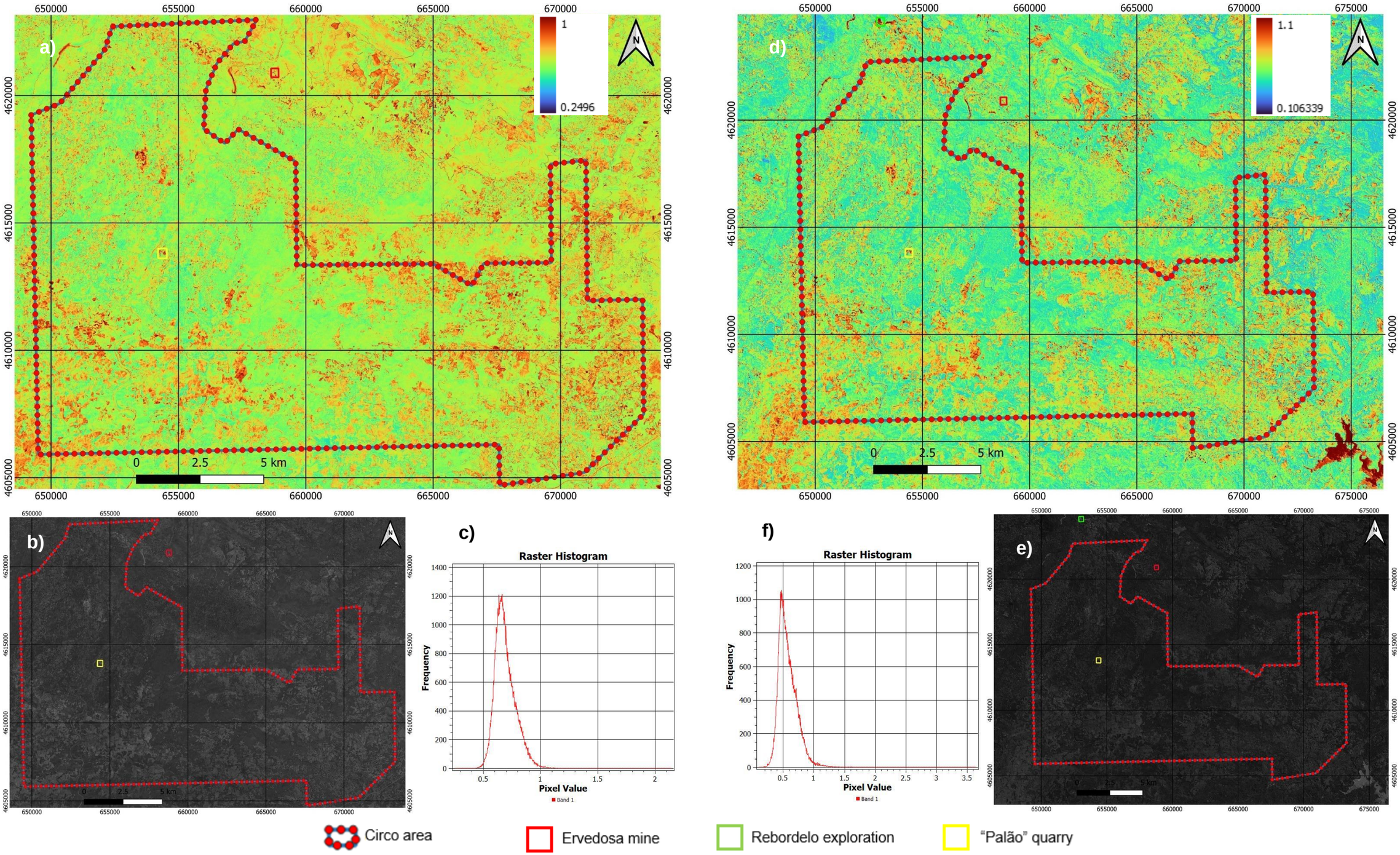


Figure 47. Lepidolite ratios: a) Sentinel-2's ratio 4/12 image with density slice (high ratio values shown in red); b) Sentinel-2's ratio 4/12 image; c) histogram for Sentinel-2's 4/12 image; d) Landsat-9's ratio 4/7 image with density slice (high ratio values shown in red); e) Landsat-9's ratio 4/7 image; f) histogram for Landsat-9's 4/7 image.

5.1.3. Principal Component Analysis (PCA)

Firstly, this analysis was applied to six Sentinel-2 bands (2, 3, 4, 8, 11, and 12) and six Landsat-9 bands (2, 3, 4, 5, 6, and 7) (Standard PCA), resulting in two eigenvector matrixes, represented in Tables 6 and 7, respectively. These results allowed identifying which PCs contain more useful spectral information from Sentinel-2 and Landsat-9 bands, whose have much higher contrast than the original bands.

The inspection of magnitude and sign (positive or negative) of the eigenvectors determine which spectral properties of vegetation, rocks, and soils are responsible for the statistical variance mapped into each principal component (PC) (Loughlin, 1991). The eigenvalues indicate decreasing variance in successive PCs (Loughlin, 1991). All eigenvalues are decimal numbers because the PCA was done after atmospheric correction. To aid in the eigenvalue interpretation, they can be expressed as a percentage of accounted variance.

For Sentinel-2, the PC1 (Table 6) accounts for 78.704% of the total variance of the raw data, is composed of a negative weighting of all 6 bands and mainly represents the albedo. According to Loughlin (1991), the strong correlation between the different image channels is due to the overall scene brightness or albedo and is therefore mapped in PC1.

Table 6. PCA on 6 Sentinel-2 bands: Eigenvector and eigenvalues matrix.

	PC1	PC2	PC3	PC4	PC5	PC6
Band 2	-0.22099	0.01097	0.36882	-0.33432	0.57716	0.60839
Band 3	-0.29443	-0.03987	0.45075	-0.19580	0.29255	-0.76461
Band 4	-0.43953	0.05648	0.55771	0.15464	-0.65297	0.20565
Band 8	-0.23147	-0.95804	-0.11501	0.11259	0.01677	0.04888
Band 11	-0.56385	0.12447	-0.52228	-0.59314	-0.20357	-0.02326
Band 12	-0.54752	0.24851	-0.25249	0.67933	0.33647	0.00381
Eigenvalues	0.021466	0.004404	0.001210	0.000115	0.000066	0.000015
Accounted variance	78.703864	16.145385	4.435888	0.420835	0.240187	0.053842
Cumulative variance	78.703864	94.849249	99.285137	99.705971	99.946158	100

The eigenvector loadings of PC2 (Table 6) indicate that this PC maps vegetated areas in dark pixels due to the high negative loading in band 8 (which coincides with the NIR reflectance peak of vegetation). PC2 accounts for 16.145% of the total variability. Because the eigenvector loadings for band 11 and band 12 in PC4 of Table 6 are opposite in sign and present high magnitude, we can predict that hydroxyl minerals are

mapped in dark pixels in PC4 due to positive eigenvector loadings of band 12. Iron oxides are mapped as dark pixels in PC5 due to the negative contribution from band 4 and a positive one from band 2 (Table 6).

PCs can be combined to create an RGB combination. For example, a combination of PC1, PC4 and PC5 was created, respectively, in red, green and blue channels. Knowing that iron oxides and hydroxyl minerals are mapped in dark pixels, a negation of PC4 and PC5 was made, making the combination PC1, -PC4 and -PC5, for an easier interpretation of the image (Figure 48).

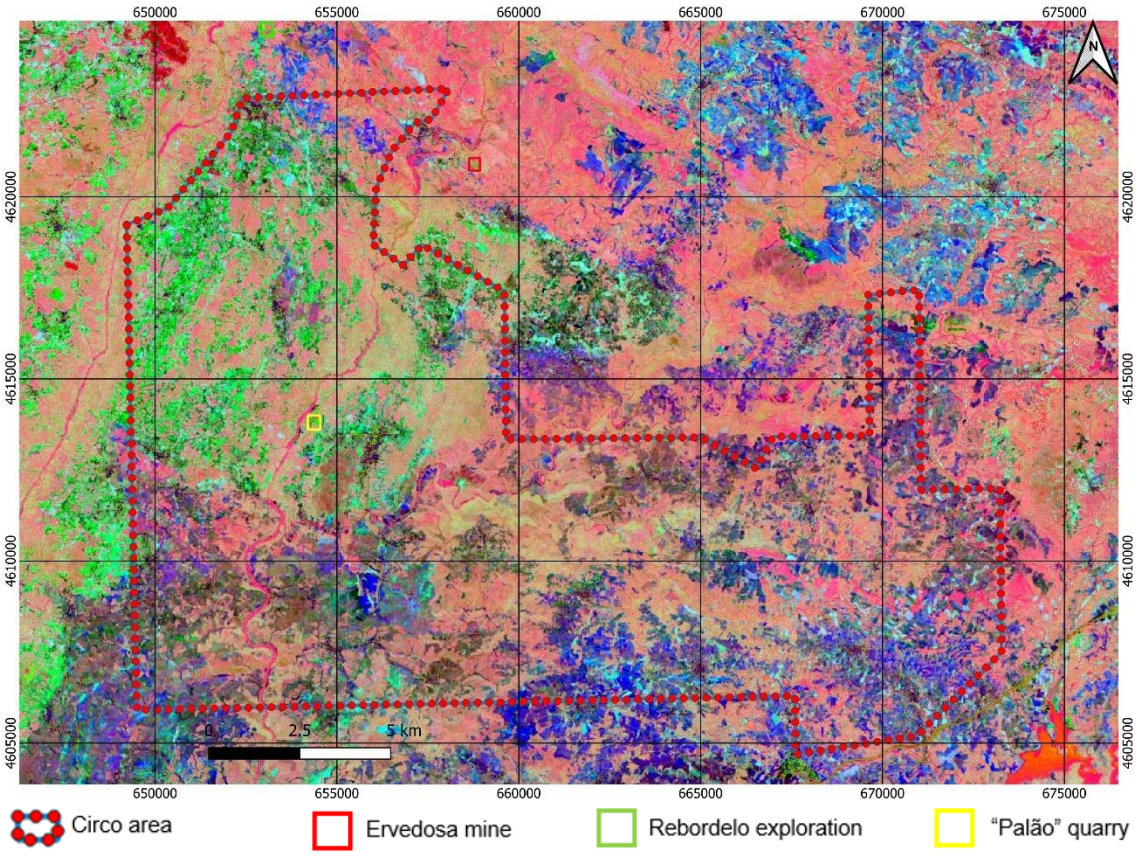


Figure 48. RGB combination of PC1, -PC4 and -PC5 for Sentinel-2. Granites appear in a green color and metasediments in blue; vegetation is discriminated in pink; high contents of iron oxides are presented in intense blue and hydroxyl minerals in light blue. The "Palão" quarry, Rebordelo exploration and Ervedosa mine, all appear in green. All burned areas appear in an intense red color.

For Landsat-9, the PC1 (Table 7) accounts for 85.047% of the total variance of the raw data, being composed of a negative weighting of all 6 bands, mainly representing the albedo. The eigenvector loadings of PC2 (Table 7) indicate that this PC maps vegetated areas in dark pixels due to the high negative loading in band 5. PC2 accounts for 9.511% of the total variability and PC3 for 4.616%. Because the eigenvector loadings for band 6 and band 7 in PC4 of Table 7 are opposite in sign and

present high magnitude, we can predict that hydroxyl minerals are mapped in dark pixels in PC4 due to positive eigenvector loadings of band 7. Iron oxides are mapped as dark pixels in PC5 due to the negative contribution from band 4 and a positive one from band 2 (Table 7).

Table 7. PCA on 6 Landsat-9 bands: Eigenvector and eigenvalues matrix.

	PC1	PC2	PC3	PC4	PC5	PC6
Band 2	-0.18547	0.08327	0.33248	-0.32849	0.71667	0.47604
Band 3	-0.26190	0.05786	0.46553	-0.14244	0.18289	-0.81093
Band 4	-0.38396	0.12297	0.61108	0.07644	-0.58654	0.33788
Band 5	-0.32011	-0.94141	0.00276	0.09044	0.04536	0.03215
Band 6	-0.61331	0.14361	-0.50525	-0.56061	-0.18185	-0.02427
Band 7	-0.52054	0.26023	-0.20982	0.73723	0.27163	-0.00200
Eigenvalues	0.015833	0.001771	0.000859	0.000089	0.000059	0.000005
Accounted variance	85.04743	9.511321	4.615664	0.480507	0.318587	0.026428
Cumulative variance	85.04743	94.558815	99.174478	99.654985	99.973572	100

A combination of PC1, PC6 and PC4 was created, respectively, in red, green and blue channels. The same process was made for PC4 in this case: hydroxyl minerals were mapped in dark pixels, so PC4 was negated (-PC4), making the combination PC1, PC6 and -PC4, for an easier interpretation of the image (Figure 49).

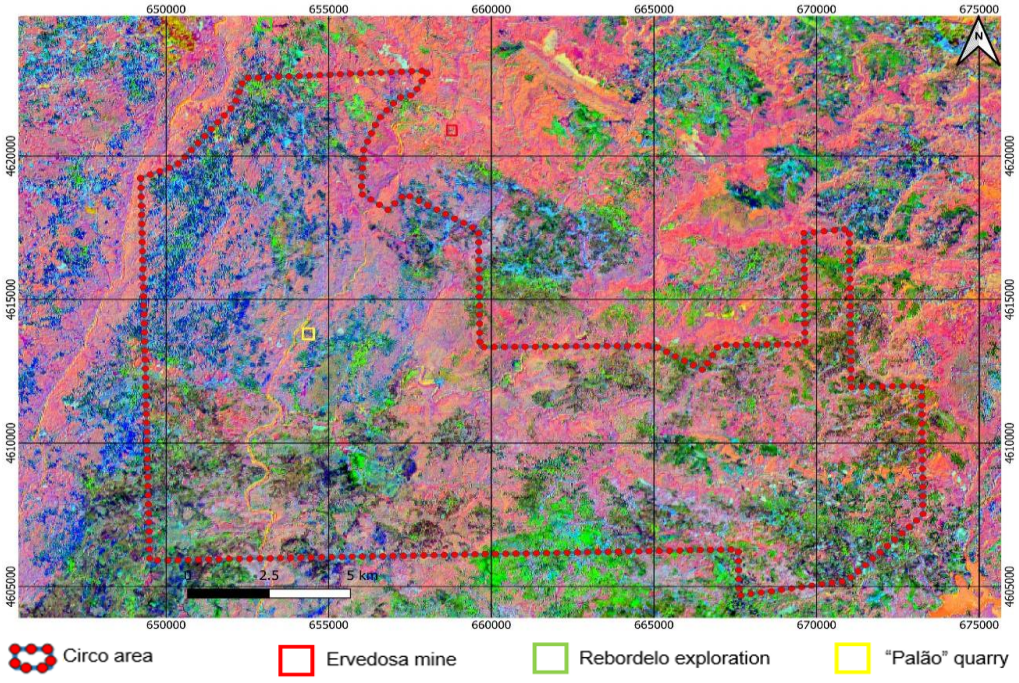


Figure 49. RGB combination of PC1, PC6 and -PC4 for Landsat-9. Granites appear in a blue color and metasediments in green to blue; vegetation is discriminated in pink; high contents of iron oxides are presented in intense blue and hydroxyl minerals in light blue. The "Palão" quarry, Rebordelo exploration and Ervedosa mine, all appear in dark blue. All burned areas appear in a greenish yellow.

In both sensors, the first three PCs explain most of the image variability (99.28% in the case of Sentinel-2 and 99.17% for Landsat-9). Normally those three PCs are used for lithological mapping with the RGB combination PC1-PC2-PC3 (Figure 50), but other combinations, for example, the combination of PC1, -PC4 and -PC5 (Figure 48) and combination PC1, PC6 and -PC4 (Figure 49) allows to better discriminate than combination PC1-PC2-PC3.

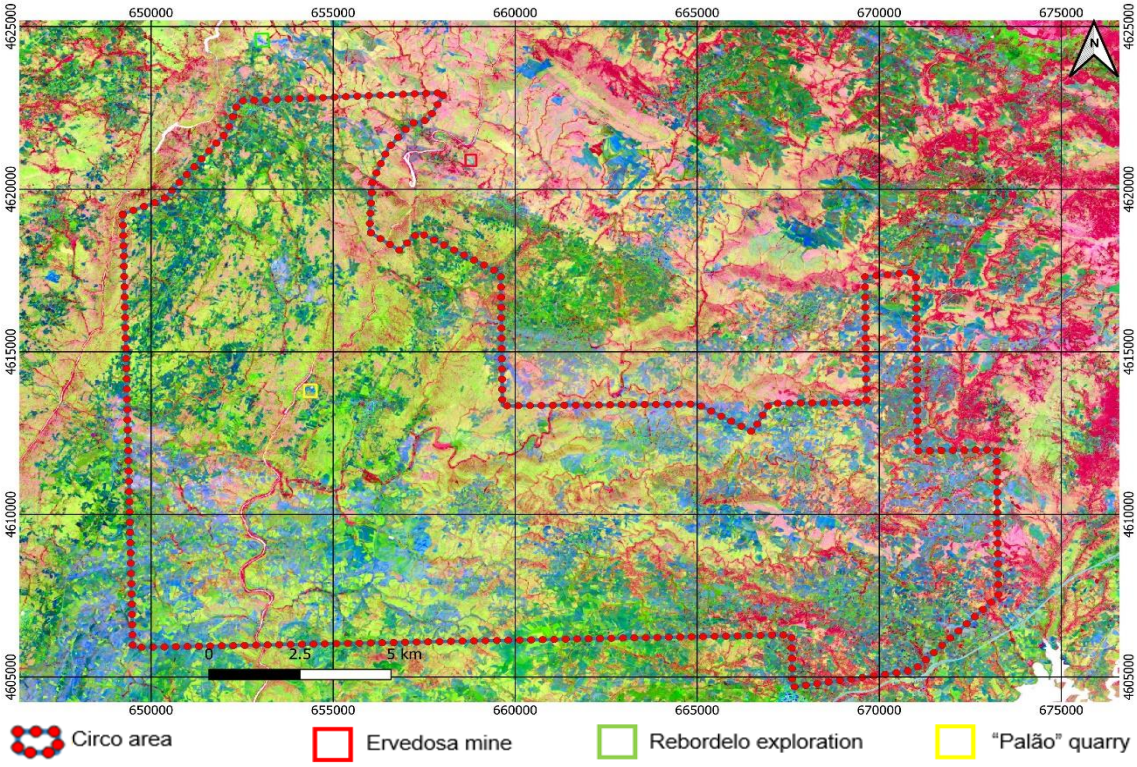


Figure 50. RGB combination of PC1, PC2 and PC3 of Landsat-9.

To try to isolate target spectral signatures, PCA was applied to selected subsets of the satellites' bands, through the application of the "Crosta technique" (Selective PCA) (Loughlin, 1991), in which the PCA is applied to a subset of four bands. This method was applied to Sentinel-2 and Landsat-9 bands to map ferric iron, hydroxyl-bearing minerals and Li-bearing minerals.

In the chosen Sentinel-2 four-band subset to discriminate ferric iron (Table 8), PC1 maps the albedo; PC2 maps the vegetation; examining the eigenvector loadings for bands 2 and 4, in both PC3 and PC4, we can predict that ferric iron is mapped in PC4 (Figure 53-a) due to strong loadings from both bands, with opposite signs. Because of the positive loading of band 2, ferric iron appears in dark pixels, so a negation of PC4 (-PC4) was made, being called the "Selective F band" for Sentinel-2 (Figure 53-b). In this case, the "Palão" quarry, Rebordelo exploration and Ervedosa mine were not discriminated by high contents of ferric iron (Figure 53-b).

Table 8. Selective PCA for ferric iron mapping (four Sentinel-2 bands): Eigenvector and eigenvalues matrix.

	PC1	PC2	PC3	PC4
Band 2	-0.27710	0.08967	-0.40695	0.86577
Band 4	-0.54851	0.20670	-0.63943	-0.49753
Band 8	-0.36141	-0.93218	0.01725	-0.01101
Band 11	-0.70124	0.28331	0.65209	0.05273
Eigenvalues	0.013354	0.003987	0.000892	0.000065
Accounted variance	72.983121	21.791898	4.872158	0.352823
Cumulative variance	72.983121	94.775019	99.647177	100

In the chosen Landsat-9 four-band subset to discriminate ferric iron (Table 9), PC1 maps the albedo; PC2 maps the vegetation; examining the eigenvector loadings for bands 2 and 4, in both PC3 and PC4, we can predict that ferric iron is mapped in PC4 (Figure 51-c) due to strong loadings from both bands, with opposite signs. Because of the positive loading of band 2, ferric iron appears in dark pixels, so a negation of PC4 (-PC4) was made, being called the “Selective F band” for Landsat-9 (Figure 51-d). In this case, the “Palão” quarry, Rebordelo exploration and Ervedosa mine were not discriminated by high contents of ferric iron once more (Figure 51-d).

Table 9. Selective PCA for ferric iron mapping (four Landsat-9 bands): Eigenvector and eigenvalues matrix.

	PC1	PC2	PC3	PC4
Band 2	-0.22290	0.14621	-0.37204	0.88911
Band 4	-0.46327	0.24743	-0.71775	-0.45716
Band 5	-0.42415	-0.90390	-0.05115	0.02091
Band 6	-0.74551	0.31679	0.58635	0.00635
Eigenvalues	0.010547	0.001583	0.000641	0.000059
Accounted variance	82.207178	12.336488	4.998359	0.457976
Cumulative variance	82.207178	94.543666	99.542024	100

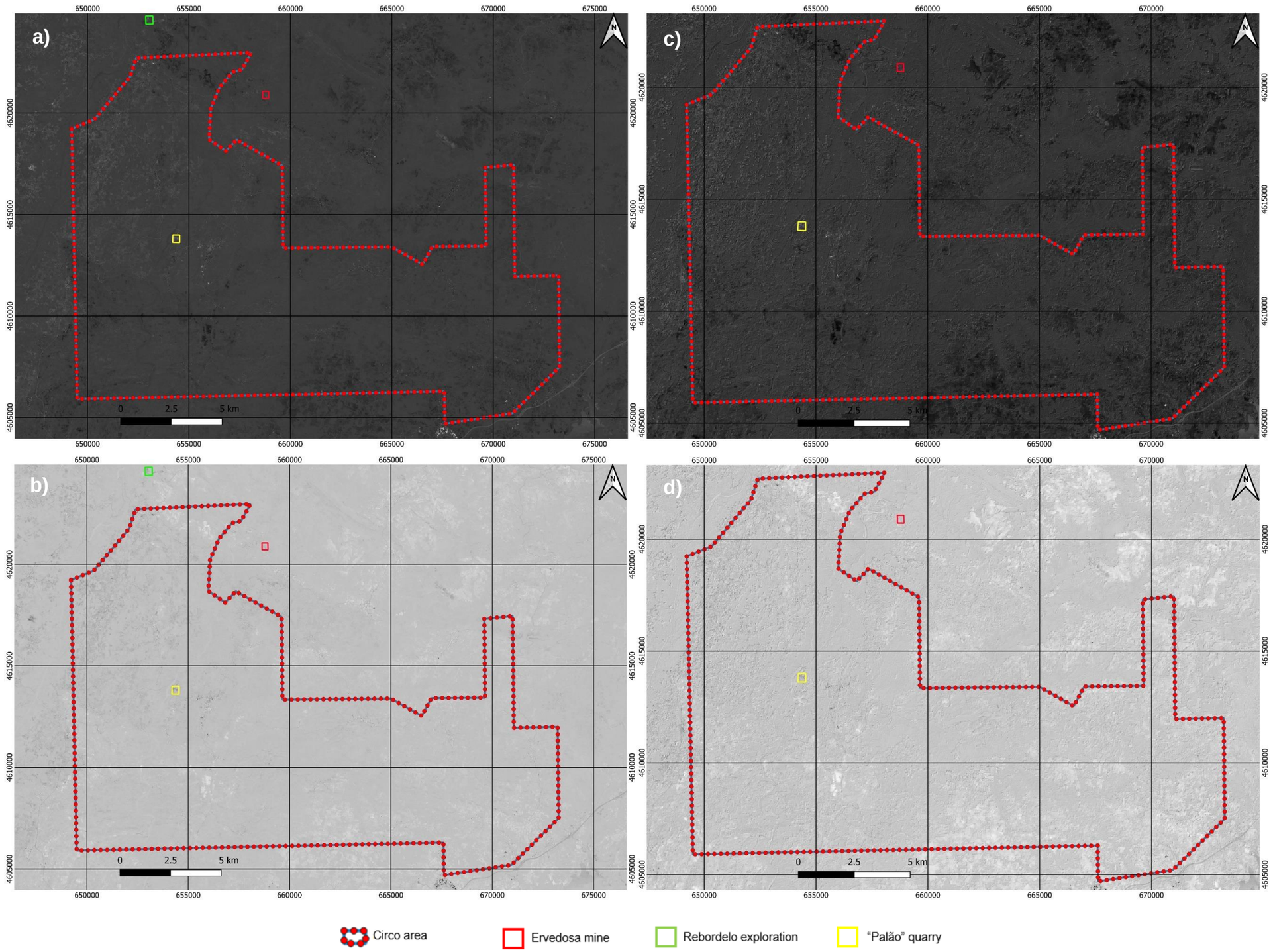


Figure 51. Selective PCA on 4 bands to highlight ferric iron: a) PC4 from Sentinel-2 subset; b) Selective F band (-PC4) from the Sentinel-2 subset; c) PC4 from Landsat-9 subset; d) Selective F band (-PC4) from the Landsat-9 subset.

In the selected Sentinel-2 four-band subset to discriminate hydroxyl minerals (Table 10), PC1 maps the albedo; PC2 maps the vegetation; examining the eigenvector loadings for bands 11 and 12, in both PC3 and PC4, we can predict that hydroxyl minerals are mapped in PC4 (Figure 52) due to strong loadings from both bands, with opposite signs. Because of the positive loading of band 11, hydroxyl minerals appear in bright pixels (Selective H band; Figure 52). In this case, the “Palão” quarry, Rebordelo exploration and Ervedosa mine were not discriminated by high contents of hydroxyl minerals (Figure 52).

Table 10. Selective PCA for hydroxyl minerals mapping (four Sentinel-2 bands): Eigenvector and eigenvalues matrix.

	PC1	PC2	PC3	PC4
Band 2	-0.24390	0.01350	0.90356	0.35200
Band 8	-0.27788	-0.95485	-0.02058	-0.10310
Band 11	-0.67119	0.13979	-0.41600	0.59742
Band 12	-0.64250	0.26181	0.10048	-0.71310
Eigenvalues	0.015709	0.004382	0.000373	0.000110
Accounted variance	76.352802	21.299070	1.813879	0.534248
Cumulative variance	76.352802	97.651873	99.465752	100

In the Landsat-9 four-band subset to discriminate hydroxyl minerals (Table 11), PC1 maps the albedo; PC2 maps the vegetation; examining the eigenvector loadings for bands 6 and 7, in both PC3 and PC4, we can predict that hydroxyl minerals are mapped in PC4 (Figure 53) due to strong loadings from both bands, with opposite signs. Because of the positive loading of band 6, hydroxyl minerals appear in bright pixels (Selective H band; Figure 53). Again, the “Palão” quarry, Rebordelo exploration and Ervedosa mine were not discriminated by high contents of hydroxyl minerals (Figure 53).

Table 11. Selective PCA for hydroxyl minerals mapping (four Landsat-9 bands): Eigenvector and eigenvalues matrix.

	PC1	PC2	PC3	PC4
Band 2	-0.19735	0.06975	0.88644	0.41282
Band 5	-0.36732	-0.92579	0.03026	-0.08415
Band 6	-0.69649	0.21353	-0.42287	0.53897
Band 7	-0.58398	0.30407	0.18574	-0.72939
Eigenvalues	0.012566	0.001746	0.000230	0.000087
Accounted variance	85.902178	11.934322	1.569461	0.594038
Cumulative variance	85.902178	97.836501	99.405962	100

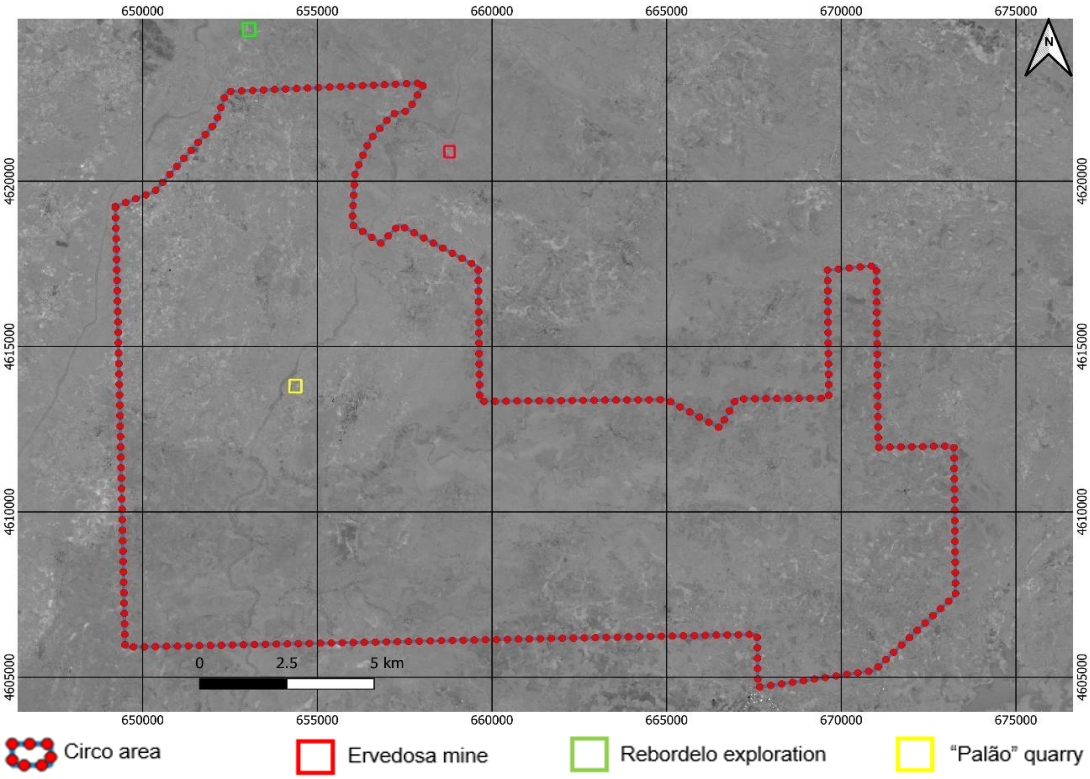


Figure 52. Selective PCA on 4 bands to highlight hydroxyl minerals: Selective H band (PC4) from the Sentinel-2 subset.

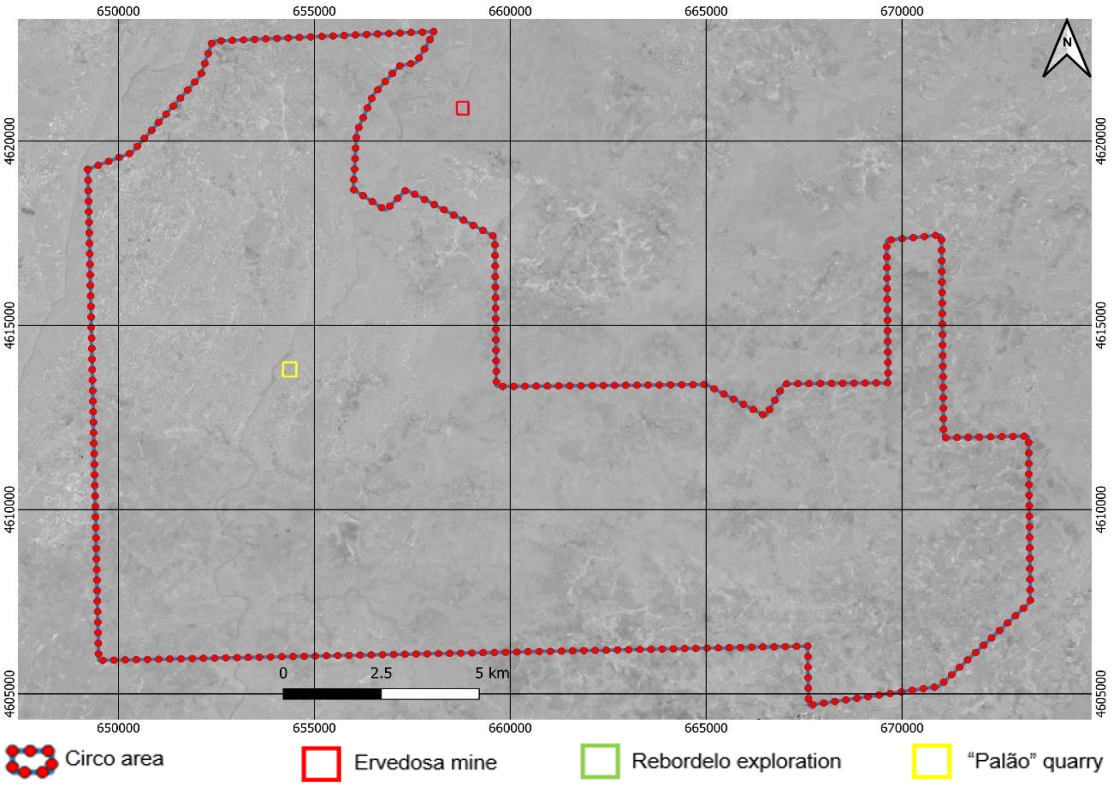


Figure 53. Selective PCA on 4 bands to highlight hydroxyl minerals: Selective H band (PC4) from the Landsat-9 subset.

In the Sentinel-2 four-band subset to discriminate Li-bearing minerals (Table 12), PC1 maps the albedo; examining the eigenvector loadings for bands 3 and 8, in PC2, PC3 and PC4, we can predict that Li-bearing minerals are mapped in PC2 (Figure 54-a) due to strong loadings of band 8, with opposite signs. Because of the positive loading of band 3, Li-bearing minerals should appear in bright pixels (Selective Li band; Figure 54-a). As expected, high contents of Li-bearing minerals were not identified in the "Palão" quarry, Rebordelo exploration and Ervedosa mine (Figure 54-a).

Table 12. Selective PCA for Li-bearing minerals mapping (four Sentinel-2 bands): Eigenvector and eigenvalues matrix.

	PC1	PC2	PC3	PC4
Band 2	-0.29137	0.12136	-0.54898	0.77395
Band 3	-0.39451	0.10200	-0.65913	-0.63206
Band 8	-0.43887	-0.89340	0.08840	0.03757
Band 11	-0.75290	0.42036	0.50631	0.00977
Eigenvalues	0.01130	0.00379	0.00075	0.00002
Accounted variance	71.21460	23.91758	4.74101	0.12681
Cumulative variance	71.21460	95.13218	99.87319	100

In the Landsat-9 four-band subset to discriminate Li-bearing (Table 13), PC1 maps the albedo; PC2 maps the vegetation; examining the eigenvector loadings for bands 3 and 5, in both PC3 and PC4, we can predict that Li-bearing minerals are mapped in PC3 (Figure 54-b) due to moderate to strong loadings from both bands, with opposite signs. Because of the positive loading of band 5, Li-bearing minerals appear in dark pixels, so a negation of PC3 (-PC3) was made, being called the "Selective Li band" for Landsat-9 (Figure 54-c). Again, high contents of Li-bearing minerals were not observed in the "Palão" quarry, Rebordelo exploration and Ervedosa mine (Figure 54-c).

Table 13. Selective PCA for Li-bearing minerals mapping (four Landsat-9 bands): Eigenvector and eigenvalues matrix.

	PC1	PC2	PC3	PC4
Band 2	-0.31758	0.15171	-0.51398	0.78228
Band 3	-0.45625	0.16833	-0.61426	-0.62145
Band 5	-0.69108	-0.65978	0.29247	0.03956
Band 11	-0.46195	0.71648	0.52247	0.01679
Eigenvalues	0.004881	0.001870	0.000554	0.000019
Accounted variance	66.644783	25.535633	7.562758	0.256826
Cumulative variance	66.644783	92.180415	99.743174	100

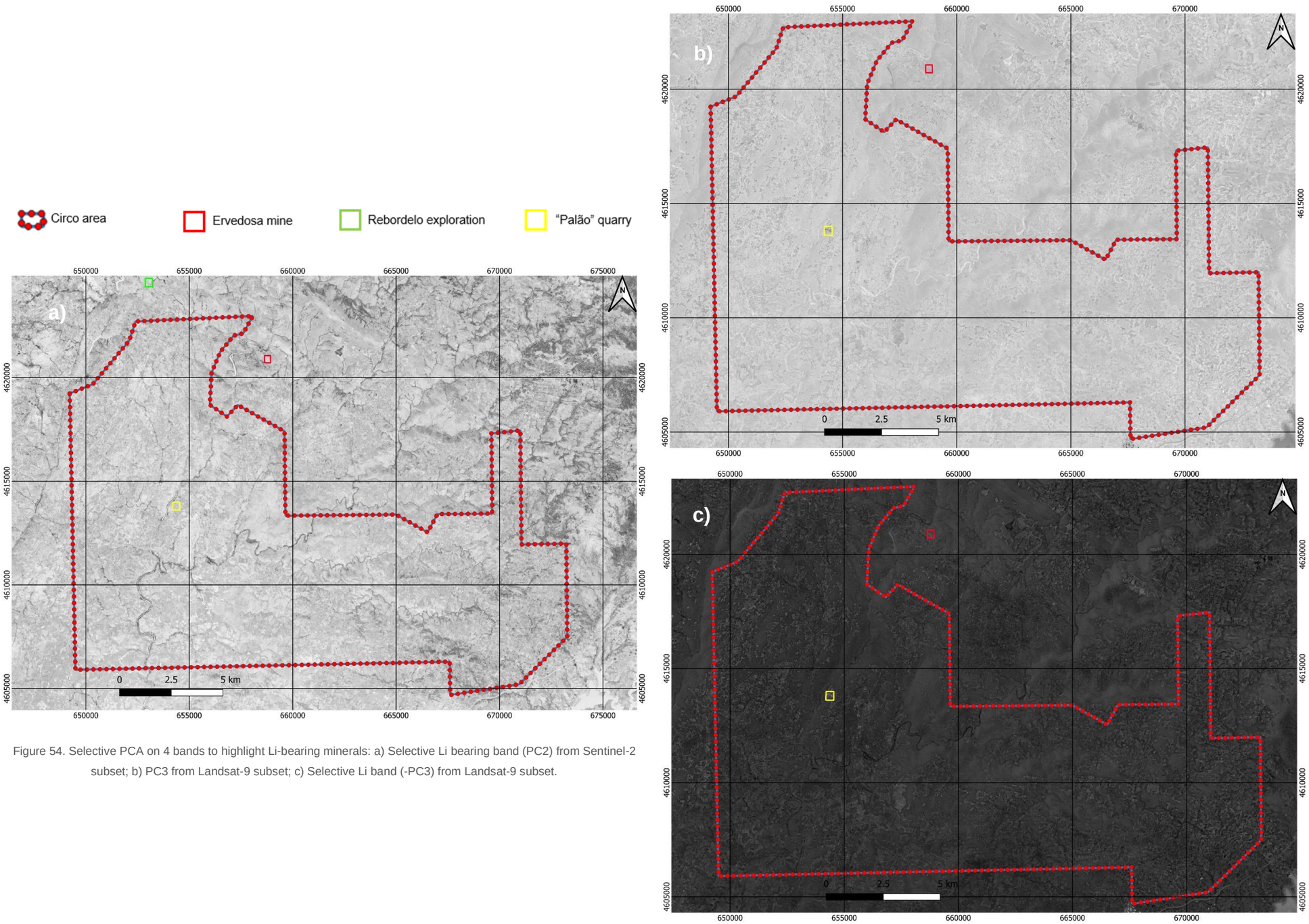


Figure 54. Selective PCA on 4 bands to highlight Li-bearing minerals: a) Selective Li bearing band (PC2) from Sentinel-2 subset; b) PC3 from Landsat-9 subset; c) Selective Li band (-PC3) from Landsat-9 subset.

An image displaying pixels with anomalous concentrations in hydroxyl minerals and ferric iron as brightest pixels was created by merging the Selective H band and Selective F band (image H+F), using the Crosta technique. These new images were combined with the other two in an RGB composite (Red - Selective H band; Green - Selective H band plus Selective F band; Blue - Selective F band) for both sensors (Figure 55 and Figure 56).

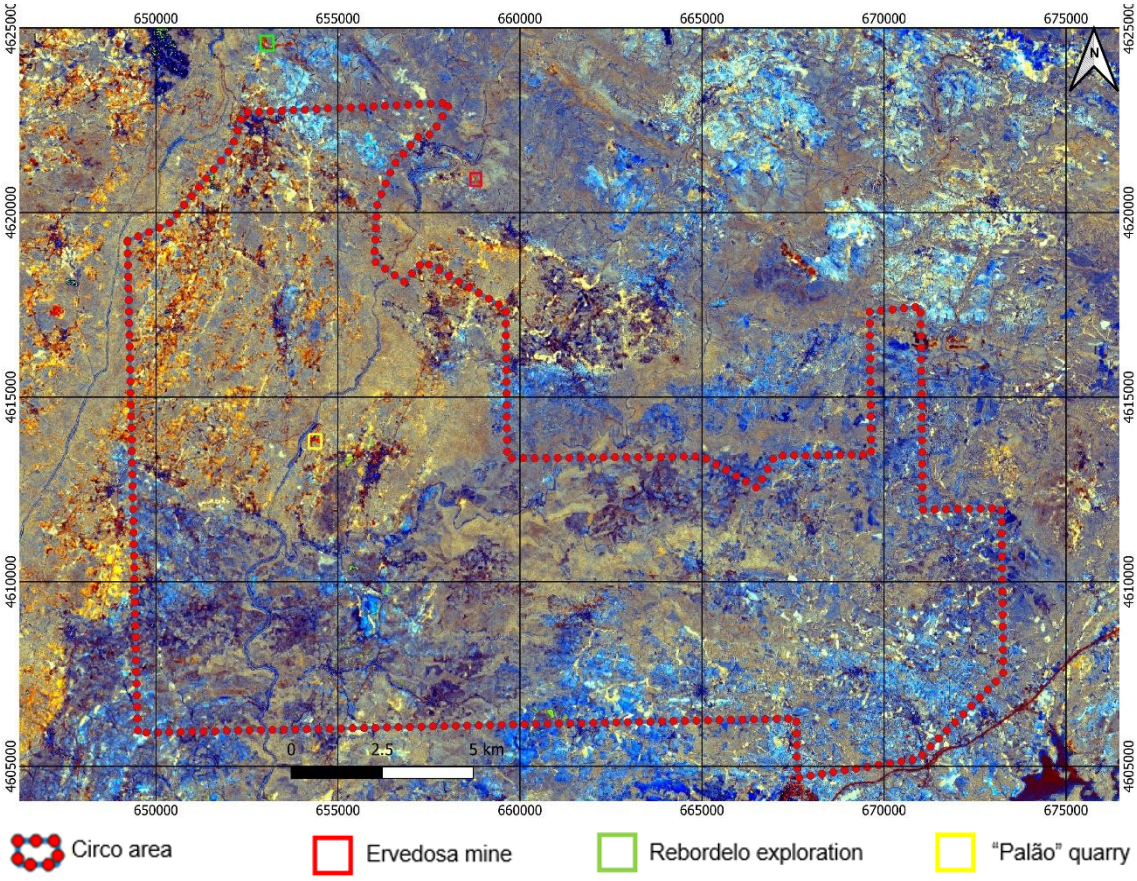


Figure 55. RGB combination of Selective H band, Selective H band + Selective F band and Selective F band for Sentinel-2. This combination maps hydrothermal alteration areas.

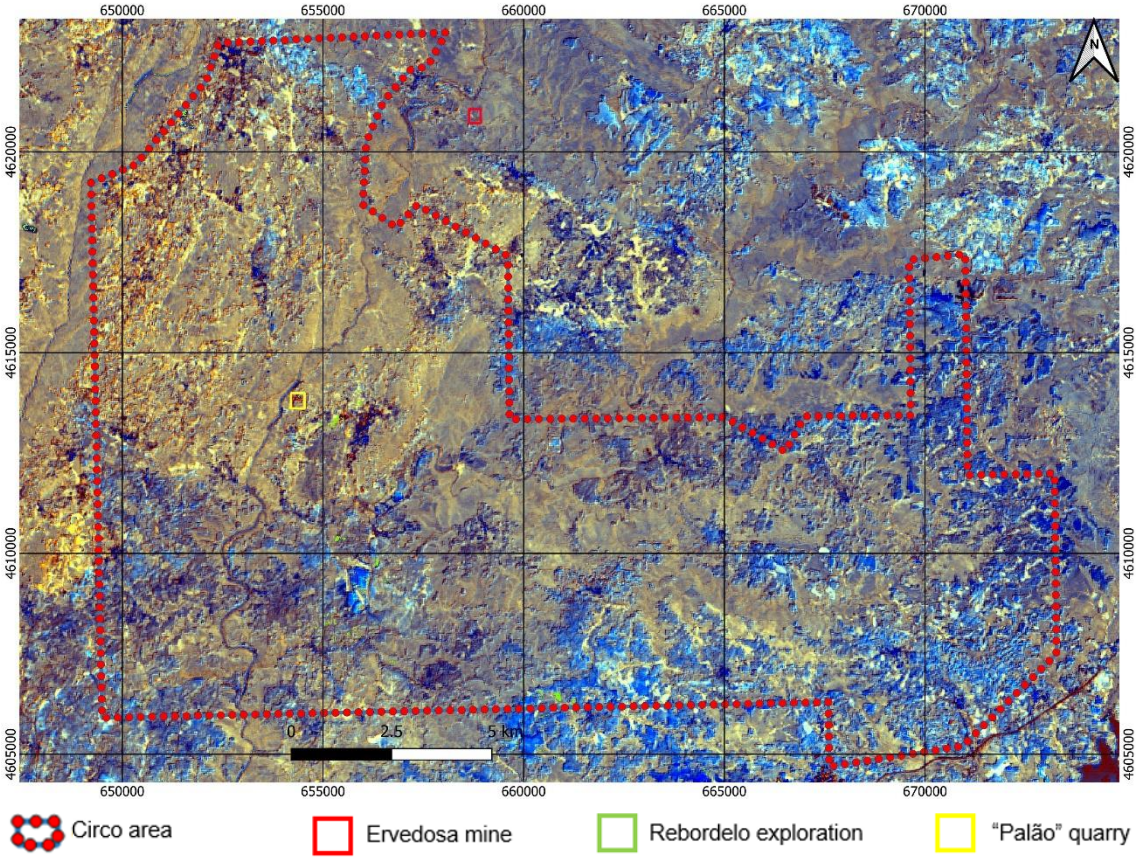


Figure 56. RGB combination of Selective H band, Selective H band + Selective F band and Selective F band for Landsat-9. This combination maps hydrothermal alteration areas.

According to Frutuoso et. al. (2021):

- Argilized and iron-stained alteration zones are presented in white to pale light blue, considered more favorable for mineral occurrence (most prospective areas);
- Areas that are more iron stained than argilized are shown in blue and light blue, while zones that are more argilized than iron stained appear in bright reddish to orange colors.
- Intense dark or deep blue pixels in association with the alteration colors can represent an alteration type associated with intensely argilized or silicified and heavily iron-stained rocks. This alteration can be recognized in hydroxyl images by very dark pixels closely associated with bright pixels, representing hydroxyl-altered areas.

In this study area, not all intense dark blue to black areas correspond to hydrothermally altered rocks. Burned vegetation can have a similar spectral response, and SWIR

bands are also sensitive to variations in vegetation. Therefore, it is important to recognize alterations around these dark areas.

5.1.4. Spectral Angle Mapper (SAM)

The results of SAM classification are represented in Figure 57 (Rebordelo exploration) and Figure 68 (Ervedosa mine). The thresholds used for the SAM analysis were 0.15 and 0.077, for Rebordelo and Ervedosa, respectively, and were determined by trial-and-error, finding a balance between having too many correlated pixels and having a very low amount of correlated pixels. Pixels with a spectral angle smaller than the threshold will be integrated into the target class.

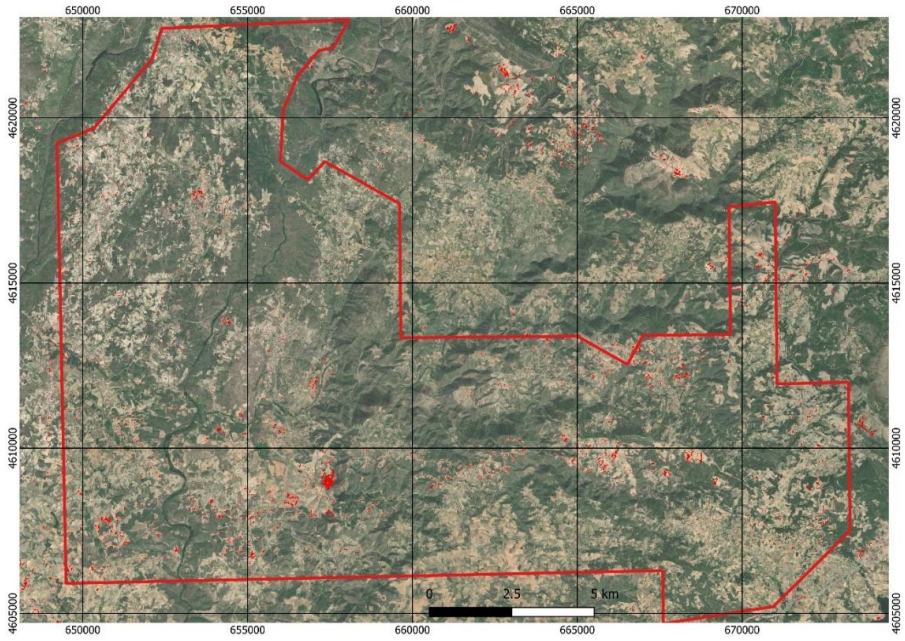


Figure 57. SAM classification result, using the Rebordelo exploration as the input spectral feature for training. The red polygon represents the Circo area.

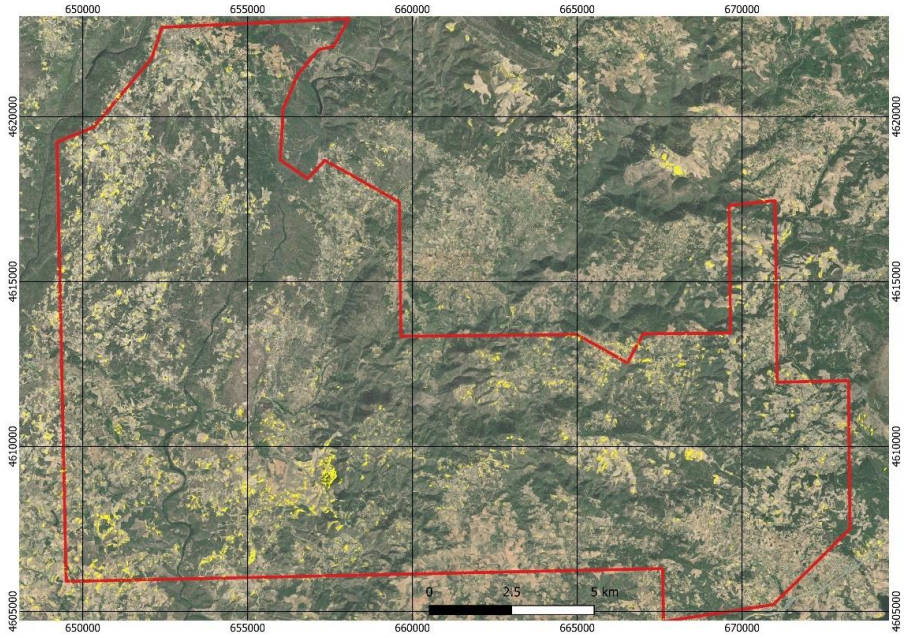


Figure 58. SAM classification result, using the Ervedosa mine as the input spectral feature for training. The red polygon represents the Circo area.

Since the selected areas are small, the use of one pixel was enough. There was no point of creating training areas since the most representative pixel from each mine was selected as the endmember spectra for classification.

The ground of Rebordelo exploration is mainly quartz, and the Ervedosa mine has slightly weathered granite with quartz veins. Comparing the two analyses, it is possible to see that the yellow areas (Ervedosa correlation) are intersecting with the red areas (Rebordelo correlation), as expected (because of the quartz). In Figure 59, both analyses were overlaid over a satellite image, and some targets (blue areas) were selected for field validation. In section 5.1.6 the results of field validation are described in detail.

The area with the highest number of pixels is the one selected by the black circle in Figure 59. That same zone has been highlighted in almost all remote sensing techniques and is explained in section 5.1.6.

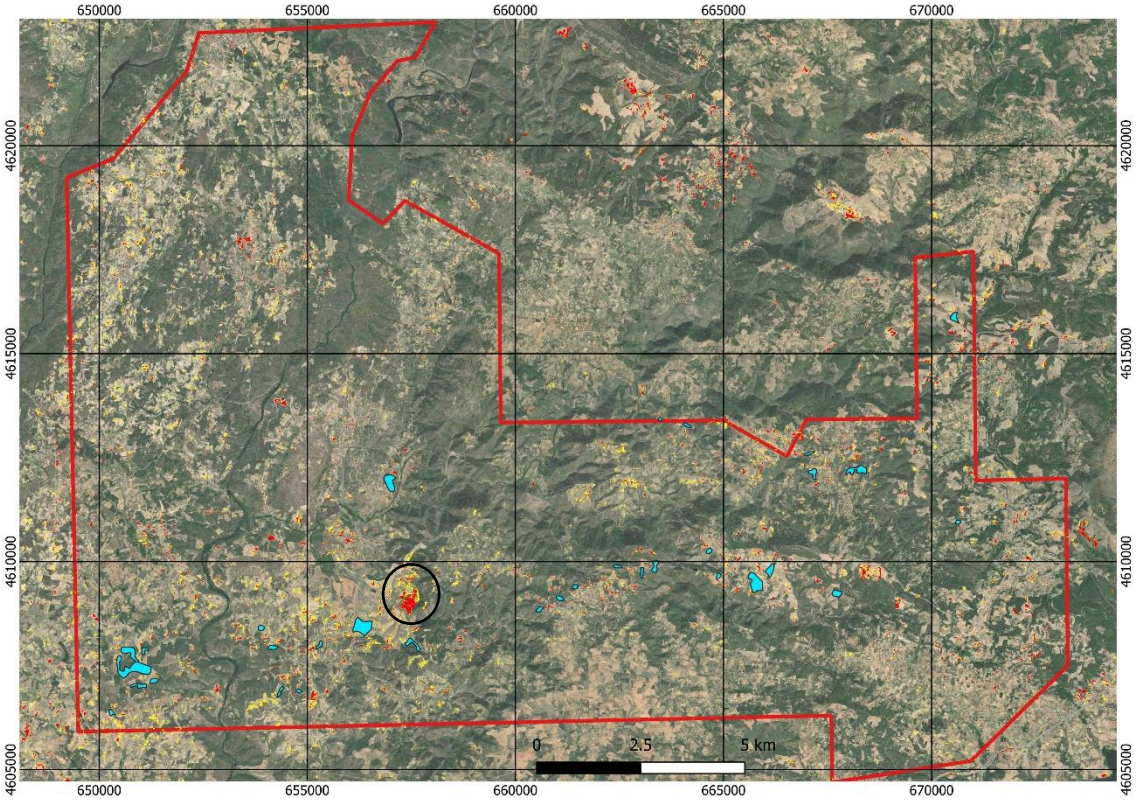


Figure 59. Both SAM analysis overlapped, over a satellite image; some of the selected remote sensing targets area represented in the blue areas. The red polygon represents the Circo area.

5.1.5. Lineament extraction

A structural map based on the manual extraction of approximately 145 lineaments from the four hill shade images, mentioned in section 4.1.3.2, was produced. The largest number of extracted lineaments was from the hill shade with an azimuth angle of N135ºE. Then, the lineaments were compared with known geological faults from the geological maps 1:200 00 (sheet 2, LNEG, 2000) and 1:50 000 (07-C (Mirandela, LNEG, 2010) and 07-D sheets (Macedo de Cavaleiros, LNEG, 1998). The final result is presented in Figure 60.

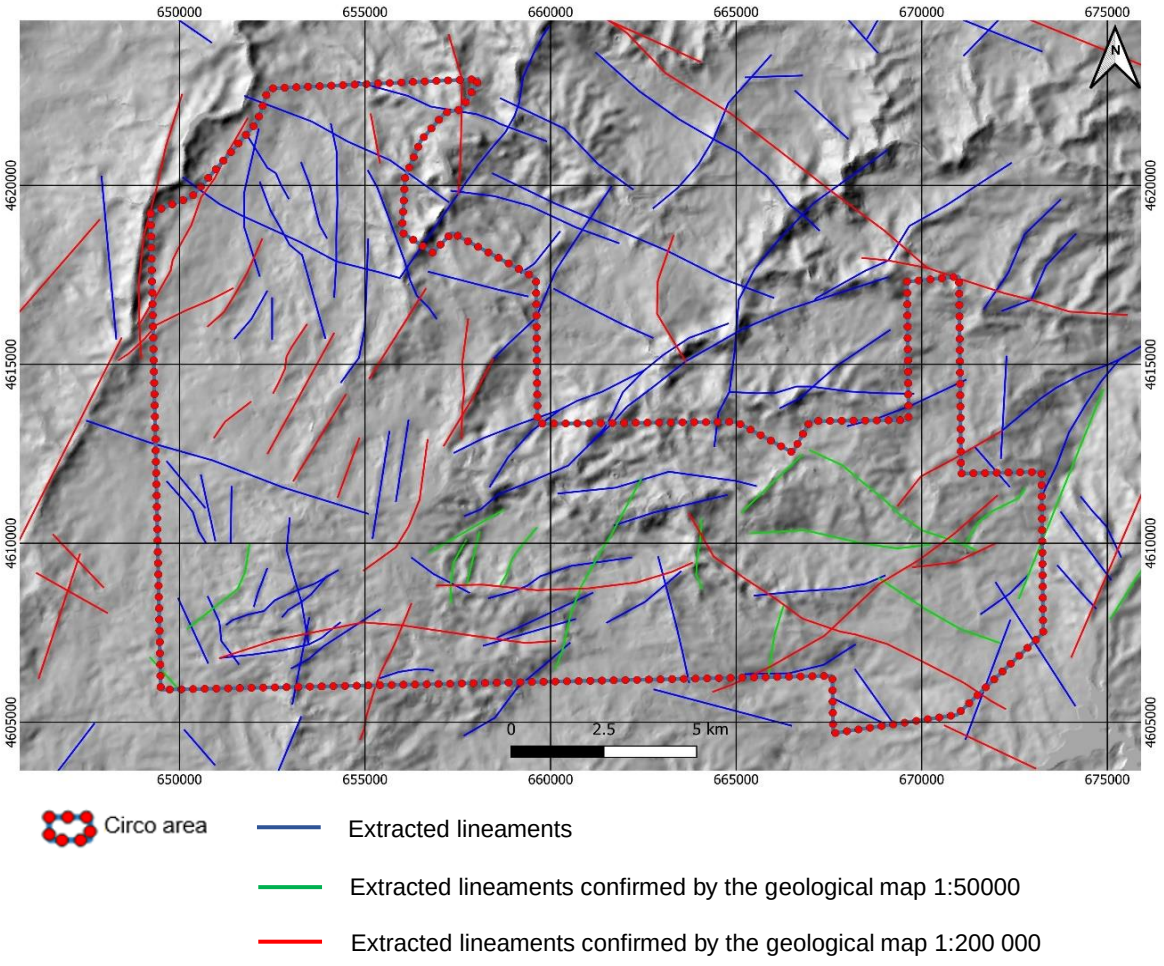


Figure 60. Extracted lineaments over a hillshade image (with 135º of azimuth of the light). Green and red lines correspond to geological faults, and blue lines are probable faults.

The mean direction of extracted lineaments was automatically computed, and then plotted in the rose diagram (using the *plugin* Line Direction histogram for QGIS) of Figure 61 to determine the predominant trends.

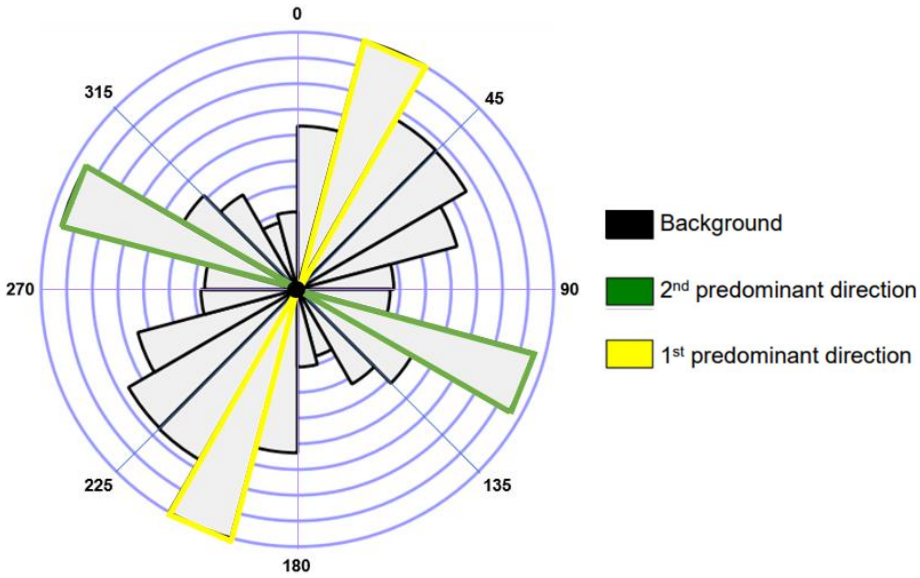


Figure 61. Rose diagram where the trends of the extracted lineaments were plotted. Two main directions are visible: the first around N22ºE, and the second, N112ºE.

The lineaments can be grouped into two main classes: one NNE-SSW trending and the other WNW-ESE trending. First predominant direction (NNE-SSW) corresponds to late brittle-D3 deformation with sigma 1 oriented NE-SW. The second predominant direction (WNW-ESE) corresponds to ductile to ductile-fragile sin-D3 deformation, which is generally marked by fold axes and foliations in the metasediments.

5.1.6. Remote sensing targets

One of the objectives of applying remote sensing methodologies in mineral exploration is to create a map with all the targets generated based on the different techniques used (band ratios, RGB combinations, PCA, image classification) and then validate all the targets in the field. The Figure 62 represents all the targets that were considered.

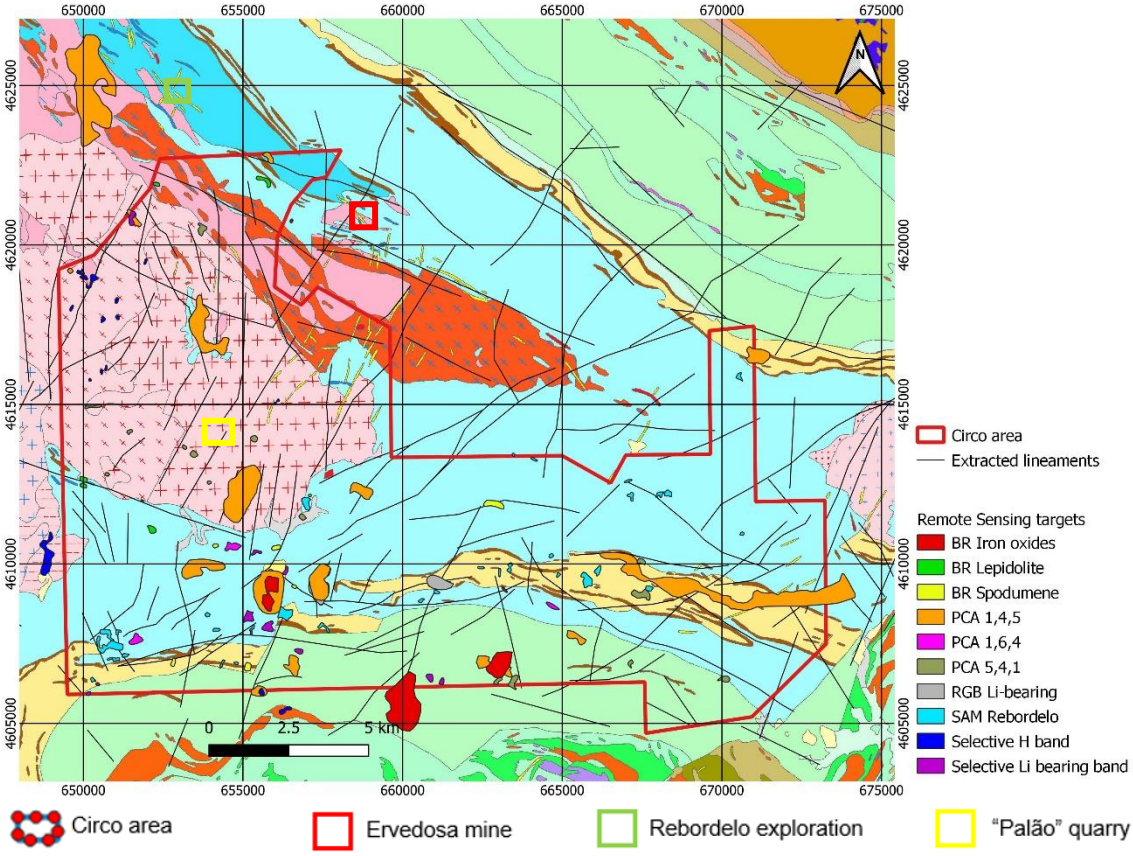


Figure 62. All the remote sensing targets considered initially, over the Portuguese geological map 1:200 000.

After field validation of the defined targets, some of them were deleted, due to correlation between areas or “false positives”. For example, after visiting the target in orange on the northern side of the area (Figure 62), it was concluded that all areas with the same response (red color in the RGB combination of PC1, -PC4 and -PC5 for Sentinel-2, as can be seen in Figure 48) were burned areas, so all the areas with the same response were not considered for further evaluation. The field validation work led to a set of thirty-nine final targets, as shown in the next image (Figure 63). The targets were numbered from T1 to T39.

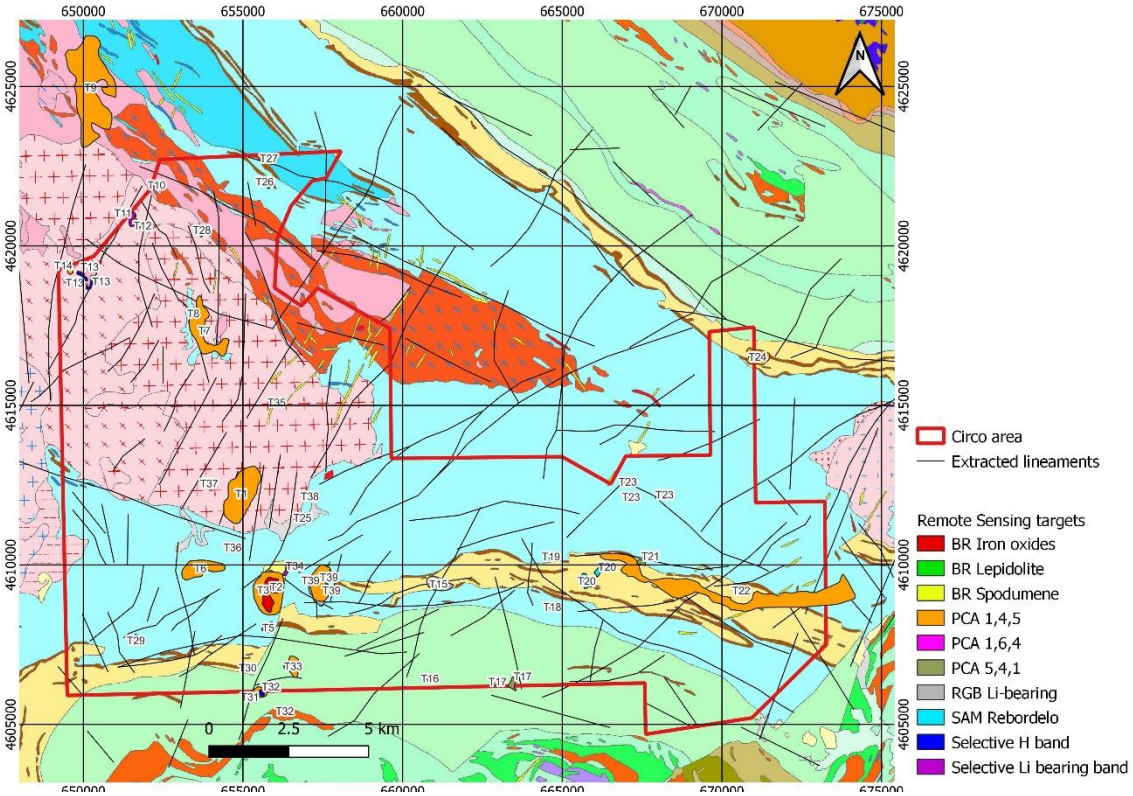


Figure 63. Remote sensing targets with field validation; numbered from T1 to T39, over the Portuguese geological map 1:200 000.

The targets selected under:

- Both iron oxides band ratios (Sentinel-2 and Landsat-9), mainly represent reddish soils with quartz in the metasediments (T2);
- Both lepidolite band ratios (Sentinel-2 and Landsat-9) show fields with quartz and schists in the granites (T10 and T26);
- Both spodumene band ratios (Sentinel-2 and Landsat-9) show fields with quartz and schists in the metasediments (T8, T30 and T38);
- RGB combination PC1, -PC4 and -PC5 for Sentinel-2 identified several different colors: dark blue areas represent iron oxides, thus a Quaternary deposit with reddish soils around (T2 and T4) and a schist zone within the granites (T7) (granites-pegmatites contacts were also found), and (T14) were found; light green to light blue areas represent hydroxyl-bearing areas: plowed fields with schists and quartz with natural small water channels due to the terrain's inclination (T24, T31, and T33) and recently plowed fields with grass vegetation ("mudflats") (T3); red areas show burned zones (T9, T12 and T27); light pink areas represent dense vegetation, where a quartzite unit with dense vegetation was found (T22); and grey shading areas show terrains where the soil was

plowed a few years ago, being now very consolidated and leaving a very hard soil compared to light green to light blue areas (T1 and T6);

- RGB combination PC1, PC6 and -PC4 for Sentinel-2 also identified grey areas, such as the last combination, representing the same type of terrains (T29 and T36);
- RGB combination -PC5, -PC4 and PC1 for Sentinel-2 allowed the selection of various yellow areas (hydroxyls response) identifying “mudflats” (T17, T21 and T28); and some red areas due to iron oxides, that allowed the identification of river deposits (T25, terrain with very rounded quartz clasts);
- RGB combination 7-3-11 for Landsat-9 enabled the identification of two zones, T15 and T39, that are fields with a lot of quartz (in the case of T15) and “new” terrains (in the case of T39, corresponding to a farm where the soil has been man disturbed with new cultivation terraces).
- SAM results in correlation with Rebordelo exploration and Ervedosa mine represent terrains with a lot of quartz and schists (T19, T20 and T23);
- Selective H band shows areas, where the soil is very light and granitic (T13 and T35); and areas just like the ones represented in RGB combination PC1, -PC4 and -PC5 as light green to light blue (T32);
- Selective Li-bearing PC band identified some burned areas such as T11, terrains with a lot of quartz (T34) and a quartzphyllite with quartz veins (T5).

A verification between sensors was made, concluding that RGB combinations of PCs, band ratios, and Selective PC bands from both sensors were having a similar response, so Sentinel-2 images were considered due to the better resolution.

A collection of some target samples was made throughout the field validation (soil and rock samples). Images and XRF/LIBS analysis results of sixteen target areas are presented on the next pages.

- Target 2 (sample T2, soil)

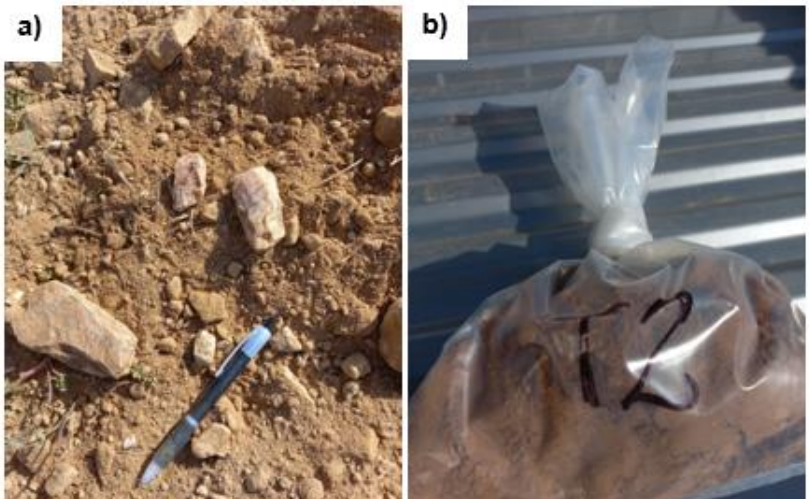


Figure 64. a) Target 2 soil; b) target 2 sample bag.

Table 14. XRF and LIBS analysis results, in ppm (T2 sample).

T2	XRF						LIBS			
	Rb	Nb	Sn	Cs	W	LE	Li	Nb	Rb	Sn
(ppm)	107.7	8.3	<LOD	<LOD	<LOD	623641	60.02	<LOD	749.50	175.80

* LOD – limit of detection * LE – Light elements

- Target 3 (sample T3, soil)



Figure 65. Target 3 sample bag.

Table 15. XRF and LIBS analysis results, in ppm (T3 sample).

T3	XRF						LIBS			
	Rb	Nb	Sn	Cs	W	LE	Li	Nb	Rb	Sn
ppm	259.3	17.0	28	89	25.5	558659	57.68	<LOD	827.00	261.40

* LOD – limit of detection * LE – Light elements

- Target 4 (sample T4, rock)

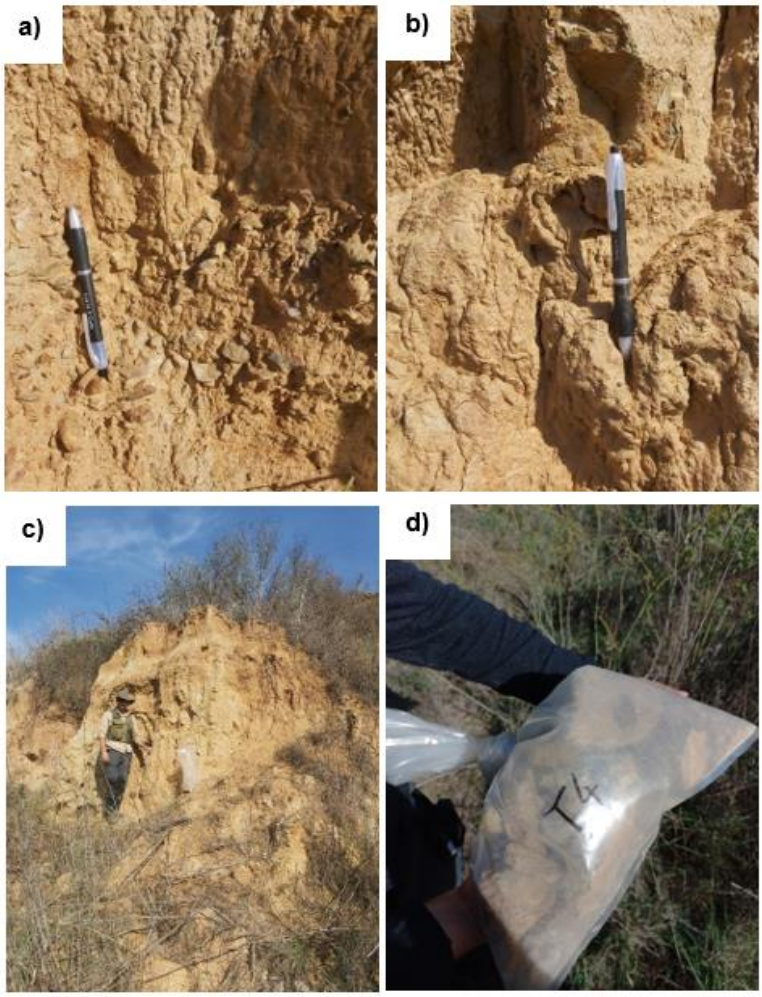


Figure 66. a) and b) T4 deitailed images; c) T4 outcrop ; d) T4 sample bag.

Table 16. XRF and LIBS analysis results, in ppm (T4 sample).

T4	XRF						LIBS			
	Rb	Nb	Sn	Cs	W	LE	Li	Nb	Rb	Sn
ppm	174.7	12.7	24	<LOD	21	566100	36.64	<LOD	503.95	138.15

* LOD – limit of detection * LE – Light elements

- Target 5 (sample T5, rock)

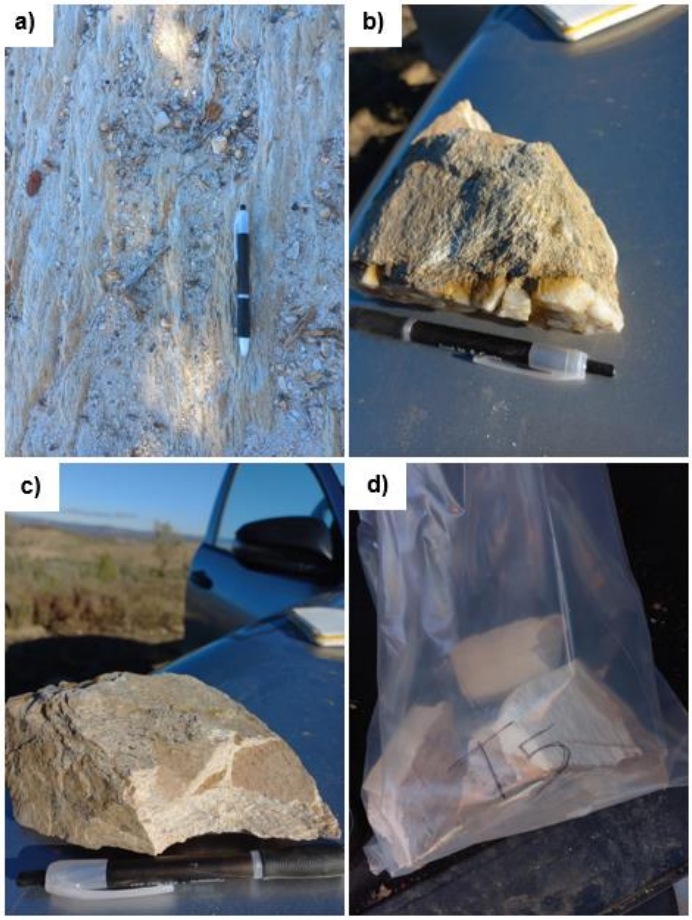


Figure 67. a) T5 outcrop; b) and c) a portion of T5`s sample; d) T5 sample bag.

Table 17. XRF and LIBS analysis results, in ppm (T5 sample).

T5	XRF					LIBS				
	Rb	Nb	Sn	Cs	W	LE	Li	Nb	Rb	Sn
ppm	-	-	-	-	-	-	9.22	<LOD	152.10	26.26

* LOD – limit of detection * LE – Light elements

- Target 7 (sample T7, soil)

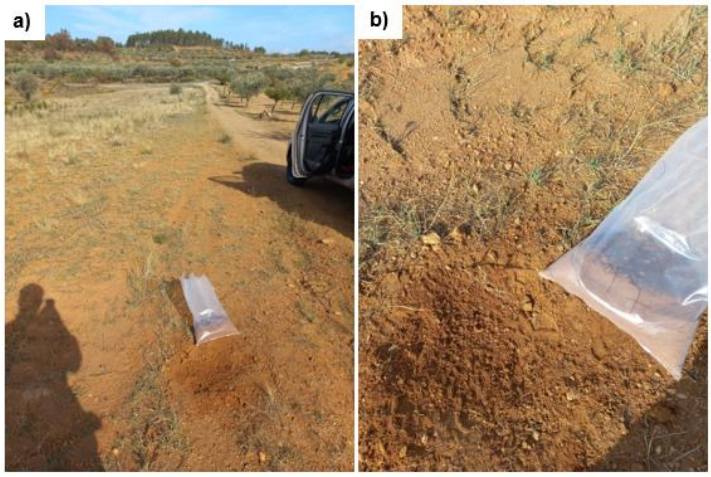


Figure 68. a) Soil found in T7; b) T7 sample bag.

Table 18. XRF and LIBS analysis results, in ppm (T7 sample).

T7	XRF						LIBS			
	Rb	Nb	Sn	Cs	W	LE	Li	Nb	Rb	Sn
ppm	233.0	14.3	<LOD	<LOD	18	601350	35.63	<LOD	680.35	120.70

* LOD – limit of detection * LE – Light elements

- Target 10 (sample T10, rock)

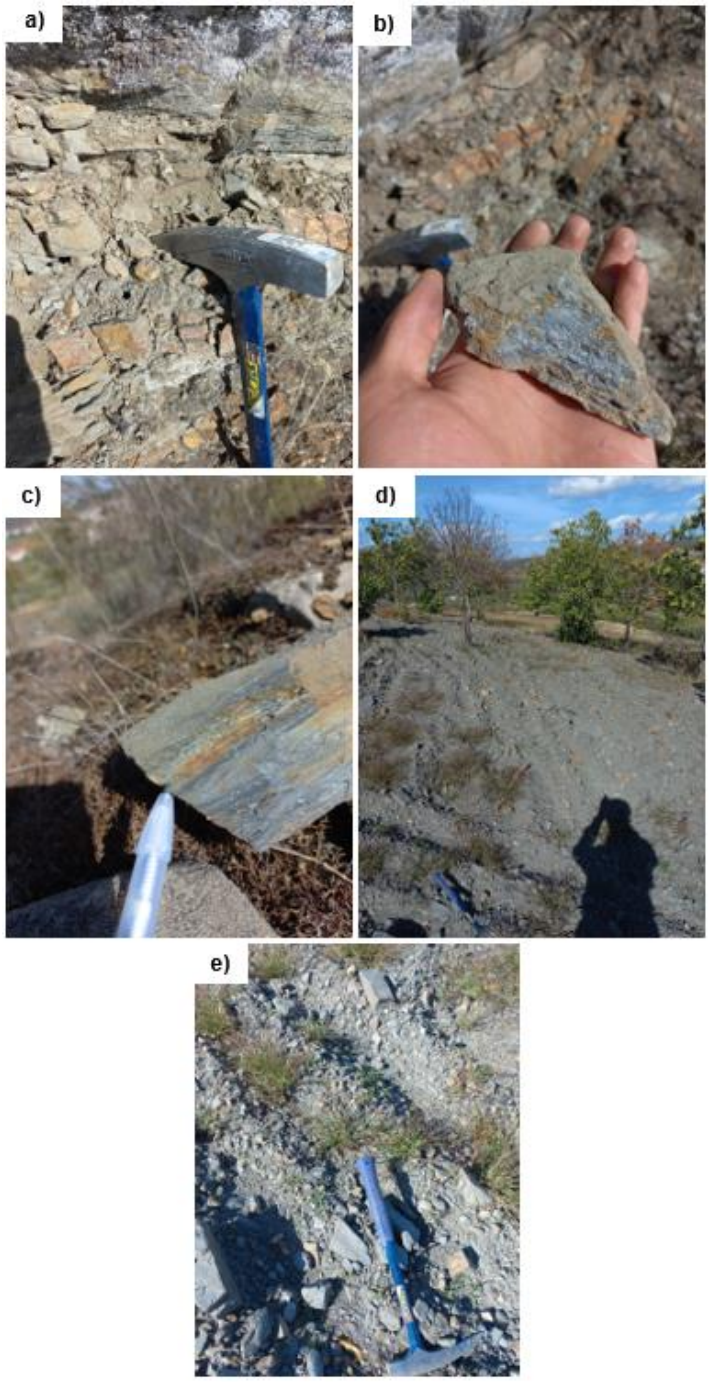


Figure 69. a) Outcrop found in T10; b) and c) a portion of T10 sample; d) soil found in T10; e) detailed picture of T10 soil.

Table 19. XRF and LIBS analysis results, in ppm (T10 sample).

T10	XRF						LIBS			
	Rb	Nb	Sn	Cs	W	LE	Li	Nb	Rb	Sn
ppm	-	-	-	-	-	-	39.63	<LOD	379.23	38.76

* LOD – limit of detection * LE – Light elements

- Targets 13 and 14 (sample T13, soil; sample T14, rock)

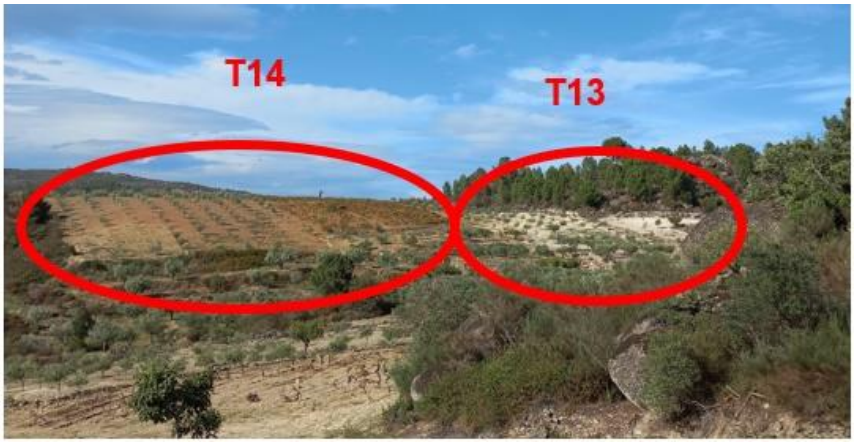


Figure 70. Distance picture that shows the different between T13 (granites zone) and T14 (metasediments zone) soil color.

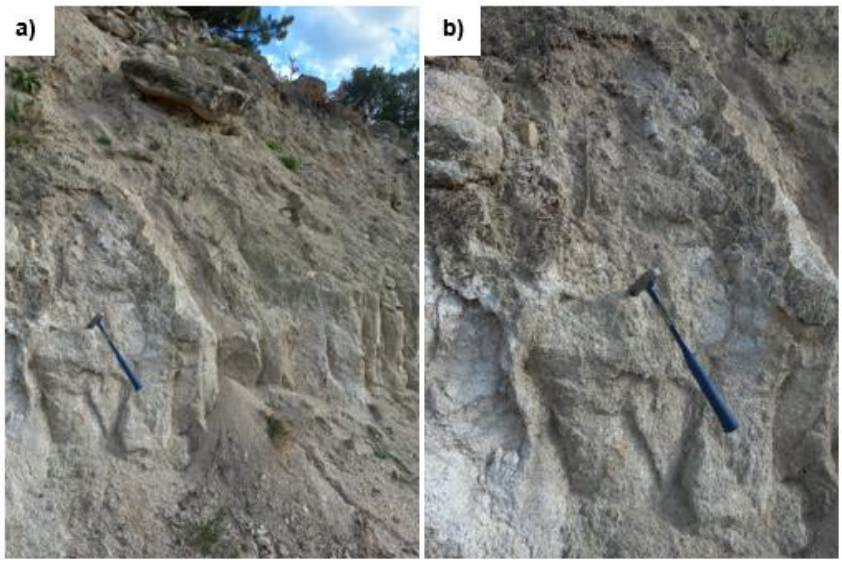


Figure 71. a) and b) Highly weathered granite outcrop in T13.

Table 20. XRF and LIBS analysis results, in ppm (T13 sample).

T13	XRF						LIBS			
	Rb	Nb	Sn	Cs	W	LE	Li	Nb	Rb	Sn
ppm	463.0	18.0	21	<LOD	<LOD	577891	64.04	<LOD	545.25	40.11

* LOD – limit of detection * LE – Light elements



Figure 72. a) T14 terrain with planted vineyards; b) a portion of T14 sample (banded (mica)-schist); c) T14 sample bag.

Table 21. XRF and LIBS analysis results, in ppm (T14 sample).

T14	XRF						LIBS			
	Rb	Nb	Sn	Cs	W	LE	Li	Nb	Rb	Sn
ppm	-	-	-	-	-	-	686.01	<LOD	854.28	118.79

* LOD – limit of detection * LE – Light elements

- <u>Target 20</u> (sample T20, soil)



Figure 73. a) T20 terrain; b) T20 sample bag.

Table 22. XRF and LIBS analysis results, in ppm (T20 sample).

T20	XRF						LIBS			
	Rb	Nb	Sn	Cs	W	LE	Li	Nb	Rb	Sn
ppm	166.0	11.3	<LOD	<LOD	<LOD	662358	22.26	<LOD	797.05	183.65

* LOD – limit of detection * LE – Light elements

- Target 22 (sample T22, rock)



Figure 74. Quartzite outcrop in T22 zone.

Table 23. XRF and LIBS analysis results, in ppm (T22 sample).

T22	XRF						LIBS			
	Rb	Nb	Sn	Cs	W	LE	Li	Nb	Rb	Sn
ppm	-	-	-	-	-	-	11.59	<LOD	642.10	79.15

* LOD – limit of detection * LE – Light elements

- Target 24 (sample T24, soil)

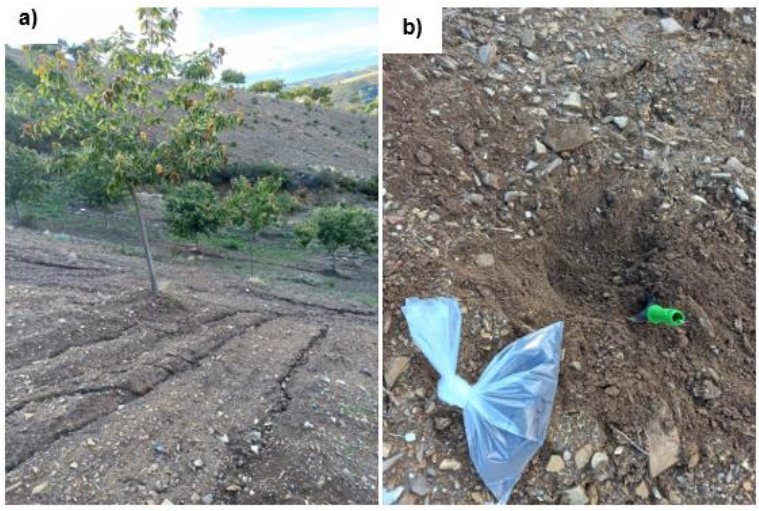


Figure 75. a) T24 terrain; b) T24 sampling site.

Table 24. XRF and LIBS analysis results, in ppm (T24 sample).

T24	XRF						LIBS			
	Rb	Nb	Sn	Cs	W	LE	Li	Nb	Rb	Sn
ppm	101.3	6.0	<LOD	<LOD	<LOD	704726	21.28	<LOD	817.15	142.35

* LOD – limit of detection * LE – Light elements

- Target 26 (sample T26, soil)

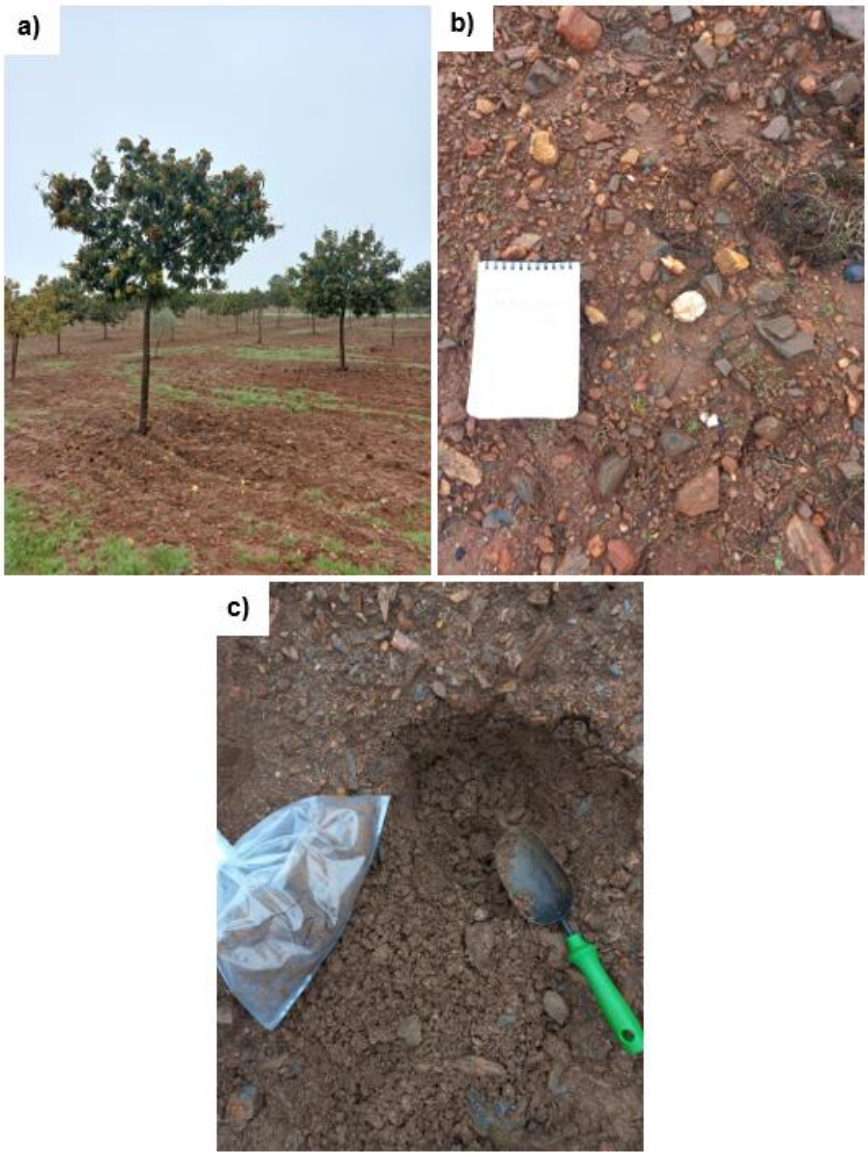


Figure 76. a) T26 terrain; b) T26 soil; c) T26 sampling site.

Table 25. XRF and LIBS analysis results, in ppm (T26 sample).

T26	XRF						LIBS			
	Rb	Nb	Sn	Cs	W	LE	Li	Nb	Rb	Sn
ppm	195.0	14	33	104	17	574367	313.60	<LOD	767.55	173.85

* LOD – limit of detection * LE – Light elements

- Targets 31/32 (sample T31/32, soil)

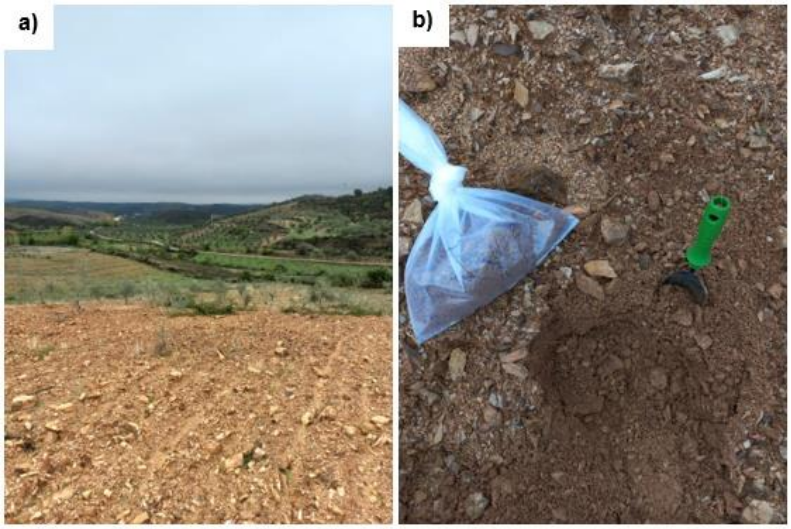


Figure 77. a) T31/32 terrain; b) T31/32 sampling site.

Table 26. XRF and LIBS analysis results, in ppm (T31/32 sample).

T31/32	XRF						LIBS			
	Rb	Nb	Sn	Cs	W	LE	Li	Nb	Rb	Sn
ppm	128.7	16	<LOD	<LOD	15	551679	19.41	<LOD	677.35	184.80

* LOD – limit of detection * LE – Light elements

- Target 33 (sample T33, soil)



Figure 78. a) and b) T33 terrain; c) T33 sampling site.

Table 27. XRF and LIBS analysis results, in ppm (T33 sample).

T33	XRF						LIBS			
	Rb	Nb	Sn	Cs	W	LE	Li	Nb	Rb	Sn
ppm	163.0	11.7	<LOD	<LOD	<LOD	600148	10.73	<LOD	705.20	234.85

* LOD – limit of detection * LE – Light elements

- Target 35 (sample T35, soil)



Figure 79. a) T35 terrain; b) detailed picture of T35 soil; c) T35 sampling site.

Table 28. XRF and LIBS analysis results, in ppm (T35 sample).

	XRF						LIBS			
	Rb	Nb	Sn	Cs	W	LE	Li	Nb	Rb	Sn
T35 ppm	453.3	14.0	22	<LOD	<LOD	618600	27.15	<LOD	<LOD	174.30

* LOD – limit of detection * LE – Light elements

- Target 39 (sample T39, stream sediments) – T39 corresponds to a fenced farm, and was not possible to access the terrain during the internship time. So, XRF analysis results from two stream sediment samples (collected previously by the Fortescue Portugal exploration team on the farm) were taken into consideration. This fenced farm presents soil that was man disturbed with new cultivation terraces.

Table 29. XRF and LIBS analysis results, in ppm (T39 samples).

	XRF (ppm)				
	Rb	Nb	Sn	W	LE
SS1	159.7	10.3	<LOD	<LOD	651793
SS2	172.0	10.3	130	17	620612

* LOD – limit of detection *SS – stream sediment sample * LE – Light elements

From all the target samples collected, T14 and T26 stand out when analyzing LIBS values, especially considering the Li contents.

5.2. Geological Mapping

The objective of geological mapping in this report was to create a 1:25 000 scaled map. Since it was not possible to finish the geological mapping activity, a geological map (in shapefile format) at scale 1:95 000 was produced based on the remote sensing (RGB combinations, PCA, lineament extraction, and targets validation) and geological field mapping (some collected rock samples) (Figure 80).

The database and the 1:25 000 geological maps are still being made by the Fortescue Portugal team. Geological mapping activities were delayed due to weather conditions and the high risk of fire during July, August and September.

The produced map allows to observe the presence of granites (cannot differentiate facies), metasediments (Phyllite-quartzite, Pelite-greywacke and Upper quartzite formations), alluvial deposits and a Quaternary deposit. The extracted lineaments are also represented.

The units that remote sensing allowed to be discriminated are outlined by a black line, with some small adjustments based on downloaded geological maps from Portugal, namely 1:50 000 maps (sheets 07-C and 07-D), and 1:200 000 map (sheet 2). Areas outlined by a red dotted line are formations extracted from those maps since remote sensing did not allow to discriminate them.

Additionally, a description of some samples collected on the field will be made in this chapter, according to the previously defined database parameters.

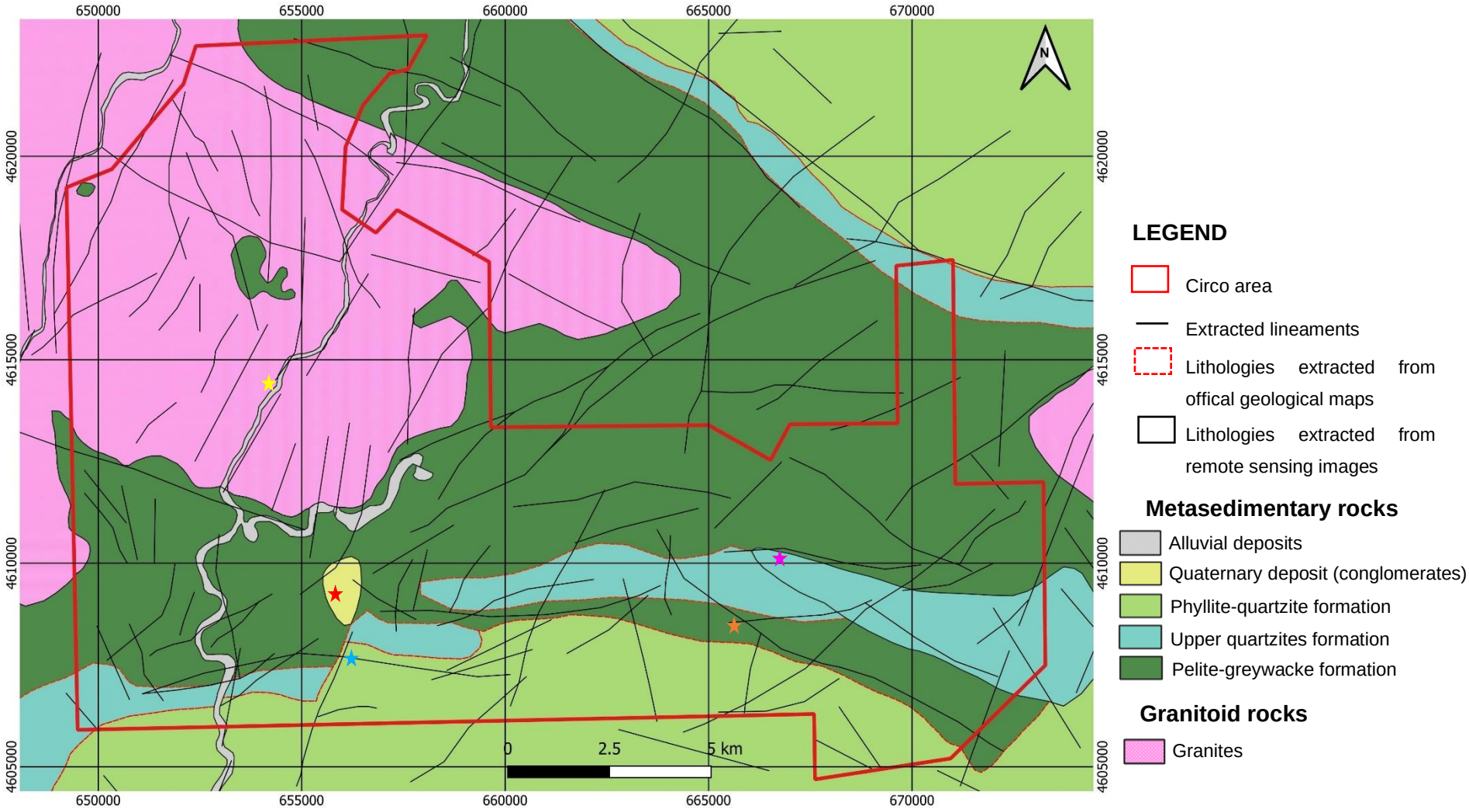


Figure 80. Geological map produced at 1:95 000 scale. Stars represent locations where samples were collected.

- **Two-mica granite, Rebordelo** (represented by a yellow star in Figure 80)

Table. 30 Main features related to Sample 1.

Features	Description
Date	DD/MM/YYYY
Sample ID	Sample 1
Coordinates (GPS)	X, Y, Z
Location	São Pedro o Velho
Square	C_
Parish	São Pedro o Velho
Relationship with surrounding rocks	Sharp contact (?)
General description	Medium- to coarse-grained granite
Predominant mineral	K-feldspar (albite?), quartz, biotite and muscovite
Texture	Porphyritic with K-feldspar megacrysts approx. **2 cm** in **width**
Enclaves	Not observed
Weathering	Moderately weathered
Deformation patterns	Brittle deformation (domino structures in K-feldspar megacrysts
Fabric	No oriented pattern
Fracturing	Moderately fractured. Three main fracturing systems were identified and measured (dip, dip direction): (1) 90º/N186º; (2) 90º/N186º; and (3) subhorizontal (giving to the outcrop a sill morphology).

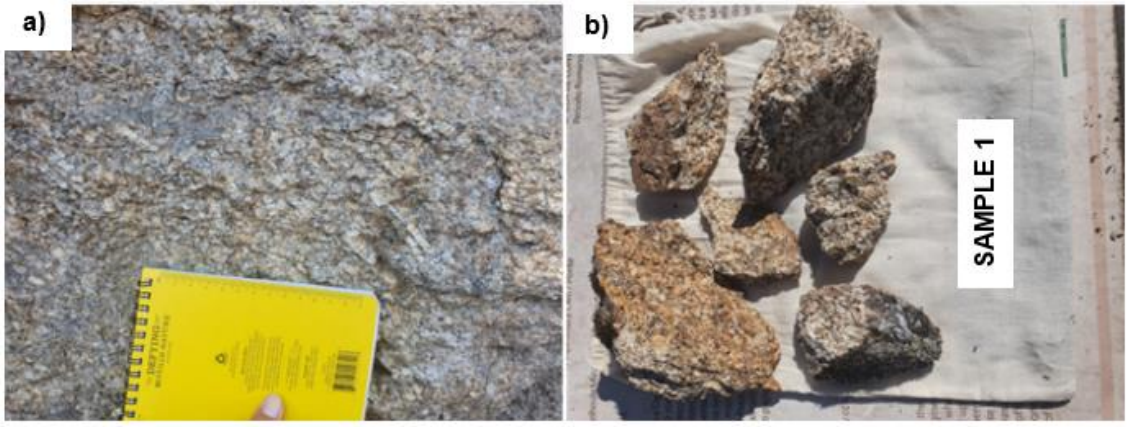


Figure 81. a) Detailed picture showing the most relevant features displayed by the two-mica granite. b) Picture of Sample 1 bag.

- **Conglomerate, Quaternary deposit, Torre de Dona Chama** (represented by a red star in Figure 80)

Table. 31 Main features related to Sample T4.

Features	Description
Date	DD/MM/YYYY
Sample ID	Sample T4
Coordinates (GPS)	X, Y, Z
Location	Torre de Dona Chama
Square	C_
Parish	Torre de Dona Chama
Relationship with surrounding rocks	Not observed
General description	Conglomerate with quartz, schist and feldspar angular to sub-rounded fragments, intercalation of levels (~20 cm width) composed of coarse-grained elements (~5 cm diameter) and levels (~1 m width) containing fine-grained elements (~2 mm)
Predominant mineral	Quartz
Texture	Conglomeratic
Enclaves	Not applicable
Weathering	Not identified
Deformation patterns	Not identified
Fabric	Not applicable
Fracturing	Not applicable

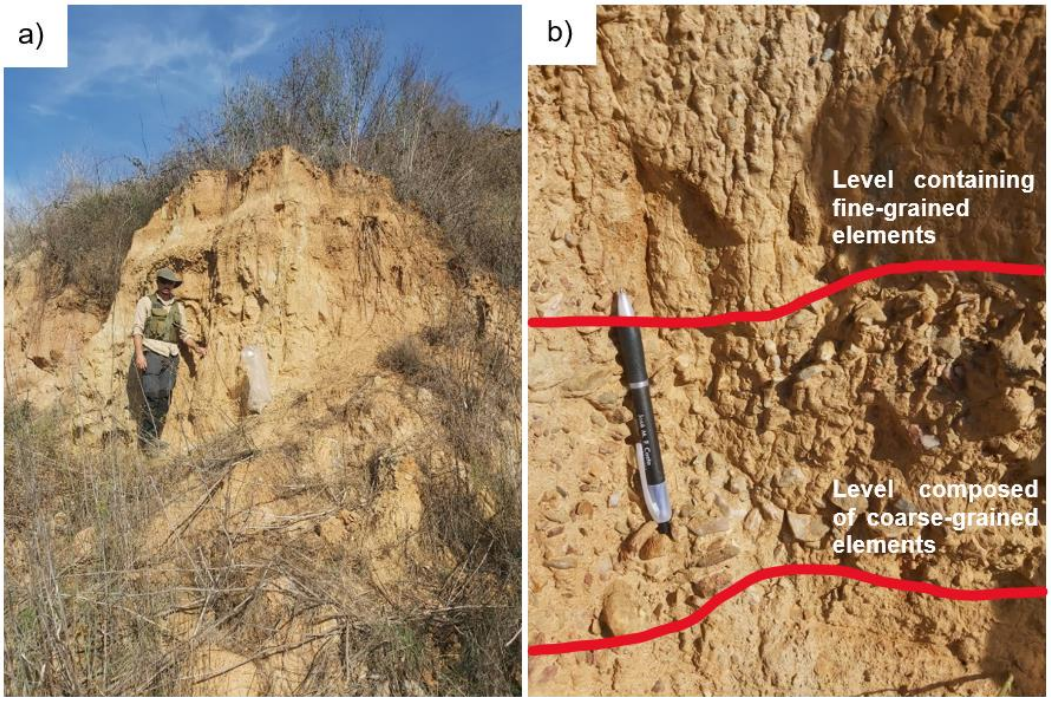


Figure 82. a) Quaternary deposit outcrop; b) intercalation of levels composed of coarse-grained elements and levels containing fine-grained elements.



Figure 83. T4 sample bag.

- **Light blue-grey pelite, Arcas** (represented by an orange star in Figure 80)

Table. 32 Main features related to Sample 2.

Features	Description
Date	DD/MM/YYYY
Sample ID	Sample 2
Coordinates (GPS)	X, Y, Z
Location	Arcas
Square	C_
Parish	Arcas
Relationship with surrounding rocks	Not observed
General description	Light blue-grey pelite. It was observed thin (~2 cm width) quartz veins – crosscutting stockwork
Predominant mineral	Quartz
Texture	Equigranular and homogeneous
Enclaves	Not identified
Weathering	Slightly weathered
Deformation patterns	Not applicable
Fabric	**Main foliation Sn: 48º/N202º**
Fracturing	Filled by quartz veins: 40º/N40º



Figure 84. General features observed in the field; a), b) and c) general overview of pelite outcrop; d) detailed picture showing the most relevant features; e) detailed picture of Sample 2 bag.

- **Light-grey quartzite, Ferreira** (represented by a purple star in Figure 80)

Table 33. Main features related to Sample T22.

Features	Description
Date	DD/MM/YYYY
Sample ID	Sample T22
Coordinates (GPS)	X, Y, Z
Location	Ferreira
Square	C_
Parish	Ferreira
Relationship with surrounding rocks	Not observed
General description	Grey quartzite, without foliation
Predominant mineral	Quartz
Enclaves	Not identified
Weathering	Slightly weathered
Deformation patterns	Not identified



Figure 85. Quartzite outcrop.

- **Quartz-phyllite, Múrias** (represented by a blue star in Figure 80)

Table. 34 Main features related to Sample 3.

Features	Description
Date	DD/MM/YYYY
Sample ID	Sample 3
Coordinates (GPS)	X, Y, Z
Location	Múrias
Square	C_
Parish	Múrias
Relationship with surrounding rocks	Irregular contacts with regional metasediments
General description	White homogeneous and compact rock. In some locations displaying a random spotted pattern, probably due to the presence of oxides and probably garnet (?)
Predominant mineral	Quartz
Texture	Homogeneous, sugar-like texture
Enclaves	Not identified
Weathering	Slightly weathered
Deformation patterns	Not applicable
Fabric	**Main foliation Sn: 25º/N70º**
Fracturing	Not identified



Figure 86. General features observed in the field; a) and b) general overview of quartz-phyllite outcrop; c) detailed picture showing the most relevant features; d) detailed picture of sample 3 bag.

5.3. Stream sediment analysis

All the stream sediment samples that were collected were shipped to ALS laboratory (Spain) for certified assay, similarly to the collected rock samples. The main objective of this campaign was to find geological anomalies, using XRF data as a preliminary assessmentof the Circo area, while waiting for ALS resultsThe stream sediments campaign was delayed due to community engagement sessions, adverse weather conditions and the high risk of fire during July, August and September. Therefore XRF results were used for anomaly definition since the ALS results were not delivered in time. The complete XRF results are presented in Appendix A.

From the 180 points that were generated for sampling the stream sediments, 157 were collected and 23 were canceled, due to three main reasons: (i) non-existence of the water stream, (ii) contamination of the water stream and (iii) main rivers. Of the total of 157 (including field duplicates): 115 were collected in schist areas, 38 in granite areas, and 4 in granite+schist areas.

5.3.1 Exploratory data analysis (EDA)

In this section, the information obtained through ioGAS is presented to perform the EDA of the XRF results, thus allowing to identify, analyze and interpret univariate data that do not follow a normal distribution.

Fifure 87 represents the basic statistics for each lithology. Yellow rows contain the values that were used for the IQR standardization (IQR and Tukey upper outlier threshold values). The analysis was done comparing three populations: visible (granite+schist), granite and schist. Plots/maps, basic statistics and PCA of all elements are presented in Appendix B, C and D, respectively.

Most of the elements have positively skewed distributions (Figure 87) (except Al, Ti, Cr, Y, La and Ce in the entire population; Mg, Al, Rb, Sn, La, Ce, and Pb in the granite; Al, K, Ti, La and Ce in the schist). Granite shows element distributions more asymmetric than schist except for Mg, P, Ca, Mn, Zn, As, Rb, Sr, Nb, Sn and Pb.

In all populations analyzed, As and W show a higher standard deviation when compared with other elements. This is also the case of Sn in the entire and the schist populations, and the case of Nd and Bi in the granite population only.

Comparing the granite population with the schist population: the granite population (i) is enriched in Al, Si, P, S, K, Ca, Rb, Sr, Sn, Pb, Th and LE (light elements); (ii) displays

higher standard deviation for Al, P, S, K, Ca, Ti, Cr, Rb, Sr, Y, Nb, Ce and W; (iii) contains a higher maximum content for Al, Si, P, S, K, Ca and Rb; and (iv) contains a higher minimum content for Si, P, K, Ca, Zn, Rb, Sr, Pb and LE (Mg, Sn, La, Ce, Nd, W, Bi and Th have the same minimum in both populations).

Overall, granites have higher values of Al, P, K, Ca, Rb and Pb when compared to metasedimentary rocks. Oppositely, the metasediments show higher contents of Mg, Ti, Cr, Mn, Fe, Ni, Cu, Y, Zr, Nb, Ba and Nd when compared with granite rocks.

The distributions of Sn, Nd, W and Bi are the ones more influenced by the detection limit. Also, the IQR for W is 0, which did not allow for anomaly standardization.

Some pathfinders were selected to correlate with Li, based on literature and Pearson correlation matrices (Appendices E), since XRF does not measure Li contents.

Firstly, the elements Sn, Rb and Nb were selected because these are common elements that define the geochemical signature of the Rare-Element pegmatite class, namely of Li-rich pegmatites worldwide (Černý & Ercit, 2005; Simmons & Webber, 2008; Roda-Robles *et al.*, 2018; Cardoso-Fernandes *et al.*, 2022). W was also selected because it can be associated with Li, as well. Cs, F, Ta and Be are very good pathfinders for Li but cannot be measured by XRF.

Secondly, Mn, K, and Al were selected too, since the association of MnO, K_2O, and Al_2O_3 can be explained by the co-occurrence of Mn oxides in Li-rich bodies of the CIZ (Central Iberian Zone)-GTMZ and due to the presence of K and Al in the structure of Li-minerals (Roda-Robles *et al.*, 2018; Cardoso-Fernandes *et al.*, 2020; Cardoso-Fernandes *et al.*, 2022).

Thirdly, the Pearson correlation matrices (Figure E1, Figure E2, Figure E3, and Figure E4, Appendix E), were used to find high correlation values (Pearson *r*) between LE and the rest of the elements (since Li is within the group of LE). Th was the only element that could be possibly correlated to Li, since it is moderately correlated ($0.5 \leq r < 0.7$) to LE in the Pearson correlations of granite, schist and granite+schist ($r = 0.55$, $r = 0.54$, and $r = 0.54$, respectively), and highly correlated ($r \geq 0.7$) to LE in Pearson correlation of granite+schist ($r = 0.77$). In the last correlation, some other elements like S, Cu, Zn and Zr were correlated to LE too, but these elements usually are not associated with Li.

Accordingly, four groups of pathfinders were created: (i) Sn, Rb, Nb and W; (ii) Sn, Rb, Nb and Th; (iii) Mn, K, Al, Sn, Rb, Nb and Th; and (iv) Mn, K, Al, Sn, Rb and Nb.

	Mg_ppm	Al_ppm	Si_ppm	P_ppm	S_ppm	K_ppm	Ca_ppm	Ti_ppm	Cr_ppm	Mn_ppm	Fe_ppm	Ni_ppm	Cu_ppm	Zn_ppm	As_ppm	Rb_ppm	Sr_ppm	Y_ppm	Zr_ppm	Nb_ppm	Sn_ppm	Ba_ppm	La_ppm	Ce_ppm	Nd_ppm	W_ppm	Pb_ppm	Bi_ppm	Th_ppm	LE_ppm
granite : Count Numeric	38	38	38	38	38	38	38	38	38	38	38	38	38	38	38	38	38	38	38	38	38	38	38	38	38	38	38	38	38
granite : Count Text	0	0	0	0	0	0	0	0	0	0	0	0	0	0	0	0	0	0	0	0	0	0	0	0	0	0	0	0	0
granite : Count Null	0	0	0	0	0	0	0	0	0	0	0	0	0	0	0	0	0	0	0	0	0	0	0	0	0	0	0	0	0
granite : Count Negative	0	0	0	0	0	0	0	0	0	0	0	0	0	0	0	0	0	0	0	0	0	0	0	0	0	0	0	0	0
granite : Count Zero	0	0	0	0	0	0	0	0	0	0	0	0	0	0	0	0	0	0	0	0	0	0	0	0	0	0	0	0	0
granite : Unique Values	37	38	38	37	37	38	38	38	19	37	38	25	24	33	22	37	34	26	38	18	21	36	32	35	17	7	28	9	27	38
granite : Minimum	1500	42877	171325	481.33	143	19007.3	1108	1905.7	5	120.67	10439.7	2.5	2.5	44.67	2.5	184.67	48.67	2.5	68	2.5	2.5	219.33	5	5	5	2.5	23.67	2.5	2.5	529397
granite : Maximum	11367.7	134250	309085	2231.7	2113	40658.3	6141	5949.7	100.67	830.33	44343.7	37.67	30.33	142.33	140.33	440.67	127.67	33.67	277.33	11.67	49	949.67	170	198.5	412	70	48.67	28	44	723705
granite : Mean	6442.32	98396.8	231521	1197.1	615.61	28350.1	2814.2	3402.3	32.917	345.66	20592.2	13.488	12.982	80.552	12.816	331.76	77.238	11.579	138.15	6.59211	21.825	471.87	109.05	131.72	119.49	6.6316	38	9.3508	17.754	605471
granite : Median	6521.17	97031.7	230884	1216.5	474.16	27827	2540.5	3152.2	40	276.83	19809.7	11	12.335	77	8	338.17	72.335	9.67	129.5	6.75	25	467	114.75	139.75	5	2.5	37.835	2.5	15.75	598365
granite : Range	9867.67	91373	137760	1750.3	1970	21651	5033	4044	95.67	709.66	33904	35.17	27.83	97.66	137.83	256	79	31.17	209.33	9.17	46.5	730.34	165	193.5	407	67.5	25	25.5	41.5	194308
granite : Interquartile Range	2861.17	18847.7	35191.5	435.33	417.83	7788.5	1820.9	1125.6	48.25	245.83	9284.83	6.42	5.5	33.998	7.0825	73.338	16.082	5.6275	63.67	3.625	31.42	228.33	34.125	39.5	264	0	6.4175	19	14.87	37586.8
granite : Standard Deviation	2225.15	16861	29943.9	399.6	384.26	5288.14	1268.8	890.92	26.54	183.91	7338.53	7.8283	5.1388	24.269	22.638	55.794	19.551	6.431	52.401	2.53014	15.567	164.12	42.321	46.087	140.21	12.727	5.3904	10.362	11.668	38737.7
granite : Variance	4951305	2.84E+08	8.97E+08	159679	147656	2.80E+07	2E+06	793741	704.35	33824	5.39E+07	61.282	26.407	588.96	512.48	3113	382.25	41.358	2745.9	6.40159	242.32	26937	1731.1	2124	19660	161.98	29.056	107.36	136.13	1.50E+09
granite : Skewness	-0.0041	-0.6814	0.399	0.4932	2.0164	0.38639	0.9186	0.8481	0.3355	1.0171	1.25362	1.2394	0.8694	0.7334	5.1485	-0.429	1.2195	1.5889	0.9792	0.00442	-0.104	0.7921	-1.431	-1.5	0.5194	4.0441	-0.371	0.9119	0.477	0.97388
granite : Tukey Upper Outlier Threshold	12247.6	1.38E+05	3.03E+05	2056.5	1427.7	4.36E+04	6346.5	5680.7	125.63	817.41	3.90E+04	25.8	23.75	144.5	21.706	479.76	106.12	21.526	261.92	13.98	81.05	896.75	185.81	218.5	665	2.5	51.291	50	47.677	6.76E+05
granite : 1 percentile	1500	42877	171325	481.33	143	19007.3	1108	1905.7	5	120.67	10439.7	2.5	2.5	44.67	2.5	184.67	48.67	2.5	68	2.5	2.5	219.33	5	5	5	2.5	23.67	2.5	2.5	529397
granite : 5 percentile	1500	67010.5	179033	519.02	210.76	19812.6	1279	2159	5	141.25	11500.2	2.5	2.5	46.884	2.5	217.28	50.57	3.925	68.314	2.5	2.5	250.37	5	5	5	2.5	25.57	2.5	2.5	537324
granite : 10 percentile	3801.95	78203.2	193643	601.13	304.4	21134	1432.1	2224.8	5	181.43	11606.8	2.5	7.9	49.164	2.5	259.87	57.903	5.9	72.8	2.5	2.5	275.5	5	76.55	5	2.5	31.57	2.5	2.5	569859
granite : 25 percentile	5094.67	91100.8	214899	968.17	383.17	24126.3	1794.2	2866.7	5	202.83	15748.9	9.75	10	59.503	4	296.41	65.918	7.4575	102.75	4.9175	2.5	325.92	100.5	119.75	5	2.5	35.248	2.5	10.503	582146
granite : 75 percentile	7955.83	109948	250091	1403.5	801	31914.7	3615.1	3992.3	53.25	448.66	25033.7	16.17	15.5	93.5	11.083	369.75	82	13.085	166.42	8.5425	33.92	554.25	134.63	159.25	269	2.5	41.665	21.5	25.373	619732
granite : 90 percentile	9461.44	118439	264177	1726.3	1072	35114.7	5119.6	4628.7	63.45	648.2	31000.8	25.367	20.67	117.4	21.27	396.84	115.24	21.803	209.37	10.05	43	737.17	158.1	175.72	304.4	15.65	45.703	27	34.7	661885
granite : 95 percentile	10761.2	127880	305455	2162.6	1478.4	39711.2	5347.7	5319.8	76.283	714.43	36568.2	31.97	22.416	137.27	48.503	433.07	123.87	24.483	275.43	11.0335	47.1	785.95	160.5	196.13	331.89	41.5	46.77	28	41.787	690294
granite : 99 percentile	11367.7	134250	309085	2231.7	2113	40658.3	6141	5949.7	100.67	830.33	44343.7	37.67	30.33	142.33	140.33	440.67	127.67	33.67	277.33	11.67	49	949.67	170	198.5	412	70	48.67	28	44	723705
granite+schist : Count Numeric	4	4	4	4	4	4	4	4	4	4	4	4	4	4	4	4	4	4	4	4	4	4	4	4	4	4	4	4	4	4
granite+schist : Count Text	0	0	0	0	0	0	0	0	0	0	0	0	0	0	0	0	0	0	0	0	0	0	0	0	0	0	0	0	0	0
granite+schist : Count Null	0	0	0	0	0	0	0	0	0	0	0	0	0	0	0	0	0	0	0	0	0	0	0	0	0	0	0	0	0	0
granite+schist : Count Negative	0	0	0	0	0	0	0	0	0	0	0	0	0	0	0	0	0	0	0	0	0	0	0	0	0	0	0	0	0	0
granite+schist : Count Zero	0	0	0	0	0	0	0	0	0	0	0	0	0	0	0	0	0	0	0	0	0	0	0	0	0	0	0	0	0	0
granite+schist : Unique Values	4	4	4	4	4	4	4	4	4	4	4	4	4	4	4	4	4	4	4	4	4	4	4	4	2	4	4	3	4	4
granite+schist : Minimum	5534.67	84133.7	189087	482	155.67	20443.7	1591.3	3329.7	52	315.33	20314.7	18	17.33	75.33	9.33	178.67	53.67	13.33	147.67	4	26	332.33	124	132	5	16	18.67	2.5	2.5	532203
granite+schist : Maximum	9066	92949.7	298449	1087.7	876	25303.3	2509.3	5737.3	90	1344.7	46171.3	49.33	44.33	108.67	48	300.33	99.67	31	288.33	13.67	253	854.33	189	205.5	239.5	31	35	32	24	634846
granite+schist : Mean	8101.54	87384.8	236813	755.5	540.5	22852.3	1915.8	4509.4	70.833	652	31248.5	29.833	25.583	86.168	30.748	217.92	66.5	20.665	199	8.835	88.5	601.42	148.67	163.79	63.625	23.375	26.335	16.75	11.875	604199
granite+schist : Median	8902.75	86227.8	229858	726.17	565.17	22831	1781.3	4485.3	70.665	474	29254	26	20.335	80.335	32.83	196.33	56.33	19.165	180	8.835	37.5	609.5	140.83	158.83	5	23.25	25.835	16.25	10.5	624874
granite+schist : Range	3531.33	8816	109362	605.67	720.33	4859.66	918	2407.7	38	1029.3	25856.7	31.33	27	33.34	38.67	121.66	46	17.67	140.66	9.67	227	522	65	73.5	234.5	15	16.33	29.5	21.5	102643
granite+schist : Interquartile Range	2684.87	7644.08	83466.1	573.17	587.17	4146.58	707.83	1929.4	31.668	800.01	20836.8	23.998	20.918	26.838	36.253	96.745	35.5	13.835	115	7.835	173	438.59	55.667	63.208	175.88	14.375	14.83	29	16.375	78362.4
granite+schist : Standard Deviation	2937822	1.76E+07	2.06E+09	99997	93160	4608220	165570	1E+06	267.46	220926	1.22E+08	183.85	159.4	239.57	395.18	3168.7	493.24	55.943	4019.5	16.4896	12076	51413	913.57	1107.3	13748	63.563	62.563	271.42	79.729	2.33E+09
granite+schist : Skewness	-1.9808	0.95248	0.88498	0.1304	-0.42	0.04208	1.6705	0.1322	0.0491	1.7947	0.93675	1.503	1.8822	1.6639	-0.173	1.7325	1.9496	1.0998	1.3675	-1.41E-15	1.9756	-0.164	0.9813	0.5862	2	0.017	0.1616	0.0127	0.8909	-1.9299
granite+schist : Tukey Upper Outlier Threshold	13070.7	103251	407223	1916.5	1702.5	31156	3398.7	8380.3	134.25	2341	73919.4	79.744	70.041	142.76	102.21	422.2	142.59	49.085	438.49	24.505	460	1474.5	263.92	292.69	444.69	52.188	56.245	75	45.313	750587
granite+schist : 1 percentile	5534.67	8.41E+04	1.89E+05	482	155.67	20443.7	1591.3	3329.7	52	315.33	2.03E+04	18	17.33	75.33	9.33	178.67	53.67	13.33	147.67	4	26	332.33	124	132	5	16	18.67	2.5	2.5	5.32E+05
granite+schist : 5 percentile	5534.67	84133.7	189087	482	155.67	20443.7	1591.3	3329.7	52	315.33	20314.7	18	17.33	75.33	9.33	178.67	53.67	13.33	147.67	4.00E+00	26	332.33	124	132	5	16	18.67	2.5	2.5	532203
granite+schist : 10 percentile	5534.67	84133.7	189087	482	155.67	20443.7	1591.3	3329.7	52	315.33	20314.7	18	17.33	75.33	9.33	178.67	53.67	13.33	147.67	4	26	332.33	124	132	5	16	18.67	2.5	2.5	532203
granite+schist : 25 percentile	6358.5	84141.2	198558	483.58	234.58	20789.6	1629.2	3556.8	55.082	341	21827.3	19.75	17.748	75.665	11.58	180.33	53.835	14.498	151	4.9175	27.5	378.08	124.75	134.67	5	16.25	19.17	2.5	4.375	554681
granite+schist : 75 percentile	9043.38	91785.3	282024	1056.8	821.75	24936.2	2337	5486.2	86.75	1141	42664.2	43.748	38.665	102.5	47.832	277.08	89.335	28.333	266	12.7525	200.5	816.67	180.42	197.88	180.88	30.625	34	31.5	20.75	633043
granite+schist : 90 percentile	9066	92949.7	298449	1087.7	876	25303.3	2509.3	5737.3	90	1344.7	46171.3	49.33	44.33	108.67	48	300.33	99.67	31	288.33	13.67	253	854.33	189	205.5	239.5	31	35	32	24	634846
granite+schist : 95 percentile	9066	92949.7	298449	1087.7	876	25303.3	2509.3	5737.3	90	1344.7	46171.3	49.33	44.33	108.67	48	300.33	99.67	31	288.33	13.67	253	854.33	189	205.5	239.5	31	35	32	24	634846
granite+schist : 99 percentile	9066	92949.7	298449	1087.7	876	25303.3	2509.3	5737.3	90	1344.7	46171.3	49.33	44.33	108.67	48	300.33	99.67	31	288.33	13.67	253	854.33	189	205.5	239.5	31	35	32	24	634846
schist : Count Numeric	115	115	115	115	115	115	115	115	115	115	115	115	115	115	115	115	115	115	115	115	115	115	115	115	115	115	115	115	115	115
schist : Count Text	0	0	0	0	0	0	0	0	0	0	0	0	0	0	0	0	0	0	0	0	0	0	0	0	0	0	0	0	0	0
schist : Count Null	0	0	0	0	0	0	0	0	0	0	0	0	0	0	0	0	0	0	0	0	0	0	0	0	0	0	0	0	0	0
schist : Count Negative	0	0	0	0	0	0	0	0	0	0	0	0	0	0	0	0	0	0	0	0	0	0	0	0	0	0	0	0	0	0
schist : Count Zero	0	0	0	0	0	0	0	0	0	0	0	0	0	0	0	0	0	0	0	0	0	0	0	0	0	0	0	0	0	0
schist : Unique Values	115	115	115	109	112	115	115	112	94	111	115	72	69	97	92	96	77	60	104	28	36	110	73	100	55	24	62	28	51	115
schist : Minimum	1500	50152	140087	143.33	156.33	15227.7	439.67	2478.3	42	329.67	18404	13.67	10	40	9.67	105.67	21.67	9.67	99	6.33	2.5	292.67	5	5	5	2.5	13	2.5	2.5	515187
schist : Maximum	21077	129107	300978	1134	1408.3	35212.3	5567.3	5958.3	114.33	3425.3	66647.3	67	47	171.33	516	304	138.67	37.67	396.33	24.33	130	1382.7	244	295	487.5	97	58.33	41	46	748890
schist : Mean	10427.6	93564.5	224804	556.19	482.99	24933.7	1645	4743	78.991	699.94	36171.9	37.734	25.135	88.111	41.747	180.31	50.581	23.053	216.08	9.99626	20.604	715.11	113.53	161.64	172.47	9.2189	28.701	13.374	17.593	600554
schist : Median	9510.5	93536.7	219251	517.33	417.33	25354	1422.3	4787	79.33	607.33	35820.7	37.33	24	83	25.67	173.33	45.33	22.33	209	9.67	23	703	127.67	165	232	2.5	28	2.5	17.33	596551
schist : Range	19577	78954.7	160891	990.67	1252	19984.7	5127.7	3480	72.33	3095.7	48243.3	53.33	37	131.33	506.33	198.33	117	28	297.33	18	127.5	1090	239	290	482.5	94.5	45.33	38.5	43.5	233703
schist : Interquartile Range	4170	17991	41932.8	203.33	328.66	5726	1049.3	797.33	22.83	298.67	9302	12	11.33	33	26	56.67	17	8	67.67	2.33	27.5	269.33	43	59	305	13.5	12	21.5	23.5	74210.7
schist : Standard Deviation	3640.83	14821.6	36130.1	190.8	255.9	3991.02	858.84	667.08	16.268	394.23	8137.6	11.016	8.6541	24.757	56.114	42.561	18.096	5.7701	56.182	2.18708	23.546	205.75	53.159	45.041	160.51	12.513	8.4152	12.184	12.147	47484.4
schist : Variance	1.33E+07	2.20E+08	1.31E+09	36406	65483	1.59E+07	737614	445000	264.66	155419	6.62E+07	121.35	74.893	612.89	3148.7	1811.4	327.46	33.294	3156.4	4.78331	554.39	42334	2825.9	2028.7	25764	156.57	70.815	148.46	147.55	2.25E+09
schist : Skewness	0.89289	-0.1711	0.18953	0.9042	1.4549	-0.1303	1.4194	-0.584	0.0926	3.8537	0.63682	0.4148	0.4639	0.8289	5.9075	0.7908	1.9065	0.213	0.7364	2.62233	2.5038	0.5481	-1.021	-0.669	0.0944	3.5913	0.9212	0.4257	0.2709	0.61053
schist : Tukey Upper Outlier Threshold	18301.7	129699	304768	951	1125.3	36417.3	3650.3	6356	123.75	1214.7	53958.3	61	47.325	151.83	83	290.67	81.5	39	349.51	14.495	71.25	1238	211.5	279.5	767.5	36.25	51.67	56.25	61.25	749665
schist : 1 percentile	2042.4	50801.8	141231	155.97	160.28	15319.1	443.03	2548.2	43.067	331.96	18497.2	14.096	10.107	40.693	9.8028	106.26	21.883	9.99	100.07	6.3844	2.5	293.95	5	5	5	2.5	13.533	2.5	2.5	515331
schist : 5 percentile	5915	68660.7	160811	296.8	203	17092.7	547.73	3437.4	52.7	364.54	23249.3	19.536	12.466	53.334	12.33	122.2	32	13.47	131.2	7.264	2.5	424.2	5	104.9	5	2.5	18.13	2.5	2.5	534143
schist : 10 percentile	6.70E+03	7.44E+04	1.83E+05	345.87	228.93	1.99E+04	773.4	3986.3	57.4	419.13	2.71E+04	24.868	14.67	61.6	13.534	134.4	35.27	15	150.6	7.67	2.5	455.27	5	114.6	5	2.5	19.67	2.5	2.5	5.43E+05
schist : 25 percentile	7876.67	84721.7	199936	442.67	303.67	22102.3	1027	4362.7	66.67	468	30703.3	31	19	69.33	18	149	39	19	180.33	8.67	2.5	564.67	104	132	5	2.5	21.67	2.5	2.5	564138
schist : 75 percentile	12046.7	102713	241869	646	632.33	27828.3	2076.3	5160	89.5	766.67	40005.3	43	30.33	102.33	44	205.67	56	27	248	11	30	834	147	191	310	16	33.67	24	26	638349
schist : 90 percentile	17103	112754	281014	832.73	847.93	29459.1	2757.8	5596.3	101.47	1025.5	46857.9	53	38.132	127.27	79.2	242.33	73.8	30.132	290.13	12.33	38.4	990.47	161.2	215.57	371.2	24.568	39.1	30	34.8	654713
schist : 95 percentile	18257.2	119207	292956	972.6	1061.3	30659.3	3201.6	5875.1	107.46	1363.1	51851	59.93	40.598	131.13	139.2	272.27	93.266	33.802	307.6	13.134	44.934	1068.5	169.8	231	418	27.07	46.464	34	40	686616
schist : 99 percentile	20895.3	128502	300950	1127.2	1401.1	35073.6	5309.3	5958.1	114.28	3223.2	65175.6	66.413	46.733	170.85	465.44	300.32	134.08	37.51	395.85	22.89	129.2	1370.2	236.48	287.48	482.3	88.84	57.904	40.52	45.84	745741

Figure 87. Basic statistics for each lithology, generated by ioGAS (pink color represents granite; bue color represents granite+schist; green color represents schist; yellow rows represent the values that were used for the IQR standardization (IQR and Tukey upper outlier threshold).

As aforementioned, several graphical tools and maps were created for all the elements (Appendix B), but this section focuses only on the EDA of the selected pathfinders.

Analyzing the graphics and the variable distribution map of Al (Figure 90-a to -e), it is possible to see two negatively skewed populations (-0.68 for granites and -0.17 for schist), but close to the normal distribution (~0) (Figure 90-a and -b). Al contents are similar in both lithologies (Figure 90-a, -b, -c, -d and -e), not allowing to discriminate the two populations (Figure 90-b and -c). Some lower outliers are discriminated when analyzing the boxplot of Al (Figure 90-a). The Q-Q plot and Split Q-Q plot of Al (Figure 90-c and -d) show a distribution near the normal, following the skewness values. Even though the Al contents are similar in both populations, the Split Q-Q plot tells that granite has a slightly higher content of Al (this fact cannot be analyzed in the histogram). The Al variable map (Figure 90-e) shows the distribution of the Al contents in the Circo area.

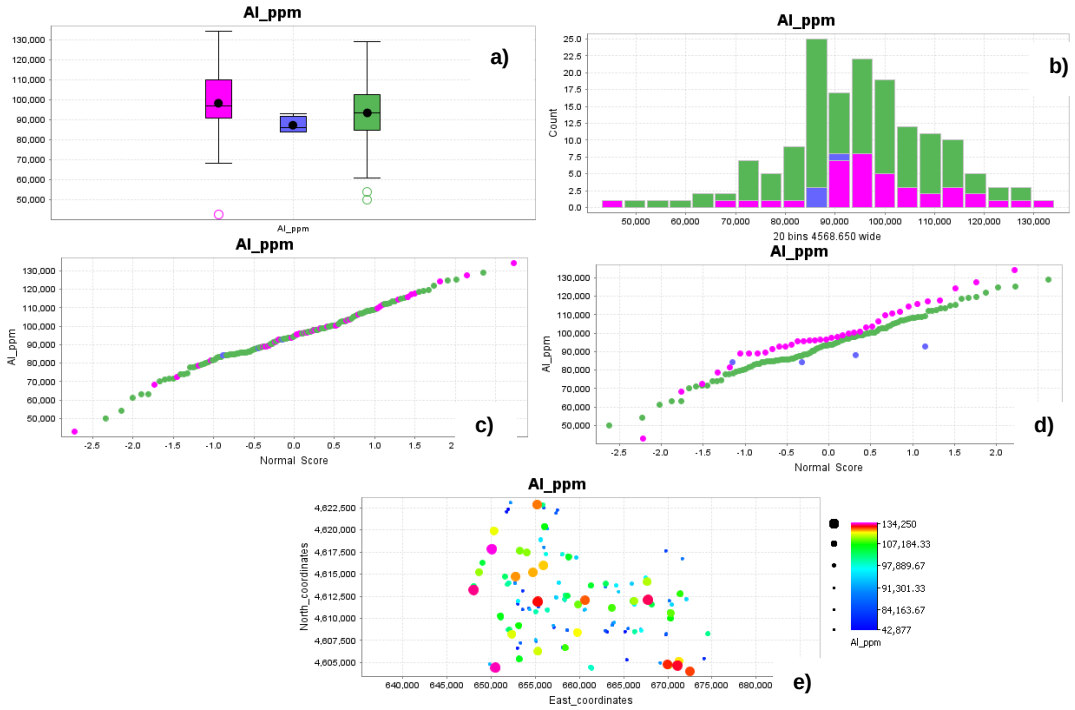


Figure 90. Al graphics and map: a) boxplot; b) histogram; c) Q-Q plot; d) Split Q-Q plot; e) variable map; (images -a to -d discriminate the difference between the lithologies (green – schist; pink – granite; blue – granite+schist), image -e presents a map where the large dots and warmer colors represent higher Al contents).

The K graphics and the variable distribution map (Figure 91-a to -e), show that skewness is positive for granite (0.38) and negative for schist (-0.19), but again, both values are close to 0 (Figure 91-a and -b). High contents of K can be found in granite samples, but also in the schist (Figure 91-a, -b and -e), being impossible to discriminate both populations (Figure 91-b and -c). Q-Q plot and Split Q-Q plot of K (Figure 91-c and -d) show similar information to Al: a distribution near the normal, and

granite with a slightly higher content of K. The K variable map (Figure 91-e) shows the distribution of the K contents in the Circo area, where higher contents tend to occur in the granites.

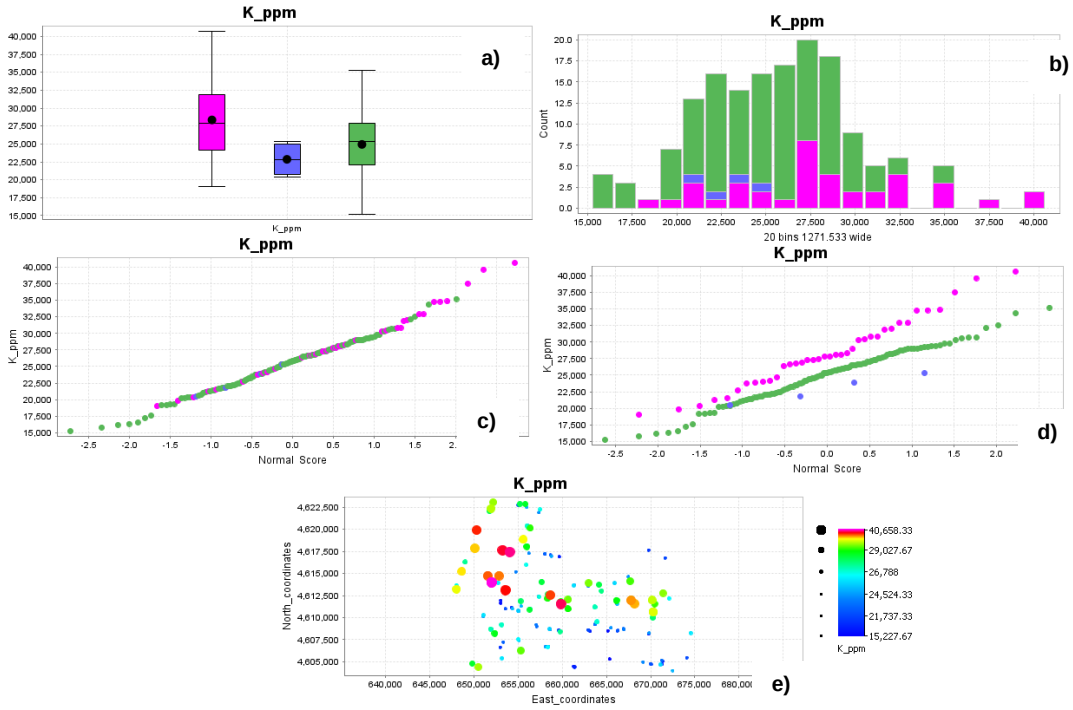


Figure 91. K graphics and map: a) boxplot; b) histogram; c) Q-Q plot; d) Split Q-Q plot; e) variable map; (images -a to -d discriminate the difference between the lithologies (green – schist; pink – granite; blue – granite+schist), image -e presents a map where the large dots and warmer colors represent higher K contents).

The Mn graphics and the variable map (Figure 92-a to -e) represent positive skewnesses for both lithologies (1 for granite and 3.8 for schist) (Figure 92-a and -b). Higher contents of Mn are observed in the schist (Figure 92-a, -b, -c, -d and -e). The histogram does not allow the discrimination of both populations, but the Q-Q plot does (Figure 92-c). Upper outliers and upper far outliers are discriminated in the Mn boxplot (Figure 92-a). The Split Q-Q plot of Mn (Figure 92-d) proves the higher contents of Mn in the schist, such as the variable map (Figure 92-e), showing the distribution of the Mn contents in the Circo area.

Analyzing the graphics and the variable map of Nb (Figure 93-a to -e), it is possible to see a high positive skewness for schist (2.62), due to the upper outliers (for example, the upper far outlier represented around 24 ppm, seen in Figure 93-a). For the granite, the skewness value is very close to 0 (0.004). The Nb contents are higher in the schist (Figure 93-a, -b, -c, -d and -e). Despite the histogram not allowing the discrimination of both populations (Figure 93-b and -c), the Q-Q plot (Figure 93-c) does. The Q-Q plot and Split Q-Q plot of Nb (Figure 93-c and -d) show some measures <LOD for granite

(the ones represented as 2.5 ppm). The Nb variable map (Figure 93-e) shows the distribution of the Nb contents in the Circo area.

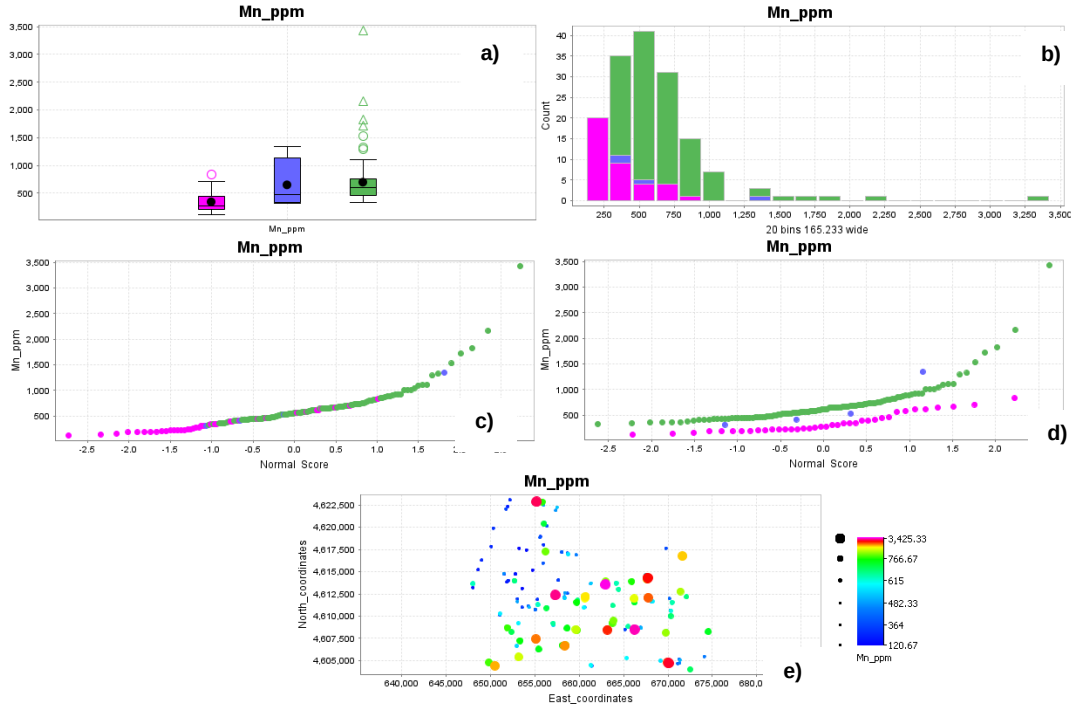


Figure 92. Mn graphics and map: a) boxplot; b) histogram; c) Q-Q plot; d) Split Q-Q plot; e) variable map; (images -a to -d discriminate the difference between the lithologies (green – schist; pink – granite; blue – granite+schist), image -e presents a map where the large dots and warmer colors represent higher Mn contents).

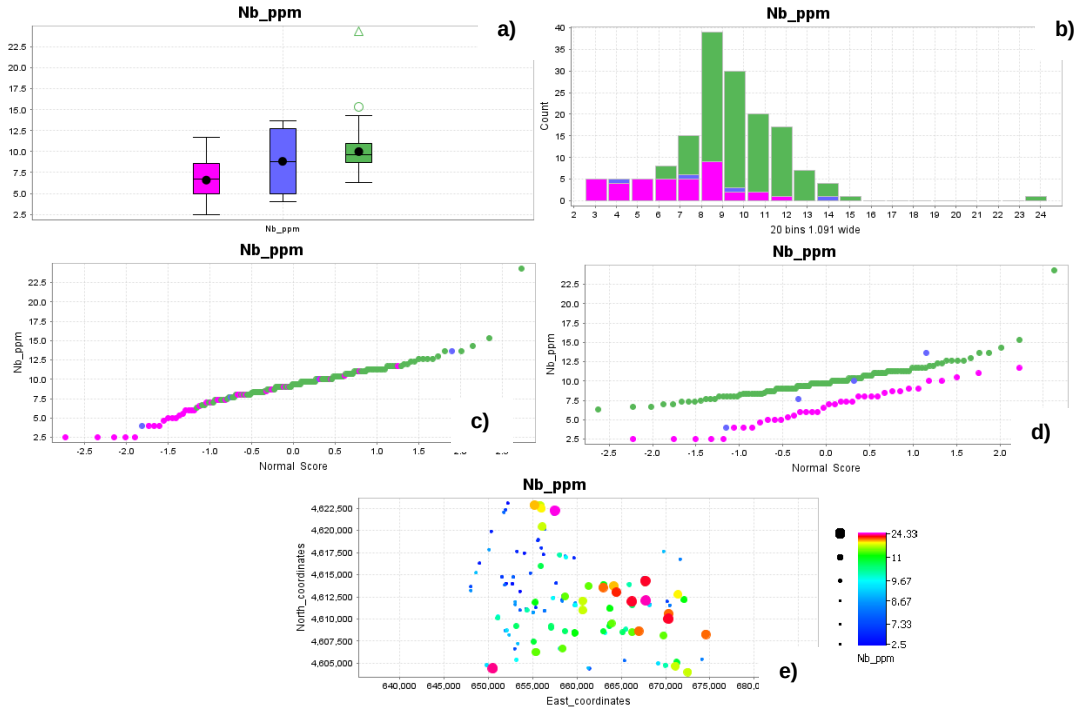


Figure 93. Nb graphics and map: a) boxplot; b) histogram; c) Q-Q plot; d) Split Q-Q plot; e) variable map; (images -a to -d discriminate the difference between the lithologies (green – schist; pink – granite; blue – granite+schist), image -e presents a map where the large dots and warmer colors represent higher Nb contents).

The Rb graphics and the variable map (Figure 94-a to -e) represent the negative skewness for granite (-0.42) and positive skewness for schist (0.79), both close to the normal distribution (Figure 94-a and -b). The Rb contents are higher in granite and both populations can be discriminated in all the graphics (Figure 94-a, -b, -c, -d and -e). One upper outlier and one lower outlier (for schist and granite, respectively) can be seen when analyzing the boxplot of Rb (Figure 94-a). The Q-Q plot and Split Q-Q plot of Rb (Figure 94-c and -d) show a near-normal distribution, following the skewness values. The Rb variable map (Figure 94-e) shows its content distribution in the Circo area.

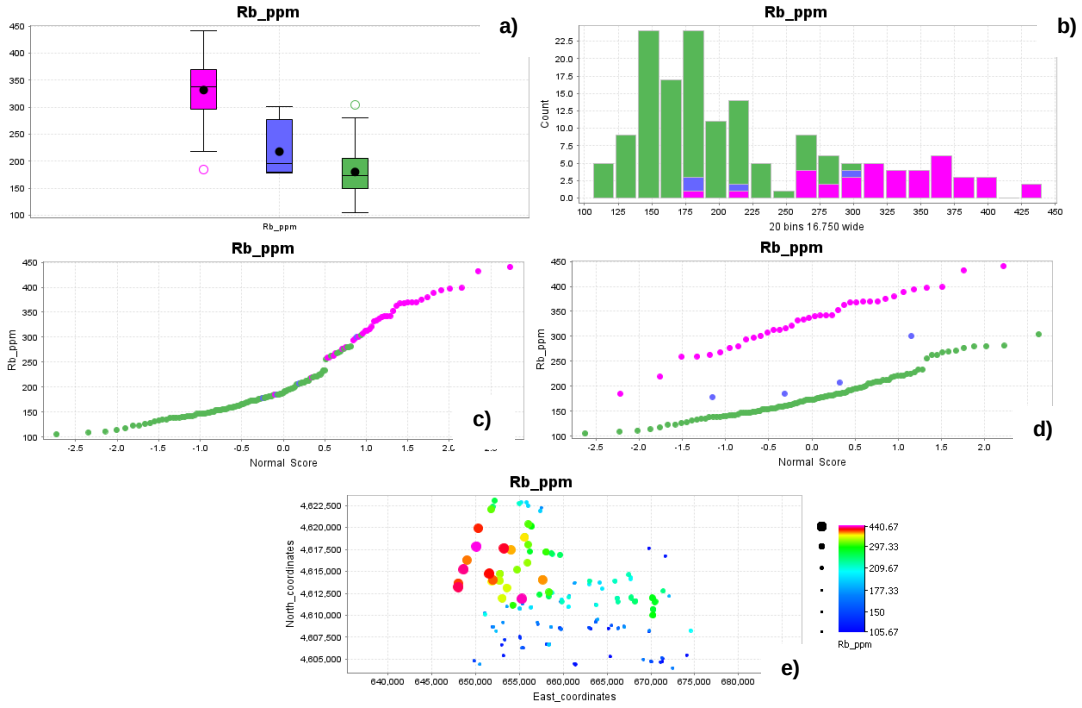


Figure 94. Rb graphics and map: a) boxplot; b) histogram; c) Q-Q plot; d) Split Q-Q plot; e) variable map; (images -a to -d discriminate the difference between the lithologies (green – schist; pink – granite; blue – granite+schist), image -e presents a map where the large dots and warmer colors represent higher Rb contents).

Analyzing the graphics and the variable map of Sn (Figure 95-a to -e), it is possible to recognize some upper outliers (including upper far outliers, Figure 95-a, -b, -c and -d) which led to a highly positive skewness for the schist (2.5); while the skewness is close to zero for the granite (-0.10). The presence of these outliers is due to the influence of measures <LOD of Sn. Tin contents are similar in both lithologies and it is impossible to distinguish the two populations (Figure 95-a, -b, -c, -d and -e). Analyzing the boxplot of Sn (Figure 95-a), in the schist, some outliers are highlighted, but these are not “real” outliers because a good portion of the measures is <LOD. The Q-Q plot and Split Q-Q plot of Sn (Figure 95-c and -d) show, again the influence of measurements <LOD. The Sn variable map (Figure 95-e) shows its content distribution in the Circo area.

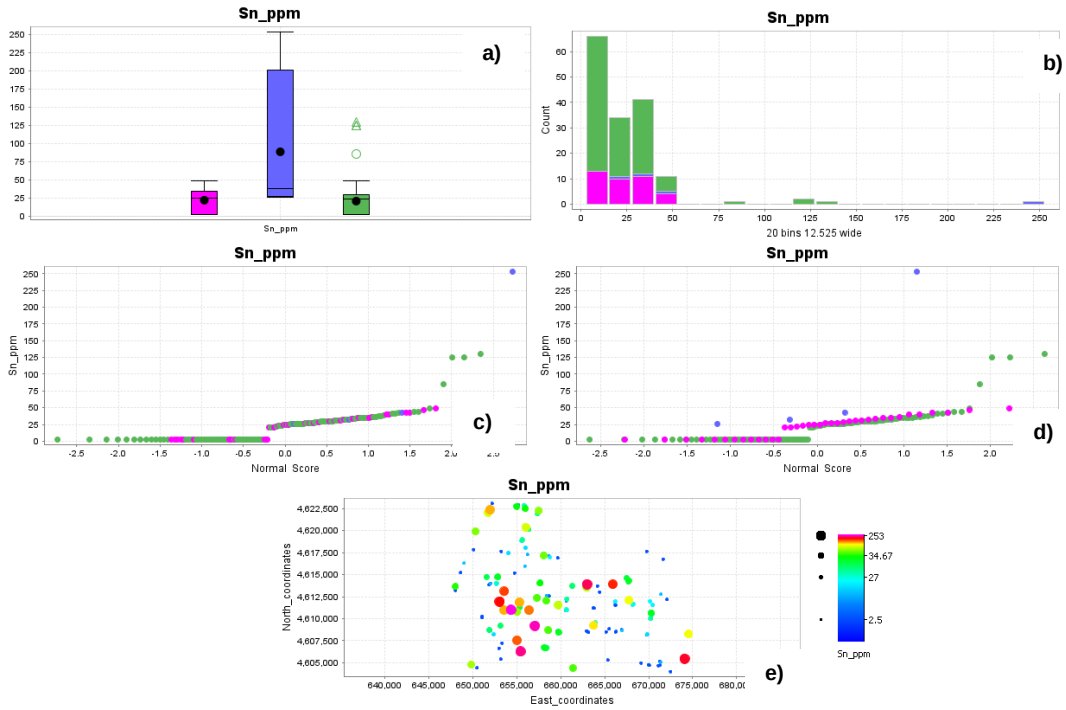


Figure 95. Sn graphics and map: a) boxplot; b) histogram; c) Q-Q plot; d) Split Q-Q plot; e) variable map; (images -a to -d discriminate the difference between the lithologies (green – schist; pink – granite; blue – granite+schist), image -e presents a map where the large dots and warmer colors represent higher Sn contents).

The Th graphics were also very affected by the XRF's LOD, with measures <LOD represented in the first column of the histogram (Figure 96-a) and in the lower line of the Q-Q plot and Split Q-Q plot (Figure 96-c and -d). Either for schist and granite, the skewness is positive and close to zero (0.27 and 0.47, respectively), and the distribution is close to normal, but the values <LOD deflect the information (Figure 96-b, -c and -d). Th contents are similar in both lithologies, and populations cannot be distinguished (Figure 96-a, -b, -c, -d and -e). The Th variable map (Figure 96-e) shows its distribution in the Circo area.

Analyzing the graphics and the variable map of W (Figure 97-a to -e), the influence of measures <LOD is the same as observed for Sn and Th. It is possible to see the presence of some upper outliers (including upper far outliers, Figure 97-a, -b, -c and -d) which led to a highly positive skewness of schist (3.6) and granite (4). The presence of these outliers is due to measures <LOD of W. The W contents are higher in schist due to a concentration of measurements <LOD in the granites. It is impossible to distinguish the two populations (Figure 97-a, -b, -c, -d and -e). The W variable map (Figure 97-e) shows the distribution of the W contents in the Circo area.

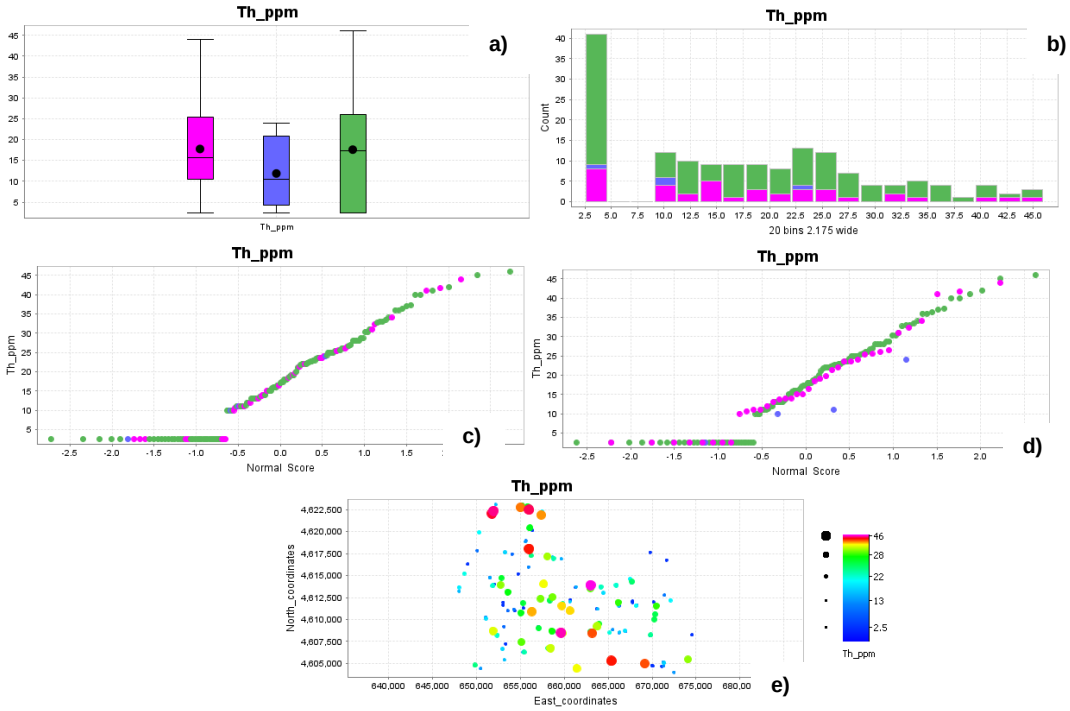


Figure 96. Th graphics and map: a) boxplot; b) histogram; c) Q-Q plot; d) Split Q-Q plot; e) variable map; (images -a to -d discriminate the difference between the lithologies (green – schist; pink – granite; blue – granite+schist), image -e presents a map where the large dots and warmer colors represent higher Th contents).

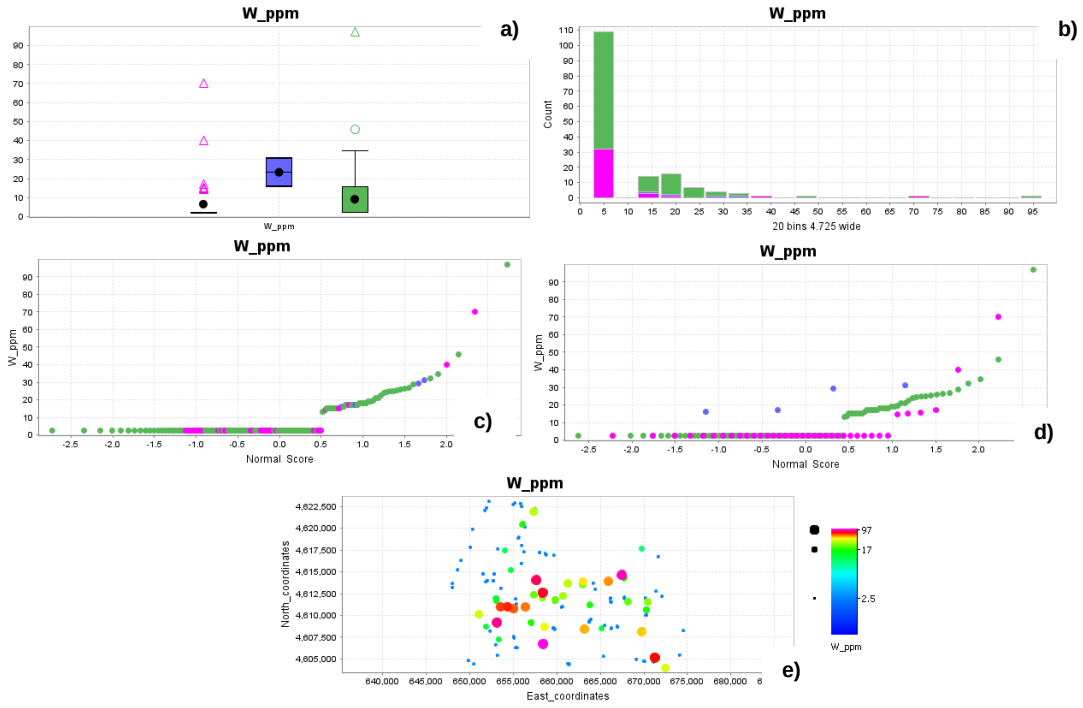


Figure 97. W graphics and map: a) boxplot; b) histogram; c) Q-Q plot; d) Split Q-Q plot; e) variable map; (images -a to -d discriminate the difference between the lithologies (green – schist; pink – granite; blue – granite+schist), image -e presents map where the large dots and warmer colors represent higher W contents).

PCA was also employed for each group of pathfinders. The eigenvectors and eigenvalues for every PCA are presented in appendix D. Also, biplots of each pathfinder group (combining the first four PCs) and a 3D biplot were produced. Two biplots of each pathfinder group were chosen to be described in this section.

The biplots represent the PCs in RQ mode. RQ is a mode of PCA for calculating variable and object loadings on the same axes, allowing elements to be displayed along with data points on a single diagram (Neff, 1994).

Biplots show the collected samples represented as points (green points are the samples collected in schist, blue points in granite+schist, and pink points are the ones collected in granite). All the elements selected for each PCA group are discriminated as vectors/arrows. When a vector has more length than the other, means that the first element is better represented in that graphic than the second one. The length of the arrows is directly proportional to the variability included in the two components (for example, the bigger the arrow, the more information the two components of the graph have about certain a element). The angle between vectors shows the correlation of the elements (for example, if two elements make an angle of 180º degrees between them, it means a high and negative correlation).

- First pathfinder group ("PATH1") – Rb, Nb, Sn and W

Analyzing the PCA information of "PATH1", PC1 accounts for 37.27% of the total variance, PC2 accounts for 29.71%, PC3 for 20.22% and PC4 for 12.8%. PC1 has high eigenvectors for Rb (0.68) and Nb (-0.66). PC2 has high eigenvectors for Sn (0.71) and W (0.64), such as PC3 (0.66 and -0.68, of Sn and W, respectively). PC4 represents high eigenvectors of Rb (0.69) and Nb (0.65). Nb has a high negative correlation with Rb (-0.46), while Sn has a weak positive correlation with W (0.21). All the other correlations between the four elements are around zero.

Biplot of components RQ1 and RQ4 (Figure 98) shows that (i) most of the graphic information is related to Nb and Rb, (ii) Nb and W are highly correlated, (iii) Sn does not correlate with Rb, (iv) granite samples have a higher content of Rb than the schist samples, (v) schist samples have higher contents of Nb, Sn and W when compared to granite samples. Biplot of components RQ1 and RQ3 (Figure 99) shows that (i) the graphic information is related to all four elements (but slightly more related to Nb and Rb), (ii) Nb, W and Sn are correlated, (iii) Nb and Rb are negatively correlated, (iv) granite samples have a higher content of Rb than the schist samples, (v) schist samples have higher contents of Nb, Sn and W when compared to granite samples.

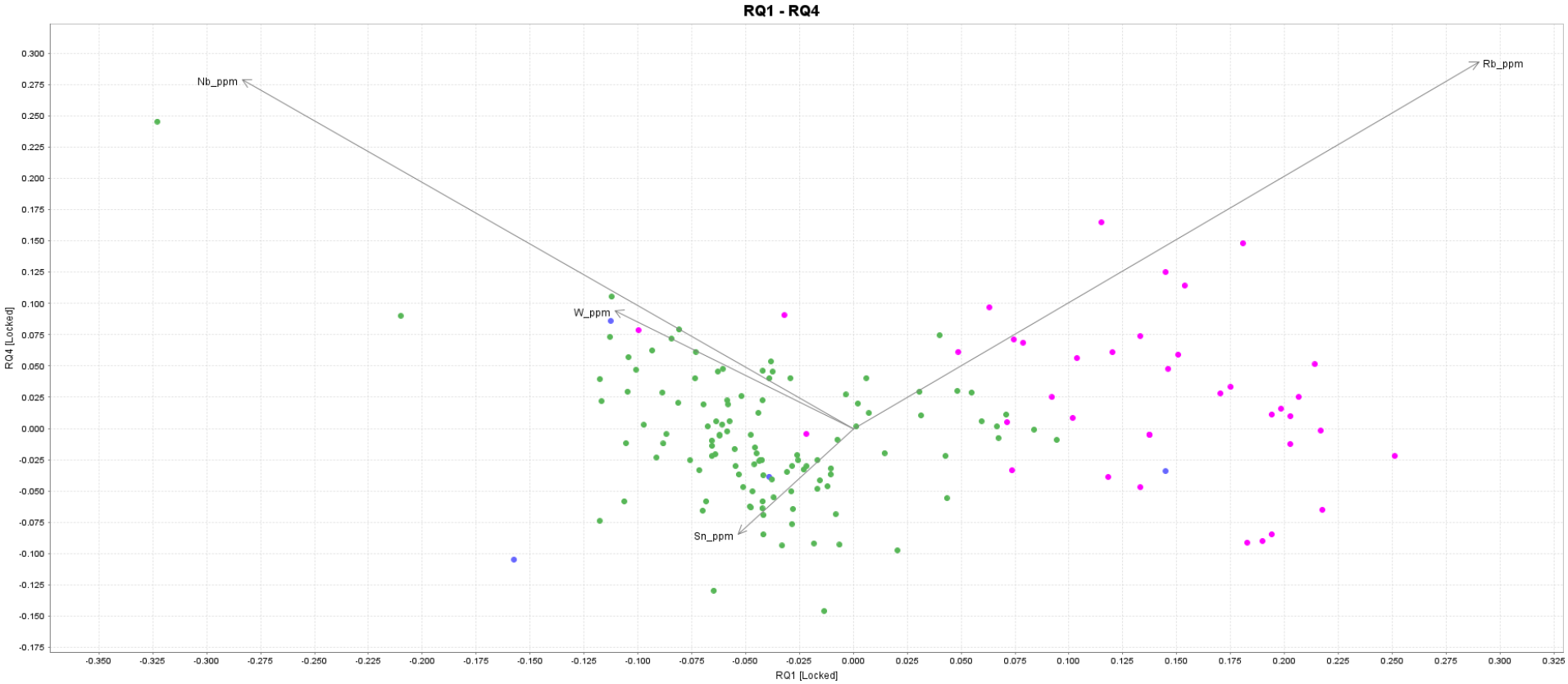


Figure 98. Biplot projecting components RQ1 and RQ4; PCA of group "PATH1".

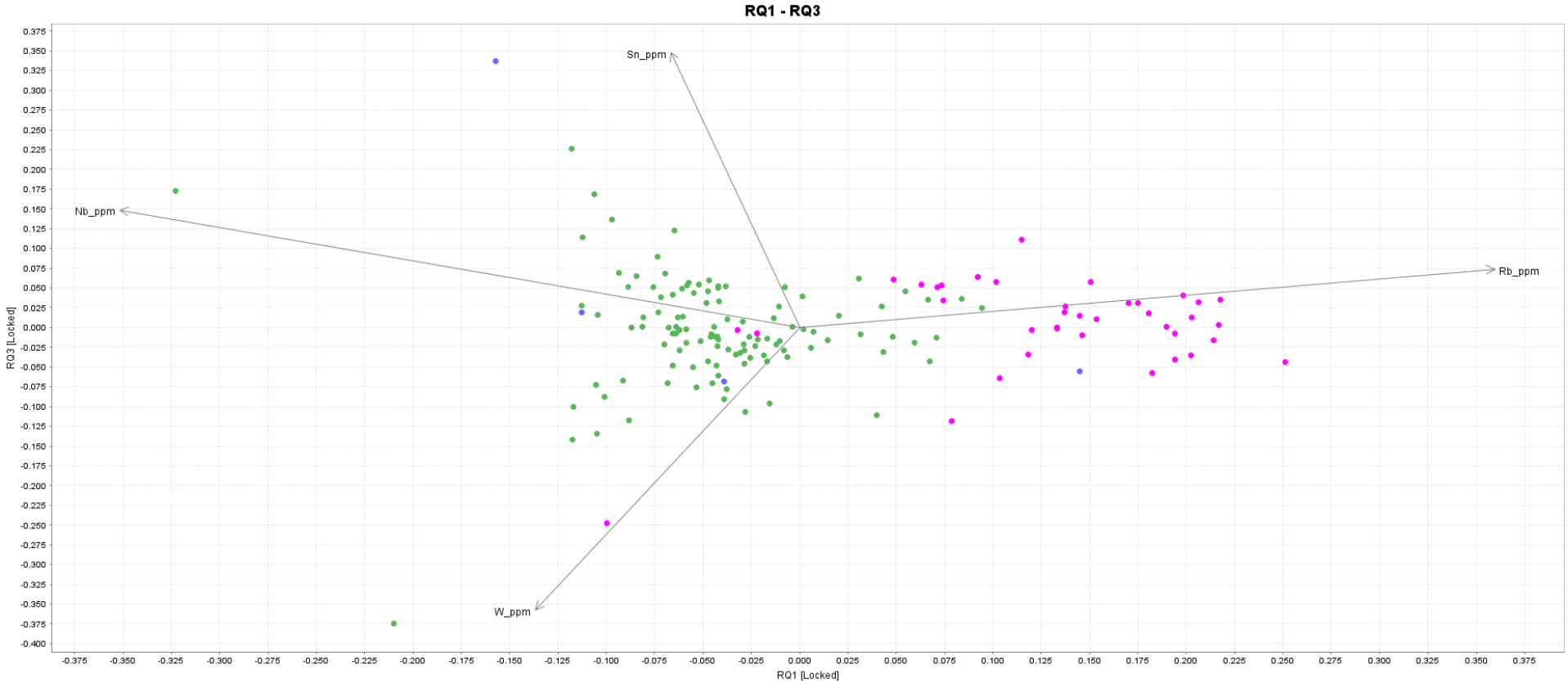


Figure 99. Biplot projecting components RQ1 and RQ3; PCA of group "PATH1".

The 3D biplot of “PATH1” (Figure 100) shows that, overall, granite samples have a higher content of Rb when compared to schist samples; schist samples have higher contents of Sn, Nb and W; and the highest (negative, in this case) correlations within these four elements is between Rb and Nb, and Sn and W.

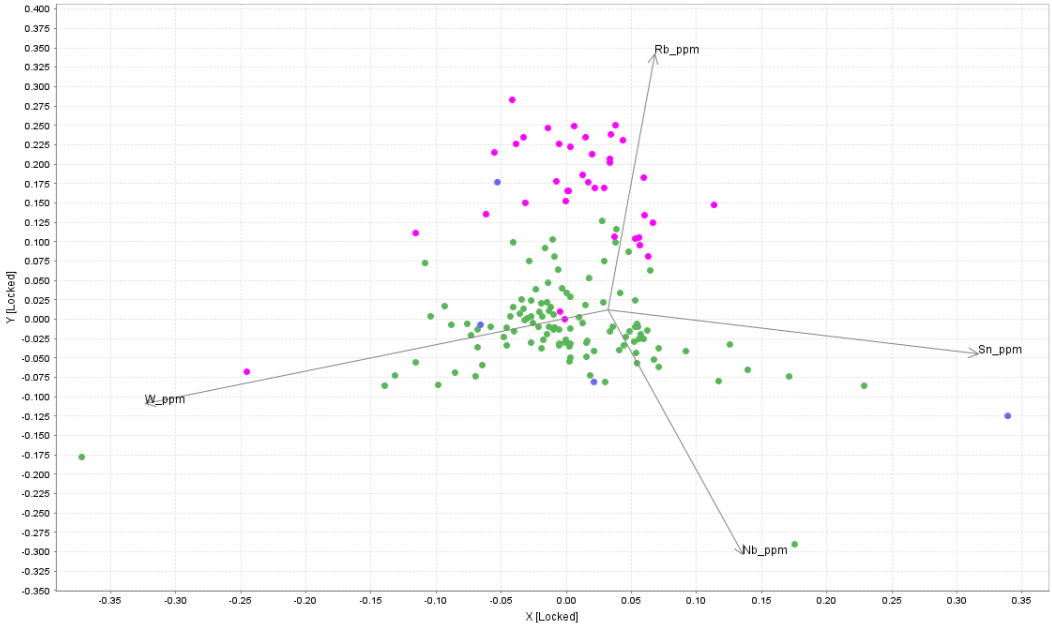


Figure 100. 3D biplot of PCA; group "PATH1".

- Second pathfinder group (“PATH2”) – Rb, Nb, Sn and Th

Analyzing the PCA information of “PATH2”, PC1 accounts for 36.85% of the total variance, PC2 accounts for 26.21%, PC3 for 23.63% and PC4 for 13.31%. PC1 has high eigenvectors for Rb (0.69) and Nb (-0.69). PC2 has high eigenvectors for Sn (0.76) and Th (0.63), such as PC3 (-0.63 and 0.75, of Sn and Th, respectively). PC4 represents high eigenvectors for Rb (0.70) and Nb (0.70). Nb has a high negative correlation with Rb (-0.46). All the other correlations between the four elements are around zero.

Biplot of components RQ1 and RQ2 (Figure 101) shows that (i) graphic information is related to all four elements (but slightly more related to Nb and Rb), (ii) Sn and Th have a good correlation, (iii) Nb does not correlate with Rb, (iv) granite samples have a higher content of Rb than the schist samples, (v) schist samples have higher contents of Nb, Sn and Th when compared to granite samples, (vi) both types of samples have close Sn contents. Biplot of components RQ2 and RQ4 (Figure 102) shows that (i) graphic information is related to all four elements, (ii) the highest correlation is between Th and Sn, (iii) Sn and Nb represent the lowest correlation, (iv) Nb and Rb have a good correlation.

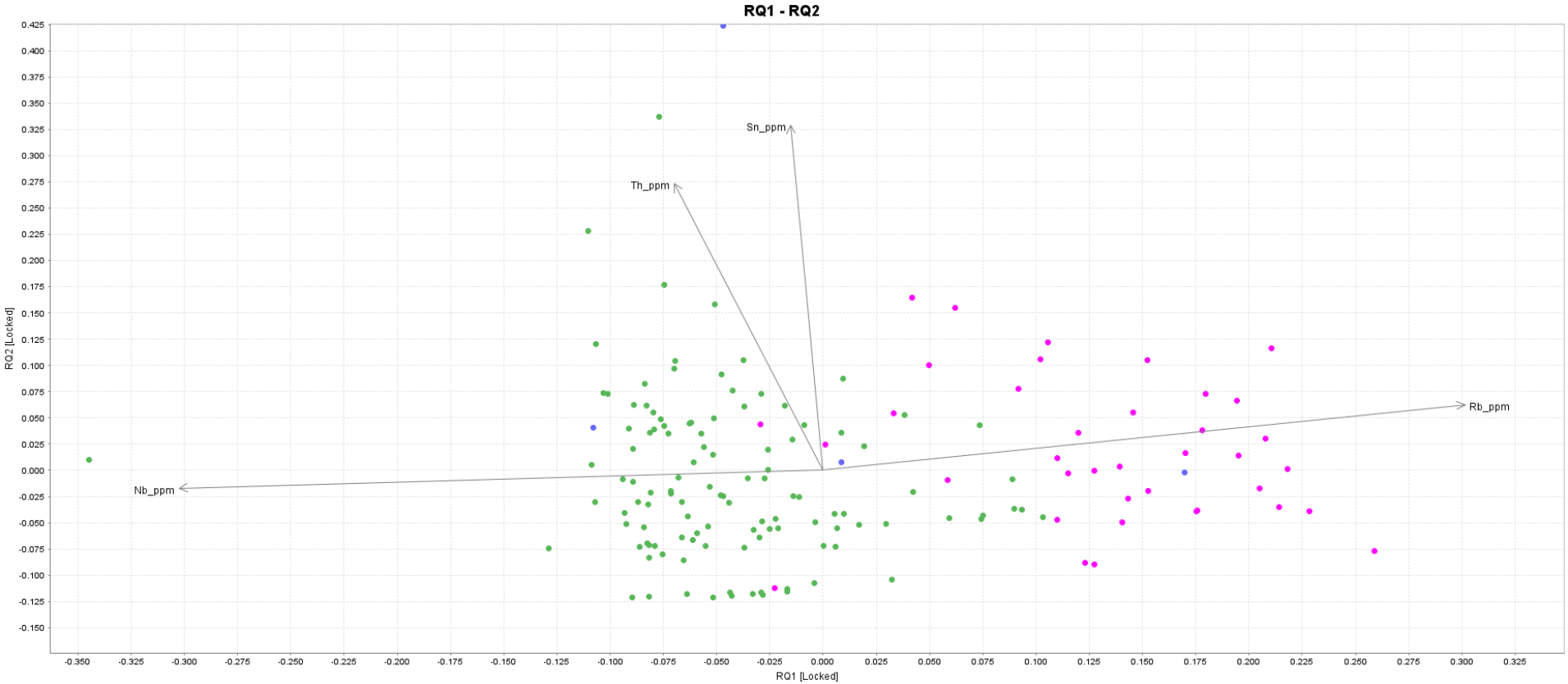


Figure 101. Biplot projecting components RQ1 and RQ2; PCA of group "PATH2".

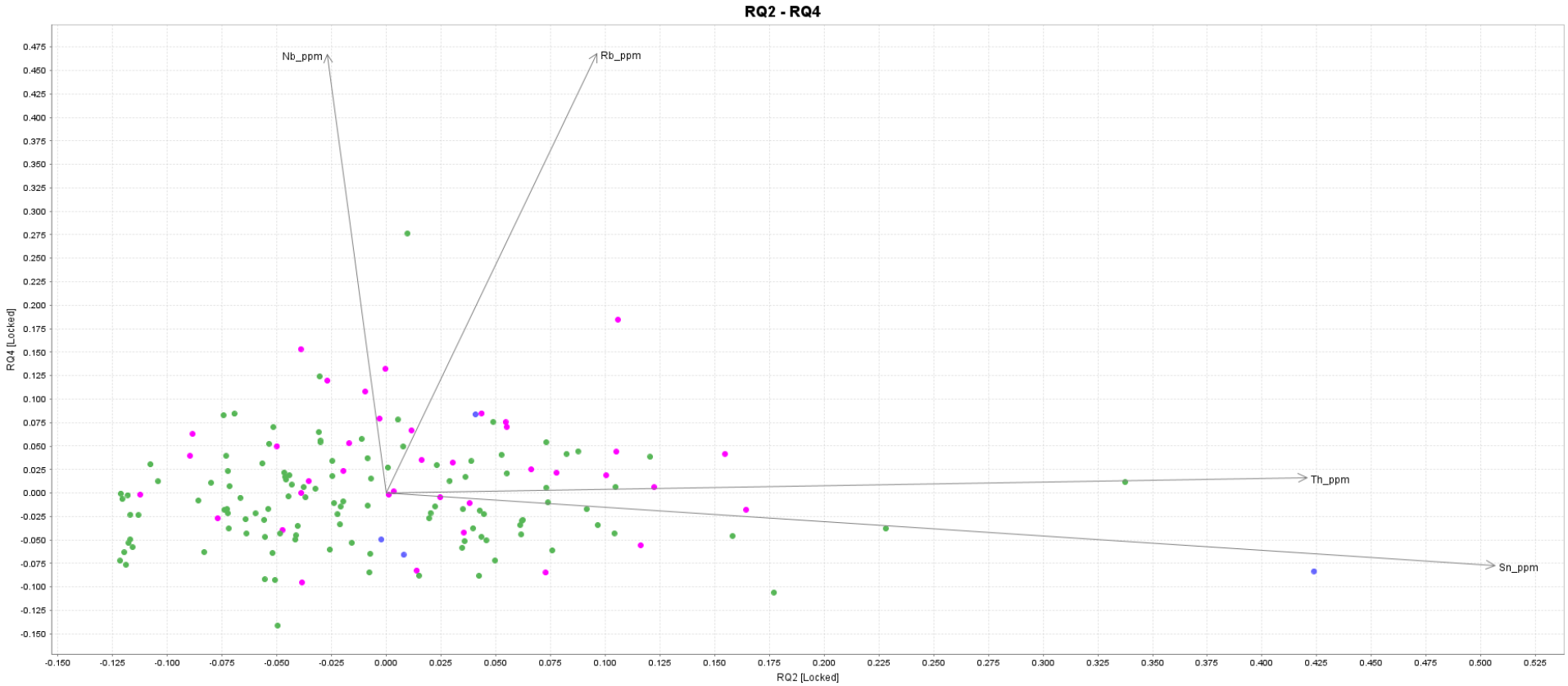


Figure 102. Biplot projecting components RQ2 and RQ4; PCA of group "PATH2".

The 3D biplot of “PATH2” (Figure 103) shows that, overall, granite samples have a higher content of Rb when compared to schist samples; schist samples have higher contents of Sn, Nb and Th; and the highest (negative, in this case) correlations within these four elements is between Sn and Th, and Rb and Nb.

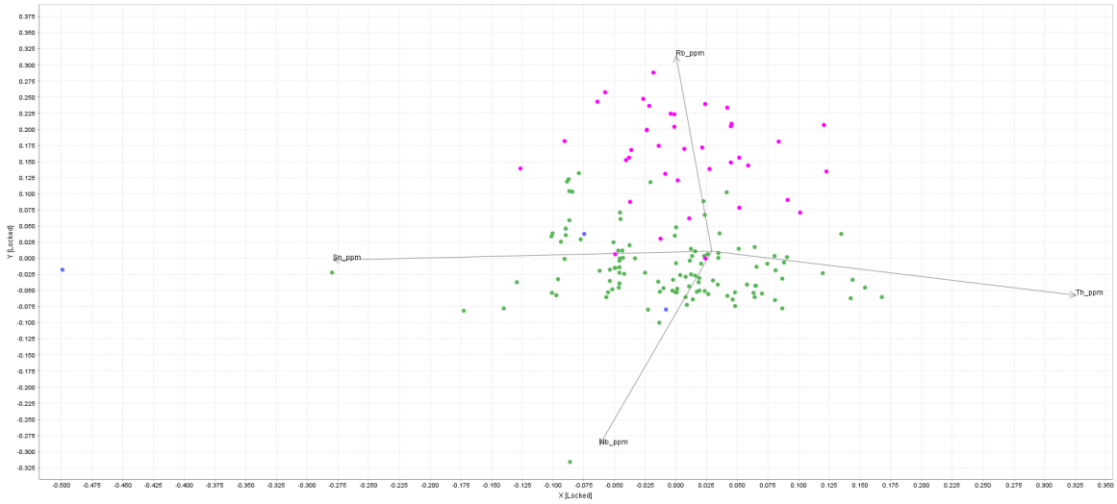


Figure 103. 3D biplot of PCA; group "PATH2".

- Third pathfinder group (“PATH3”) – Al, K, Mn, Rb, Nb, Sn and Th

Analyzing the PCA information of “PATH3”, PC1 accounts for 32.59% of the total variance, PC2 accounts for 21.09%, PC3 for 15.3% and PC4 for 13.04%. PC1 has high eigenvectors for K (0.51) and Rb (0.56). PC2 has high eigenvectors for Al (0.63) and Nb (0.51), PC3 for Sn (0.77) and Th (0.44), such as PC4 (-0.61 and 0.66, for Sn and Th, respectively). K has a high positive correlation with Al (0.47), as well as K and Rb (0.57). Nb and Rb are negatively correlated (-0.46). All the other correlations between the six elements are around zero.

Biplot of components RQ1 and RQ3 (Figure 104) shows that (i) graphic information is, mainly, related to Nb, Mn, Sn, K and Rb (ii) Al, Rb and K are correlated, (iii) Mn, Nb and Th are also correlated, (iv) the correlation between Mn and Nb is close to 1, (v) granite samples have a higher content of Al, Rb and K than the schist samples, (vi) schist samples have higher contents of Nb, Mn and Th when compared to granite samples, (vii) both types of samples have similar Sn contents. Biplot of components RQ1 and RQ2 (Figure 105) shows that (i) most of the graphic information is related to K, Al, Nb, Mn and Rb (ii) Nb and Mn are highly correlated, (iii) Rb and K too, (iv) Th and Al are correlated negatively, (v) granite samples have a higher content of Rb and K than the schist samples, (vi) schist samples have higher contents of Nb, Mn and Th when compared to granite samples, (vii) both types of samples have similar Sn and Al contents.

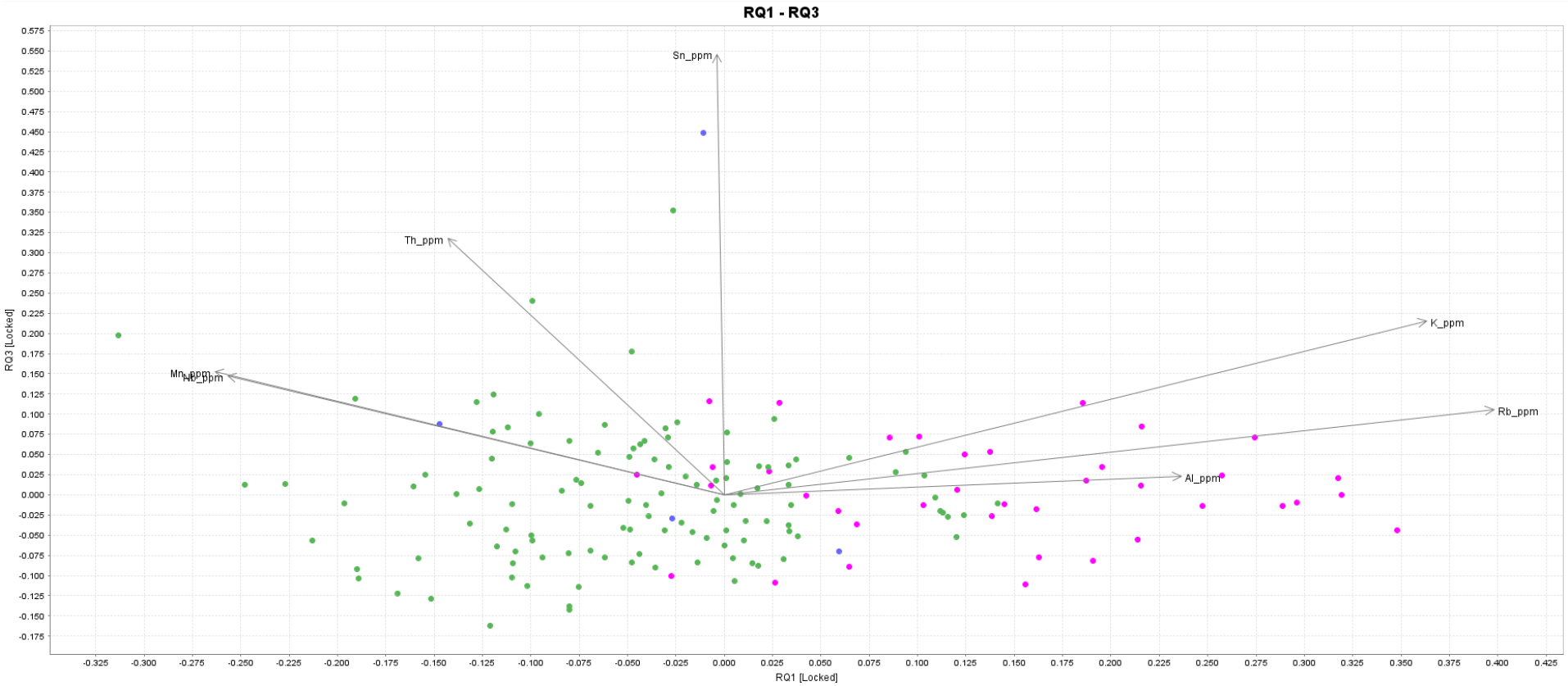


Figure 104. Biplot projecting components RQ1 and RQ3; PCA of group "PATH3".

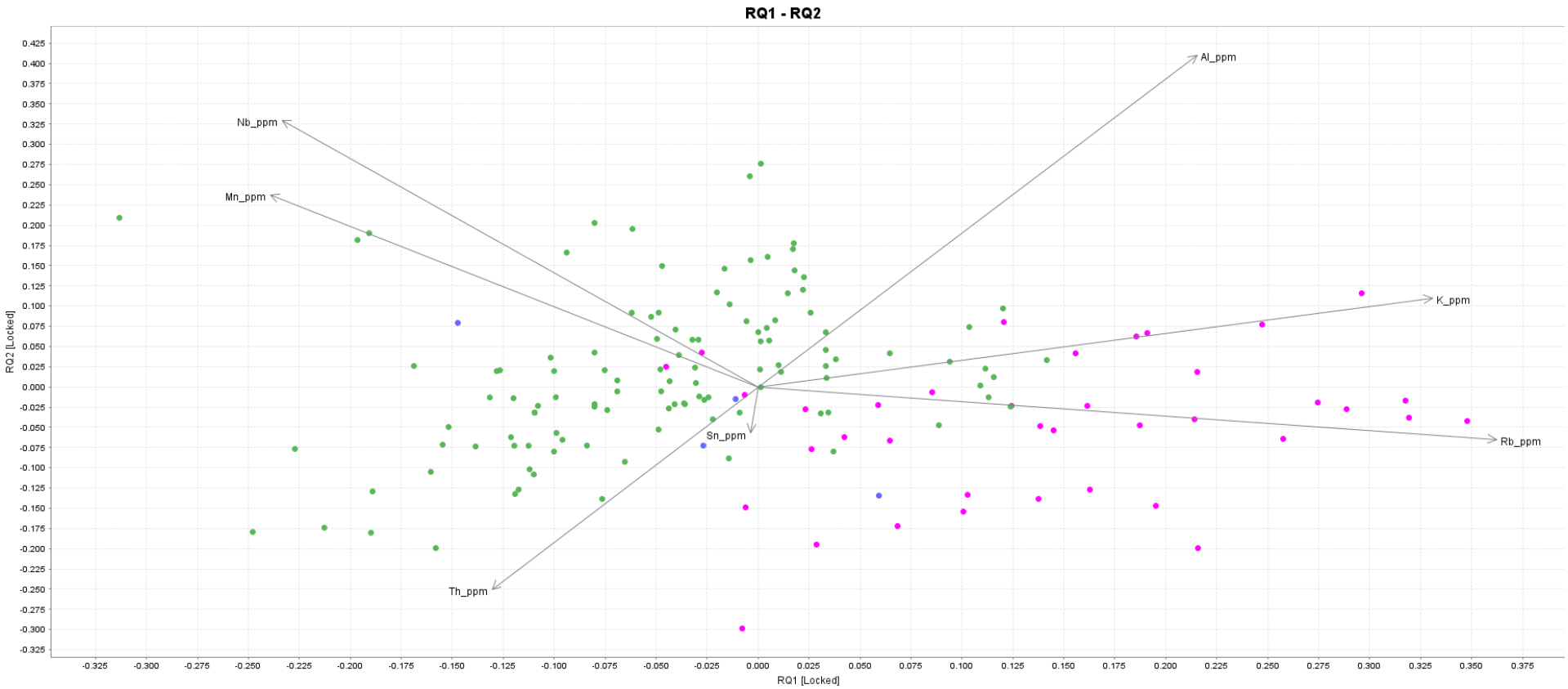


Figure 105. Biplot projecting components RQ1 and RQ2; PCA of group "PATH3".

The 3D biplot of “PATH3” (Figure 106) shows that, overall, granite samples have higher contents of Rb, K and Al when compared to schist samples; schist samples have higher contents of Nb, Mn and Th; Sn contents are similar in granite and schist; and Nb and Mn are very positively correlated.

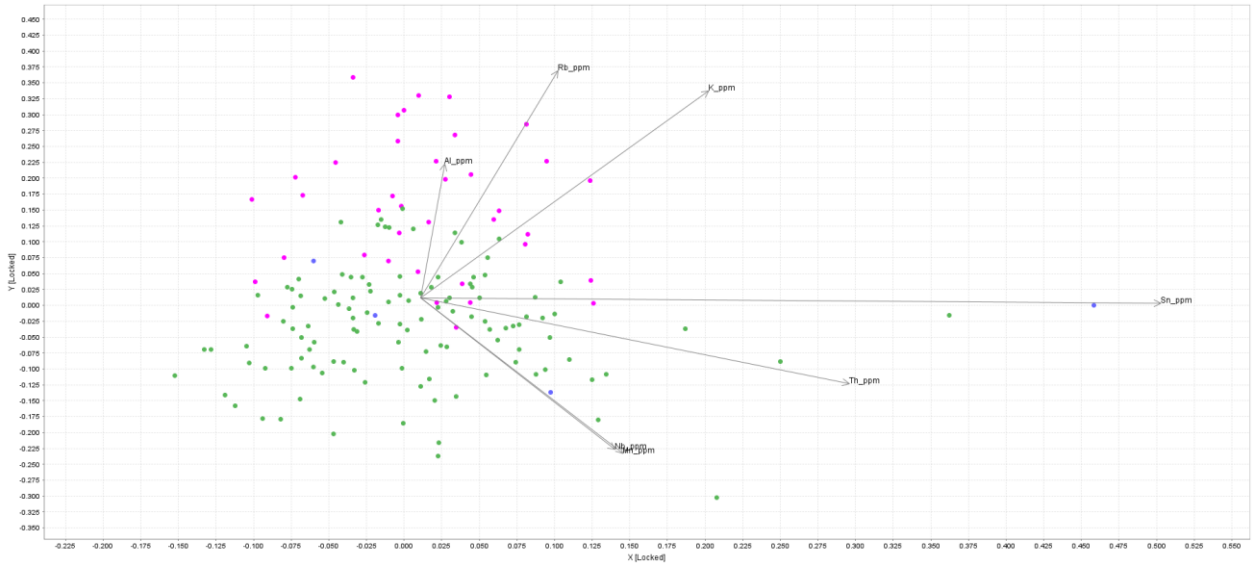


Figure 106. 3D biplot of PCA; group "PATH3".

- Fourth pathfinder group (“PATH4”) – Al, K, Mn, Rb, Nb and Sn

Analyzing the PCA information of “PATH4”, PC1 accounts for 37.17% of the total variance, PC2 accounts for 23.11%, PC3 for 17.01% and PC4 for 10.66%. PC1 has high eigenvectors for K (0.52) and Rb (0.58). PC2 has high eigenvectors for Al (0.67) and Nb (0.53), PC3 for Sn (-0.98), and PC4 for Mn and Nb (-0.82 and 0.48, respectively). K has a high positive correlation with Al (0.47), such as K and Rb (0.57). Nb and Rb are negatively correlated (-0.46). All the other correlations between the six elements are around zero.

Biplot of components RQ1 and RQ2 (Figure 107) shows that (i) graphic information is, mainly, related to Al, K, Mn, Rb and Nb (ii) Sn information is almost not represented, (iii) Al, Rb and K are correlated, (iv) Mn and Nb present a high correlation, (v) granite samples have a higher content of Al, Rb and K than the schist samples, (vi) schist samples have higher contents of Nb and Mn when compared to granite samples, (vii) both types of samples have similar Sn contents. Biplot of components RQ2 and RQ4 (Figure 108) shows that (i) graphic information is, mainly, related to Al, Mn and Nb (ii) Sn information is almost not represented, and (iii) Sn is not correlated to any other element.

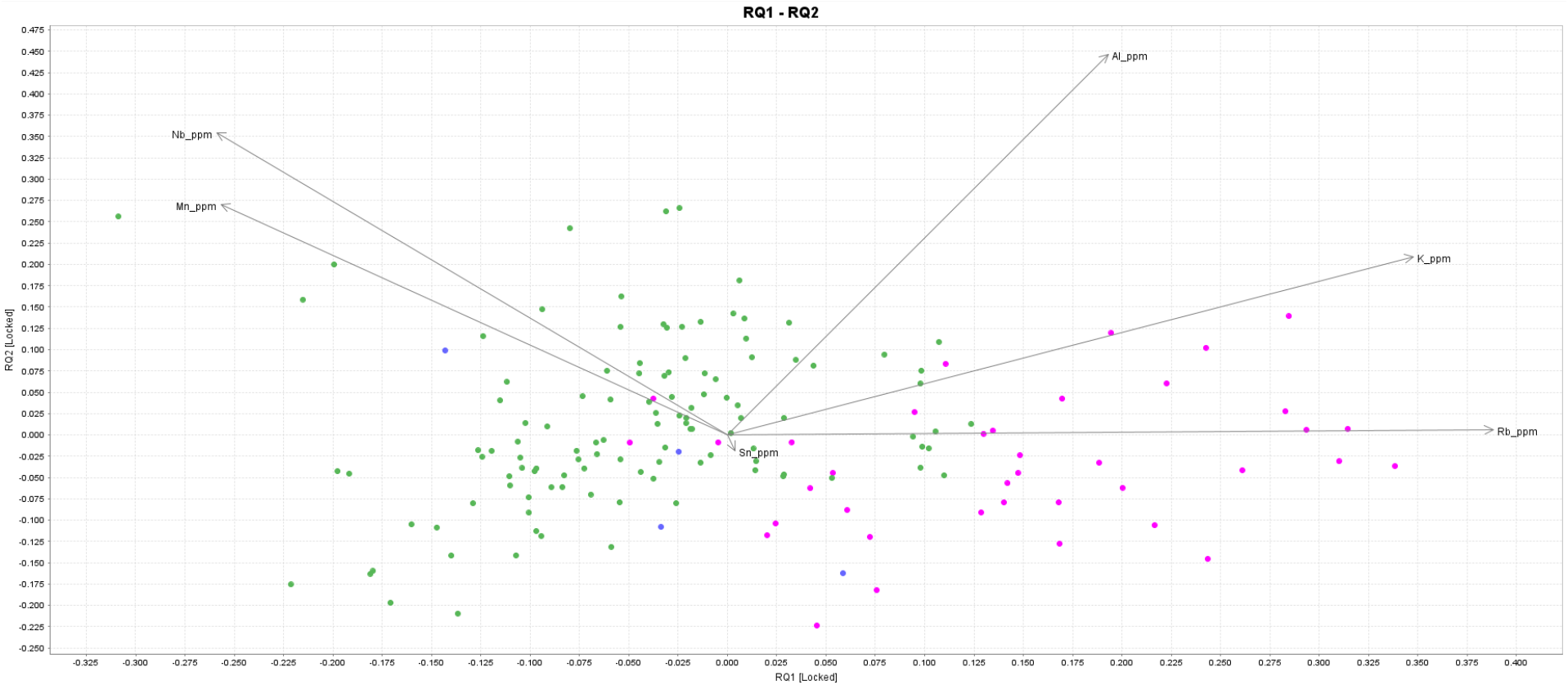


Figure 107. Biplot projecting components RQ1 and RQ2; PCA of group "PATH4".

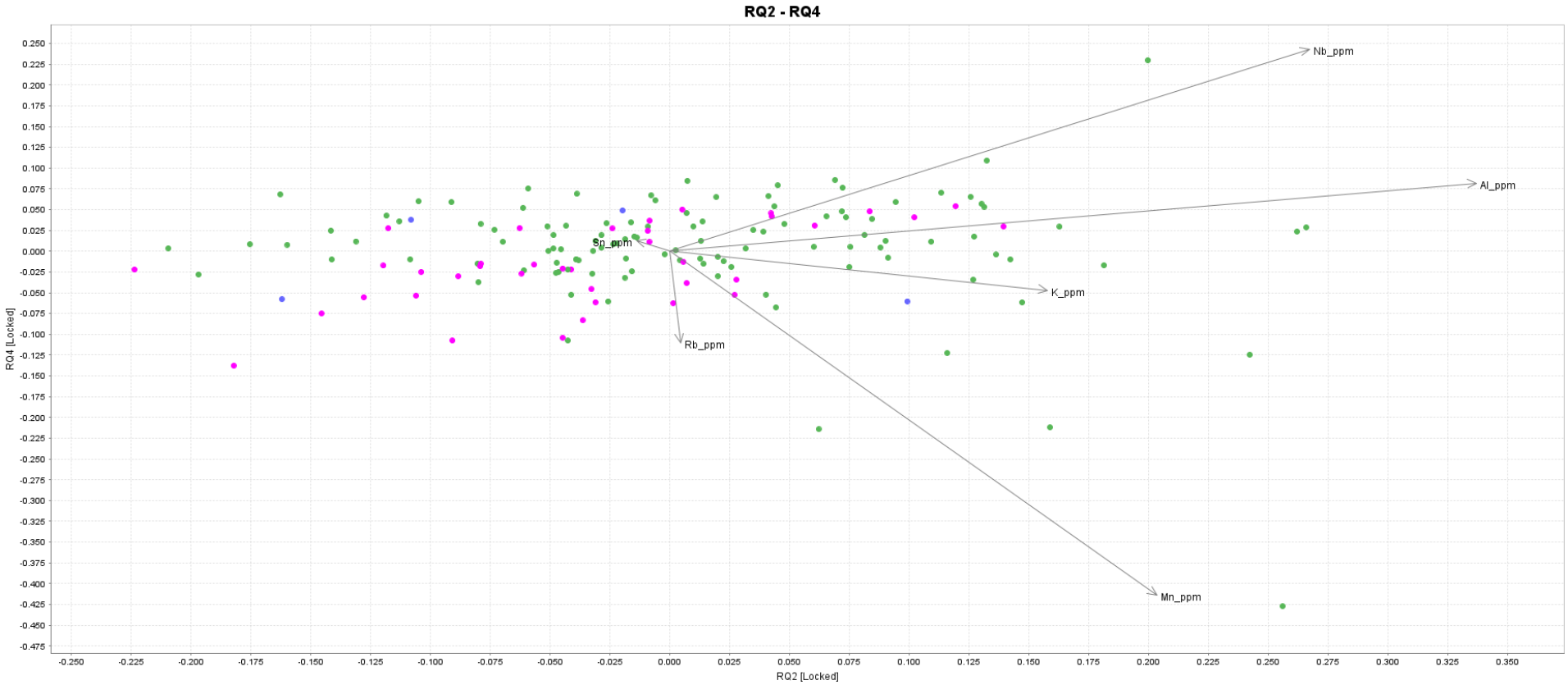


Figure 108. Biplot projecting components RQ2 and RQ4; PCA of group "PATH4".

The 3D biplot of “PATH4” (Figure 109) shows that, overall, granite samples have higher contents of Rb, K and Al when compared to schist samples; schist samples have higher contents of Nb and Mn; Sn contents are similar in granite and schist; and Nb and Mn are very positively correlated, such as K and Rb.

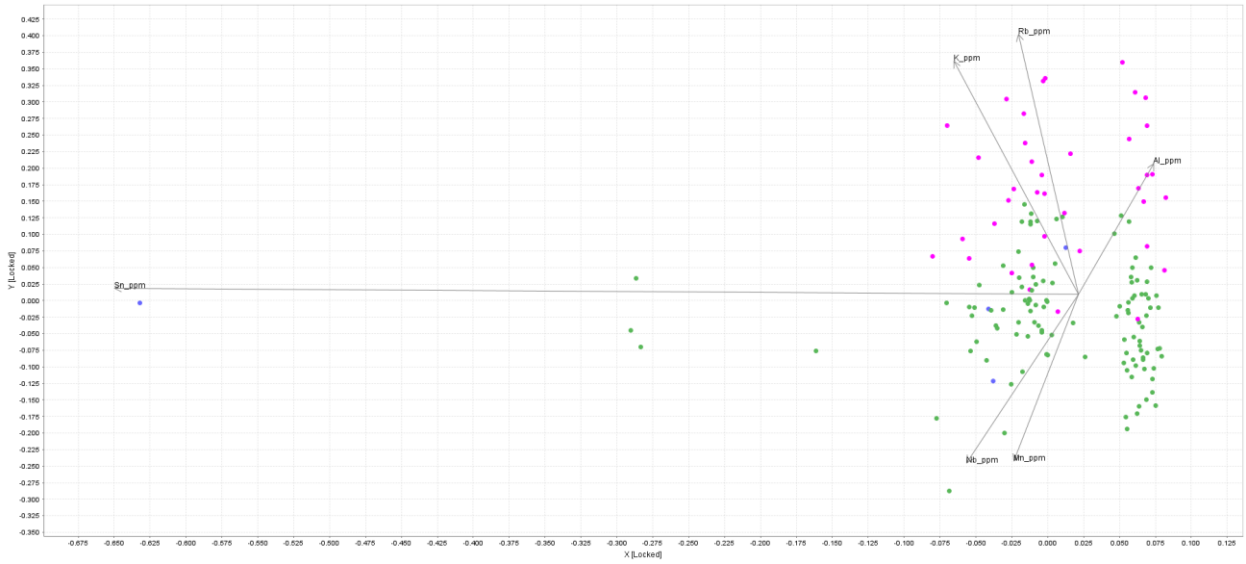


Figure 109. 3D biplot of PCA; group "PATH4".

5.3.2. Anomalies determination and creation of thematic maps

The Anomaly Assessment tool was used to test the capacity to define target areas without discriminating the lithology of each basin. The Tukey upper outlier threshold used in this tool was the one calculated for all the samples in general. Based on the basic statistics, it would be also possible to use the percentiles method to find the anomalies, but the Tukey method is much more robust considering that there are distributions that stray from the normal (Cardoso-Fernandes *et al.*, 2022; Carranza, 2009). The anomaly assessment tool creates a column for each element containing Tukey values (0, 1 or 2). These values indicate which samples have anomalous (1) or very anomalous (2) contents of a certain geochemical element. 0 represents the background. These values are represented in Appendix F.

Thematic maps were created for the selected pathfinders, as shown in figures 110, 111, 112, 113, 114, 115, 116 and 117. For the Tukey maps, the values were categorized into three classes (0 – Background, blue polygons; 1 – Anomaly, yellow polygons; and 2 – High anomaly, red polygons), and for the standardized Tukey maps

the values were set in a gradual scale (in an equal count, based on the quantiles), creating five different categories (Extremely low background, blue polygons; Low background, green polygons; Background, yellow polygons; Anomaly, orange polygons; and High anomaly, red polygons).

Analyzing Al maps (Figure 110-a and -b), it`s possible to see that most of the basins classified as anomalous in the Tukey maps turn into extremely low background basins after the standardization. Conversely, some basins represented as background in the Tukey maps, turn into anomalous basins in the standardized Tukey maps.

The opposite scene is shown in K maps (Figure 111-a and -b), where anomalous basins stayed as anomalous basins after the standardization. Also, a noticeable amount of basins classified as background turned anomalous when standardized.

There are no basins with high anomalies in terms of Al and K.

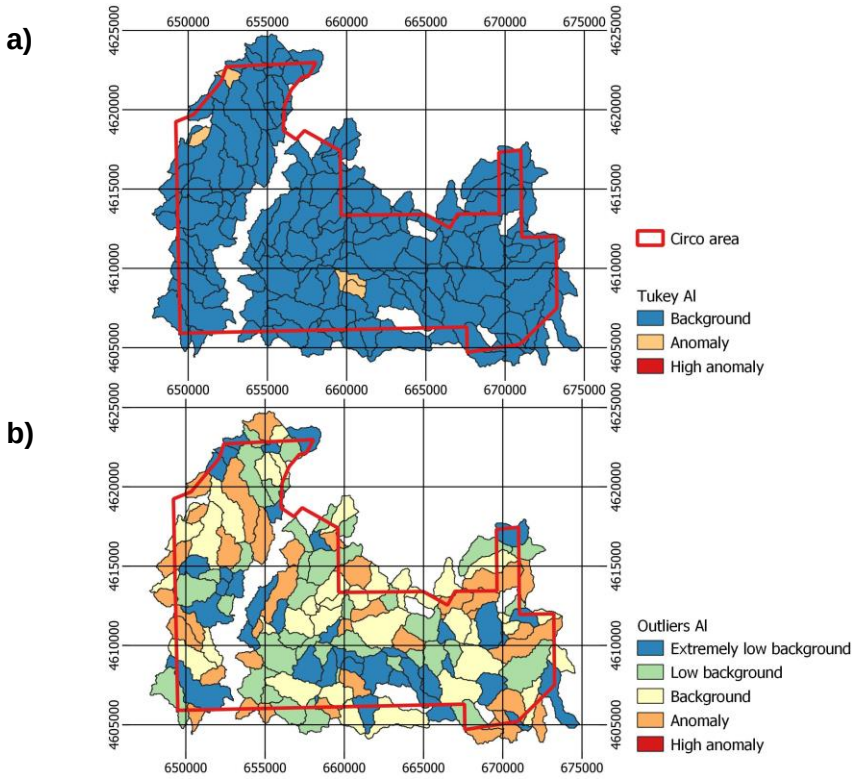


Figure 110. a) Thematic map based on the Tukey values of Al; b) thematic map based on standardized Tukey values of Al.

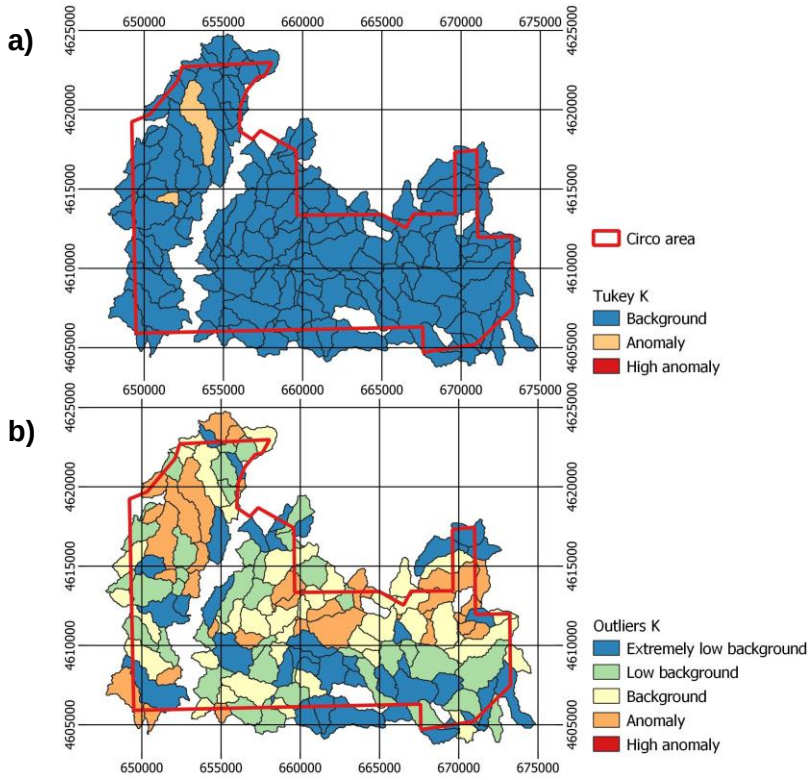


Figure 111. a) Thematic map based on the Tukey values of K; b) thematic map based on standardized Tukey values of K.

The Mn maps (Figure 112-a and -b) show that basins with high anomalies represented in the Tukey map stayed represented as highly anomalous basins after standardization, and some anomalous basins turned highly anomalous.

In the Nb maps (Figure 113-a and -b), anomalous basins in the granites changed into background when standardized, and in the metasediments, a lot of background basins were transformed into anomalous basins after the standardization.

In both cases, highly anomalous basins appear in both lithologies.

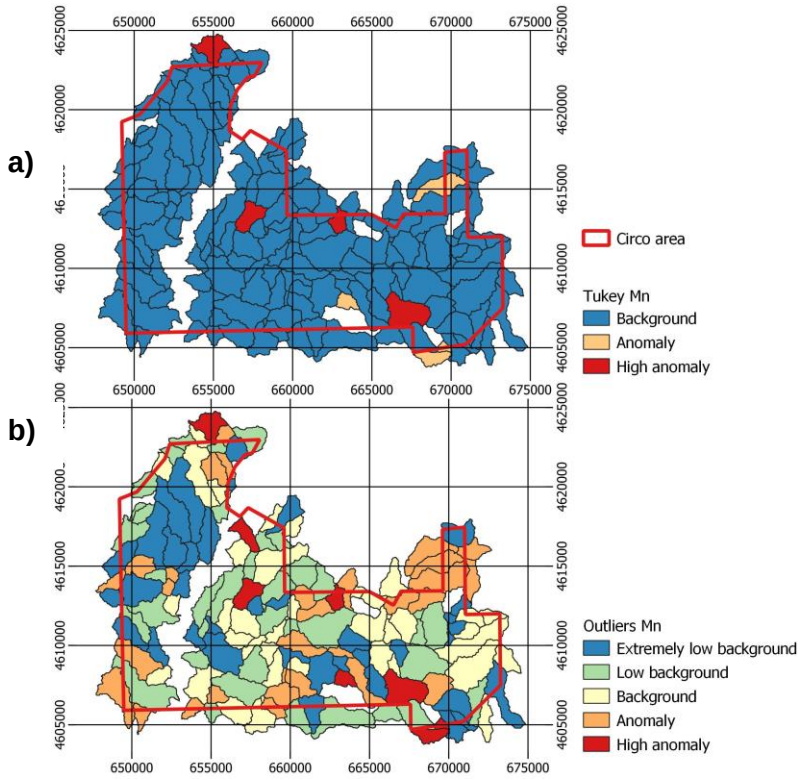


Figure 112. a) Thematic map based on the Tukey values of Mn; b) thematic map based on standardized Tukey values of Mn.

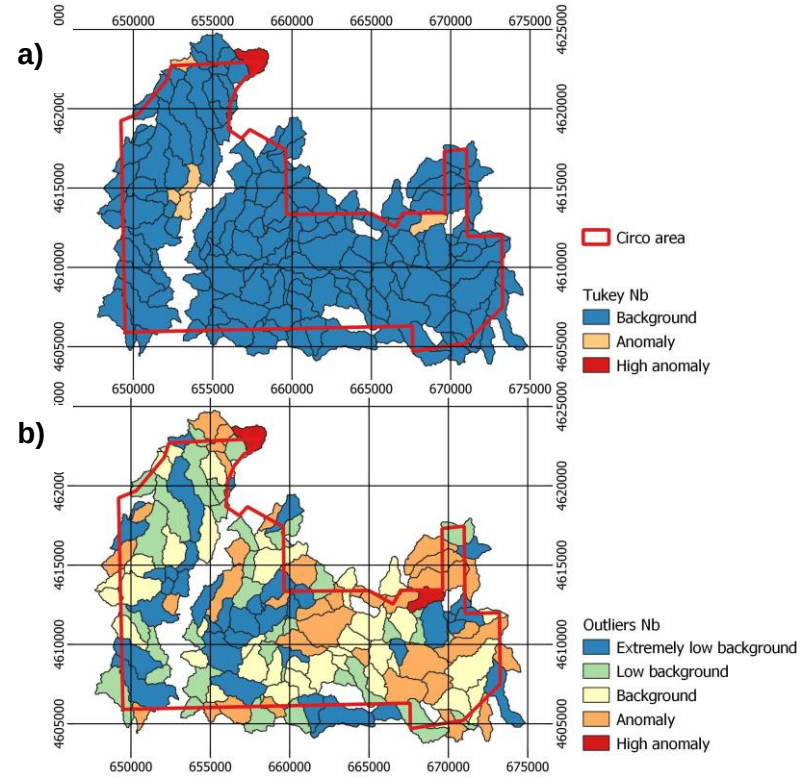


Figure 113. a) Thematic map based on the Tukey values of Nb; b) thematic map based on standardized Tukey values of Nb.

In the case of Rb (Figure 114-a and -b), Tukey values did not classify any basin as highly anomalous. Interesting to see that, after standardization, a background basin near the contact of the granites and the metasediments, turned into a highly anomalous basin.

The Sn maps (Figure 115-a and -b) show that basins with high anomalies only appear in the metasediments, and after standardization, one basin in the southeast part of the map that was anomalous turned highly anomalous. XRF results showed a considerable number of measures <LOD.

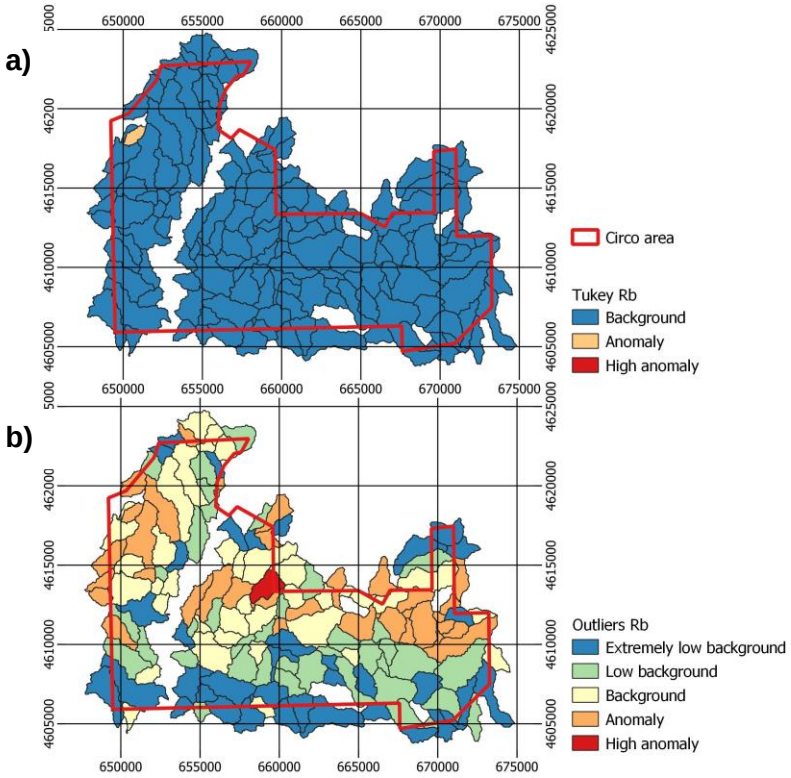


Figure 114. a) Thematic map based on the Tukey values of Rb; b) thematic map based on standardized Tukey values of Rb.

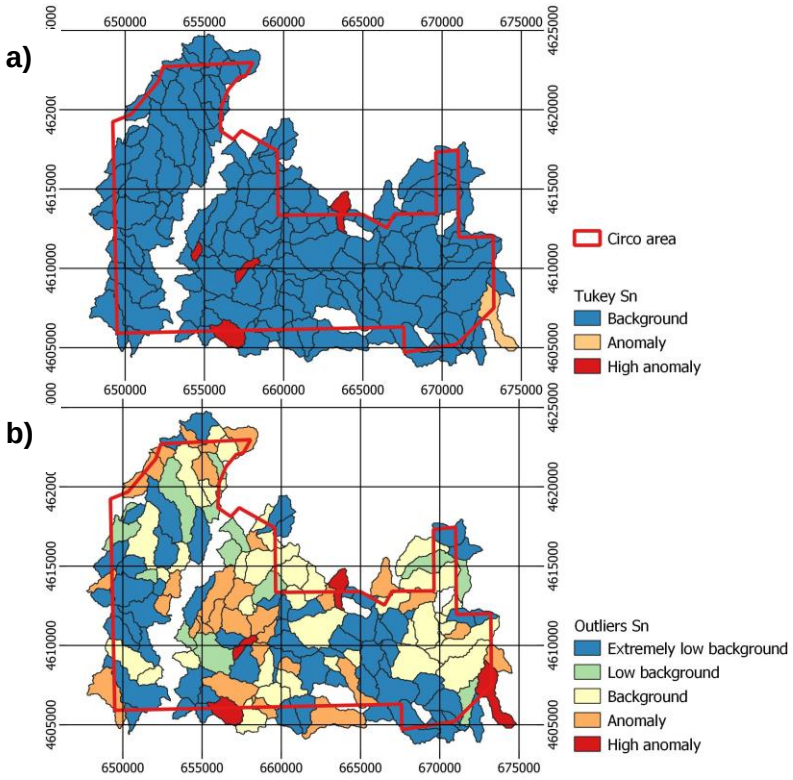


Figure 115. a) Thematic map based on the Tukey values of Sn; b) thematic map based on standardized Tukey values of Sn.

There are no anomalous basins in the Th maps (Figure 116-a and -b). After standardization, some basins turned into anomalous in both lithologies.

For W (Figure 117), it was impossible to create a map based on standardized Tukey values because the IQR was zero. The majority of measures done for W were <LOD, so the map is not representative of the real values. The anomalous basins are just the ones that measured some value. High anomalous basins represented in the map are classified as anomalous because all the other basins are <LOD (in this case replaced by 2.5).

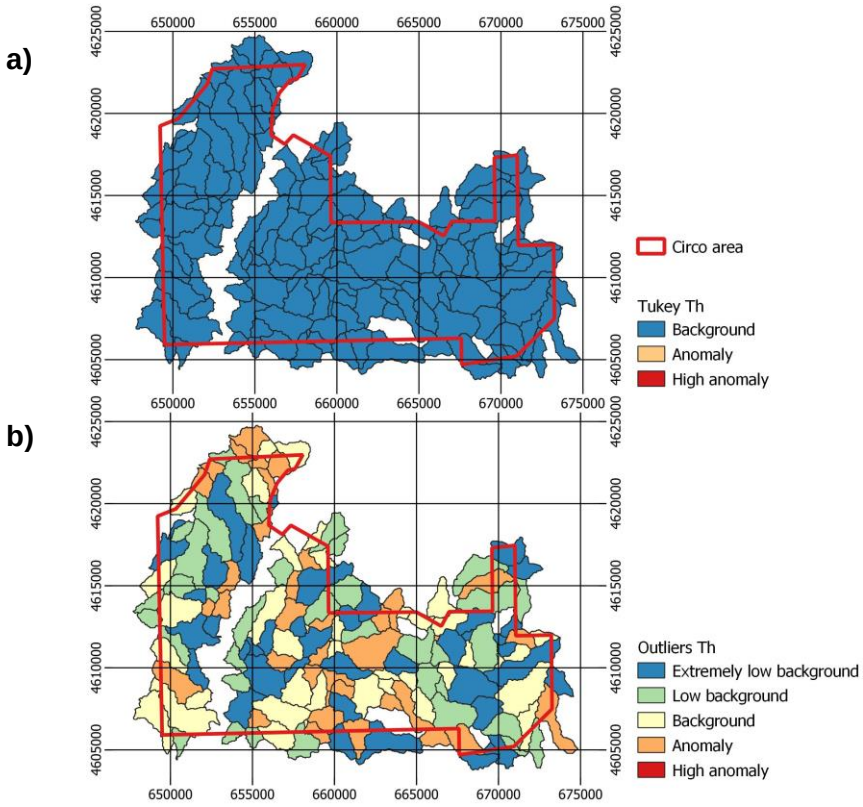


Figure 116. a) Thematic map based on the Tukey values of Th; b) thematic map based on standardized Tukey values of Th.

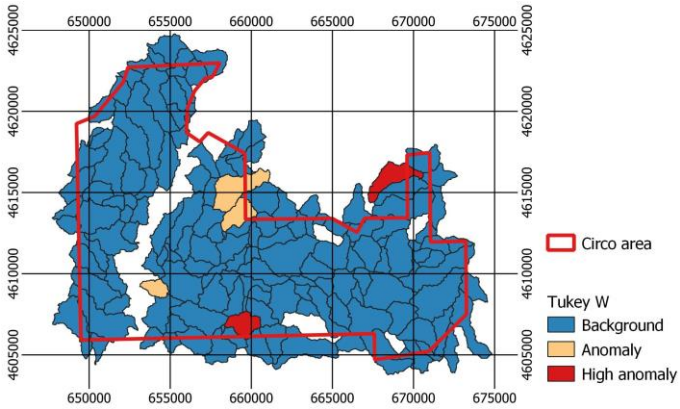


Figure 117. Thematic map based on the Tukey values of W.

6. Discussion

6.1. Remote Sensing

RGB COMBINATIONS

All the RGB combinations of Landsat-9 were self-proposed based on Landsat-8 literature. RGB combinations 2-5-7 and 2-8-12 for Landsat-9 and Sentinel-2 (Figure 35), respectively, were made to map iron oxides and clay minerals. According to Ali & Pour, 2014, the equivalent of RGB 2-5-7 combination for Landsat 8 mapped iron oxides in dark blue color. Both combinations made good discrimination of the granites and the metasediments. The colors are the same in both images, the granites appearing in bright purple to blue color, the metasediments in pink to blue color, and the selected sites (Ervedosa mine, Rebordelo exploration and “Palão” quarry) are presented in a pink color (light pink in Sentinel-2 and bright pink in Landsat-9) with some white areas within it (probably due to simultaneous presence of clay minerals and iron oxides or a mixture of signals from other minerals). Dark/intense blue areas appear in both granite and metasediments, the latter corresponding mainly to agricultural fields. This shows that, in general, granites are richer in iron oxides.

To map hydrothermally altered rocks, RGB combinations 5-7-3 (for Landsat-9) and 8-12-3 (for Sentinel-2) were also applied (Figure 36). According to Mia & Fujimitsu, 2012, the equivalent of RGB 5-7-3 combination for Landsat-7 ETM+ mapped hydrothermally altered rocks in intense green and blue colors. Again, both combinations showed the difference between both lithologies, presenting the granites in light to medium green and the metasediments mainly in blue to purple. Areas with a deep green tint appear in both granitic and metasedimentary zones indicating hydrothermal alteration. The selected sites appear in a bluish tint that may also indicate hydrothermal alteration. Spectral studies must be done to understand and interpret these images and the cause for this response in both lithological groups.

An attempt to discover Li-mineralizations was done in two sets (based on Cardoso-Fernandes et. al. 2019). The first one using the RGB combination 7-3-11 for Landsat-9 (Figure 37) and the second (Figure 39) using the combinations 3-2-11 (Landsat-9) and 3-2-12 (Sentinel-2). The first set (combination 7-3-11) shows the granites (purple color) distinguished from the metasediments (blue color). Li-bearing pegmatites should appear in a yellowish-green or green color, which happens in all the selected sites and in some other zones. In the second set, RGB combination 3-2-11 of Landsat-9 imagery

could not discriminate between the two lithologies (both appearing in blue) but the same spots appeared in a yellowish color. The second combination of set two (3-2-12) shows granites in blue and metasediments in yellow. Selected zones appear in white to yellow color, but present low contrast, opposed to the observed in the other combinations. After field validation, we can conclude that: (i) combinations 7-3-11 and 3-2-11 highlight quartz areas and, in the case of T39, a farm where the soil has been man disturbed with new cultivation terraces (i.e. fresh soil).

RGB combinations 6-7-4 (Landsat-9) and 11-4-12 (Sentinel-2) were tried to help the geological mapping activity (Figure 40 and Figure 41). Both lithologies were well distinguished (with other nice contrast colors) but not bringing new information not seen in other combinations before. Thus other combinations can highlight the difference in the lithologies, besides the combinations specific for lithological contrast.

As stated by Cardoso-Fernandes et. al., 2019, and as has been seen throughout the work, RGB combinations are the most difficult technique to interpret/understand, due to a mixture of signals from different minerals that creates a mixture of colors often quite different from the results in the bibliography.

BAND RATIOS

All the band ratios of Landsat-9 were self-proposed based on Landsat-8 literature. Band ratios were also applied to discriminate iron oxides and ferric iron (4/2 and 4/3 for both sensors; Figure 42 and Figure 43). It is noteworthy that the ratios employed were not sensible to the compositional differences between the lithologies. Both ratios and sensors highlighted the same areas. Urbanized areas and agricultural fields were discriminated with high ferric iron. This can happen because: (i) these areas can have a similar response to iron oxides or (ii) the agricultural fields are in fact enriched in ferric iron due to agricultural fertilizers and/or the presence of rusted materials. A highly prominent area was T2, which corresponds to a Quaternary deposit (according to Silva and Ribeiro (1991, 1994), these sedimentary deposits certainly contain iron oxides). The selected zones don't discriminate any content of ferric iron/iron oxides.

Band ratios 6/5 (Landsat 9) and 11/8 (Sentinel-2) were applied to discriminate ferrous minerals (Figure 44). Overall, ferrous minerals ratios show higher content in the granites when compared to metasedimentary rocks (this is explained by the presence of biotite, a ferromagnesian mineral that is easily weathered). The selected zones do not present signs of any content of ferrous minerals.

To map alunite and clay minerals (kaolinite and montmorillonite), band ratios 6/7 (for Landsat-9) and 11/12 (for Sentinel-2) were used (Figure 45). As expected, higher contents of these minerals appear near the water streams and in the metasediments compared to the granites. Selected areas do not show any content of alunite and clay minerals.

Attempting to find Li-mineralizations using band rationing, ratios 3/8 and 3/5 (for spodumene; Figure 46), and 4/12 and 4/7 (for lepidolite; Figure 47) were employed. The first two band ratios highlighted exactly the same areas as the ones emphasized by the RGB combinations 7-3-11 and 3-2-11, which means that these ratios also highlight mainly quartz-enriched fields. The second two ratios highlighted the farm (T39), and show a very low content of lepidolite in the granites when compared to the metasediments. Selected areas are still emphasized by these four ratios.

In general, band ratios were easier to interpret but present less information since they only use spectral information of two bands. The performance of Landsat-9 and Sentinel-2 was similar.

PCA

PCA were applied to certain bands based on Landsat-8 literature. PCA presented the best performance in this study, being a good tool to define lithology, map iron/oxides, map hydroxyls, and other features. For example, RGB combinations PC1-PC4-PC5 were made for each sensor (Figure 48). These are the images that show the most information and better discriminate all the geology and land occupation of the area. The combination identified hydroxyl-bearing minerals in light blue color (mainly in fields with small water channels), iron oxides as dark blue colors (which showed a response in the quaternary deposit), and also allowed to find a burned zone outside the area (intense red), which consequently led to the identification of other burned areas.

In an attempt to map iron oxides, hydroxyls and Li-bearing minerals, three Selective PCA images were produced, for each sensor. Each Selective PCA was based on a subset of bands capable of discriminating those minerals. Selective F bands (Figure 53) map ferric iron/iron oxides, while Selective H bands (Figure 52 and Figure 53) and Selective Li bands (Figure 54) map hydroxyl minerals and Li-bearing minerals, respectively. None of these bands identified a high content of the mentioned minerals in the Ervedosa mine, Rebordelo exploration and “Palão” quarry. Nonetheless, these bands highlighted other zones, which were considered for field validation. Selective H band represented lightly altered granitic soils (with water infiltration) and recently

plowed fields (with small water channels too), the selective F band represented the same areas as the band ratios of ferric iron (showing reddish soils with quartz) and the selective Li band identified quartz fields, burned areas and a quartzphyllite with quartz veins. All three bands showed the expected zones with high content of ferric iron, hydroxyls and quartz, respectively for each band.

SAM

The SAM algorithm was applied to make a correlation with Rebordelo exploration and Ervedosa mine, i.e., to identify areas with similar spectral behavior. The approach resulted in two target maps (Figure 57 and Figure 58) that intersected areas selected from the other remote sensing techniques (Figure 59). The zone with a more intense response was, again, the farm with fresh soil. As expected, the "Palão" quarry presented a similar spectral response. The selected areas for field validation based on the SAM analysis proved to be mainly quartz fields.

Lineament extraction

When referring to the extracted lineaments (Figure 60), they seem to be divided into two main classes: NNE-SSW trending and WNW-ESE trending (Figure 61). As stated by Noronha et al., 2006, the D3 phase developed large open folds with sub-vertical axial planes and a WNW-ESE orientation, and Post-D3 late phases developed a ductile-brittle and brittle regime, responsible for two conjugates fractures, including NNE-SSW sinistral faults. This method proved to be a powerful tool when it comes to structural mapping, even though it did not discriminate all the existing faults (probably because of urbanized areas). There was no time during the internship to validate these structures in the field, but future works could help update the geological maps and understand the area.

Targets analysis

From the collected samples of remote sensing targets, only T14 and T26 stand out considering Li contents. T14 sample is a banded (mica)-schist rock outcrop located in the vicinity of reddish soils and T26 is a plowed field containing reddish soil with quartz and schist.

6.2. Geological mapping

A map (at scale 1:95 000) was made based on the remote sensing data/techniques and geological field mapping. The objective of creating a map at the scale of 1:25 000 was not fulfilled, but the produced map is satisfactory considering the previously

delineated goals, especially when compared to the 1:200 000 geological map. Remote sensing only allowed distinguishing two types of rocks: granite and metasediments. The contacts between both these rocks are precisely well marked. Overall, granite facies and metasediments units could not be discriminated.

Rocks and targets samples collection did not provide new information, but confirmed some units represented in existing maps, for example, the upper quartzites formation (southeast part of the area) and the Quaternary deposit (south of the granites). The produced map does not completely satisfy the initial goal, but it proves that remote sensing can at least identify some lithologies and units with precision.

6.3. Stream sediments analysis

The geochemical results of each sample were obtained via XRF analysis, which was not planned at the beginning of the study. Again, due to weather conditions and the high risk of fire during July, August and September, the stream sediments campaign got delayed and ALS results did not arrive in time to use them. XRF results are not as accurate as any data from a specialized laboratory.

Basic statistics and graphics analysis proved that elements such as W, Nd, Bi and Sn have standard deviations higher than the mean, this happens due to the influence of the LOD. Since a lot of measures made for these elements are <LOD, normal content measures are, subsequently classified as outliers. This also proves that those elements present distributions far from the normal. Overall, granite showed higher contents of Al, P, K, Ca, Rb and Pb, while metasediments presented higher contents of Mg, Ti, Cr, Mn, Fe, Ni, Cu, Y, Zr, Nb, Ba and Nd (Figure 87 and Figures in Appendix B).

Pathfinders were selected based on bibliography and Pearson correlation matrices. Th was the only element with a possible correlation to LE (the correlation to light elements was made because Li is within it). Sn, Rb and Nb were selected according to Cerný and Ercit, 2005; Simmons and Webber, 2008; Roda-Robles et al., 2018; and Cardoso-Fernandes et al., 2022 and Mn, K, and Al based on Cardoso-Fernandes et al., 2020; Cardoso-Fernandes et al., 2022; and Roda-Robles et al., 2018. W was also selected but that was not a good pathfinder to use, again because of the LOD influence.

From the eight selected pathfinders, Al, K and Rb present higher contents in the granites, as can be proven by the graphics and maps (Figure 90, Figure 91 and Figure

94). Metasediments have higher contents of Mn and Nb (Figure 92 and Figure 93). Analyzing the graphics of these elements we can see a separation of both populations.

The analyzed bibliography states that Mn, Al and K are correlated, such as Nb, Sn and Rb. The first group of pathfinders shows a negative correlation between Nb and Rb in PC1 and a positive one for Sn and W in PC2. PC3 and PC4 identify a negative correlation between Sn and W, and a positive correlation between Rb and Nb, respectively. This information reveals that in most of the samples the correlation between Rb and Nb is negative, while Sn and W correlate positively. A lower number of samples exhibit a positive correlation of Nb and Rb and a negative correlation of Sn and W. Most of the biplots (Figure 98 and Figure 99) and the 3D biplot (Figure 100) represent a good separation between both lithologies, where the granites have higher contents of Rb.

The second group of pathfinders shows a negative correlation between Nb and Rb in PC1 and a positive one for Sn and Th in PC2. PC3 and PC4 identify a negative correlation between Sn and Th, and a positive correlation between Rb and Nb, respectively. Thus, this group did not contribute with additional information.

The third group of pathfinders detected positive correlations for K-Rb, Al-Nb, Sn-Th in PC1, PC2 and PC3, respectively. Negative correlations can be found in PC4 (Sn and Th), PC5 (Mn and Nb), PC6 (K and Rb) and PC7 (Rb and Nb are not correlated to Al). This information states that most of the samples present a positive correlation between K and Rb, as well as Al and Nb and Sn and Th. A lower number of samples reveal negative correlations of these pairs of elements: Sn-Th, Mn-Nb, K-Rb and Al-Rb/Nb. Most of the biplots (Figure 104 and Figure 105) and the 3D biplot (Figure 106) represent a separation between both lithologies, where the granites have higher contents of Rb and K, while the metasediments are more enriched in Nb and Mn.

In the fourth group of pathfinders, positive correlations K-Rb, Al-Nb and Rb-Nb can be found in PC1, PC2 and PC6, respectively. PC3 to PC5 present negative correlations between Al and Sn, Mn and Nb and Al and K. This information tells that in most of the samples the correlation between K and Rb is positive as well as correlations Al-Nb and Rb-Nb. Granites seem to be more enriched in K, Rb and Al.

Groups “PATH1” and “PATH2” demonstrated the correlation between Rb and Nb stated in the bibliography. The other groups did not present any of the expected correlations.

Standardized maps are more reliable when compared to Tukey maps because they are not as affected by the lithological background. Sn, W and Th maps (Figure 115, Figure 117, Figure 116) do not have good statistical representativeness due to measures <LOD affecting the results. Although all elements have anomalous basins, the following elements stand out as having extremely anomalous basins: Mn, Nb and Rb (Figure 112, Figure 113, Figure 114). Very anomalous basins of these three elements are distributed over the granites and the metasediments (in the case of Mn); one basin in each lithology (for Nb); and one basin near the contact between the two lithologies (in the case of Rb). Considering all the results, the most favorable variables for future field investigation were Nb and Rb, given the correlation found through PCA.

7. Conclusions

- Geological contacts, burned areas and lineaments can be well identified using remote sensing techniques.
- PCA was considered the best remote sensing method in this study, in terms of quality and quantity of obtained information. Methods to find hydroxyl minerals showed a good response, identifying fields with clay minerals. Methods to find iron oxides also worked properly, recognizing reddish soils and a Quaternary deposit.
- Methods to find Li-bearing pegmatites did not show quality results, once they mainly responded to fields with a lot of quartz floats. However, one of the favorable targets (T26) was found by the response of the band ratio to map lepidolite.
- After the field validation, it is possible to conclude that the results produced by the remote sensing methods have showed low valid targets, due to pixel size, high vegetation coverage, etc. , It should be noted that the study area is a green field for Li minerals, being also a possibility for the low returning of valid field targets
- The influence of the values obtained <LOD compromised the creation of targets based on certain elements, classified as pathfinders, such as Sn, W and Th.
- Anomaly definition based on XRF data is not the most appropriate method since XRF does not measure Li. However, correlations between XRF data and ALS results will allow identifying if, in fact, Nb and Rb are good pathfinders and help to analyze the XRF results in the preliminary stages of exploration.
- Most of the basins classified as background were changed to anomalous basins after the IQR standardization, which proves a higher capacity for delineating anomalous basins. In some cases, anomalous basins were changed to background basins, demonstrating that the IQR standardization is also effective in mitigating the effect of the lithologic background.
- Overall, it was possible to achieve the initial goal of identifying field targets based on all approaches although not all targets were validated.
- For next steps, anomalous basin should be validated in the field; the geological map should be completed to produce maps at scale 1:25 000; and the stream sediments analysis should be performed based on the ALS results.

8. References

Ali, A., & Pour, A. (2014). Lithological mapping and hydrothermal alteration using Landsat 8 data: a case study in ariab mining district, red sea hills, Sudan. *International Journal of Basic and Applied Sciences, 3*(3). doi: 10.14419/ijbas.v3i3.2821.

Bachri, I.; Hakdaoui, M.; Raji, M.; Teodoro, A.C.; Benbouziane, A. (2019). Machine Learning Algorithms for Automatic Lithological Mapping Using Remote Sensing Data: A Case Study from Souk Arbaa Sahel, Sidi Ifni Inlier, Western Anti-Atlas, Morocco. *ISPRS Int. J. Geo-Inf.*, *8*, 248. https://doi.org/10.3390/ijgi8060248

Ballèvre, M., Martínez Catalán, J. R., López-Carmona, A., Pitra, P., Abati, J., Fernández, R. D., Ducassou, C., Arenas, R., Bosse, V., Castiñeiras, P., Fernández-Suárez, J., Gómez Barreiro, J., Paquette, J.-L., Peucat, J.-J., Poujol, M., Ruffet, G., Sánchez Martínez, S., Schulmann, K., Martínez Catalán, J. R., Oggiano, G. (2014). Correlation of the nappe stack in the Ibero-Armorican arc across the Bay of Biscay: a joint French–Spanish project. In *The Variscan Orogeny: Extent, Timescale and the Formation of the European Crust* (Vol. 405, pp. 0). Geological Society of London. https://doi.org/10.1144/sp405.13

Bolton, T., (1989). Geological maps, their solution and interpretation. Cambridge University Press, 144 pp.

Cardoso-Fernandes, J. (2018). Remote sensing applied to the Bajoca lithiniferous area. Tese de Mestrado.

Cardoso-Fernandes, J., Lima, A., Roda-Robles, E., & Teodoro, A. (2019). Constraints and Potentials of Remote Sensing Data/techniques Applied To Lithium (li)-pegmatites. *The Canadian Mineralogist*, *57*, 723-725. https://doi.org/10.3749/canmin.AB00004

Cardoso-Fernandes, J., Lima, A., Roda-Robles, E., Ribeiro, M. A., & Teodoro, A. (2020). *Geochemical pathfinder analysis for lithium (Li) exploration in the Iberian Peninsula.* Paper presented at the X Congresso Jovens Investigadores em Geociências, LEG, Estremoz, 12-15.

Cardoso-Fernandes, J., Lima, J., Lima, A., Roda-Robles, E., Köhler, M., Schaefer, S., Barth, A., Knobloch, A., Gonçalves, M. A., Gonçalves, F., & Teodoro, A. C. (2022). Stream sediment analysis for Lithium (Li) exploration in the Douro region (Portugal): A comparative study of the spatial interpolation and catchment basin approaches.

Journal of geochemical exploration, 236, 106978. doi: https://doi.org/10.1016/j.gexplo.2022.106978.

Cardoso-Fernandes, J., Silva, J., Dias, F., Lima, A., Teodoro, A., Barres, O., Cauzid, J., Perrotta, M., Roda Robles, E., & Ribeiro, M. (2021). Tools for Remote Exploration: A Lithium (Li) Dedicated Spectral Library of the Fregeneda-Almendra Aplite-Pegmatite Field. *Data*, *6*. https://doi.org/10.3390/data6030033

Cardoso-Fernandes, J., Silva, J., Perrotta, M., Lima, A., Teodoro, A., Ribeiro, M., Dias, F., Barres, O., Cauzid, J., & Roda-Robles, E. (2021). Interpretation of the Reflectance Spectra of Lithium (Li) Minerals and Pegmatites: A Case Study for Mineralogical and Lithological Identification in the Fregeneda–Almendra Area. *Remote Sensing*, *13*, 3688. https://doi.org/10.3390/rs13183688

Cardoso-Fernandes, J., Teodoro, A. C., & Lima, A. (2019). Remote sensing data in lithium (Li) exploration: A new approach for the detection of Li-bearing pegmatites. *International Journal of Applied Earth Observation and Geoinformation, 76*, 10-25. doi: https://doi.org/10.1016/j.jag.2018.11.001.

Cardoso-Fernandes, J., Teodoro, A., Lima, A., & Roda-Robles, E. (2019). Evaluating the performance of support vector machines (SVMs) and random forest (RF) in Li-pegmatite mapping: preliminary results. 26. https://doi.org/10.1117/12.2532577

Carranza, E. J. (2009). Geochemical Anomaly and Mineral Prospectivity Mapping in GIS. *Handbook of Exploration and Environmental Geochemistry*, *11*.

Carranza, E. J. M., & Hale, M. (1997). A catchment basin approach to the analysis of reconnaissance geochemical - geological data from Albay province, Philippines. *Journal of geochemical exploration, 60*(2), 151-171.

Catalán, J. R. M., Pascual, F. J. R., Montes, A. D., Fernández, R. D., Barreiro, J. G., Silva, Í. D. D., Clavijo, E. G., Ayarza, P., & Alcock, J. E. (2014). The late Variscan HT/LP metamorphic event in NW and Central Iberia: relationships to crustal thickening, extension, orocline development and crustal evolution. *Geological Society, London, Special Publications*, *405*(1), 225-247. https://doi.org/doi:10.1144/SP405.1

Černý, P., & Ercit, T. S. (2005). Classification of granitic pegmatites revisited. *Can. Mineral., 43*, 2005–2026.

Chavez, P. S. (1996). Image-Based Atmospheric Corrections - Revisited and Improved. *Photogrammetric Engineering and Remote Sensing, 62*, 1025–1036.

Cheng, Q., Agterberg, F. P., & Ballantyne, S. B. (1994). The separation of geochemical anomalies from background by fractal methods. *Journal of geochemical exploration, 51*(2), 109-130. doi: https://doi.org/10.1016/0375-6742(94)90013-2.

Congedo, L. (2016). Semi-Automatic Classification Plugin Documentation. Retrieved from DOI: http://dx.doi.org/10.13140/RG.2.2.29474.02242/1

Dias, C. (2016). Abordagem multidisciplinar às mineralizações de lítio no Campo Aplito-Pegmatítico do Barroso-Alvão, Norte de Portugal. Dissertação de Mestrado.

Dias, R. & Ribeiro, A., (1993). Porto–Tomar shear zone, a major structure since the beginning of the Variscan orogeny. Comun. Inst. Geol. Min., Lisboa. 79, pp.31-40.

Dias, R. & Ribeiro, A., (1995). The Ibero-Armorican arc: a collision effect against an irregular continent? Tectonophysics. 246, pp.113–128.

Dias, R., (2010). Evolução geodinâmica de Portugal no contexto do ciclo Varisco. VIII Congresso Nacional de Geologia. GEOTIC – Sociedade Geológica de Portugal. e - Terra. Volume 8–nº 3

Drury, S. 2001. Image Interpretation in Geology. Blackwell Science, 290p. USA.

European Commission: DG Internal Market Industry Entrepreneurship and SMEs. (2020). *Critical Raw Materials Resilience: Charting a Path towards greater Security and Sustainability* (COM(2020) 474 final). Brussels. Retrieved from: https://eur-lex.europa.eu/legal-content/EN/ALL/?uri=COM:2020:474:FIN

Farias, P., Gallastegui, G., González Lodeiro, F., Marquínez, J., Martin Parra, L., Martínez Catalán, J., Paolo Macia, J., Rodriguez Fernandes, L. (1987). Aportaciones al conocimiento de la litoestratigrafia y estrutura de Galiza Central. Memórias Fac.Ciênc. Univ. Porto

Fernández, F.J., Chaminé, H.I., Fonseca, P.E., Munhá, J.M., Ribeiro, A., Aller, J., FuertesFuentes, M., Borges, F.S., (2003). High-temperature fabrics in garnetiferous quartztectonites from W Portugal: geodynamic implications for the Iberian Variscan Belt. Terra Nova 15, 2, pp. 96–103.

Ferreira, N., Iglésias, M., Noronha, F., Pereira, E., Ribeiro, A. & Ribeiro, M. L., (1987). Granitóides da zona Centro Ibérica e seu enquadramento geodinâmico. In: Geología de los Granitóides y Rocas Asociadas del Macizo Hesperico. Libro de Homenaje a L. C. García de Figuerola, Editorial Rueda. Madrid

Fortescue (2021). Circo Exploration Program.

Frutuoso, R., Lima, A. C., & Teodoro, A. C. (2021). Application of remote sensing data in gold exploration: targeting hydrothermal alteration using Landsat 8 imagery in northern Portugal. Arabian Journal of Geosciences. 14(6). doi: 10.1007/s12517-021-06786-0.

Fyzollahhi, N., Torshizian, H., Afzal, P., & Jafari, M. R. (2018). Determination of lithium prospects using fractal modeling and staged factor analysis in Torud region, NE Iran. *Journal of geochemical exploration, 189*, 2-10. doi: https://doi.org/10.1016/j.gexplo.2017.09.017.

Gabr, S., Ghulam, A., & Kusky, T. (2010). Detecting areas of high-potential gold mineralization using ASTER data. Ore Geol. Rev., 38. pp. 59–69.

Gao, Y., Bagas, L., Li, K., Jin, M., Liu, Y., & Teng, J. (2020). Newly Discovered Triassic Lithium Deposits in the Dahongliutan Area, NorthWest China: A Case Study for the Detection of Lithium-Bearing Pegmatite Deposits in Rugged Terrains Using Remote-Sensing Data and Images. *Frontiers in Earth Science, 8*(553). doi: 10.3389/feart.2020.591966.

Ghezelbash, R., & Maghsoudi, A. (2018). Comparison of U-spatial statistics and C–A fractal models for delineating anomaly patterns of porphyry-type Cu geochemical signatures in the Varzaghan district, NW Iran. *Comptes Rendus Geoscience, 350*(4), 180-191. doi: https://doi.org/10.1016/j.crte.2018.02.003.

GIS Geography (2022). Sentinel 2 Bands and Combinations. Available at https://gisgeography.com/sentinel-2-bands-combinations/. Accessed July 2022.

Goetz, A. F. H., Rowan, L. C. & Kingston, M.J. 1982. Mineral identification from orbit: initial results from the Shuttle Multispectral Infrared Radiometer. Science, 218, pp. 1020-1031.

Gomes, E. P. (1996). Mineralogia, Petrologia e Geoquímica das Rochas Granitóides da Área de Rebordelo-Bouça-Torre de D.Chama-Agrochão e Mineralizações Associadas. Dissertação de Doutoramento.

Gomes, M. E. P. (2008). Geochemistry of microgranular enclaves and host granite from Telões (Vila Pouca de Aguiar), Northern Portugal. Chemie der Erde - Geochemistry, 68, 1, 69-80, 2008.

Gomes, M. E. P., & Favas, P. J. C. (2006). Mineralogical controls on mine drainage of the abandoned Ervedosa tin mine in north-eastern Portugal. *Applied Geochemistry*, *21*(8), 1322-1334. https://doi.org/https://doi.org/10.1016/j.apgeochem.2006.06.007

Gomes, M. E. P., & Neiva, A. M. R. (2002). Petrogenesis of Tin-bearing Granites from Ervedosa, Northern Portugal: The Importance of Magmatic Processes. *Geochemistry*, *62*(1), 47-72. https://doi.org/https://doi.org/10.1078/0009-2819-00002

Gomes, M. E. P., Antunes, I. M. H. R., Neiva, A. M. R., Teixeira, R. J. S., & Santos, A. (2011). Geoquímica dos minerais dos filões W> Sn e das águas das antigas minas de Murçós (NE de Portugal). In VIII Congresso Ibérico de Geoquímica, Castelo Branco, 24-28 Setembro, 2011 (pp. 111-116). IPCB

Gomes, M. E. P., Favas, P., & Figueiredo, N. (2008). O passado mineiro e o presente, na região de Rebordelo, Ervedosa e Murçós. 11 p.

Google Earth (2015). Available at earth.google.com/web/. Accessed July 2022.

Gourcerol, B., Gloaguen, E., Melleton, J., Tuduri, J., & Galiegue, X. (2019). Re-assessing the European lithium resource potential – A review of hard-rock resources and metallogeny. *Ore Geology Reviews, 109*, 494-519. doi: https://doi.org/10.1016/j.oregeorev.2019.04.015.

Han, T., & Nelson, J. (2015). Mapping hydrothermally altered rocks with Landsat 8 imagery: A case study in the KSM and Snow field zones, northwestern British Columbia. In *Geological Fieldwork 2014* (Vol. 2015-1, pp. 103-112): British Columbia Ministry of Energy and Mines, British Columbia Geological Survey Paper.

Hawkes, H. E. (1976). The downstream dilution of stream sediment anomalies. *Journal of geochemical exploration, 6*(1), 345-358. doi: https://doi.org/10.1016/0375-6742(76)90023-6.

Hung, L., Batelaan, O., & De Smedt, F. (2005). *Lineament extraction and analysis, comparison of LANDSAT ETM and ASTER imagery. Case study: Suoimuoi tropical karst catchment, Vietnam.* Paper presented at the SPIE Remote Sensing, Bruges, Belgium, 12. doi: https://doi.org/10.1117/12.627699.

Inzana, J., Kusky, T., Higgs, G., & Tucker, R. (2003). Supervised classifications of Landsat TM band ratio images and Landsat TM band ratio image with radar for geological interpretations of central Madagascar. *Journal of African Earth Sciences, 37*(1-2), 59-72. doi: 10.1016/s0899-5362(03)00071-x.

Japan Association on Remote Sensing (JARS). (1993). Remote Sensing Note. Retrieved from http://www.jars1974.net/pdf/rsnote_e.html. Accessed December 2017.

Julivert, M. (1972). *Mapa tectónico de la Península Ibérica y Baleares Escala 1:1.000.000*. Madrid: Ministerio de Industria y Energía, Servicio de Publicaciones, 1 mapa.

Julivert, M., Fontboté, J.M., Ribeiro, A. & Conde, L.E.N., (1974). Mapa Tectónico de la Península Ibérica y Baleares, Escala 1:1000.000. Memória Explicativa. Instituto Geologico y Minero de España, Madrid.

Köhler, M., Hanelli, D., Schaefer, S., Barth, A., Knobloch, A., Hielscher, P., Cardoso-Fernandes, J., Lima, A., & Teodoro, A. C. (2021). Lithium Potential Mapping Using Artificial Neural Networks: A Case Study from Central Portugal. *Minerals, 11*(10), 1046. doi: 10.3390/min11101046.

Kruse, F. A., A. B. Lefkoff, J. B. Boardman, K. B. Heidebrecht, A. T. Shapiro, P. J. Barloon, and A. F. H. Goetz, (1993). "The Spectral Image Processing System (SIPS) - Interactive Visualization and Analysis of Imaging spectrometer Data." Remote Sensing of Environment 44 (1993): 145-163.

L. A. Currie, "Detection and quantitation in x-ray fluorescence spectrometry," in X-Ray Fluorescence Analysis of Environmental Samples, Ed. T. G. Dzubay, Ann Arbor Science Publishing, Inc., Ann Arbor, MI, (1978), pp. 289-295.

Laboratório Nacional de Energia e Geologia (LNEG) (2022). Download de Cartografia Geológica e Hidrogeológica. Available at https://geoportal.lneg.pt/pt/dados_abertos/cartografia_geologica/. Accessed July 2022.

Lillesand, T., Kiefer, R., & Chipman, J. (2015). Remote Sensing and Image Interpretation. 7th Edition, Wiley, New York, 784.

Lima, A. (2000). Estrutura, mineralogia e génese dos filões aplitopegmatíticos com espodumena da região do Barroso-Alvão. Dissertação de Doutoramente em Geologia.

Lotze, F. (1945). Zur Gliederung der Varisziden der Iberichen Meseta. Geotektonische Forschungen, 6.

Loughlin, W. P. (1991). Principal component analysis for alteration mapping; Photogrammetric Eng. Rem. Sens. 57(g) 1163–1169.

Martínez Catalán, J. R., Rubio Pascual, F. J., Montes, A. D., Fernández, R. D., Barreiro, J. G., Dias Da Silva, Í., Clavijo, E. G., Ayarza, P., Alcock, J. E., Schulmann, K., Martínez Catalán, J. R., Lardeaux, J. M., Janoušek, V., & Oggiano, G. (2014). The late Variscan HT/LP metamorphic event in NW and Central Iberia: relationships to

crustal thickening, extension, orocline development and crustal evolution. In *The Variscan Orogeny: Extent, Timescale and the Formation of the European Crust* (Vol. 405, pp. 0): Geological Society of London.

Matte, P., (1986). Tectonics and plate tectonics model for the Variscan belt of Europe. Tectonophysics 126, 329 – 374.

Matte, P., (1991). Accretionary history of the Variscan belt in western Europe. Tectonophysics 196, 309 – 337

Matte, P., (1998). Accretionary history of the Variscan belt in western Europe. Tectonophysics 196, 309 – 337.

Matte, P., (2001). The Variscan collage and orogeny (480-290 Ma) and the tectonic definition of the Armorican microplate: a review. Terra Nova. 13, pp.122–128.

Mia, M.B. & Fujimitsu, Y., (2012). Mapping hydrothermal altered mineral deposits using Landsat 7 ETM+ image in and around Kuju volcano, Kyushu, Japan. Journal of Earth System Science, 121(4), pp. 1049 – 1057

Mokhtari, A. R., & Garousi Nezhad, S. (2015). A modified equation for the downstream dilution of stream sediment anomalies. *Journal of geochemical exploration, 159*, 185-193. doi: 10.1016/j.gexplo.2015.09.007.

Moradi, M., Basiri, S., Kananian, A. & Kabiri, K., (2015). Fuzzy logic modeling for hydrothermal gold mineralization mapping using geochemical, geological, ASTER imageries and other geo-data, a case study in Central Alborz, Iran. Earth Sci Inform, 8, pp. 197-205

Mukaka, M. M. (2012). Statistics corner: A guide to appropriate use of correlation coefficient in medical research. *Malawi medical journal : the journal of Medical Association of Malawi, 24*(3), 69-71.

Mwaniki, M. W., Moeller, M. S., & Schellmann, G. (2015). A comparison of Landsat 8 (OLI) and Landsat 7 (ETM+) in mapping geology and visualising lineaments: A case study of central region Kenya. *ISPRS - International Archives of the Photogrammetry, Remote Sensing and Spatial Information Sciences, XL-7/W3*, 897-903. doi: 10.5194/isprsarchives-XL-7-W3-897-2015.

National Aeronautics and Space Administration (NASA) (2021). Landsat 9. https://landsat.gsfc.nasa.gov/satellites/landsat-9/ . Accessed July 2022.

Neff, H. (2007). RQ-mode Principal Components Analysis of ceramic compositional data. *Archaeometry*, *36*, 115-130. https://doi.org/10.1111/j.1475-4754.1994.tb01068.x

Njue, L. M. (2013). Geological field mapping.

Noronha, F., Ramos, J. M. F., Rebelo, J. A., Ribeiro, A., & Ribeiro, M. L. (1979). Essai de corrélation des phases de déformation hercynienne dans le Nord-Ouest Péninsulaire. *Bol. Soc. Geol. Portugal, 21*(2-3), 227-237.

Noronha, F., Ribeiro, M.A., Almeida, A., Doria, A., Guedes, A., Lima, A., Martins, H. C., Sant' Ovaia, H., Nogueira, P., Martins, T., Ramos, R. & Vieira, R. (2006). Jazigos filonianos hidrotermais e aplitopegmatiticos espacialmente associados a granitos (norte de Portugal). In: Geologia de Portugal no contexto da Iberia (Dias, R. Araujo, A., Terrinha, P. e Kulberg, Editores). Univ.Evora, Evora, 123-138.

Obidya McXherm, A. (2019). A FIELD REPORT ON THE GEOLOGICAL MAPPING EXERCISE AT IFON-IJADO AREA, NORTH-WEST OF OSUN STATE, NIGERIA. https://doi.org/10.13140/RG.2.2.36140.80004

Pereira, E., Ribeiro, A. & Meireles, C., (1993). Cisalhamentos Hercínicos e controlo das mineralizações de Sn-W, Au e U na Zona Centro Ibérica, em Portugal. Cuaderno Lab. Xeolóxico de Laxe. Coruña. Vol. 18, pp.89-119.

Pérez Estaún, A., Bea, F., Bastida, F., Marcos, A., Martínez Catalán, J. R., Martínez Poyatos, D., Arenas, R., Díaz García, F., Azor, A., Simancas, J. F., González Lodeiro, F. (2004). La Cordillera Varisca Europea: el Macizo Ibérico. In: Geología de España (Vera, J. A. ed.). Sociedad Geológica de España, IGME, Madrid, 21-25.

Plant, J. & Hale, M. (1994). Drainage Geochemistry. Handbook of Exploration Geochemistry, Elsevier, Amsterdam.

Pour, A., & Hashim, M., (2015). Hydrothermal alteration mapping from Landsat-8 data, Sar Chesmeh copper mining district, south-eastern Islamic Republic of Iran. Journal of Taibah University for Science, 9, 155-166.

Rajesh, H. M. (2004). Application of remote sensing and GIS in mineral resource mapping - An overview. *Journal of Mineralogical and Petrological Sciences, 99*(3), 83-103. doi: 10.2465/jmps.99.83.

Ramsay, J. G., & Huber, M. I. (1987). *The Techniques of Modern Structural Geology* (Vol. 2: Folds and Fractures). London: Academic Press Limited, Elsevier Science, 391.

REFLEX (2022). IMDEX ioGAS. Available at https://reflexnow.com/product/iogas/. Accessed October 2022

Ribeiro, A., Pereira, E., Chaminé, H. I. & Rodrigues, J., (1995). Tectónica do megadomínio de cisalhamento entre a Zona de Ossa-Morena e a Zona Centro-Ibérica na região de PortoLousã. In: Sodré Borges, F., Marques, M. Mem. Mus. Lab. Min. Geol. Fac. Ciênc. Univ. Porto, 4, pp. 299-303.

Richards, J. A., & Jia, X. (2006). *Remote Sensing Digital Image Analysis: An Introduction* (4th edition ed.). Berlin, Germany: Springer, 454.

Roda-Robles, E., Pesquera, A., Gil-Crespo, P. P., Vieira, R., Lima, A., Garate-Olave, I., Martins, T., & Torres-Ruiz, J. (2016). Geology and mineralogy of Li mineralization in the Central Iberian Zone (Spain and Portugal). *Mineralogical Magazine, 80*(1), 103-126. doi: 10.1180/minmag.2016.080.049.

Roda-Robles, E., Villaseca, C., Pesquera, A., Gil-Crespo, P. P., Vieira, R., Lima, A., & Garate-Olave, I. (2018). Petrogenetic relationships between Variscan granitoids and Li-(F-P)-rich aplite-pegmatites in the Central Iberian Zone: Geological and geochemical constraints and implications for other regions from the European Variscides. *Ore Geology Reviews, 95*, 408-430. doi: https://doi.org/10.1016/j.oregeorev.2018.02.027.

Rossi, C., Bateson, L., Bayaraa, M., Butcher, A., Ford, J., & Hughes, A. (2022). Framework for Remote Sensing and Modelling of Lithium-Brine Deposit Formation. *Remote Sensing*, *14*, 1383. https://doi.org/10.3390/rs14061383

Sabins, F. F. (1997). *Remote sensing principles and interpretation* (3rd ed.). New York: W. H. Freeman, 494.

Sabins, F. F. (1997). Remote sensing principles and interpretation. New York, W. H. Freeman.

Sabins, F. F. (1999). Remote sensing for mineral exploration. *Ore Geology Reviews, 14*(3), 157-183. doi: https://doi.org/10.1016/S0169-1368(99)00007-4.

Shahrestani, S., & Mokhtari, A. R. (2017). Improved detection of anomalous catchment basins by incorporating drainage density in dilution correction of geochemical residuals. *Geochemistry: Exploration, Environment, Analysis, 17*(3), 194-203. doi: 10.1144/geochem2016-015.

Silva, A. F. d., & Ribeiro, M. L. (1991). *Notícia Explicativa da folha 15-A Vila Nova de Foz Côa*. Lisboa, Portugal: Serviços Geológicos de Portugal, 52.

Silva, A. F. d., & Ribeiro, M. L. (1994). *Notícia Explicativa da folha 15-B Freixo de Espada à Cinta*. Lisboa, Portugal: Instituto Geológico e Mineiro, 48.

Simmons, W. B. S., & Webber, K. L. (2008). Pegmatite genesis: state of the art. *European Journal of Mineralogy, 20*(4), 421-438. doi: 10.1127/0935-1221/2008/0020-1833.

Singh, A., & Harrison, A. (1985). Standardized principal components. Int. J. Rem. Sens, 6(6), pp. 883–896. In: Mia, M.B. & Fujimitsu, Y. (2012). Mapping hydrothermal altered mineral deposits using Landsat 7 ETM+ image in and around Kuju volcano, Kyushu, Japan. Journal of Earth System Science, 121(4), pp. 1049 – 1057.

Thadeu, D., (1951). Geologia do Couto Mineiro da Panasqueira. Comunicações dos Serviços Geológicos de Portugal, Tomo XXXII, pp. 5-64

The European Space Agency (ESA) (2012). ESA SP-1322/2 Sentinel 2. Available at https://www.esa.int/About_Us/ESA_Publications/ESA_SP-1322_2_Sentinel_2. Accessed July 2022.

The European Space Agency (ESA) (2021). Sentinel 2. Available at https://sentinel.esa.int/web/sentinel/user-guides/sentinel-2-msi/overview. Accessed July 2022.

United States Geological Survey (USGS) (2004). https://www.usgs.gov/programs/national-cooperative-geologic-mapping-program/introduction-geologic-mapping. Accessed July 2022.

United States Geological Survey (USGS) (2018). https://earthexplorer.usgs.gov/. Accessed July 2022.

United States Geological Survey (USGS) (2022). Introduction to Geological Mapping. Available at https://www.usgs.gov/programs/national-cooperative-geologic-mapping-program/introduction-geologic-mapping. Accessed September 2022.

United States Geological Survey (USGS) (2022). Landsat 9 Data User's Handbook. Available at https://www.usgs.gov/media/files/landsat-9-data-users-handbook. Accessed July 2022.

USGS Landsat Program (2017). "Comparison of #Landsat 7, 8, #Sentinel 2, #ASTER & #MODIS bands. View band designations for all #Landsat sensors at https://on.doi.gov/2mOjwjR". 3 March 2017, 8:30 am. Tweet. Available at https://twitter.com/usgslandsat/status/837696716417687553. Accessed July 2022.

van der Meer, F. D., van der Werff, H. M. A., van Ruitenbeek, F. J. A., Hecker, C. A., Bakker, W. H., Noomen, M. F., van der Meijde, M., Carranza, E. J. M., Smeth, J. B. d., & Woldai, T. (2012). Multi- and hyperspectral geologic remote sensing: A review. *International Journal of Applied Earth Observation and Geoinformation, 14*(1), 112-128. doi: 10.1016/j.jag.2011.08.002.

Vigneresse, J.L., (1999). Intrusion level of granitic massifs along the Hercynian belt: balancing the eroded crust. Tectonophysics, 307, pp.277–295

Weier, J. & Herring, D. (2000). Measuring vegetation (NDVI&EVI). Available at: https://earthobservatory.nasa.gov/Features/MeasuringVegetation/. Accessed July 2012.

Zuo, R. (2011). Identifying geochemical anomalies associated with Cu and Pb–Zn skarn mineralization using principal component analysis and spectrum–area fractal modeling in the Gangdese Belt, Tibet (China). *Journal of geochemical exploration, 111*(1-2), 13-22. doi: 10.1016/j.gexplo.2011.06.012.

Appendices

Appendix A – XRF results of the stream sediment samples

Sample ID	Mg_ppm	Al_ppm	Si_ppm	P_ppm	S_ppm	K_ppm	Ca_ppm	Ti_ppm	Cr_ppm	Mn_ppm	Fe_ppm	Ni_ppm	Cu_ppm	Zn_ppm	As_ppm	Rb_ppm	Sr_ppm	Y_ppm	Zr_ppm	Nb_ppm	Sn_ppm	Ba_ppm	La_ppm	Ce_ppm	Nd_ppm	W_ppm	Pb_ppm	Bi_ppm	Th_ppm	LE_ppm	Lithology
PT001042	8846.3	107184	299957	488.33	327	32527	439.67	4191.3	79.67	540.67	27852	25	11.67	62	14	233.67	32.33	12.67	153.67	9	2.5	735	51	104.5	5	2.5	18.67	33.67	2.5	516088	schist
PT001043	11744	125327	235898	346	356	28751	946.67	5622.7	108	1109.3	43018	44.33	26	87	20	225.33	63.33	27	240.67	15.33	41	1382.7	150.5	223	332	2.5	29	38	2.5	544082	schist
PT001044	9312.7	102713	280803	682	419.33	32099	790.67	4475.7	90.5	530.67	29367	29	16.33	76.33	13	255.33	40	15.33	172.33	9.33	26	914.33	138.5	159	273	18	25	21	20	536905	schist
PT001045	8540.3	84278	236920	702	632.33	27729	1391.7	4646.3	76	572.67	29861	24.67	14.67	65.33	18.67	233.67	42.33	14	163.33	8	26	643	111.5	130	5	2.5	24	2.5	10	603423	schist
PT001046	11882	77961	222253	600	345.67	21737	1311.7	4624	75	445.33	34193	31	20.67	75.33	12.67	117.67	40	21	172.33	8.33	85	505	197	295	326	2.5	17.33	28	31	623030	schist
PT001047	11035	109112	272068	536.67	331.67	35212	460.67	4807.3	75.67	561.67	40857	34.67	17.33	80.67	19.33	217.67	42.67	18.33	161.67	9.67	2.5	1052	5	207	394	2.5	19.67	2.5	22	522945	schist
PT001048	7743.7	74126	201780	646	732.33	25386	2753	5030	66.67	750.33	33050	38.67	28.67	80.33	22.67	155.33	62.67	24	268	9.33	39	431.67	101	120	5	2.5	26.33	2.5	36	646580	schist
PT001049	8928.7	96923	238832	687.33	478.67	28996	797	4050.3	114	607	38907	33	21	77.67	19	199.67	39.33	20.33	151	8.67	2.5	840.33	117.5	140	383	2.5	20.33	2.5	11	578904	schist
PT001061	9287	87890	300978	558.67	226.67	27349	1014.7	4030	55.33	659.67	28607	27.33	12.33	65.33	61.67	164.67	47.67	18.33	165.67	7.67	2.5	790.67	158	191	252	18	19.33	24	23	537659	schist
PT001062	12242	100304	278546	638.67	237	26463	1095	5385.7	76	1009.7	41428	29.33	37.67	73.67	81.33	181.33	47	21	167.33	8.33	28.5	937.67	137	176.5	455	19.33	20.33	2.5	2.5	530420	schist
PT001063	9810.7	102360	240962	610.33	322.33	29782	1514	4808.7	89.5	851	40879	39.33	25	95.33	516	220.67	66	24	204.67	11	124.67	840.33	133.67	194.67	335	25	26.33	34	46	565346	schist
PT001064	11306	119073	231772	607.33	497	29488	2076.3	5497	101.67	1009	46215	53	24	101.33	168.33	209.67	73	35	285.33	11.67	2.5	1082.3	147	220.67	285	2.5	35.67	20	16	549784	schist
PT001065	9731.7	106004	230794	405	274	25978	1526.3	4858.3	73.33	573.33	36695	35.67	24.33	97.33	26	169.33	61	28.33	256	9.67	2.5	695.67	155	185.67	272	2.5	49.33	2.5	12	581112	schist
PT001066	7924.3	103687	187335	377.67	417.33	24524	1342.3	4726.7	90	364.67	43871	48	32	119.67	27.33	208	68.67	28.33	184.33	10	2.5	582.33	130.67	198.5	191	22.67	38.67	2.5	17.33	623588	schist
PT001067	9736.3	97797	241869	674.5	806.25	27249	3944.8	4326.5	67.25	794.5	33562	43	29	84.5	20.75	157.25	64.5	24.25	239.75	8.25	30	590.5	123	173	310	15	39.25	2.5	33.5	577485	schist
PT001068	11190	101205	243998	641.33	862.33	24406	2095	4116.7	91	455.67	35215	38	24.33	86.33	15.33	173.33	57	27.67	204	9.33	2.5	720	137.5	139.5	5	2.5	32.67	20	2.5	574066	schist
PT001069	10893	113609	259951	823.67	762.67	28915	2974	4243.3	77	682.67	39395	43	31	93	49.33	184.33	57.67	24	229.33	9	25	768.67	125.5	198.67	255	2.5	33.67	20	22	535718	schist
PT001070	6715	71399	218605	488	447.33	20725	1820.7	4233	79.33	557.33	26261	30.33	21.67	78.33	22	131.33	36.33	18.33	240	7.33	2.5	457	5	115	5	2.5	25.67	2.5	17	647455	schist
PT001071	17174	105389	210027	789	482.67	26074	3704	5293.7	98	919.67	46143	53	40	129	25.67	133	48.67	28	218.67	9.67	2.5	585	168	185.5	5	2.5	31.67	2.5	15.67	582337	schist
PT001072	18409	113368	196259	473	263	29440	1660.7	5534.3	102	510.67	45752	52.33	41.67	129.67	29	156.33	42.33	33	202.67	11.33	2.5	718	153	164.67	5	2.5	34.33	21	13.5	586387	schist
PT001073	11243	88541	176401	507.67	369.33	24896	1858.3	5160	86	731	44601	45.67	35.67	113	27.33	146.67	38.33	26	213	11.33	125	467.33	111	128	364	2.5	46.33	2.5	22.67	643963	schist
PT001074	18219	93275	197653	527	365	22636	2450	4992.3	98	887	43114	49.33	38.33	113.33	200	149.33	45	27	198	10	26	571.33	118	132	5	97	33	2.5	33	614155	schist
PT001075	19942	108138	203898	535.67	334	26568	3136	5123.7	100.67	1099	51497	63	44.33	120.33	172.67	185.67	50.67	36.33	234	11.33	31	706.33	134.33	191.5	258	2.5	38	2.5	28	577408	schist
PT001076	13383	77698	180579	483.33	361.33	20346	1912	4670	74.33	758.33	40005	40.67	36.33	101	137.33	142.67	41.33	22.33	171.67	9	32	477.33	158	179.5	5	2.5	31.67	2.5	23.5	658091	schist
PT001077	14950	86238	204606	521	228.33	24536	1101	4362.7	83.33	676.33	36775	34.67	28	84.67	39.33	141.67	34.67	19	178.33	9.33	29.5	536.67	113	182	301	2.5	20.67	2.5	13	624510	schist
PT001078	9682.3	87843	187013	588.33	367.33	25317	1243	4951.3	73.67	1103.3	40480	41	33.67	103.33	44	142.67	37.67	28	210	10.67	2.5	430.67	125	147	5	2.5	38	2.5	28.67	640014	schist
PT001079	13697	93032	216008	647.67	468	26507	2052	4720.7	85	564	36108	36	28.67	95.67	48.67	139.33	45	22.67	217.67	8.67	44	564.67	77	126.67	5	2.5	25.33	2.5	21	604641	schist
PT001080	12289	85945	228773	726	221.67	22490	803.33	4315	83	736	36189	34.67	19.33	81.67	37	140.67	32	20.33	196	9	2.5	705	127	126	303	15	19	2.5	2.5	605852	schist
PT001081	11158	107067	220054	460.67	253.67	26976	2172.3	4721.7	97.67	575	38234	38.67	29.33	84.33	54.33	173.33	63.67	29	209	10.33	30	690.33	143.33	188	293	46	28	24	10	586416	schist
PT001082	5534.7	84134	232747	1087.7	659	20444	2509.3	3329.7	52	418	20315	18	19	84	9.33	300.33	58.33	13.33	161	4	26	332.33	124	132	5	16	31	2.5	11	627635	granite+schist
PT001083	9066	92950	298449	964	155.67	25303	1820	4238	64.33	530	32143	25	17.33	76.67	47.33	185.33	54.33	18	147.67	10	253	854.33	154.67	205.5	5	31	20.67	32	2.5	532203	granite+schist
PT001084	3863	98708	309085	1178	384	40658	1108	2227.7	45	223	11590	2.5	10	47	4	367.33	71.67	2.5	68	2.5	2.5	603.33	144	198.5	291	2.5	39.33	2.5	2.5	529397	granite
PT001085	4382	95686	305264	1375.3	370.33	39661	1561.3	1905.7	42.5	217.33	10440	7	2.5	44.67	2.5	370	74	6	68.33	4	21	589	117	5	308	2.5	41.33	27	2.5	537742	granite
PT001087	6534	99759	200868	1214.7	407.33	27268	3176.7	4064.3	5	187.33	21769	10.67	17	117.33	7.33	352.67	76	10	199.67	8	2.5	319.33	105	124	234	2.5	36.33	2.5	22	633327	granite
PT001088	6894.5	89045	196608	1057.7	508.67	21221	1809.3	3172.7	41	455.67	19812	10.67	8.5	93	8	343	62	8.67	154.33	7	2.5	306.33	5	104	5	2.5	33.67	28	11	660566	granite
PT001089	5017.7	101002	230192	1088	214.33	32862	1424.3	3061	5	142.33	13105	2.5	10	76.33	2.5	388.33	65.67	7.33	143	5	30.5	377.33	111	153.33	327.67	2.5	42.67	2.5	13.67	610184	granite
PT001091	4260	72472	218330	1443	532.33	24706	1288	2693.3	5	665	16160	24.67	14.5	59.67	8	297.33	66	7.5	86.33	2.5	27	325.67	5	103	5	2.5	35.33	2.5	14	659259	granite
PT001092	6448.5	89652	216177	1557.7	1051	26404	2903.3	2982.7	5	617.33	18749	10.5	11.5	70.67	2.5	339.67	68.67	7.33	112.67	4	2.5	354	112	5	157	2.5	38	18	31	634419	granite
PT001093	6634.3	117797	239984	1720	946	27825	2911.7	3824.7	40	189	19808	7.67	13	90.33	2.5	334	68.67	10	149	8	2.5	431.33	136.5	153.67	263.33	2.5	35.33	25	2.5	576595	granite
PT001094	3826	92575	257253	1143.7	326.33	32859	1535.3	2917.7	55	200.33	13962	12	16.33	58.33	4	293.67	65	9.67	95	2.5	32	414.33	114	5	5	2.5	37	21	25.5	593510	granite
PT001095	6962	74109	206745	307.33	262.67	22854	548.33	5388.3	56.5	552	31103	33.33	20	77.33	55	159.67	39.33	24	387.33	10.33	2.5	551	137	137.33	5	2.5	30	2.5	25.33	651793	schist
PT001096	10433	91860	213606	400.33	189.33	23453	1446.3	4394.3	70.67	650.67	30967	35.67	25	68.67	97	172	45.33	25.33	266	10.33	130	833.33	122	173	5	17	34.67	21	2.5	620612	schist
PT001097	6686	63187	161400	542	320.67	21054	843	4421.3	64	733.67	37872	42	29	100	42.67	160.67	36.33	21.67	197.33	10.33	30	452.67	101	149	202.5	2.5	28.67	2.5	24.33	701270	schist
PT001098	10756	86404	215214	473	501	25709	1929.3	4367	85	615	34968	41.33	28.33	78.33	56.33	177.33	54	26.33	248	9	35	723.33	92	149.33	255	24.5	31.67	22	27	620663	schist
PT001099	9510.5	50152	140087	222.33	227	16177	981.33	4163.7	62.5	680	30703	38.67	26.33	101.33	69.67	150.33	50.67	27	261	11	32	292.67	82	105	5	2.5	55.67	2.5	33	748890	schist
PT001100	17434	114834	250152	527	229.33	27536	932.33	4908.7	114.33	820.33	39421	42	28.67	112.33	54	162	39.33	30	222	11	26	1065	155.5	170.33	5	2.5	32	27.67	2.5	540867	schist
PT001101	5304	54213	167759	143.33	373.33	19141	1089.7	4045.3	74	442.67	26207	30.67	19	62	60.67	147.67	41.33	19.67	283.33	8	2.5	398	5	103	185	2.5	27.67	2.5	28	723548	schist
PT001102	12991	84969	194758	459.67	188.67	22191	984	4874	86	912	37027	44.67	28.33	113	37.67	146.33	39.33	25.67	194	9.67	2.5	571	137	155	5	2.5	40	2.5	45	639104	schist
PT001103	8830	84164	226970	488.33	876	21827	1591.3	4732.7	77	315.33	26365	27	21.67	75.33	18.33	178.67	53.67	20.33	199	7.67	43	515.33	127	142.67	239.5	23.5	18.67	30	10	622113	granite+schist
PT001104	9091	85543	228864	452	489	21389	1387	4302	72.67	424.33	28094	28	19.67	74	24.67	181	50	20.33	220	8.67	21	823.67	5	166	270	15	23.33	26.33	2.5	618218	schist
PT001105	9194.5	69992	229112	274.67	334.67	22937	1394.3	4402	61	430.33	25375	20.67	17.67	67.33	28.67	183.67	55	18	179	8.33	36.5	564.67	87	127.5	5	28.67	21	2.5	26	638203	schist
PT001106	9596.7	98879	278407	329	390	25628	1491	4394	84.33	411.33	29697	25.67	20.67	66.67	24.33	186.67	56	16.33	179.67	8.33	34.67	914	177	208.5	5	17	24.33	20	2.5	548781	schist
PT001107	12047	92655	213054	502.33	239	28507	866.33	4714	80.67	800.67	36756	34	27.67	95.33	26.33	146.33	39	22	188	9.33	37	688.33	111	137	273	2.5	35	2.5	23.5	608056	schist
PT001108	6508.3	124212	203714	1284.7	221	27829	1944	4009.3	5	306	27452	19	12.67	137	11	432.67	68	12.33	190.67	11	43	275.67	144.5	137.33	5	2.5	37.33	2.5	25.33	601021	granite

PT001108	6508.3	124212	203714	1284.7	221	27829	1944	4009.3	5	306	27452	19	12.67	137	11	432.67	68	12.33	190.67	11	43	275.67	144.5	137.33	5	2.5	37.33	2.5	25.33	601021	granite
PT001109	8276.3	83102	284060	1091.7	448	25269	1005.7	3855.3	62.33	642.33	28062	23.33	14.67	65.33	30.67	166	43	15	113	6.67	30.67	677	150	138	5	2.5	16.33	21	2.5	562768	schist
PT001110	5624.7	88917	247286	521	414.33	30281	2657.3	3128.3	40	240	17541	11	12	47.67	8	268	107.67	9	106	2.5	2.5	669.33	5	112	272	2.5	45.67	2.5	15	601886	granite
PT001111	7087.3	84630	212494	524.33	523.33	26695	1027	5957	80.67	535.67	38235	31.33	20	91.33	17.33	173.33	40	23.67	259.33	24.33	36.33	692.33	127.67	192.33	321	2.5	20.33	2.5	18.67	620261	schist
PT001112	6517.5	85419	184915	353.67	494	24115	2385.3	5140.7	71.5	465.67	47338	50	33.67	124.67	34.33	186.33	64.33	26.67	201.33	9.33	29	499.33	5	166	248	21	33	2.5	37	643465	schist
PT001113	8980	97890	211066	815.33	143	22683	5306	4587.7	53	412	28484	15.33	16	80.33	11	301.33	120.33	21.67	206.67	10	30	523.33	123.5	131.67	5	2.5	37.67	2.5	24	617858	granite
PT001114	7208.7	81417	197276	481.33	364.67	21547	5173.3	5286.7	72	256.33	30584	25	15.5	85	9	280	123.67	21.67	233.67	8	35.33	470	170	170	5	2.5	39.67	2.5	32.33	648744	granite
PT001115	1500	85946	199936	512.67	367.33	28286	1422.3	4198.7	59	696	30488	32	24.67	77	29	194	53.33	22.67	181.67	7	2.5	414.33	92	109	5	2.5	30.67	2.5	36.33	646922	schist
PT001116	8920.7	98808	236480	514.67	527	26188	2058.7	4772	69.33	607.33	32551	27.67	21.67	82	55	185.33	51.67	18.67	180.33	8.33	43.67	705.33	5	172	360.5	26.67	24.33	2.5	18	586767	schist
PT001117	5590.7	85093	191391	1050	265.67	23106	2192.3	4876	61.67	1825.3	37358	36	27.33	171.33	78	268.33	66.67	21.67	299.33	9.67	35	426.67	107.67	146.67	232	2.5	47	2.5	30.33	645326	schist
PT001118	10577	94394	292774	411.33	196.33	26788	825	4419.7	70.33	464.33	33117	30.33	14	69.33	81	177	48	17.67	139.33	7.67	30	917.67	153	183	5	18	19.67	25.5	2.5	534154	schist
PT001119	9186.7	93469	287143	415.33	406	25729	1064.7	4139	71.67	542	29057	32	15	70	105	180.33	46.33	19	145.67	8.33	35	949	131	199.5	436	19	22	20	2.5	546634	schist
PT001120	7286	98879	254175	590	267.33	29028	1331	4054.3	67	482.33	34040	25.67	15	61	33	262.33	70.67	18	195	6.67	23.33	835.67	128	152.67	5	16	31.67	2.5	25	567922	schist
PT001123	4890	102669	214737	260	250.33	34345	1258	5958.3	77	404.33	36431	32	18	64.33	13.67	212	110	32.33	393.33	11.33	2.5	771	134.5	165	5	2.5	31.67	2.5	30.33	596690	schist
PT001124	7070.3	100232	240954	578.67	364.33	28087	2466.7	4387	63	472.67	29145	20.33	16.67	83	45.33	304	96	15	189	8	21	703	156	179	304	34.67	33	2.5	13	584254	schist
PT001125	21077	129107	217803	811	472.67	30312	2548.7	5948.3	107.33	1048.7	54092	62.33	47	139.67	16.33	176	52	37.67	243.33	14.33	2.5	886.67	165	229	5	2.5	48	27	13	534421	schist
PT001126	18472	124904	270602	462.67	365	25905	700.33	5578.7	80.33	427.33	35532	39	30	86	9.67	138	34.67	21.67	210.33	11.67	2.5	882	153	213.5	5	2.5	18.33	27	2.5	515187	schist
PT001127	8678.7	79444	263132	474	156.33	17232	718	5490.3	54.33	449.67	26171	29	21.33	57.67	33.67	105.67	21.67	17.67	282.33	9.67	2.5	486.67	5	130	281	2.5	20.67	19	12	596700	schist
PT001128	17056	99858	213039	248.67	1056.3	19186	2082	4714	88.67	513	36194	51	38.33	130.67	25.33	135.33	39	33.67	215.33	10.33	21	652	121	230.5	292	24.67	38.67	2.5	16.5	604168	schist
PT001129	18539	115183	241438	388	1173	23280	2468.7	5035.7	95.67	436.67	35189	52.67	39.67	131	33.33	154.67	44.33	30.67	216.33	10.67	2.5	818.33	133	206	5	32.33	39	20	10	554814	schist
PT001130	18146	119741	209334	340.33	399	24899	1682	5629	106	678	52486	59.33	34.33	126	34.67	169	47.67	36.67	220.67	11.67	2.5	776.33	126	191	5	24	40	2.5	13	564658	schist
PT001131	17622	121974	214301	913.33	838.33	22010	2730.3	5194.3	106	1287.7	46991	57	36.33	102.33	25.33	154.67	48.33	26	209	10	2.5	821.33	131	237	352	2.5	58.33	22	2.5	564006	schist
PT001132	18161	112344	202615	751.67	1021.7	21692	3954.3	4854	101.33	1526.3	51967	63.33	38	102.67	21.33	146.33	54.33	30.33	199	9	2.5	758.67	158	207.33	418	2.5	33.33	21	2.5	578965	schist
PT001133	9138.7	80484	193631	594.67	765.67	22372	2607.3	4696	79.33	846.33	35335	39.33	28.67	104.67	22	160	51.33	20.33	214	11	2.5	543.67	5	118	206	2.5	29	2.5	22.5	648101	schist
PT001134	9215	92185	217077	533.67	718	26790	1030.7	5071	68.67	329.67	34136	31.33	20.67	77.67	18.33	179	45.33	21.33	271.33	11.33	27.5	692.33	112.5	131	327	2.5	27	2.5	25.5	614129	schist
PT001135	8447	79017	191369	449.33	666.33	23740	2526	4699.3	63.5	811.67	33193	39.33	29.33	93	23	159.67	49.67	23.67	242.67	9.67	42	511.33	179	127.67	297	2.5	35	2.5	32.67	653393	schist
PT001136	12660	88847	207732	452.33	479.33	20574	1120.7	5083.3	88	455.33	38090	40.67	30.33	110	20.67	144.33	42	29.67	194.33	10.67	27	649.33	118	176.33	264	2.5	29	2.5	23	622770	schist
PT001137	11241	71561	177411	443.67	360.33	20191	1672.3	4545.7	74.5	1322.3	38763	51	33.67	132.33	36	135.33	40	24.67	180.67	9.67	2.5	473	98	126	5	26	37	2.5	40	671112	schist
PT001138	7555.7	86769	236760	494	507	24143	1305	4774.3	78	650	30386	32	18.67	71	30	154.67	45	23	259.67	10	2.5	688.33	107.5	143	5	2.5	28.33	2.5	13	604947	schist
PT001139	8277.7	63334	157140	427.67	1408.3	16534	2652	4280.3	53	357.33	27159	41.33	33.33	96	17.33	123.33	46.33	27	197.33	10.33	2.5	300.67	5	5	202	15	30.67	2.5	21.67	717292	schist
PT001140	11124	84443	195296	607.67	660	20351	1924.7	4495.3	78	391	32875	40.67	32.33	105.67	21	140.33	42.33	25.33	202.67	10.67	2.5	612.67	137	175	260	2.5	32.67	41	18	646165	schist
PT001141	13252	83325	198327	642.33	683.33	21794	1710.7	4767	64.67	440	35224	40	35.33	109.33	24.33	150	43	25.67	225.67	10	2.5	533.33	5	178	5	2.5	33.67	2.5	25	642693	schist
PT001142	11200	74661	209154	523.33	204.67	16331	3464	3311.7	63	486	26999	28.33	24.33	68.33	13.33	149	78.33	20	155	8.5	2.5	635.67	123	114	421	15	21	28	2.5	652147	schist
PT001143	6667	96330	171325	1150	813	19007	2702.7	3510.7	47	333.67	23020	18	15.33	142.33	9	341.67	67	15.33	146.67	8.67	49	326	104.5	123	5	15.5	46	24	2.5	673757	granite
PT001144	3585.5	78840	266930	1053.7	469	34819	1488.3	2199.3	5	184	11556	10	2.5	49.33	2.5	341.67	73	4	73	2.5	47	384.67	110	119	5	2.5	40.33	2.5	26.5	598967	granite
PT001145	1500	42877	179439	2159	2113	30427	4175	2377.3	5	218	11609	2.5	17	58.33	7	258.67	73.33	7.67	80	7	43	219.33	62	84.5	5	2.5	43.33	2.5	44	723705	granite
PT001146	1500	68281	183855	921.33	901.33	28106	3734	3234.7	5	350.67	20904	14.33	20.67	80.67	12.33	312.67	82	9.67	101	8	40	298.33	96	91	5	2.5	43.33	2.5	41.67	688536	granite
PT001148	7149	85728	147236	846.33	1363	21253	2881.3	5033.7	77.67	723.33	45518	57.33	40.33	127	54	212	75	27.33	181.33	9.67	33	391	92	119.5	349	2.5	39.33	2.5	37.33	682952	schist
PT001149	7539.3	118518	178350	1017.7	1081.3	28175	2606.3	4802.7	96.33	1720.3	57449	67	43	168.33	41.33	195	81.67	28.67	179	12.33	2.5	587.33	143.33	182.33	257	2.5	38.67	2.5	26.67	596551	schist
PT001150	7531.7	100267	199124	803.67	1188.7	28719	2695.3	5206.7	84.67	785.67	51822	52.67	40	118.33	43.33	192.33	61.33	29	227.33	11.67	27	697	5	233	258	2.5	36	2.5	26	599796	schist
PT001151	7308	84661	183950	536.67	653	24860	1126	5111.3	85.67	492.67	48919	43.33	32.33	131.67	34	188.67	69.67	25.67	175	12	34	446.67	110.5	106	277	2.5	33.67	2.5	42	645681	schist
PT001152	6908.5	114550	230563	1222	469	34755	2730	3229.3	5	279.33	17092	11	9.5	76.33	7	379.33	82	7.5	162.33	5	36	544.33	159	149.33	412	2.5	46.67	2.5	19.67	588659	granite
PT001153	5534.3	134250	239830	1649	407.67	32057	2261.3	2826.3	5	239.33	17740	11.67	8	97.33	10.67	440.67	50.67	9	140.67	8.67	2.5	274	114.5	173.5	5	2.5	35	2.5	10.67	561900	granite
PT001154	10729	103712	194731	740	547.67	20354	4773.3	5949.7	53	615.33	44344	28.67	20.67	118	43.67	263.33	103.33	33.67	277.33	11.67	24.5	543	121.5	195.67	285	17	48.67	2.5	26	611426	granite
PT001155	9027	106279	226761	975.67	398	26911	3187.3	3986.7	54	708.33	25341	12.67	15.5	75.33	16.67	307.33	86.67	14.33	143.33	7.33	40	505.33	95	127.67	224	2.5	38	2.5	23.5	594847	granite
PT001156	5120.3	102984	256620	2231.7	1261.3	27460	4125.3	2172.3	5	226.33	14291	8	7	66	7	369.67	48.67	7	71	4.67	23	290	114	131	263	2.5	31.67	25.33	2.5	582293	granite
PT001157	5705.7	111605	220052	1783	380.67	31867	2603	3131.7	5	203.67	16875	10	10	90.33	2.5	398.33	58.67	8.5	132.33	9	2.5	252	102	139.5	268	2.5	33.67	2.5	21.33	604447	granite
PT001158	5544	127545	226807	1218.3	313.67	30807	2478	3286.3	5	197.33	20770	15.67	15.33	113.33	13.33	396.67	70.33	9.67	121	8.5	2.5	431.33	131	133	282	2.5	43.33	28	15	579515	granite
PT001159	4870	100445	219579	1218.3	651.67	26775	1997.7	3074.3	5	646.33	19940	11	11	93	7.33	375.67	65	7.33	115.33	7.33	34.67	355	82	120	5	2.5	37.67	2.5	18.5	622848	granite
PT001160	7911.3	115737	231905	1513	447.33	26685	3689.3	3839.3	40	393.33	24931	17.67	11.67	107.67	8.33	332.33	75.67	10.67	166	10.5	22	464	115	171	261.5	2.5	33	2.5	12	581139	granite
PT001162	11368	97524	224345	1220.3	479.33	24001	6141	4031.3	51	830.33	26368	20.5	14.33	71.67	10	277	127.67	17.67	160.67	5	21	734.67	132.5	140	5	2.5	35.33	2.5	23.5	601911	granite
PT001163	6711.5	88819	263871	1004.3	333.33	28941	2201.7	2961.7	42.5	274.33	16721	2.5	15	59	5	313.33	80.67	10.67	103.33	6	25	567	96	163	5	2.5	38.67	23	41	588951	granite
PT001164	13329	96235	228540	803.67	299.33	22283	5567.3	4937	66.33	381	30889	19	14	68	12.33	262.33	138.67	22	211	8	2.5	860	164	186.67	5	2.5	35.67	23	15	594635	schist
PT001165	9343	105000	219251	1134	265	24612	2765	5668.3	59	568.33	39132	34.67	22.33	89	20.33	221.33	94.33	29.33	312.67	9.67	26	721	144	207	5	2.5	37	2.5	22.67	590216	schist
PT001166	10152	93894	229127	697.33	511.67	19855	5113.7	4355.3	56.67	446.33	25719	12.67	10.5	58.33	11.33	260	114.67	23	175.33	5.5	2.5	759.67	143.67	150.67	5	2.5	39.33	2.5	14	608285	granite

PT001166	10152	93894	229127	697.33	511.67	19855	5113.7	4355.3	56.67	446.33	25719	12.67	10.5	58.33	11.33	260	114.67	23	175.33	5.5	2.5	759.67	143.67	150.67	5	2.5	39.33	2.5	14	608285	granite
PT001167	8252	82165	300804	378	251	21165	588.5	3437.5	51.5	364	18987	18	13	40	10.5	114	23	12.5	215.5	9	2.5	627	138	151	295	13	13	21	2.5	561896	schist
PT001168	6946.3	87577	257978	525	659	21594	1475.7	3459	53.33	1010	27530	25.33	12.5	50.67	20	127.67	36.33	18	242	8.33	2.5	632.33	117	141	246	2.5	21.33	27.5	2.5	589654	schist
PT001169	9033.7	107629	239366	517.33	435.67	29784	911.33	5242.7	87.33	887	39633	36.33	20.67	84	28.33	228	38.33	21.67	256.67	12	22	1037.7	136.5	174.67	373	2.5	20.67	20	11	564138	schist
PT001170	7869.3	94609	229904	370.33	586.33	26509	1019	5090.7	74.5	663	36258	37.33	24	79.33	21	181	36.67	24.33	304.33	11	2.5	815.33	5	133.5	5	2.5	23.67	2.5	19	595276	schist
PT001171	7437.7	88324	196740	763.33	261	23420	1618.3	4937	75	3425.3	66647	57.67	19	96.67	146.67	196.33	95.33	30	256	12.67	38	748	133.67	212.33	5	18	29	2.5	28.67	604205	schist
PT001172	6919	96201	229752	338.33	181	28198	1506	5889	48.67	648.33	41587	43	21.67	85.33	44.33	191.67	80	32.67	330	12.33	2.5	760.67	163	134.33	250	2.5	30	2.5	22.33	586754	schist
PT001173	7876.7	93679	237701	436	277	27580	1607	5823.7	89	650	38785	41	20.33	83	24.67	195.67	69	34.33	396.33	13	2.5	834	124.5	248	332	2.5	31.67	2.5	17.33	583460	schist
PT001174	10056	97927	266477	491	212.67	25963	1753.7	5302	87.67	527.33	31252	32	17	68.67	76.33	168	52.33	21	186.33	9.67	26	869.33	5	160.67	5	21	18.67	36	2.5	558179	schist
PT001175	11748	104210	240237	345.67	354.67	22145	1920.7	5573	85.67	539	45677	41.33	25.67	87.33	19.67	180.33	65.33	30	199	11.33	30	974.33	244	218.67	5	15	25.67	27.5	14	565071	schist
PT001176	7362	90508	281330	961.33	312.67	29143	2788.7	3437	42	407.67	20961	13.67	10.67	60.67	15	281	93	14.33	125.33	7.5	29.5	791	125.5	161.5	318	2.5	40.67	22.5	2.5	560963	schist
PT001177	12075	106923	241135	462.67	431.67	26991	1359.7	5635.3	112.67	666	37732	38.67	21.67	83.33	25	209	42	21.67	250.67	13.67	23	1304.7	150	172	327	2.5	22	30	2.5	563887	schist
PT001178	8235.7	81678	206796	704.67	731	27828	1166.3	3920.7	49.5	434.33	27094	25.67	16.33	58.33	17.33	280.67	39	14.33	133.67	9	28	521	109	198	335	2.5	29.67	19	25	639923	schist
PT001179	8958	108722	235826	302.33	657	30652	1489.7	5940.3	99.67	610	36873	42.33	19.33	87	14.33	225	51	20.33	287.33	12.67	32	1173.3	167	185	338	17	23	28.5	25	567465	schist
PT001180	7960.3	102550	285613	519.67	428.67	30687	1026.7	3770.3	81.33	442	21550	22	10	46.67	15	271	37.33	13.67	124	7.33	30.5	747.67	186	166	305	15	21.67	26.33	2.5	543687	schist
PT001181	8574.7	97107	288882	498	330	29397	777	3147.7	58	450.67	23674	16.67	16	54	14	269.33	32	11.67	132.67	8	28	707	5	5	5	2.5	20.33	30.67	2.5	545776	schist
PT001182	7802.3	95104	293684	421.67	303.67	29206	666.33	2915	61.33	344	20394	19.67	10.67	47	11.33	277.33	32	12.33	99	8.33	26	659	137	148.5	368	13.5	19.67	23	2.5	547546	schist
PT001183	5709.7	61097	151452	457.33	877.67	15799	2160.7	3576.7	53.5	648.67	27665	34	23	74	16.67	139.33	37.67	24.67	186.33	7.33	2.5	508	153	116.5	5	19	24.33	19	28	729206	schist
PT001184	6362.7	87321	298071	502	397	30579	845.33	2478.3	49.33	425.33	18404	16.33	13	44.33	12.33	280	34	9.67	105.67	7	26	644.33	142	5	5	2.5	20.67	22	2.5	553246	schist
PT001185	10081	99995	237744	432.67	453.67	26101	1916.3	5871.7	113.33	727	37983	41	23.33	81.67	18.67	205.67	46.33	19	268	12.67	41	1053.7	138	192.67	394	2.5	23.67	28.5	2.5	576209	schist
PT001186	9617.3	78295	208400	1022.7	503.33	17568	1369	4058.3	92.67	870.33	34024	38.33	21	86.67	95.67	139.33	35.67	21.67	231.67	11.33	2.5	744.67	166	200	5	25.33	26.67	34	2.5	642350	schist
PT001187	15011	89279	158451	447.67	427	23861	1555	5389.3	94	567	49266	62.33	45.33	127.67	11.67	166	44.67	23.33	187.33	9.33	2.5	533	5	140	250	2.5	29.67	2.5	40	659126	schist
PT001188	6473.5	85596	205922	667.67	663.33	24366	535.67	4983	69	658.67	33654	32.33	18.33	65	42	172.67	38.67	17.67	294.33	10	25	632.67	151	156.5	5	17	23	2.5	23.33	636963	schist
PT001189	8451.7	96539	238368	590.33	797	24168	1433	4555	75	563.33	36159	31.67	30.33	95	140.33	219	59	20.33	168.33	9	31	777.33	134	196	5	70	25.67	2.5	19	586404	granite
PT001190	8975.5	88292	189087	482	471.33	23835	1742.7	5737.3	90	1344.7	46171	49.33	44.33	108.67	48	207.33	99.67	31	288.33	13.67	32	703.67	189	175	5	17	35	2.5	24	634846	granite+schist
PT001191	11682	112309	246457	441.67	283	29303	768	5508.7	89	923	42130	41	22	82.33	18	205.33	38.33	19.33	228.33	11.33	26	1143.7	5	182	5	2.5	21.67	31	11	548130	schist
PT001192	9984	108640	237308	520.33	506	28987	1211.3	4809	85.67	597.67	37101	37	27	79.33	17.67	219.67	44.33	20	204	10	2.5	933	123	165	5	2.5	22.67	26.5	28	568337	schist
PT001193	10532	112098	235144	415.67	420.33	26577	1490	5351.7	104	923	40791	47.33	23	80	23.33	197.67	84.33	27.33	297	13.67	26	1014.7	160	224	413	2.5	28	22	19	563878	schist
PT001194	8809	84722	216726	442.67	404	21999	1370.3	4825.3	81	718	35981	34.67	26.33	73	30.33	173	47	20.67	238	9	2.5	807.67	157	239	5	2.5	24.67	2.5	16	622191	schist
PT001197	9565.3	96363	218262	793.67	699.67	25465	1735.3	4699.3	90	691.67	35821	38.33	23	79	20.67	220.67	48	21.67	214.67	10.33	2.5	949	141.5	159.33	302	2.5	28.33	24.5	2.5	603688	schist
PT001198	11799	108255	278778	510.67	336.67	27125	545.33	4045	99	449	32040	33	15	65.67	15.33	155	39.67	20	187.67	11	2.5	1054.7	139	162.67	5	2.5	17.33	36	2.5	534099	schist
PT001199	8723	90594	219174	522	478	25354	1406.7	5286.3	75.67	655	34170	34.33	24.67	79.33	17.67	209.33	48.67	22	306	10.67	2.5	779.67	110	143.5	323	17	24	2.5	15	611697	schist
PT001200	15084	98075	203245	930.67	877.67	19248	3034	4781.7	92.33	594	37750	47	35.33	104	16	126.67	39	24	171	9	2.5	617.33	136.5	173.67	5	2.5	28.33	22.33	2.5	614784	schist
PT001201	16803	98298	256392	882.67	414.67	20271	1037.3	4906.3	80.67	530.67	34879	32.67	22.33	72	27	109.33	24.33	18.67	139.33	6.33	35	702	5	180	5	2.5	16.33	29	2.5	564168	schist
PT001202	12904	83270	185015	587.33	837.33	19346	2067.3	4700.3	76	360	32762	39	30.33	90.67	15	123.67	38.33	25.33	190.67	7.67	2.5	472	105.33	128	5	2.5	26	23	34	656695	schist
PT001203	14014	71164	189087	676	880.33	15228	1185.7	4558.7	60	586	35203	39	24	79.67	13	111.67	33.33	18	150	8	2.5	440.33	119	111.5	5	2.5	23.33	2.5	41	670943	schist
PT001204	5966.3	91301	220822	428.67	437	23288	1213	4701	63.67	468	30064	29.67	19	60.67	22	161.33	46.33	20	276.33	8.67	2.5	627.67	5	119.67	418	2.5	21.67	2.5	18	619679	schist
PT001205	9069	96937	235842	481	473.67	23750	1236.3	4787	86.67	529.67	30816	30.33	15	64	27.67	174.67	46	21	270.67	12.67	23	964.33	159	166.5	370	2.5	20	30	2.5	593905	schist
PT001206	13411	99510	192857	852	597.67	21330	1949	4873.3	92	2162	46769	56.67	37.67	128.33	50.67	162	44.33	27.67	205	11.33	2.5	826.33	142.5	135.5	5	2.5	33	2.5	11.33	613735	schist
PT001207	6495.5	80117	215113	609.67	687.33	22102	1339.3	4797.3	60.33	703.33	30329	32.33	15.33	68	28	153.33	42.67	18.33	238.67	10	2.5	591.33	104	121.33	5	2.5	22	2.5	16	638349	schist
PT001208	6406	92638	231205	1445.7	529	27290	3403.3	2865	5	222.33	15926	10	10	79.33	20.67	369.33	81	10.67	104	6	27	410.33	160	123	304	2.5	35.33	2.5	34	618694	granite
PT001209	8130	95867	255885	1238.3	418.67	28280	1748.7	3071	62.5	346.67	20527	13.5	13	72.67	26.67	336.67	68.67	9	126.67	6.5	33.67	531	110	158	5	40	30.67	2.5	2.5	583004	granite
PT001210	6926.7	117214	238947	1315.3	841	23833	2270	3490	48	158.33	21612	15.33	13	106.33	6.5	320.67	69.33	12.67	167.67	7.33	2.5	488.33	141.33	151.67	278	15	35.67	27	2.5	581703	granite
PT001211	5575.5	109666	238596	984	1025.7	34847	1741	2991	5	120.67	15217	9	9.5	77.67	2.5	394.33	80	7	114	5.33	2.5	481.33	5	146.67	5	2.5	45.33	2.5	16.5	589719	granite
PT001212	7527.7	110795	249363	945.67	1445	37524	2045.3	2867.3	57	184.33	15161	10	10	71	4	367.67	67.33	5	87.67	4	25	546.33	158	165	5	14.5	35	2.5	10	570743	granite
PT001213	9285.7	93537	251612	449.33	363	29004	540.33	5069.3	80.5	495	33778	32.67	19.67	67	13	201.33	38	15	156.33	11.67	27	884	117.5	109	5	2.5	21	30.5	36	574185	schist
PT001214	9384.7	91584	231626	602.33	745	23769	2182.3	4998	100.67	580.33	34749	37.67	22	78	18.33	184.67	51	24	275.33	10	2.5	949.67	122	140.5	5	2.5	23.67	23	2.5	597762	granite
PT001215	8699	93718	242917	444	282.33	25904	1131.3	5282	85.67	766.67	37098	41	20.67	91	72	212.33	52	26	306.33	10	48.67	794.67	131	167.67	487.5	26.33	22.67	2.5	22	581233	schist
PT001216	8089.3	95836	262695	1341	438.33	28114	3590.3	2613.3	37	307.33	16446	9	11	51.67	6	315.67	79.33	11.67	105.67	6	28.67	589	126	144	5	2.5	38.33	21	11	579000	granite
PT001217	5300.7	96136	252275	1390.3	772.33	30847	2325.3	3808.3	58	393.33	20031	11	11	65	8	362.67	82.67	10.33	117.67	6	27.5	550	116.5	166	5	2.5	41	2.5	13	585173	granite

Figure A1. Final XRF results for all stream sediment samples collected discriminated according to the catchment basin lithology.

Appendix B – Graphics and maps of all elements (stream sediments)

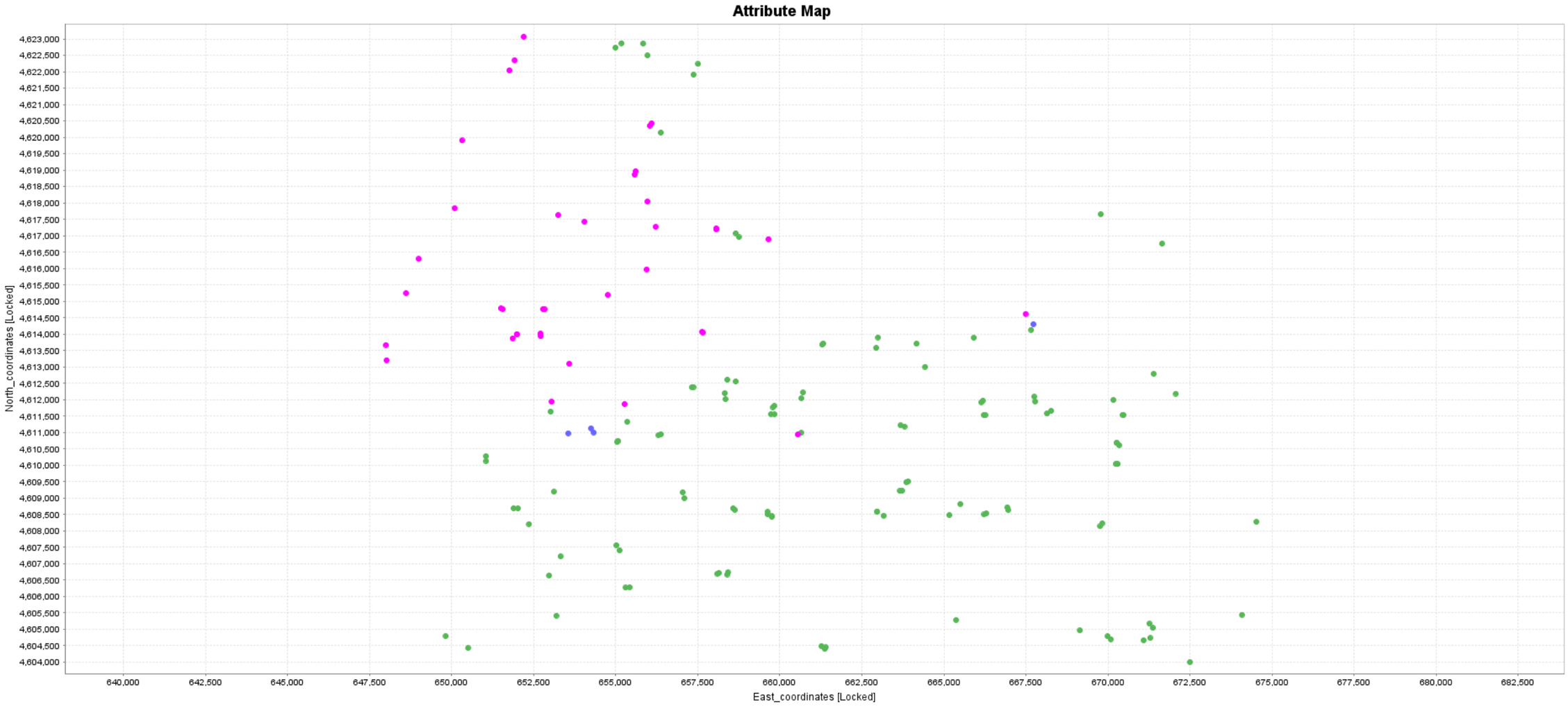


Figure B1. Geographic distribution of the lithological attributes of the stream sediment samples: green – schist, pink – granite; blue – schist+granite.

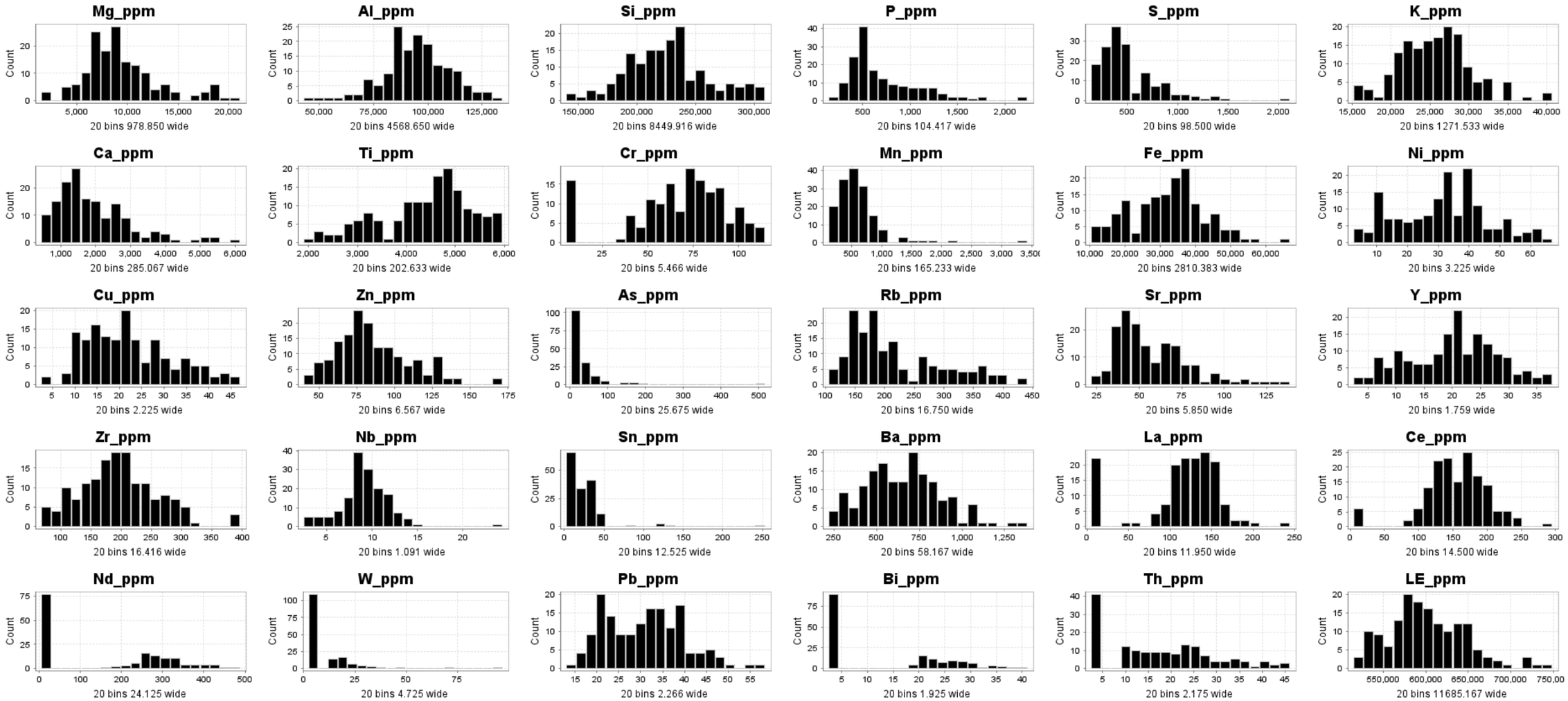


Figure B2. Histograms for all elements analyzed with XRF considering all samples (no lithological discrimination). LE – light elements.

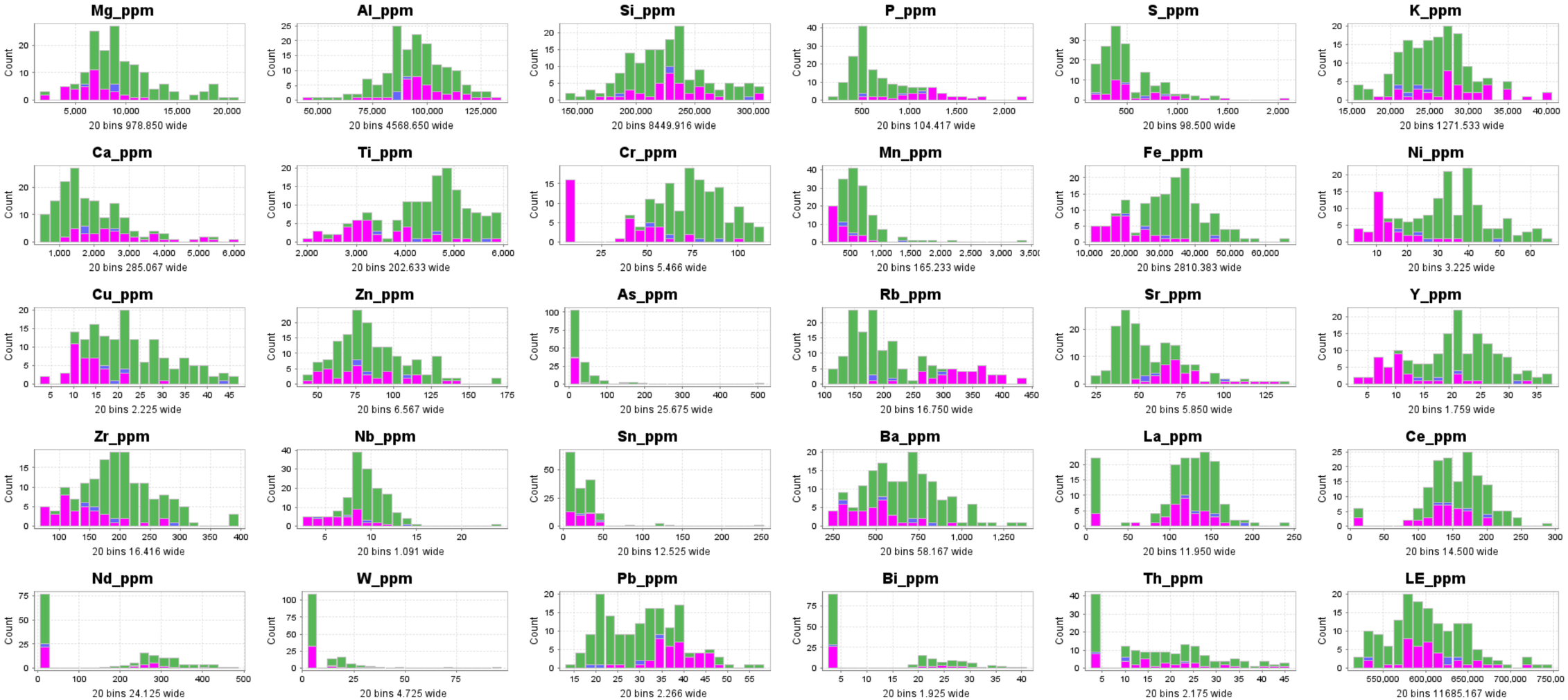


Figure B3. Histograms for all elements analyzed with XRF considering the distinct catchment basin lithologies: green – schist, pink – granite; blue – schist+granite. LE – light elements.

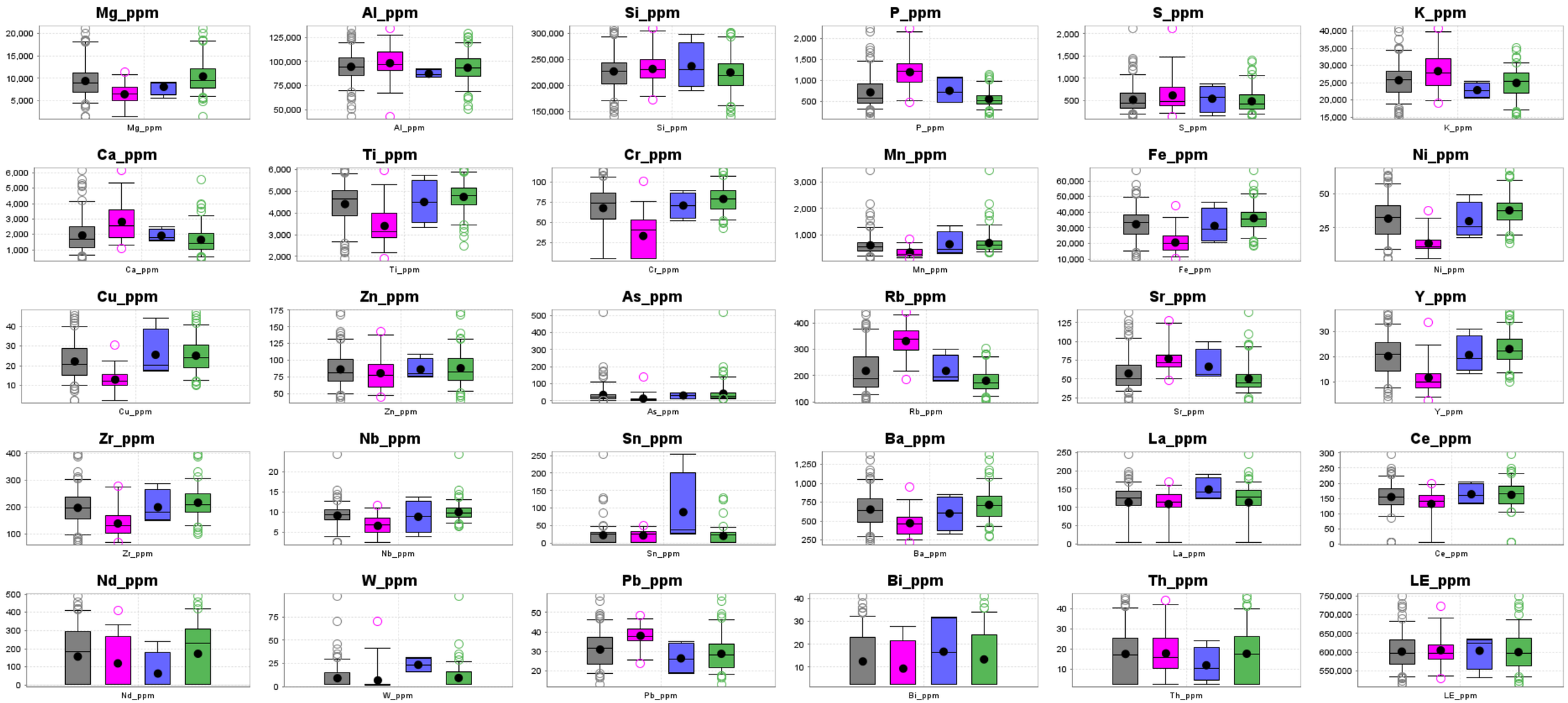


Figure B4. Boxplots for all elements analyzed with XRF considering the distinct catchment basin lithologies: green – schist, pink – granite; blue – schist+granite, grey – all lithologies. LE – light elements.

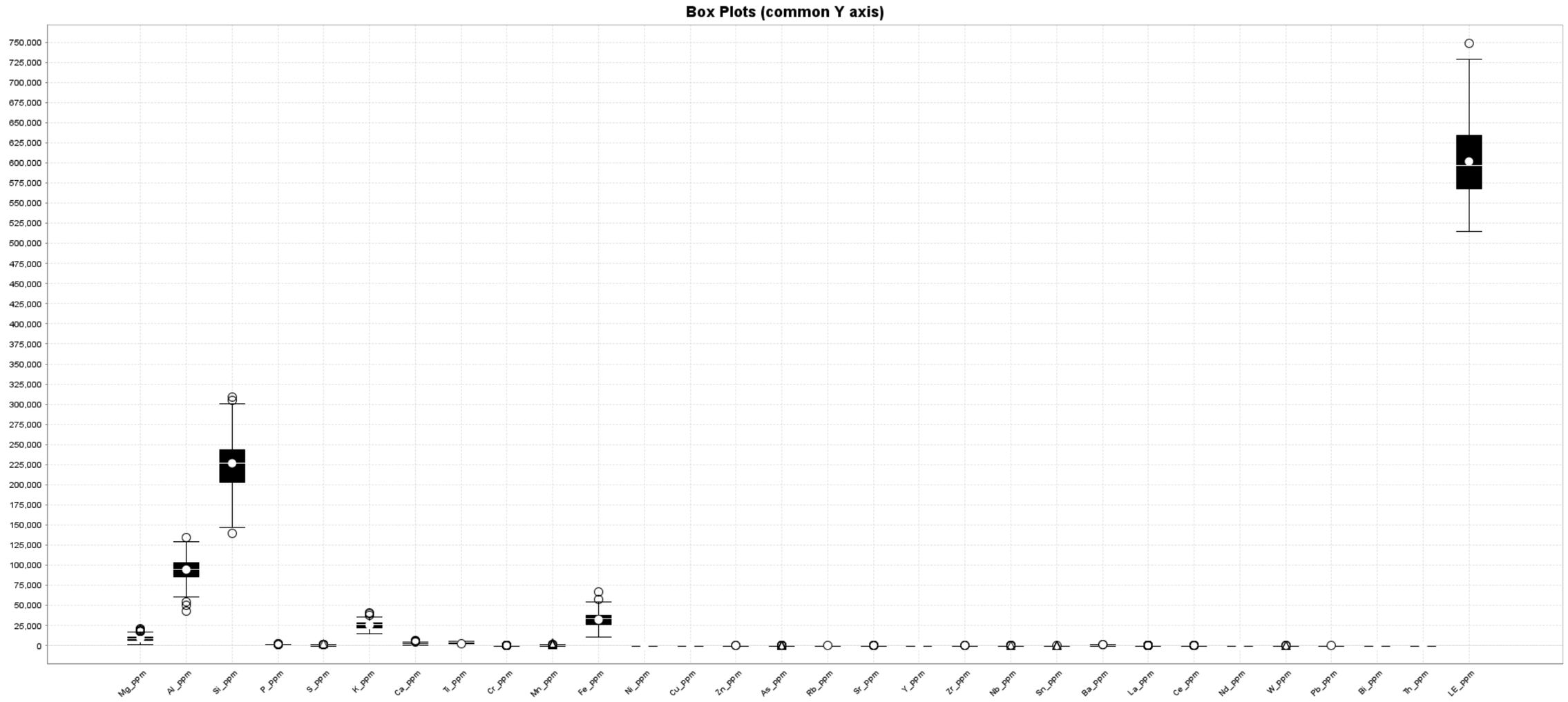


Figure B5. Boxplots for all elements analyzed with XRF (no lithological discrimination) with a common X axis (Tukey plot). LE – light elements.

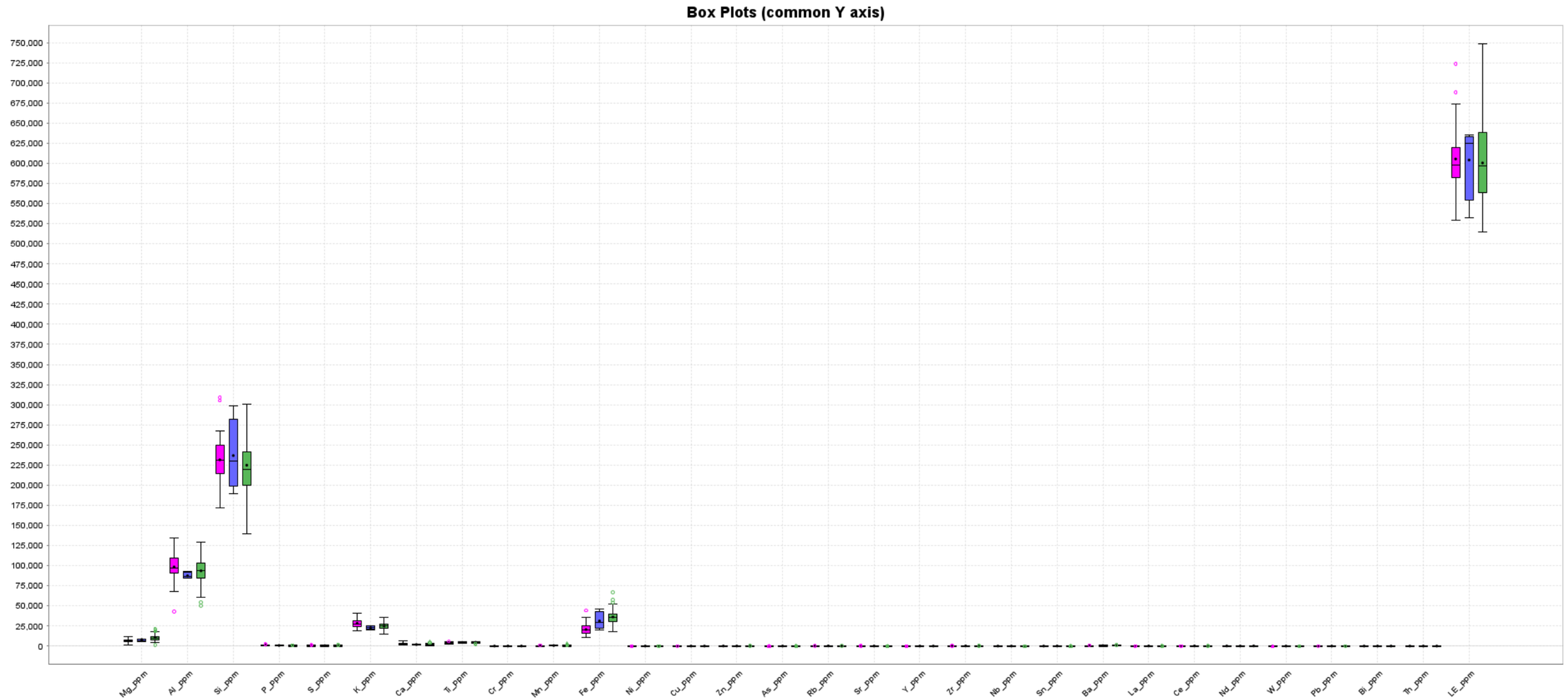


Figure B6. Boxplots for all elements analyzed with XRF with a common X axis (Tukey plot) considering the distinct catchment basin lithologies: green – schist, pink – granite; blue – schist+granite. LE – light elements.

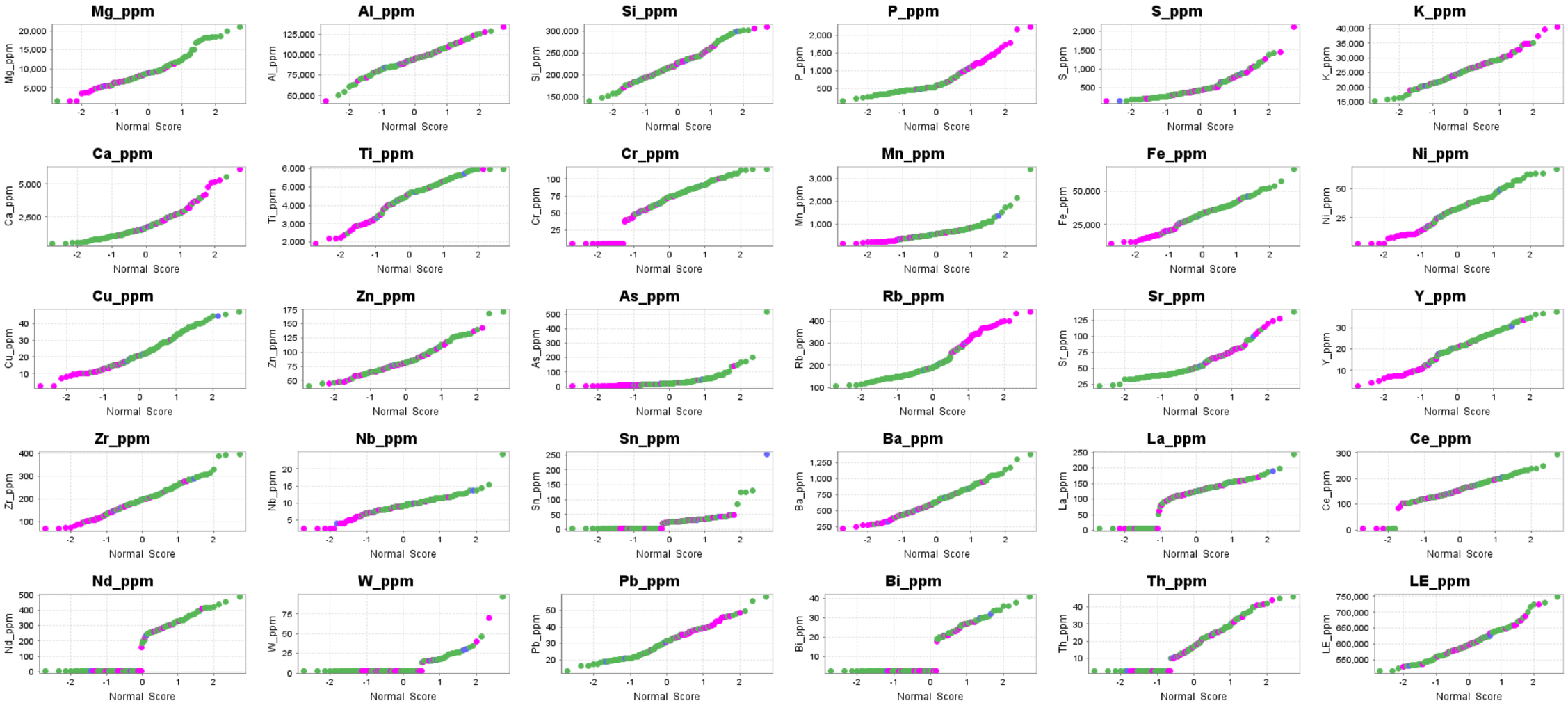


Figure B7. Normal Q-Q plots for all elements analyzed with XRF considering the whole dataset but distinguishing the catchment basin lithologies: green – schist, pink – granite; blue – schist+granite, grey – all lithologies. LE – light elements.

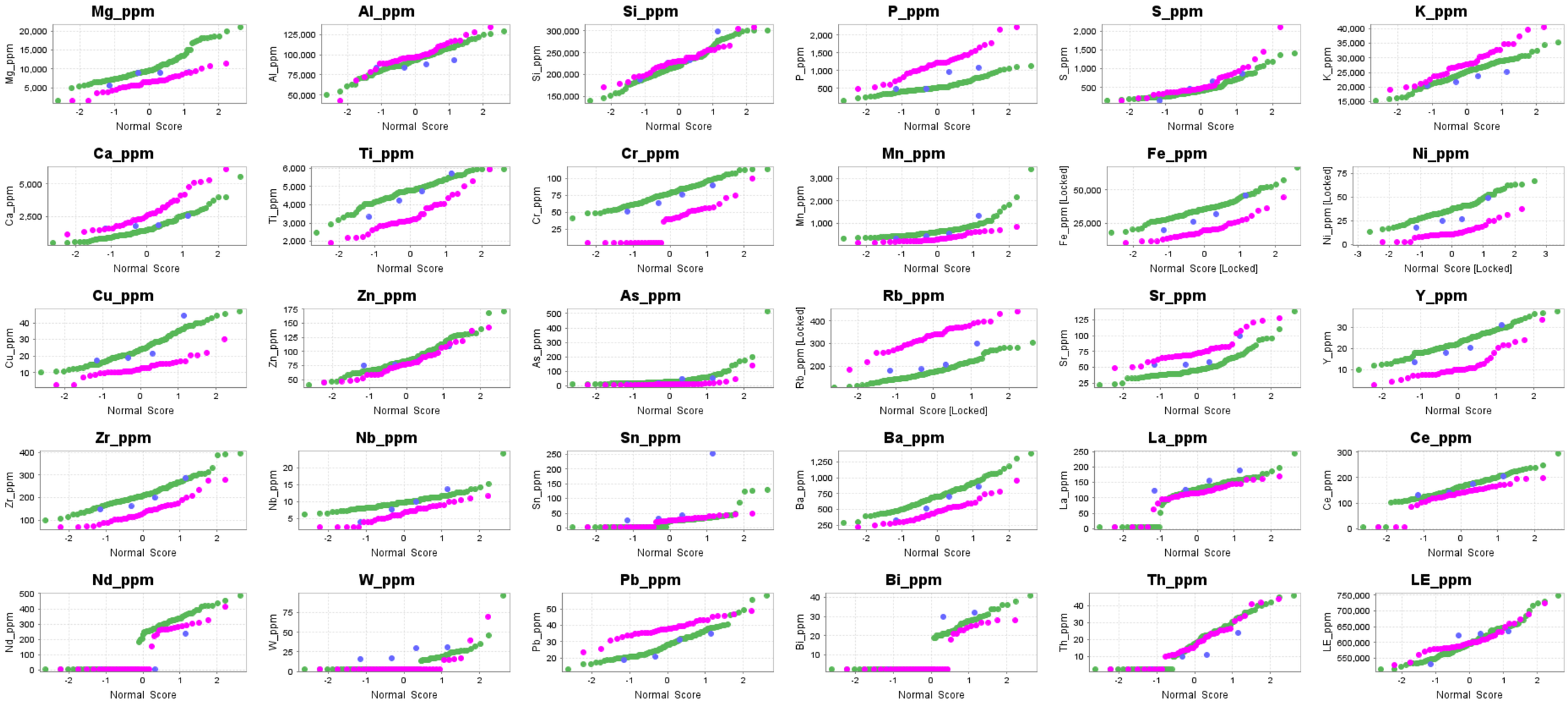
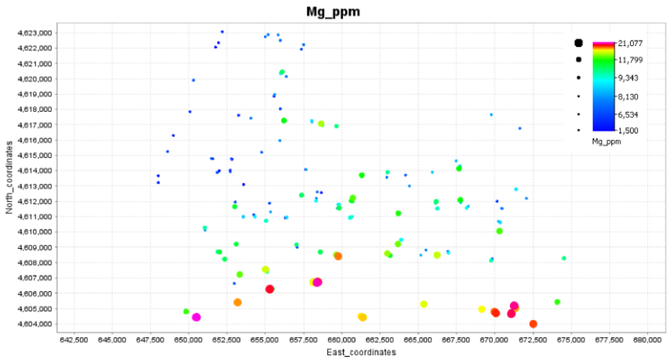
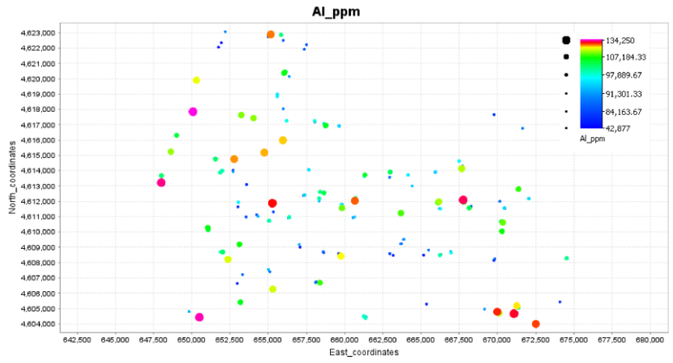
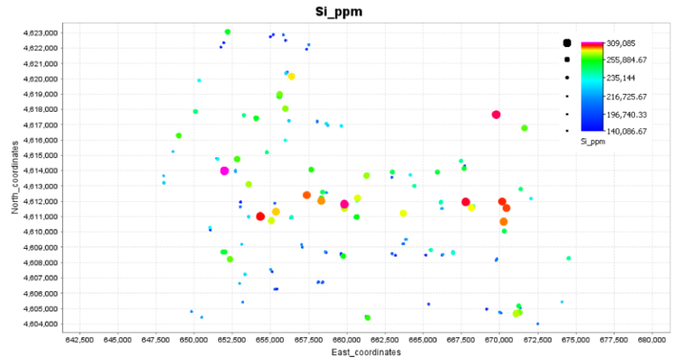
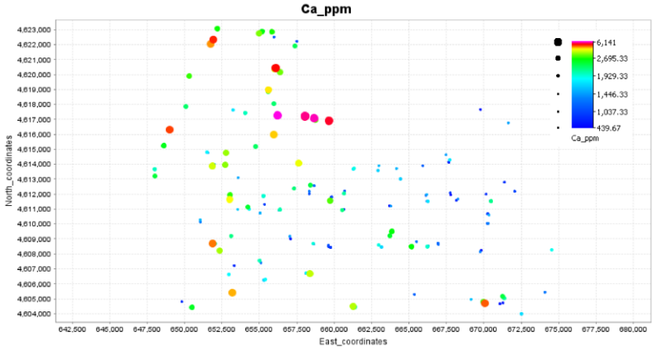


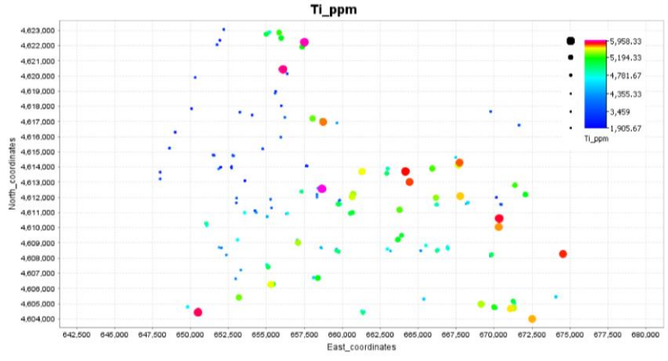
Figure B8. Split normal Q-Q plots for all elements analyzed with XRF considering a distinct population according to the catchment basin lithologies: green – schist, pink – granite; blue – schist+granite, grey – all lithologies. LE – light elements.

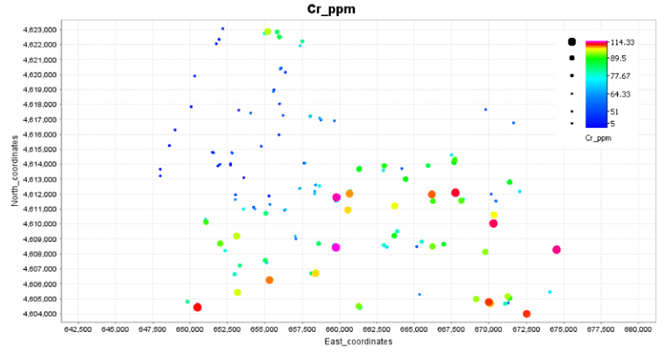

Mg_ppm
21,077
11,799
9,343
8,130
6,534
1,500
Mg_ppm
North_coordinates
East_coordinates

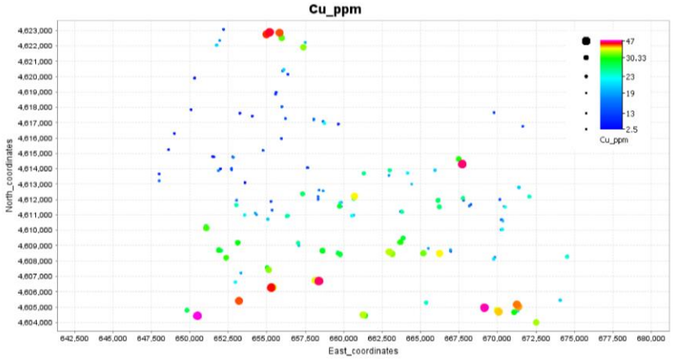

Al_ppm
134,250
107,184.33
97,889.67
91,301.33
84,163.67
42,677
Al_ppm
North_coordinates
East_coordinates

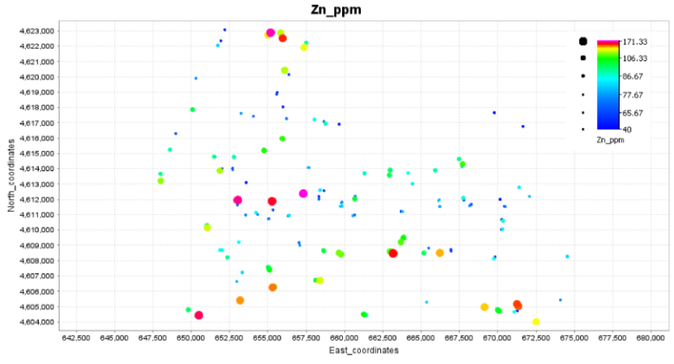

Si_ppm
309,085
255,884.67
235,144
216,725.67
196,740.33
140,086.67
Si_ppm
North_coordinates
East_coordinates

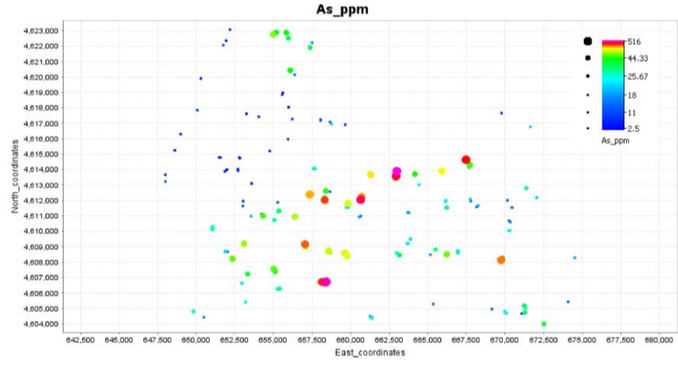

Ca_ppm
6,141
2,695.33
1,929.33
1,446.33
1,037.33
439.67
Ca_ppm
North_coordinates
East_coordinates

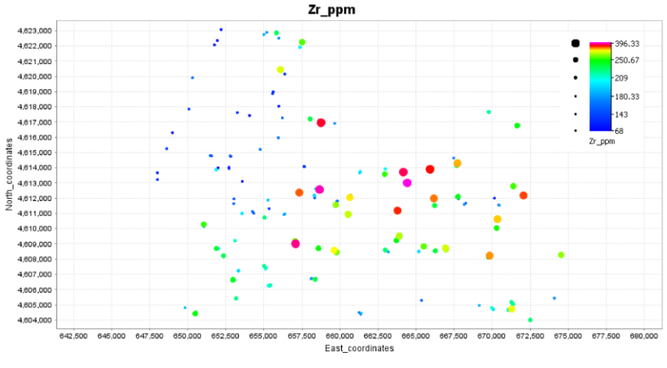

Ti_ppm
5,958.33
5,194.33
4,781.67
4,355.33
3,459
1,905.67
Ti_ppm
North_coordinates
East_coordinates

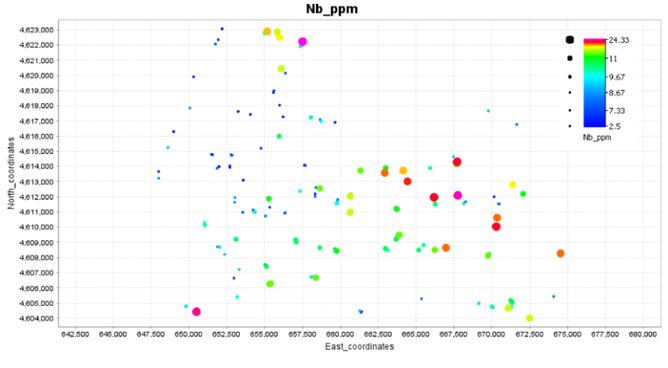

Cr_ppm
114.33
89.5
77.67
64.33
51
5
Cr_ppm
North_coordinates
East_coordinates

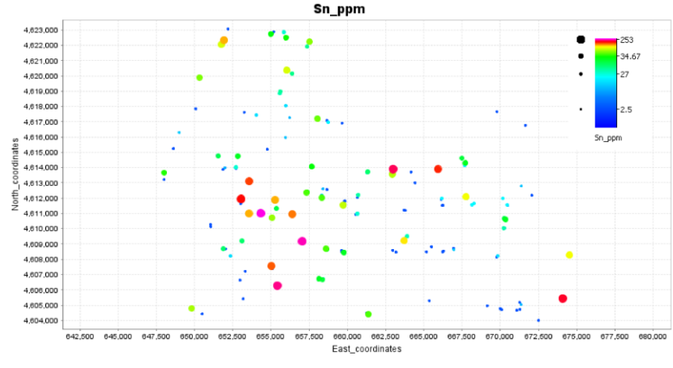

Cu_ppm
47
30.33
23
19
13
2.5
Cu_ppm
North_coordinates
East_coordinates

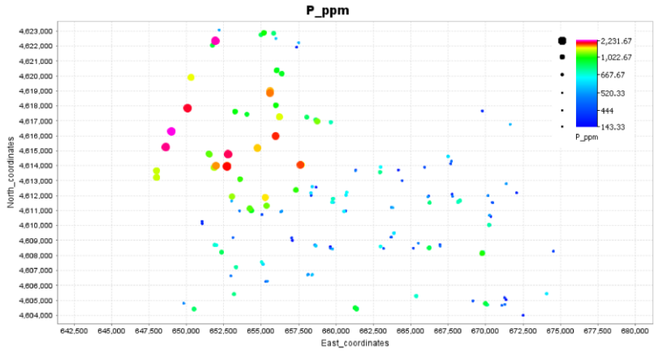

Zn_ppm
171.33
106.33
86.67
77.67
65.67
40
Zn_ppm
North_coordinates
East_coordinates

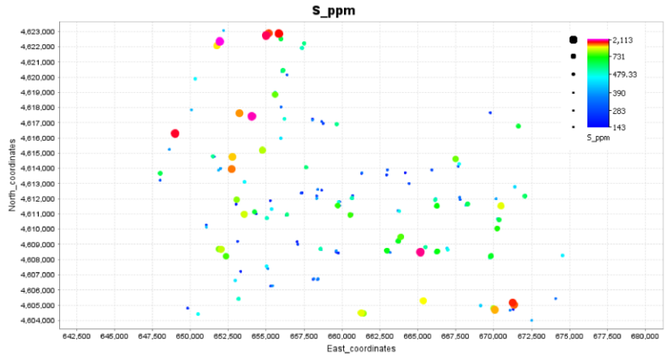

As_ppm
516
44.33
25.67
18
11
2.5
As_ppm
North_coordinates
East_coordinates

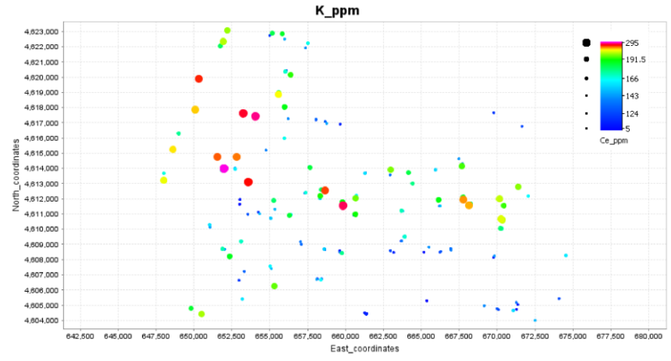

Zr_ppm
396.33
250.67
209
180.33
143
68
Zr_ppm
North_coordinates
East_coordinates

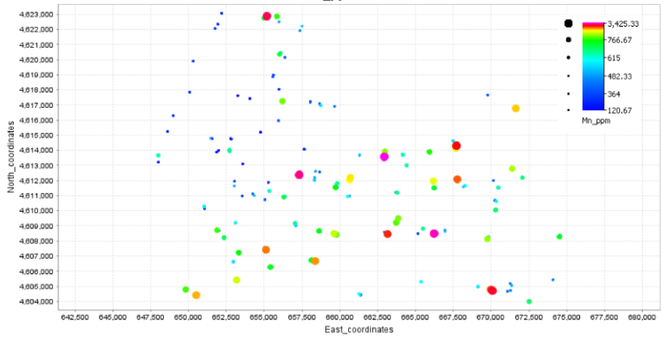

Nb_ppm
24.33
11
9.67
8.67
7.33
2.5
Nb_ppm
North_coordinates
East_coordinates

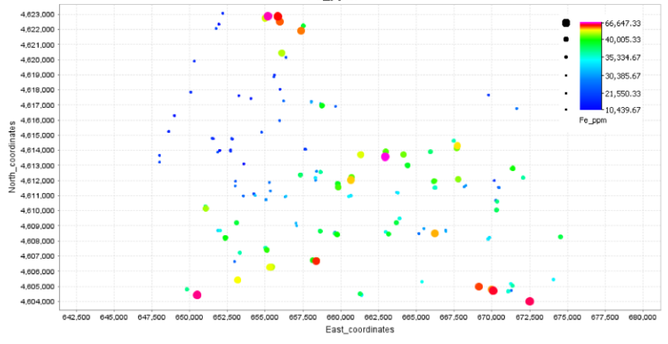

Sn_ppm
253
34.67
27
2.5
Sn_ppm
North_coordinates
East_coordinates

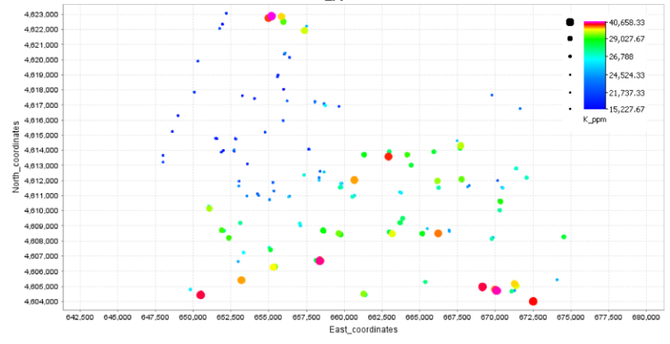

P_ppm
North_coordinates
East_coordinates
2,231.67
1,022.67
667.67
520.33
444
143.33
P_ppm

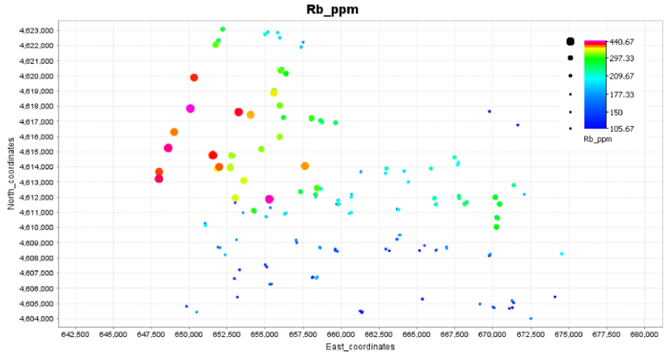

S_ppm
North_coordinates
East_coordinates
2,113
731
479.33
390
283
143
S_ppm

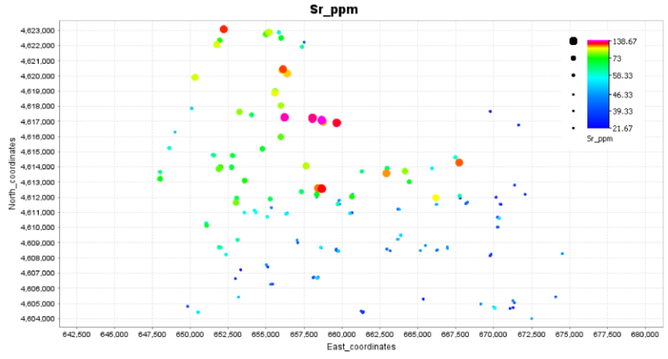

K_ppm
North_coordinates
East_coordinates
295
191.5
166
143
124
5
Ce_ppm

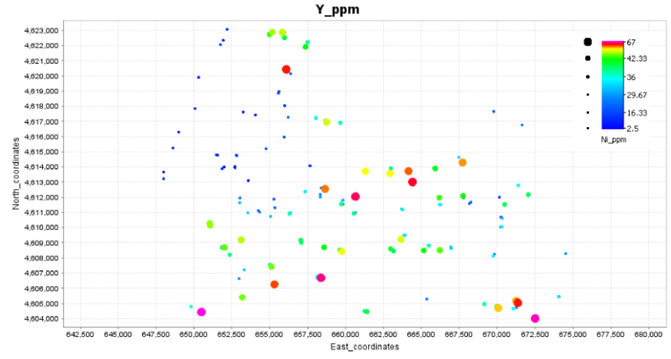

Mn_ppm
North_coordinates
East_coordinates
3,425.33
766.67
615
482.33
364
120.67
Mn_ppm

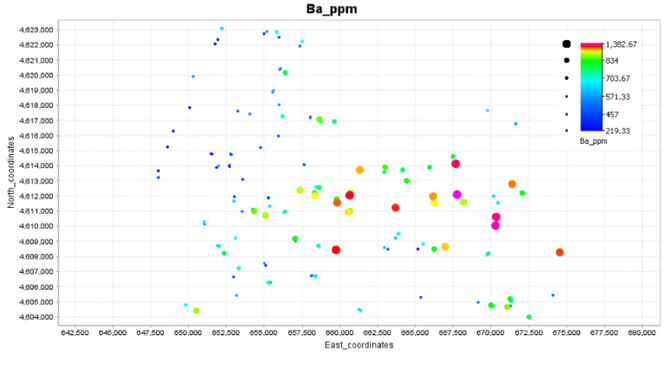

Fe_ppm
North_coordinates
East_coordinates
66,647.33
40,005.33
35,334.67
30,385.67
21,550.33
10,439.67
Fe_ppm

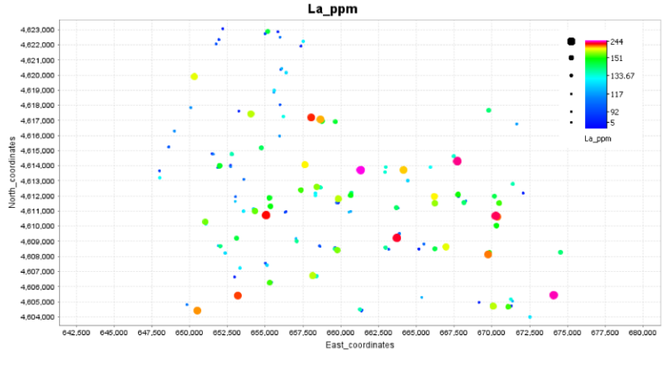

Ni_ppm
North_coordinates
East_coordinates
40,658.33
29,027.67
26,788
24,524.33
21,737.33
15,227.67
K_ppm

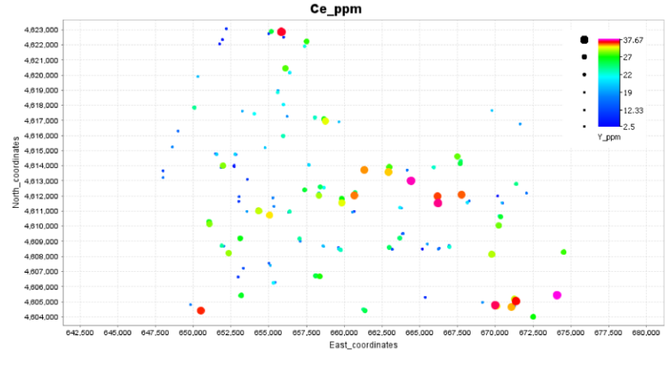

Rb_ppm
North_coordinates
East_coordinates
440.67
297.33
209.67
177.33
150
105.67
Rb_ppm


Sr_ppm
North_coordinates
East_coordinates
138.67
73
58.33
46.33
39.33
21.67
Sr_ppm


Y_ppm
North_coordinates
East_coordinates
67
42.33
36
29.67
16.33
2.5
Ni_ppm


Ba_ppm
North_coordinates
East_coordinates
1,382.67
834
703.67
571.33
457
219.33
Ba_ppm


La_ppm
North_coordinates
East_coordinates
244
151
133.67
117
92
5
La_ppm


Ce_ppm
North_coordinates
East_coordinates
37.67
27
22
19
12.33
2.5
Y_ppm

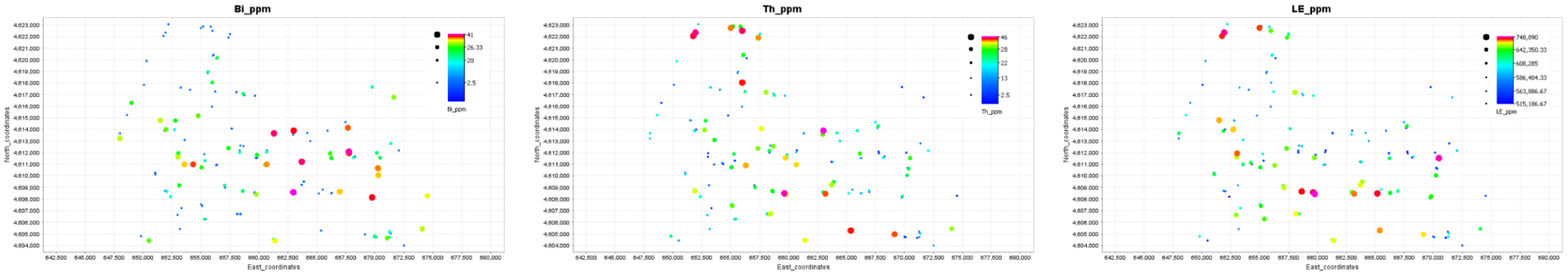
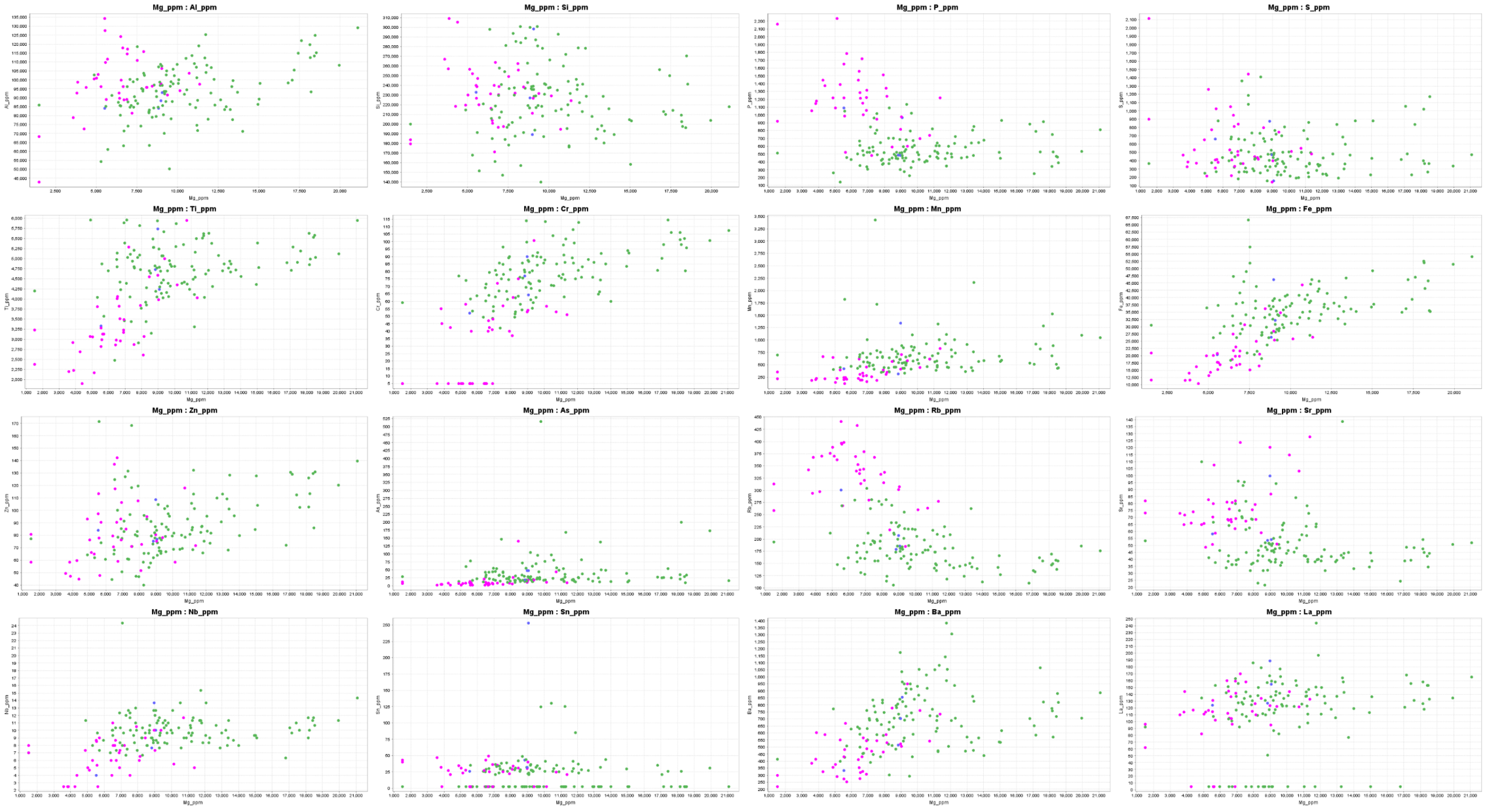


Figure B9. Geographical distribution of the all elements analyzed with XRF within the Circo license. LE – light elements.


Mg_ppm : Al_ppm
Mg_ppm : Si_ppm
Mg_ppm : P_ppm
Mg_ppm : S_ppm
Mg_ppm : Ti_ppm
Mg_ppm : Cr_ppm
Mg_ppm : Mn_ppm
Mg_ppm : Fe_ppm
Mg_ppm : Zn_ppm
Mg_ppm : As_ppm
Mg_ppm : Rb_ppm
Mg_ppm : Sr_ppm
Mg_ppm : Nb_ppm
Mg_ppm : Sn_ppm
Mg_ppm : Ba_ppm
Mg_ppm : La_ppm
Mg_ppm

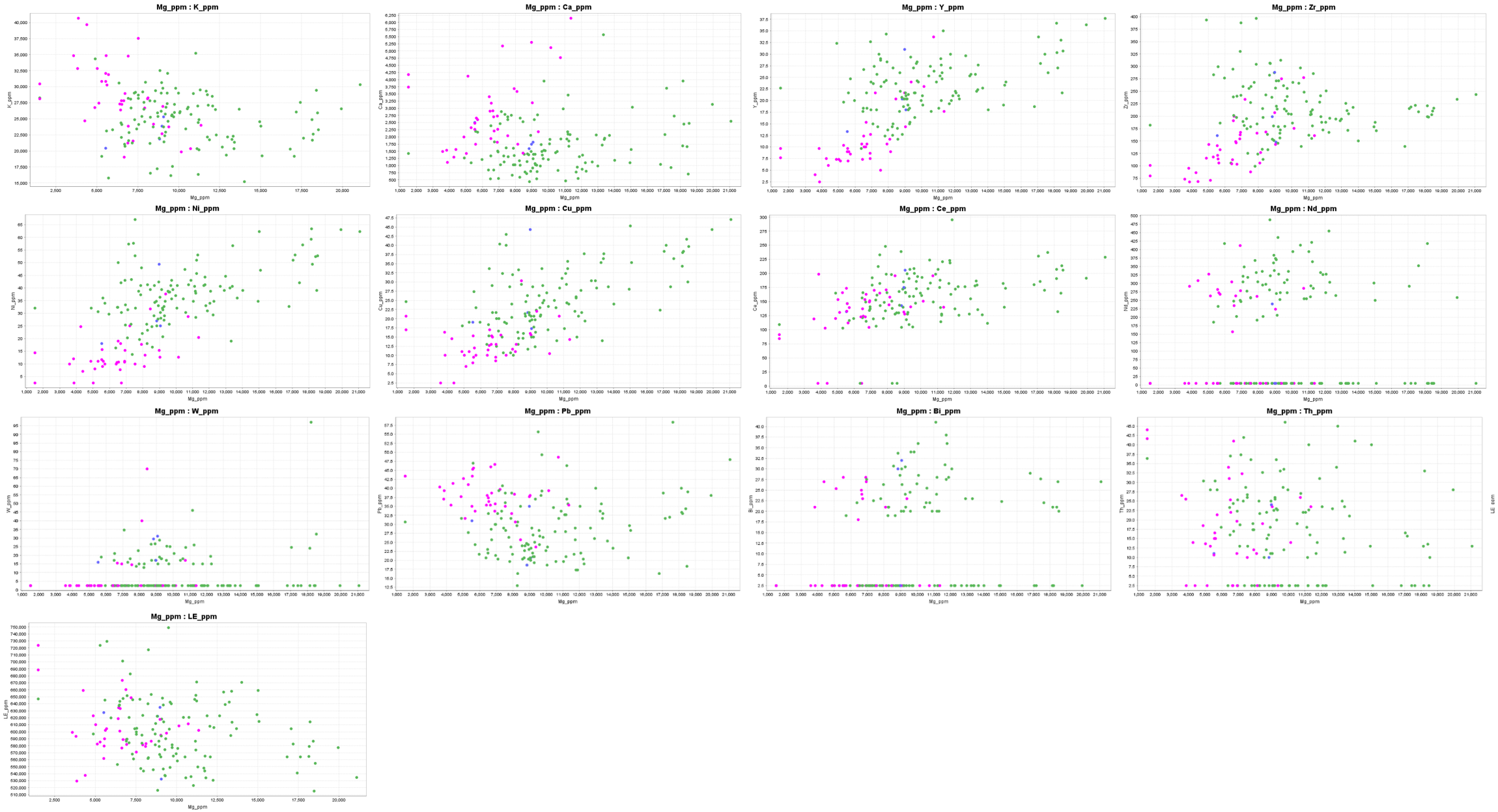


Figure B10. Dispersion plots considering the distinct catchment basin lithologies: green – schist, pink – granite; blue – schist+granite. LE – light elements.

Appendix C – Basic statistics of all stream sediment samples

	Mg_ppm	Al_ppm	Si_ppm	P_ppm	S_ppm	K_ppm	Ca_ppm	Ti_ppm	Cr_ppm	Mn_ppm	Fe_ppm	Ni_ppm	Cu_ppm	Zn_ppm	As_ppm	Rb_ppm	Sr_ppm	Y_ppm	Zr_ppm	Nb_ppm	Sn_ppm	Ba_ppm	La_ppm	Ce_ppm	Nd_ppm	W_ppm	Pb_ppm	Bi_ppm	Th_ppm	LE_ppm
[Visible] : Count Numeric	157	157	157	157	157	157	157	157	157	157	157	157	157	157	157	157	157	157	157	157	157	157	157	157	157	157	157	157	157
[Visible] : Count Text	0	0	0	0	0	0	0	0	0	0	0	0	0	0	0	0	0	0	0	0	0	0	0	0	0	0	0	0	0
[Visible] : Count Null	0	0	0	0	0	0	0	0	0	0	0	0	0	0	0	0	0	0	0	0	0	0	0	0	0	0	0	0	0
[Visible] : Count Negative	0	0	0	0	0	0	0	0	0	0	0	0	0	0	0	0	0	0	0	0	0	0	0	0	0	0	0	0	0
[Visible] : Count Zero	0	0	0	0	0	0	0	0	0	0	0	0	0	0	0	0	0	0	0	0	0	0	0	0	0	0	0	0	0
[Visible] : Unique Values	155	157	156	148	150	157	157	154	110	151	157	94	82	119	111	135	107	76	143	37	46	149	95	124	69	30	79	32	61	157
[Visible] : Minimum	1500	42877	140086.7	143.33	143	15227.67	439.67	1905.67	5	120.67	10439.67	2.5	2.5	40	2.5	105.67	21.67	2.5	68	2.5	2.5	219.33	5	5	5	2.5	13	2.5	2.5	515186.7
[Visible] : Maximum	21077	134250	309085	2231.67	2113	40658.33	6141	5958.33	114.33	3425.33	66647.33	67	47	171.33	516	440.67	138.67	37.67	396.33	24.33	253	1382.67	244	295	487.5	97	58.33	41	46	748890
[Visible] : Mean	9403.719	94576.64	226735.7	716.396	516.553	25707.56	1934.88	4412.51	67.6313	612.9689	32275.56	31.7082	22.2048	86.2322	34.4641	217.923	57.4383	20.2152	196.785	9.14274	22.6296	653.336	113.34	154.452	156.876	8.95331	30.8916	12.4862	17.4862	601837
[Visible] : Median	8928.67	94608.67	226969.7	587.33	431.67	25904.33	1672.33	4646.33	73.67	557.33	33193.33	32.67	20.67	81.67	21	188.67	51	21	196	9.33	25	643	125	155	185	2.5	31.67	2.5	17	596700.3
[Visible] : Range	19577	91373	168998.3	2088.34	1970	25430.66	5701.33	4052.66	109.33	3304.66	56207.66	64.5	44.5	131.33	513.5	335	117	35.17	328.33	21.83	250.5	1163.34	239	290	482.5	94.5	45.33	38.5	43.5	233703.3
[Visible] : Interquartile Range	4272.165	18218.33	40527.34	464.33	330.5	6069.495	1344.84	1164.5	31.835	301.5	12289.5	21	13.67	32.495	24.5	113.375	27.34	11.34	84.335	2.67	29	305.335	39.25	53.665	291	12.5	13.835	20.5	22.915	65743.33
[Visible] : Standard Deviation	3724.265	15295.02	34888.57	376.365	296.48	4551.114	1083.66	928.526	27.4689	385.8339	10391.62	14.6633	9.56017	24.5487	50.8308	79.5172	21.7189	7.70218	64.3999	2.73041	28.4478	221.85	50.4374	46.6242	156.518	12.6789	8.7305	11.9422	11.9365	45310.32
[Visible] : Variance	1.39E+07	2.34E+08	1.22E+09	141650	87900.6	2.07E+07	1174315	862161	754.541	148867.8	1.08E+08	215.011	91.3968	602.639	2583.77	6322.99	471.71	59.3235	4147.35	7.45512	809.277	49217.5	2543.94	2173.82	24497.8	160.754	76.2216	142.617	142.48	2.05E+09
[Visible] : Skewness	0.869534	-0.24118	0.20024	1.47642	1.90544	0.349322	1.39625	-0.5763	-0.8879	3.391048	0.122512	0.02086	0.51718	0.79078	6.19313	0.91242	1.2613	-0.1259	0.39614	0.65535	4.36469	0.46492	-1.0703	-0.8099	0.23418	3.417	0.38005	0.53088	0.33061	0.603629
[Visible] : Tukey Upper Outlier Threshold	17603.25	131026.8	304248.3	1622.5	1154.75	37500.91	4510.92	6799.25	133.753	1165.415	56668.75	72.5	49.175	149.907	74.085	440.227	109.68	42.68	364.838	14.675	75	1250.84	202.375	263.163	732.5	33.75	57.9175	53.75	59.7875	732488
[Visible] : 1 percentile	1500	47096.5	144233.1	189.15	150.349	15559.04	451.85	2060.33	5	133.2328	11087.14	2.5	2.5	42.5114	2.5	107.793	22.4414	3.37	68.1914	2.5	2.5	238.279	5	5	5	2.5	14.9314	2.5	2.5	515709.3
[Visible] : 5 percentile	4369.8	69821.16	170968.7	326.833	203.836	18863.43	658.547	2685.33	5	196.497	15073.7	8.9	9.95	49.164	3.85	126.37	33.23	7.33	94.267	4	2.5	300.436	5	90.35	5	2.5	18.67	2.5	2.5	534148.2
[Visible] : 10 percentile	5534.602	77090.86	184722.3	377.934	229.13	20331	820.666	2989.33	5	236.73	17450.94	10.67	10.67	58.33	7	139.33	36.602	9	111.336	5.9	2.5	372.864	5	109	5	2.5	20.264	2.5	2.5	544003.1
[Visible] : 25 percentile	6922.835	85481	202930	461.67	328.5	22327.17	1148.83	3888	54.165	411.665	25945	20	15	68.67	12.835	156.79	41.33	14.33	154	8	2.5	487.5	104.25	129	5	2.5	23.33	2.5	2.5	568129.7
[Visible] : 75 percentile	11195	103699.3	243457.3	926	659	28396.67	2493.67	5052.5	86	713.165	38234.5	41	28.67	101.165	37.335	270.165	68.67	25.67	238.335	10.67	31.5	792.835	143.5	182.665	296	15	37.165	23	25.415	633873
[Visible] : 90 percentile	14962.36	114606.8	279183.3	1225.27	878.202	30815.26	3415.46	5542.06	99.134	940.2	45830.27	51.266	36.598	124.936	70.136	344.934	83.002	30	282.53	11.736	41	949	159.2	207.066	361.2	24.534	41.598	28.6	34	656974
[Visible] : 95 percentile	18147.2	119964.3	294122.4	1452.4	1090.5	34386.26	4130.3	5828.47	106	1291.136	49489.13	57.364	40.033	131.067	108.233	376.036	103.764	33.067	304.497	12.703	47.167	1053.77	168.2	224.5	412.1	29.65	46.364	32.167	40.1	683510.4
[Visible] : 99 percentile	20418.51	131266.9	306868.6	2189.52	1725.56	40080.07	5808.27	5957.56	114.139	2692.599	61312.3	64.8714	46.0314	169.59	332.72	436.03	132.29	37.09	394.59	19.11	181.66	1337.43	216.74	267.74	468.65	81.34	56.7872	39.26	45.42	737473.5

Figure C1. Basic statistics for the entire dataset (all samples), generated by ioGAS.

Appendix D – PCA applied to the stream sediment samples

Eigenvectors	PC1	PC2	PC3	PC4	PC5	PC6	PC7	PC8	PC9	PC10	PC11	PC12	PC13	PC14	PC15	PC16	PC17	PC18	PC19	PC20	PC21	PC22	PC23	PC24	PC25	PC26	PC27	PC28	PC29	PC30
Mg_ppm	0.226	0.080	0.093	0.194	0.308	0.060	0.180	0.081	0.152	0.078	0.220	0.232	0.011	0.169	0.141	0.143	0.060	0.461	0.291	0.077	0.046	0.098	0.065	0.117	0.448	0.023	0.111	0.048	0.061	0.053
Al_ppm	0.034	0.241	0.410	0.168	-0.006	-0.173	0.073	0.057	0.147	0.034	0.024	-0.198	-0.060	0.055	0.110	0.058	-0.065	-0.187	0.241	0.245	0.269	-0.004	0.193	0.051	-0.277	0.287	-0.335	-0.021	-0.117	0.258
Si_ppm	-0.114	0.399	-0.011	-0.045	0.019	-0.005	0.101	0.080	-0.111	0.016	-0.003	0.091	0.096	0.016	0.052	0.171	-0.282	-0.012	-0.368	0.104	-0.341	-0.033	-0.074	0.026	0.036	0.057	0.239	0.048	-0.025	0.577
P_ppm	-0.225	-0.073	0.251	0.094	0.176	-0.083	-0.115	-0.240	-0.084	-0.101	-0.013	-0.166	0.170	0.199	0.145	0.146	-0.073	0.064	0.074	-0.595	-0.228	0.366	0.090	-0.151	-0.050	0.121	-0.015	0.025	-0.066	0.004
S_ppm	-0.048	-0.180	0.057	0.292	0.272	-0.046	-0.372	0.131	-0.352	0.179	-0.540	-0.077	0.089	0.001	-0.157	0.149	-0.004	-0.016	0.047	0.303	-0.043	0.049	0.043	0.120	0.137	0.011	0.026	-0.026	0.046	0.002
K_ppm	-0.137	0.204	0.215	-0.061	-0.215	-0.411	0.097	0.047	-0.096	0.195	-0.274	0.176	-0.086	-0.104	-0.047	0.038	0.066	0.095	-0.012	-0.380	0.264	-0.181	-0.064	0.049	0.285	-0.327	-0.160	-0.032	-0.006	0.082
Ca_ppm	-0.066	-0.191	0.338	0.032	0.122	0.418	-0.078	0.132	-0.202	0.169	0.172	0.014	0.036	0.066	0.303	0.150	-0.012	0.083	-0.084	-0.072	0.108	-0.481	-0.085	-0.161	-0.230	-0.250	-0.011	0.001	0.025	0.031
Ti_ppm	0.292	0.008	0.038	-0.016	-0.211	0.086	-0.004	0.052	0.073	0.174	-0.069	-0.114	0.079	0.071	0.162	0.042	-0.010	-0.052	0.196	-0.023	-0.253	0.249	-0.166	0.460	-0.207	-0.452	0.047	-0.138	-0.300	0.021
Cr_ppm	0.282	0.126	-0.040	0.059	0.063	0.040	0.030	0.069	-0.117	0.091	-0.060	0.110	-0.057	-0.179	-0.066	-0.067	0.328	-0.114	0.132	-0.323	-0.396	-0.385	0.392	0.142	-0.090	0.268	0.046	-0.053	-0.033	0.003
Mn_ppm	0.191	-0.057	0.091	-0.092	0.016	-0.131	0.116	-0.362	-0.531	-0.396	0.134	-0.081	0.193	-0.197	0.025	-0.118	-0.209	0.178	0.109	0.115	0.059	-0.169	-0.047	0.182	0.076	0.021	-0.049	-0.195	-0.118	0.013
Fe_ppm	0.306	-0.034	0.108	-0.011	-0.021	-0.104	0.041	-0.061	-0.131	0.000	0.010	0.018	0.095	-0.037	0.134	-0.132	0.061	-0.154	-0.056	-0.011	0.090	0.241	0.210	-0.007	-0.154	-0.234	0.120	0.124	0.733	0.163
Ni_ppm	0.308	-0.062	0.028	0.083	0.065	-0.129	0.014	-0.019	-0.106	-0.003	-0.013	0.081	-0.026	-0.072	-0.026	-0.034	-0.089	-0.156	-0.015	-0.027	0.180	0.034	0.086	-0.232	-0.030	-0.110	0.287	0.643	-0.458	-0.008
Cu_ppm	0.266	-0.150	0.054	0.114	0.186	-0.153	0.032	0.072	0.036	0.095	-0.001	0.188	-0.021	-0.092	0.028	0.040	-0.014	-0.132	-0.162	-0.231	0.185	0.038	-0.619	0.165	-0.156	0.404	0.123	-0.137	0.067	-0.004
Zn_ppm	0.174	-0.207	0.259	0.096	0.126	-0.253	0.003	-0.078	0.286	-0.058	0.066	-0.198	-0.055	-0.058	0.093	-0.113	0.017	-0.260	-0.117	0.138	-0.441	-0.197	-0.182	-0.219	0.367	-0.162	-0.175	-0.023	0.026	0.005
As_ppm	0.121	0.010	0.025	-0.494	0.218	-0.193	0.007	0.012	-0.235	-0.030	0.132	-0.145	-0.315	0.458	-0.191	0.312	0.308	-0.065	-0.064	0.075	-0.012	0.005	-0.049	0.049	-0.037	-0.032	-0.022	0.022	-0.014	0.003
Rb_ppm	-0.259	0.014	0.279	-0.061	-0.094	-0.117	0.007	-0.027	0.091	-0.031	-0.032	-0.218	-0.083	-0.052	0.028	-0.140	0.200	-0.003	0.240	0.103	0.047	-0.089	-0.051	-0.034	0.000	0.046	0.765	-0.174	0.006	-0.006
Sr_ppm	-0.098	-0.106	0.362	-0.210	-0.202	0.359	0.089	0.145	-0.230	0.122	0.079	-0.028	-0.046	-0.122	0.043	-0.219	0.148	-0.168	-0.154	0.013	-0.006	0.290	0.000	0.219	0.381	0.256	-0.094	0.187	-0.061	-0.010
Y_ppm	0.302	-0.069	0.072	0.002	-0.045	0.119	0.039	0.063	-0.004	0.063	0.001	0.036	-0.091	-0.050	-0.095	0.156	-0.133	-0.112	-0.249	-0.049	0.183	0.210	0.322	-0.328	0.141	-0.043	0.129	-0.608	-0.192	0.011
Zr_ppm	0.229	-0.031	-0.032	-0.064	-0.395	0.176	-0.061	0.030	0.041	-0.014	-0.059	-0.298	-0.024	0.036	-0.172	0.411	-0.358	-0.070	0.295	-0.156	0.007	-0.185	-0.101	-0.043	0.219	0.172	0.068	0.156	0.241	-0.005
Nb_ppm	0.250	0.027	0.038	-0.002	-0.197	-0.036	-0.216	-0.202	0.166	0.071	-0.171	-0.339	-0.057	-0.033	0.184	0.000	0.191	0.535	-0.460	0.032	0.061	-0.050	0.067	0.061	-0.048	0.166	0.004	0.106	-0.035	0.000
Sn_ppm	-0.004	0.046	0.015	-0.499	0.206	-0.031	-0.247	-0.334	0.189	0.453	0.079	0.106	0.347	-0.306	0.016	0.133	-0.046	-0.073	0.129	0.090	0.045	-0.004	0.049	-0.028	0.033	0.059	-0.011	0.004	-0.020	0.000
Ba_ppm	0.170	0.331	0.045	-0.008	-0.096	0.109	0.000	0.034	-0.250	0.141	-0.070	-0.009	-0.033	-0.108	-0.088	-0.148	0.192	0.219	0.253	0.093	-0.180	0.197	-0.359	-0.563	-0.114	0.031	-0.132	-0.038	0.017	0.004
La_ppm	0.054	0.118	0.229	-0.141	0.071	0.319	-0.087	-0.296	0.202	-0.451	-0.433	0.382	-0.268	-0.068	0.094	0.154	0.054	-0.079	0.045	0.050	-0.011	0.023	-0.058	0.026	-0.026	-0.047	-0.016	0.033	0.019	0.003
Ce_ppm	0.169	0.144	0.230	-0.081	-0.002	0.113	-0.162	0.069	0.162	-0.109	-0.085	0.081	0.479	0.470	-0.398	-0.376	-0.028	0.002	-0.078	-0.070	0.083	-0.151	-0.032	0.011	0.026	0.000	0.022	-0.028	-0.023	0.003
Nd_ppm	0.033	0.087	0.064	-0.021	-0.184	-0.202	-0.735	0.289	-0.047	-0.218	0.359	0.239	-0.131	-0.079	0.117	-0.012	-0.051	0.031	0.051	-0.007	-0.046	0.057	0.026	0.030	0.041	0.010	0.005	-0.032	-0.007	0.001
W_ppm	0.059	0.036	-0.025	-0.374	0.393	0.014	0.053	0.532	0.119	-0.217	-0.207	-0.305	-0.018	-0.272	0.090	-0.162	-0.214	0.162	0.057	-0.155	0.041	0.038	0.032	-0.003	-0.032	-0.052	-0.034	0.017	0.010	0.001
Pb_ppm	-0.060	-0.239	0.361	0.022	-0.013	-0.050	0.097	0.009	0.109	0.060	0.150	0.128	-0.175	-0.243	-0.594	0.074	-0.177	0.319	-0.056	0.040	-0.210	0.083	0.066	0.089	-0.278	-0.074	-0.011	0.080	0.060	-0.001
Bi_ppm	0.012	0.280	-0.051	0.121	0.265	0.183	-0.196	-0.300	-0.048	0.247	0.105	-0.184	-0.495	0.065	-0.108	-0.364	-0.316	-0.067	0.001	-0.140	0.079	-0.027	-0.030	0.140	0.076	-0.095	0.031	-0.023	0.056	0.000
Th_ppm	0.031	-0.310	0.000	-0.256	-0.162	-0.176	0.076	0.012	-0.053	0.220	-0.235	0.286	-0.199	0.335	0.278	-0.278	-0.364	0.140	0.123	0.089	-0.173	-0.057	0.108	-0.100	-0.077	0.210	0.007	-0.035	0.000	-0.007
LE_ppm	-0.005	-0.408	-0.201	-0.031	-0.015	0.110	-0.129	-0.079	0.076	-0.051	0.000	-0.037	-0.075	-0.027	-0.125	-0.148	0.214	0.059	0.193	-0.121	0.125	0.003	-0.050	-0.051	0.053	-0.028	-0.076	-0.032	-0.095	0.750

Figure D1. Eigenvector table for the PCA conducted for all available variables.

	Eigenvalues	Percent	Cumulative %
PC1	9.17	30.55	30.55
PC2	4.73	15.76	46.31
PC3	2.96	9.86	56.17
PC4	1.70	5.66	61.82
PC5	1.56	5.19	67.01
PC6	1.29	4.28	71.30
PC7	1.05	3.48	74.78
PC8	0.91	3.04	77.82
PC9	0.84	2.79	80.60
PC10	0.76	2.53	83.13
PC11	0.74	2.48	85.60
PC12	0.71	2.36	87.97
PC13	0.60	2.01	89.98
PC14	0.52	1.73	91.71
PC15	0.44	1.48	93.19
PC16	0.39	1.28	94.47
PC17	0.27	0.89	95.36
PC18	0.23	0.77	96.13
PC19	0.20	0.67	96.80
PC20	0.18	0.61	97.41
PC21	0.15	0.49	97.90
PC22	0.13	0.42	98.33
PC23	0.11	0.38	98.71
PC24	0.10	0.32	99.03
PC25	0.08	0.28	99.31
PC26	0.07	0.24	99.55
PC27	0.06	0.19	99.74
PC28	0.05	0.16	99.90
PC29	0.03	0.10	100.00
PC30	0.00	0.00	100.00

Figure D2. Eigenvalue table for the PCA conducted for all available variables, showing decreasing amount of explained variance.

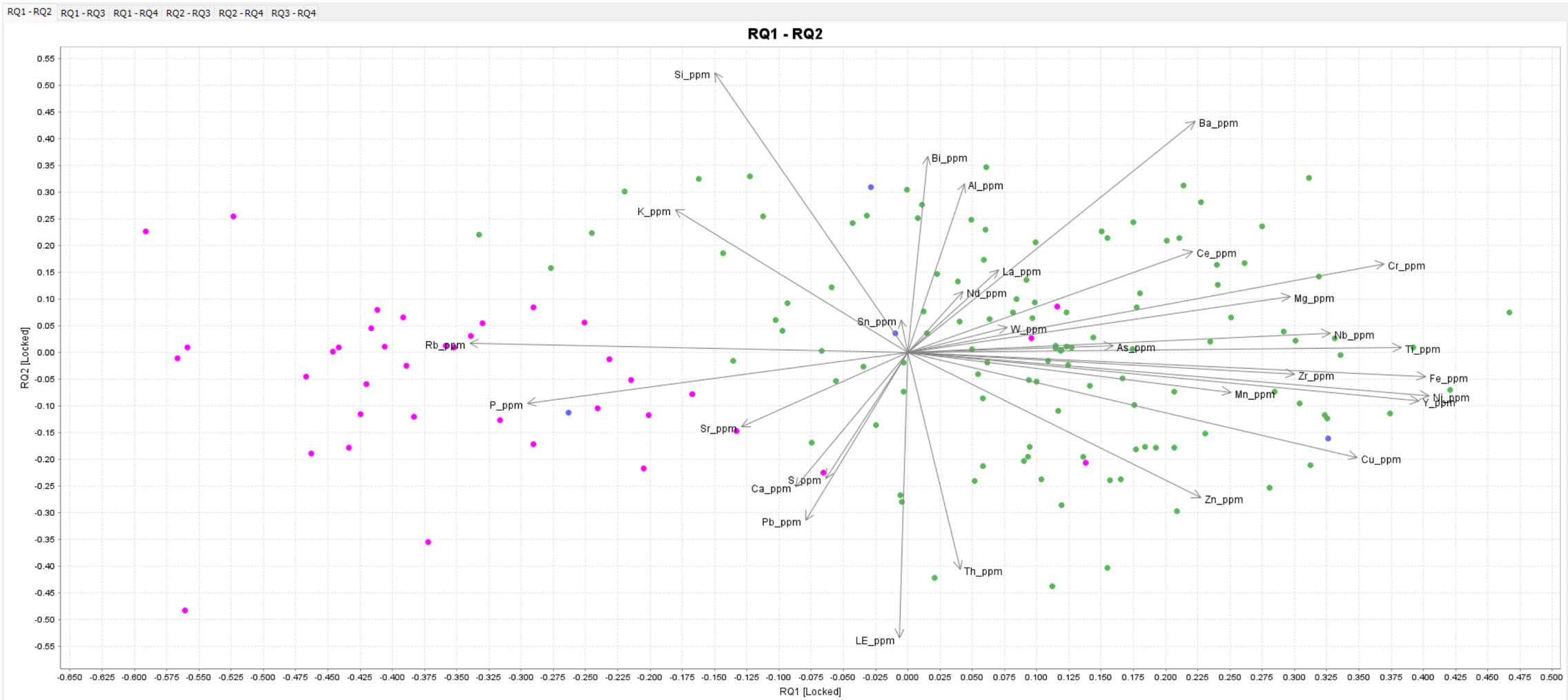


Figure D3. Biplot projecting components RQ1 and RQ2 for the PCA conducted for all available variables. A good separation of the granite (pink dots) and schist (green dots) was achieved. Blue dots represent granite+schist.

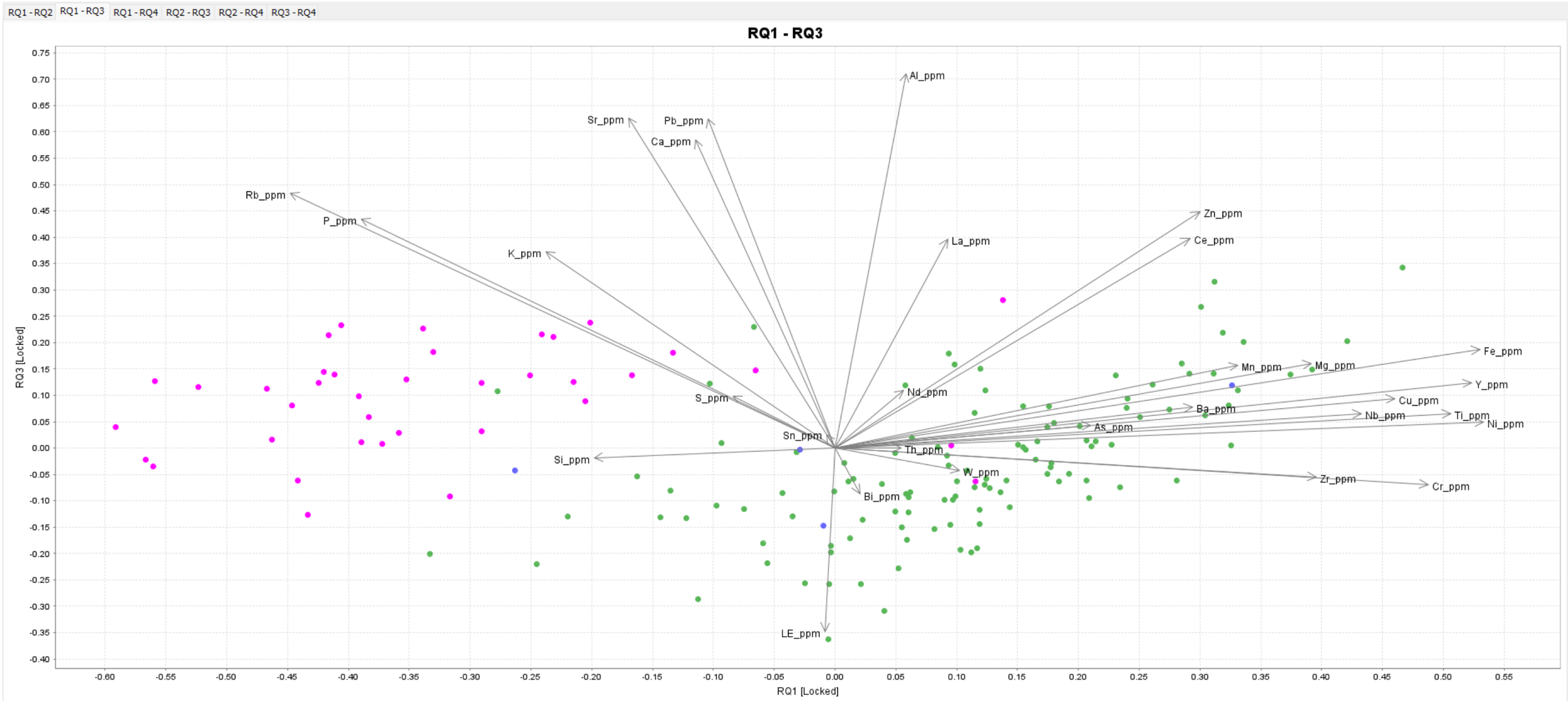


Figure D4. Biplot projecting components RQ1 and RQ3 for the PCA conducted for all available variables. A generally good separation of the granite (pink dots) and schist (green dots) was achieved. Blue dots represent granite+schist.

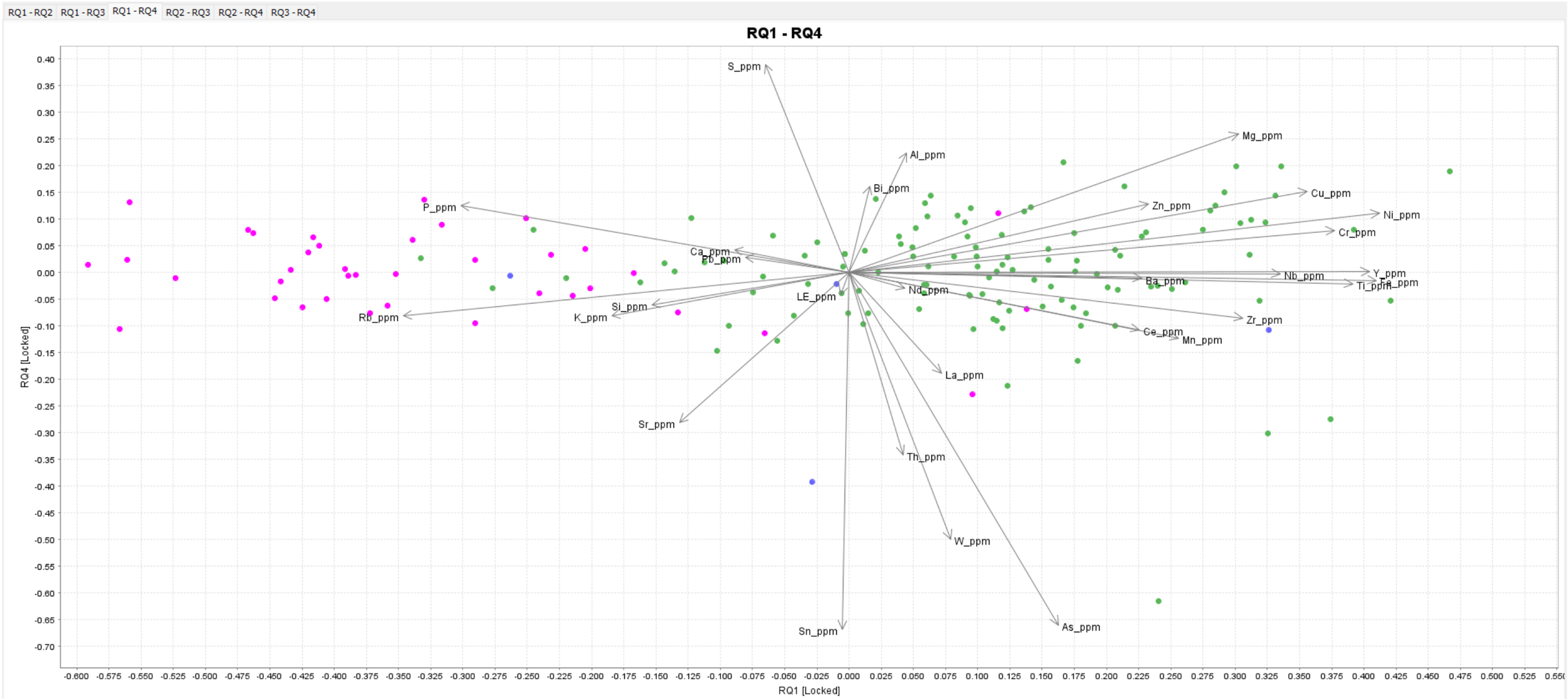


Figure D5. Biplot projecting components RQ1 and RQ4 for the PCA conducted for all available variables. A relatively good separation of the granite (pink dots) and schist (green dots) was achieved. Blue dots represent granite+schist.

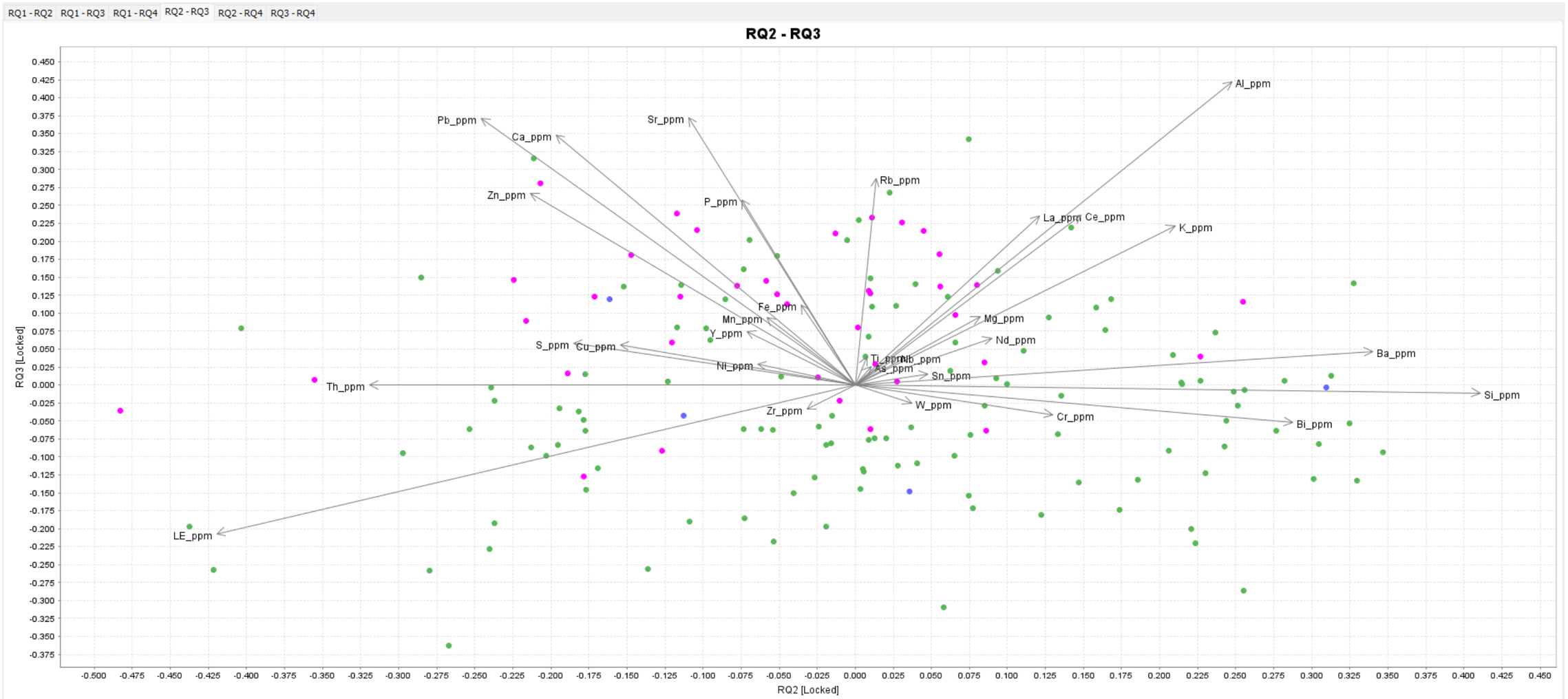


Figure D6. Biplot projecting components RQ2 and RQ3 for the PCA conducted for all available variables. A considerable separation of the granite (pink dots) and schist (green dots) could not be achieved. Blue dots represent granite+schist.

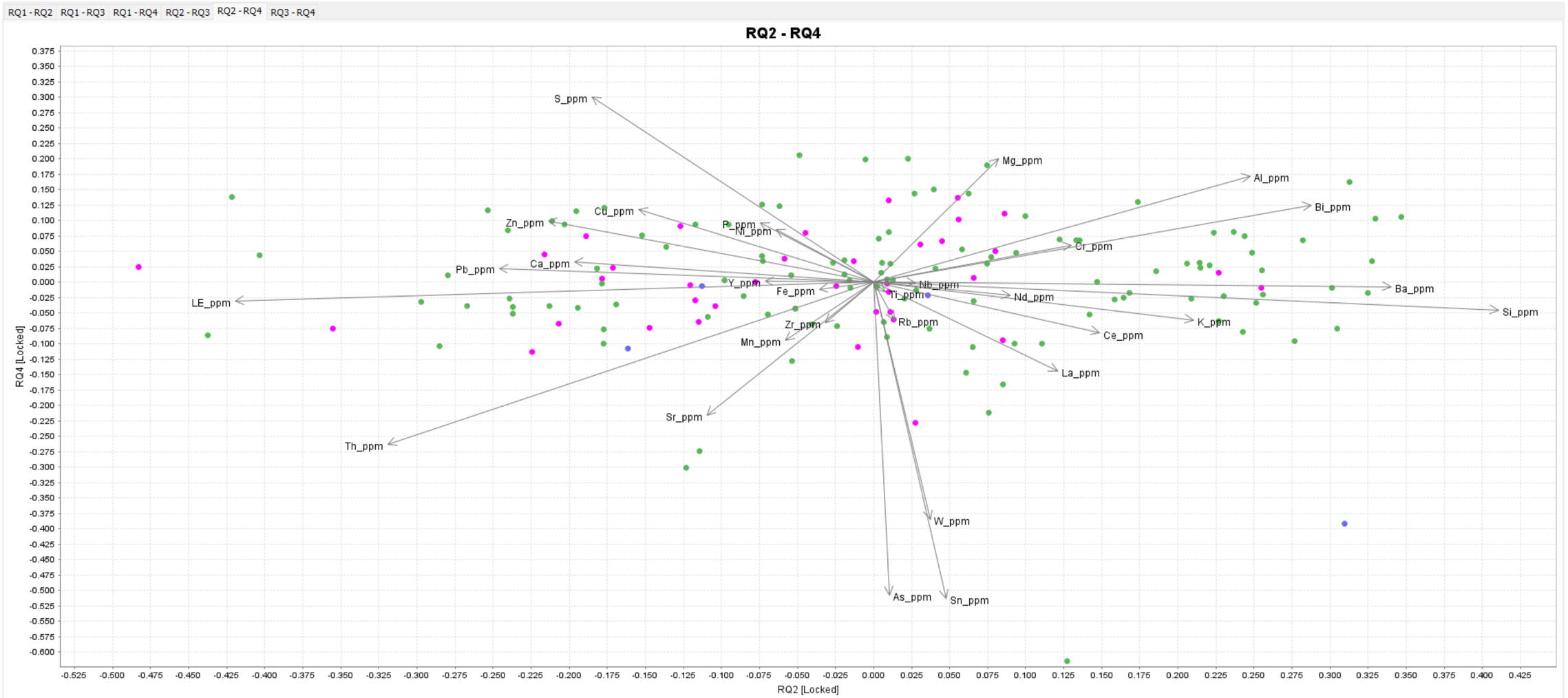


Figure D7. Biplot projecting components RQ2 and RQ4 for the PCA conducted for all available variables. A considerable separation of the granite (pink dots) and schist (green dots) could not be achieved. Blue dots represent granite+schist.

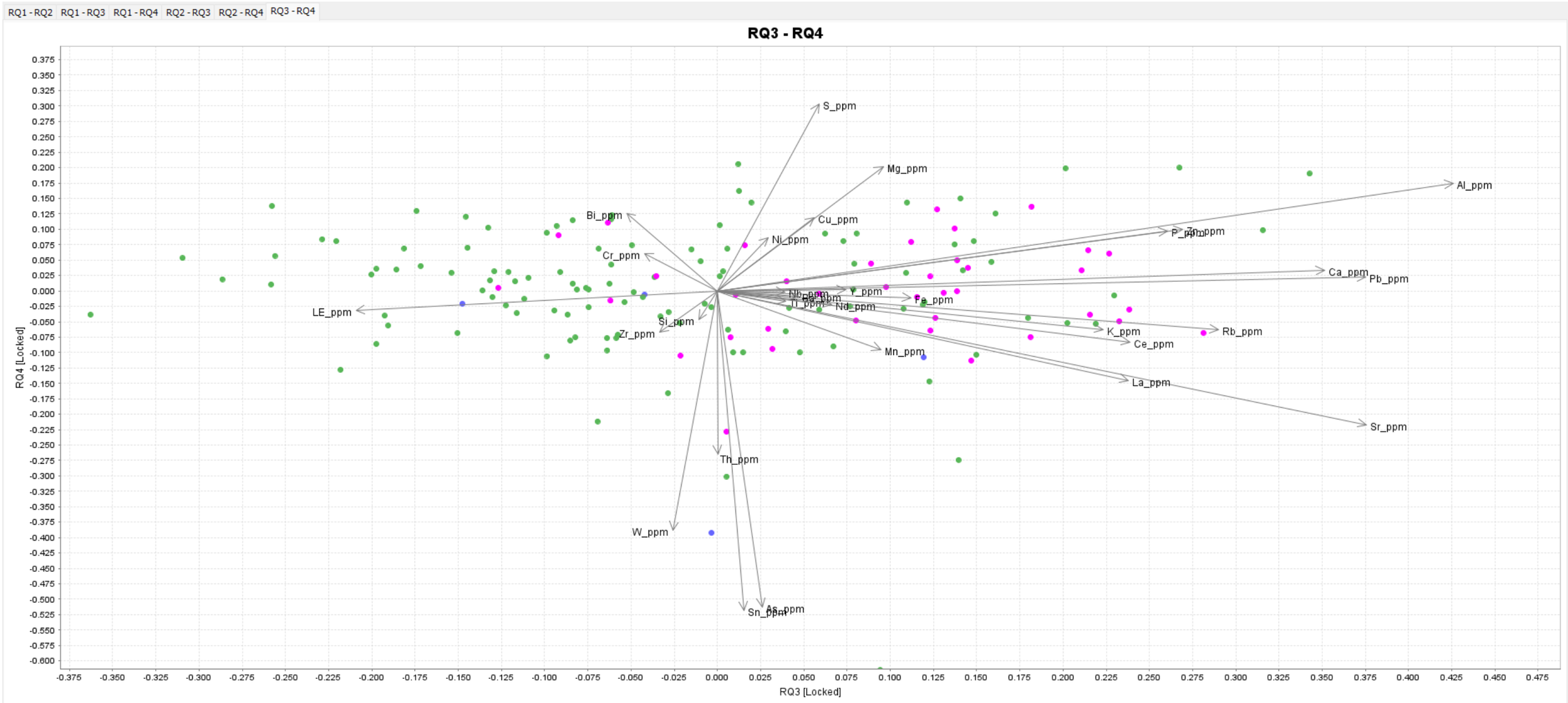


Figure D8. Biplot projecting components RQ3 and RQ4 for the PCA conducted for all available variables. A considerable separation of the granite (pink dots) and schist (green dots) could not be achieved. Blue dots represent granite+schist.

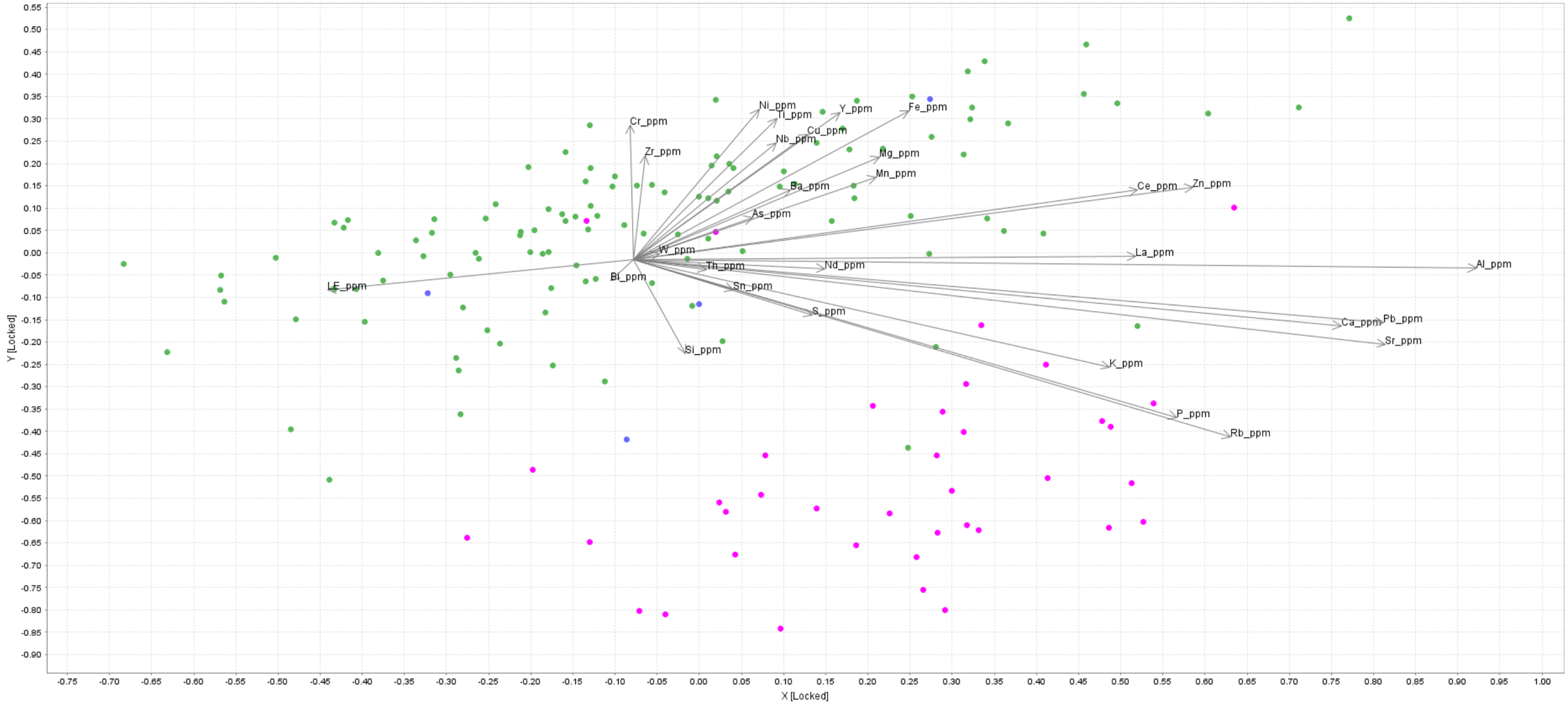


Figure D9. 3D biplot for the PCA conducted for all available variables. A good separation of the granite (pink dots) and schist (green dots) was achieved. Blue dots represent granite+schist.

Table D1. PCA of Rb, Nb, Sn and W (group “PATH1”): Eigenvector and eigenvalues matrix.

	PC1	PC2	PC3	PC4
Rb	0.6847	0.1855	0.1397	0.6908
Nb	-0.6689	-0.1968	0.283	0.6586
Sn	-0.1262	0.7117	0.6616	-0.1998
W	-0.2604	0.6484	-0.6802	0.2216
Eigenvalues	1.491	1.188	0.8087	0.5121
Accounted variance	37.27	29.71	20.22	12.8
Cumulative variance	37.27	66.98	87.2	100

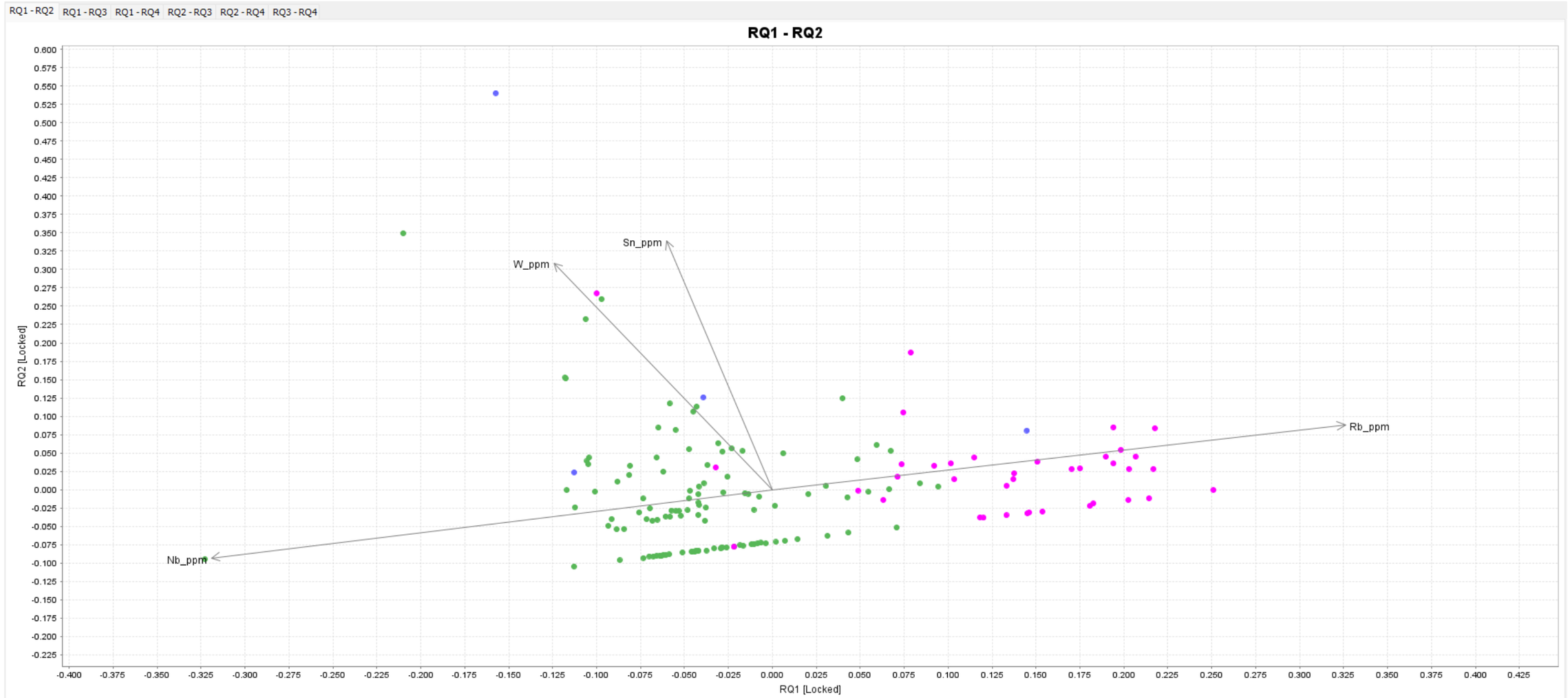


Figure D10. Biplot projecting components RQ1 and RQ2; PCA of group "PATH1".

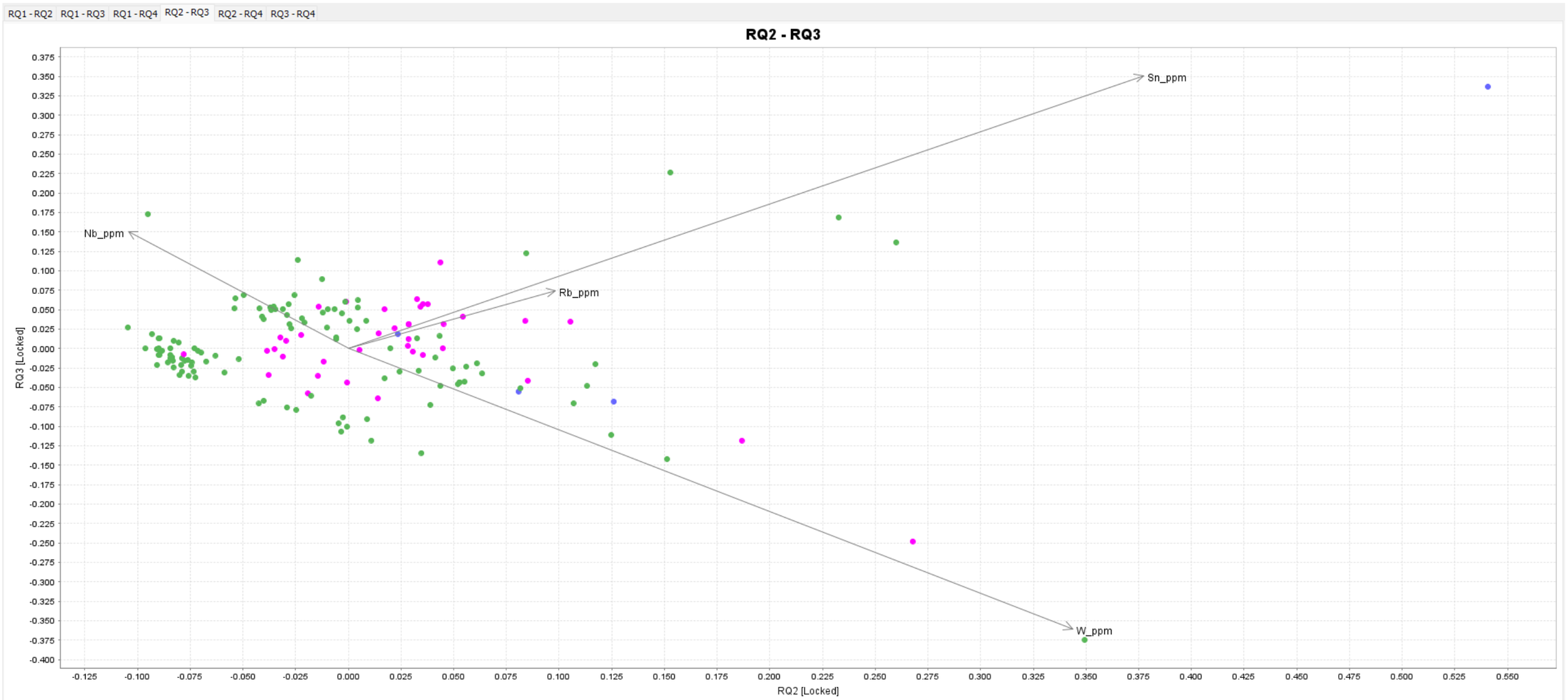


Figure D11. Biplot projecting components RQ2 and RQ3; PCA of group "PATH1".

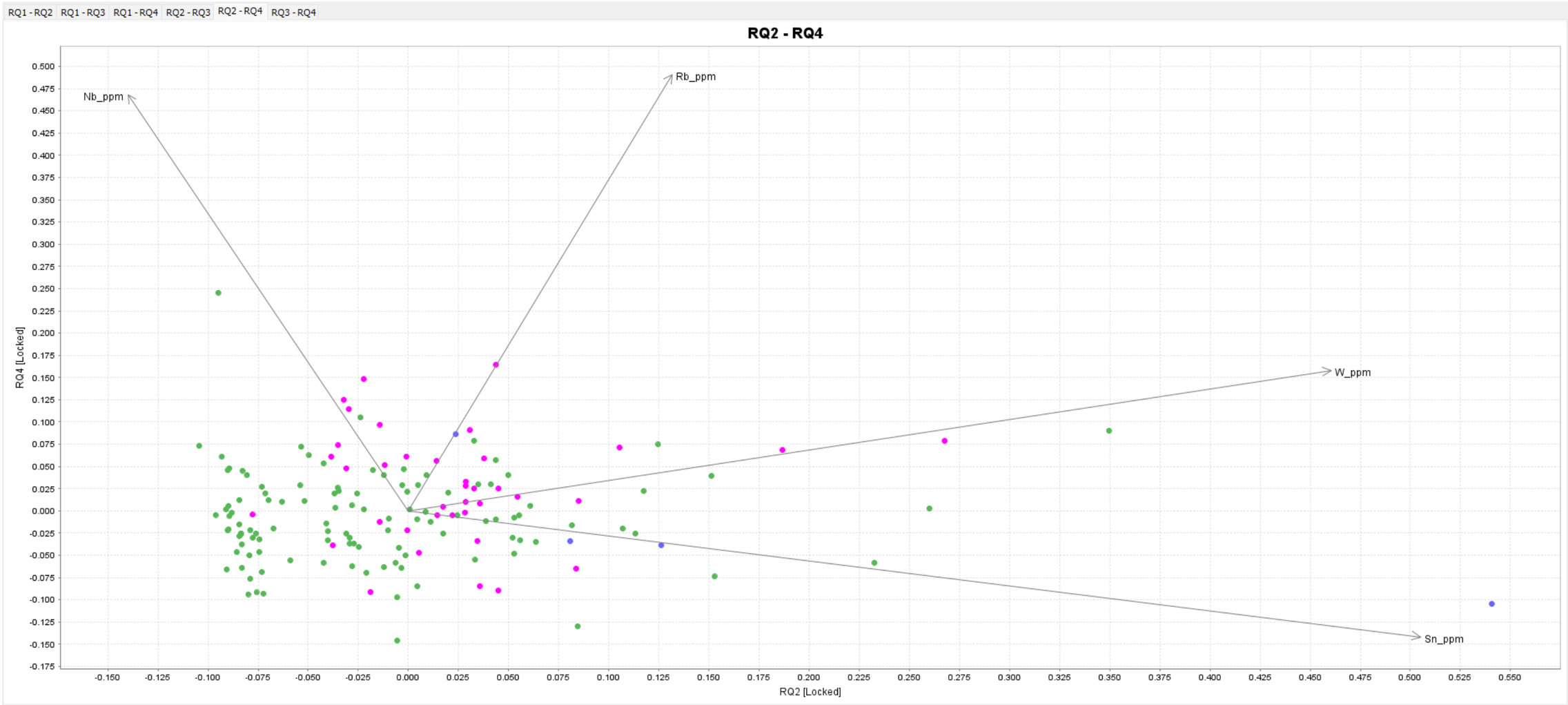


Figure D12. Biplot projecting components RQ2 and RQ4; PCA of group "PATH1".

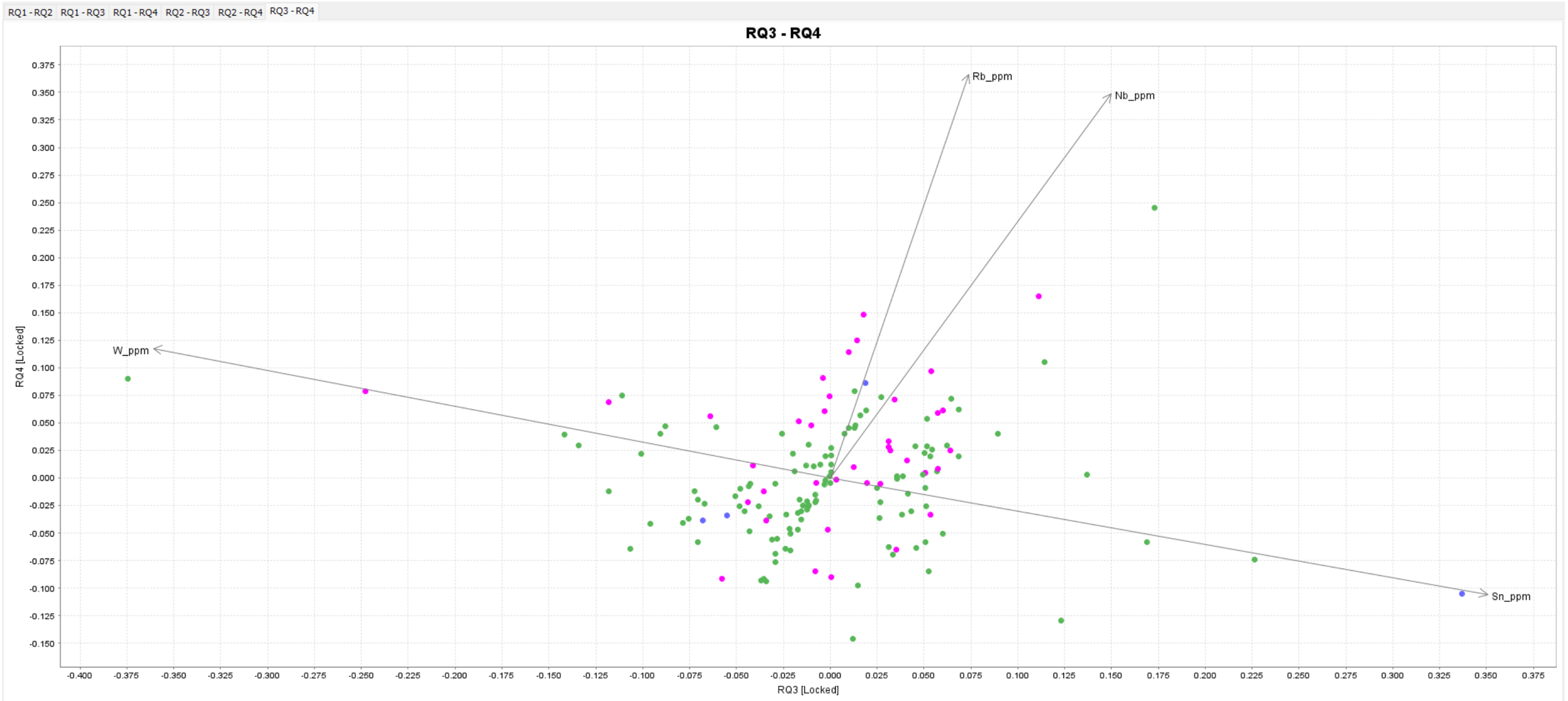


Figure D13. Biplot projecting components RQ3 and RQ4; PCA of group "PATH1".

Table D2. PCA of Rb. Nb, Sn and Th (group “PATH2”): Eigenvector and eigenvalues matrix.

	PC1	PC2	PC3	PC4
Rb	**0.6966**	**0.1443**	**0.005665**	**0.7028**
Nb	**-0.6982**	**-0.04056**	**-0.1377**	**0.7014**
Sn	**-0.03514**	**0.7605**	**-0.6379**	**-0.1162**
Th	**-0.1616**	**0.6318**	**0.7577**	**0.02436**
Eigenvalues	**1.474**	**1.048**	**0.9452**	**0.5324**
Accounted variance	**36.85**	**26.21**	**23.63**	**13.31**
Cumulative variance	**36.85**	**63.06**	**86.69**	**100**

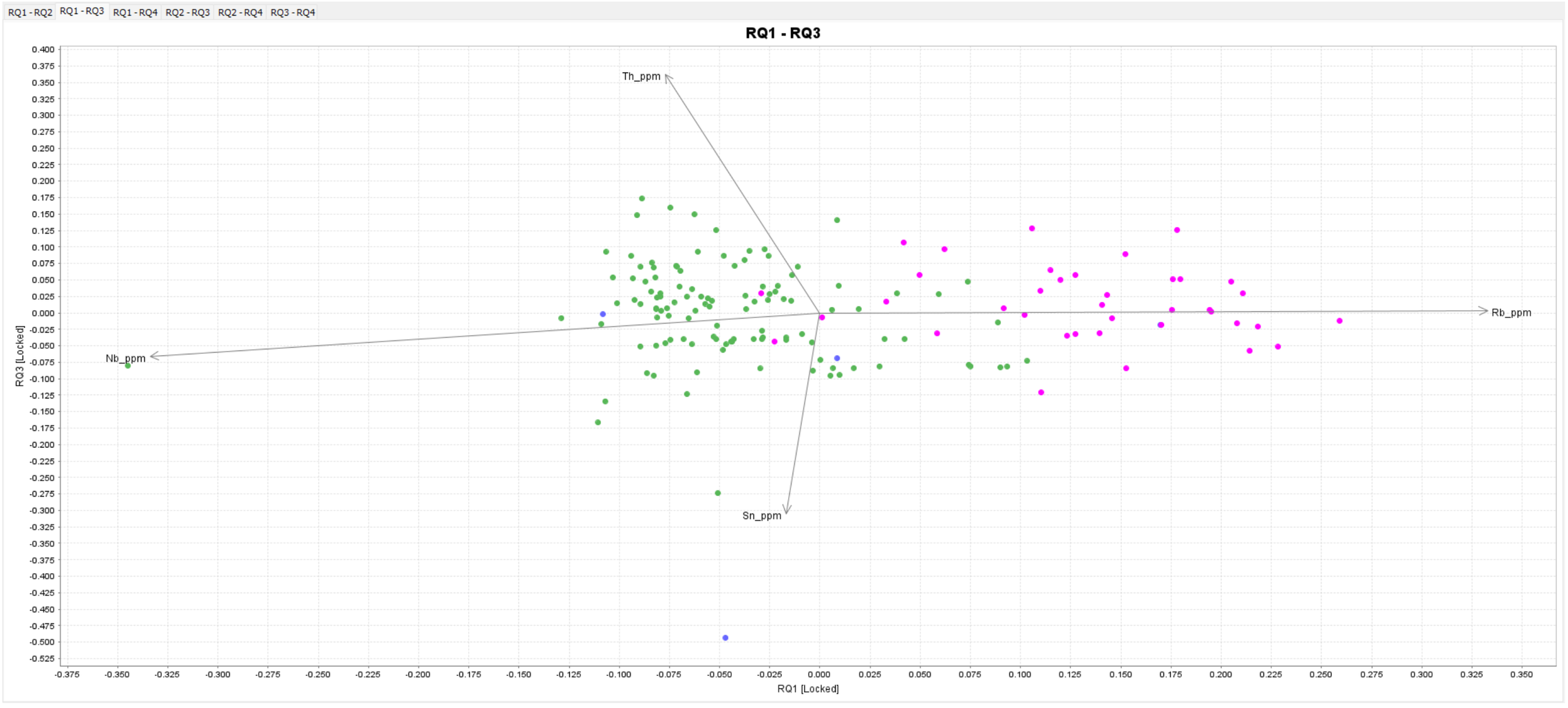


Figure D14. Biplot projecting components RQ1 and RQ3; PCA of group "PATH2".

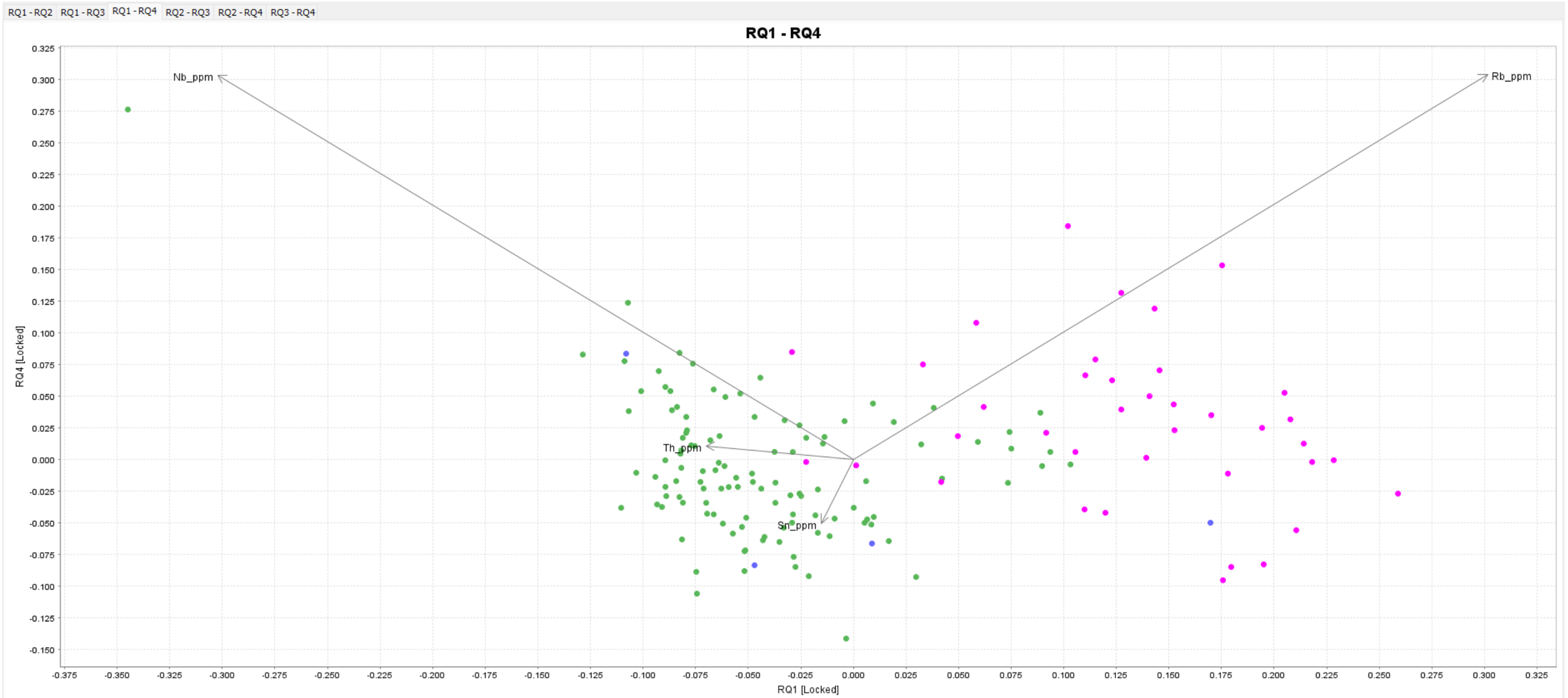


Figure D15. Biplot projecting components RQ1 and RQ4; PCA of group "PATH2".

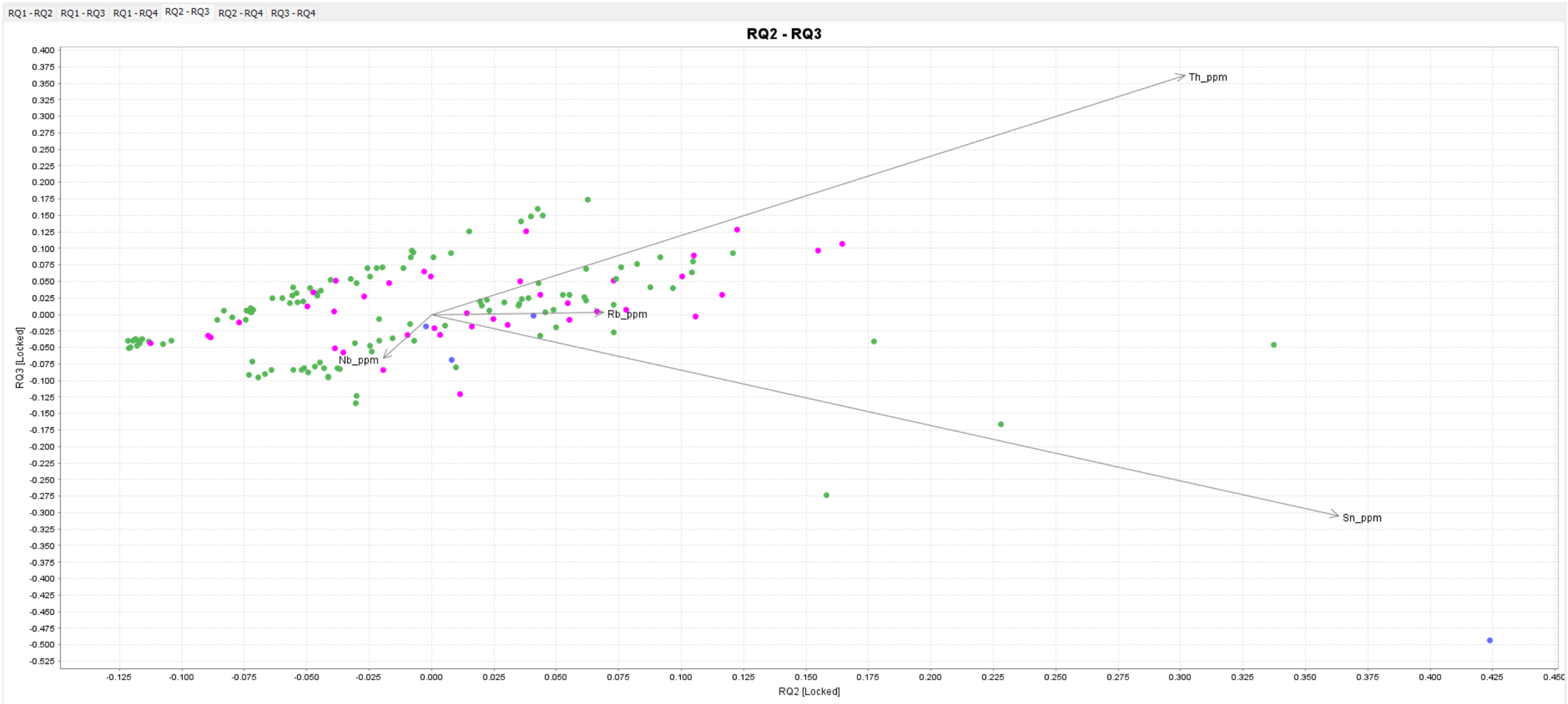


Figure D16. Biplot projecting components RQ2 and RQ3; PCA of group "PATH2".

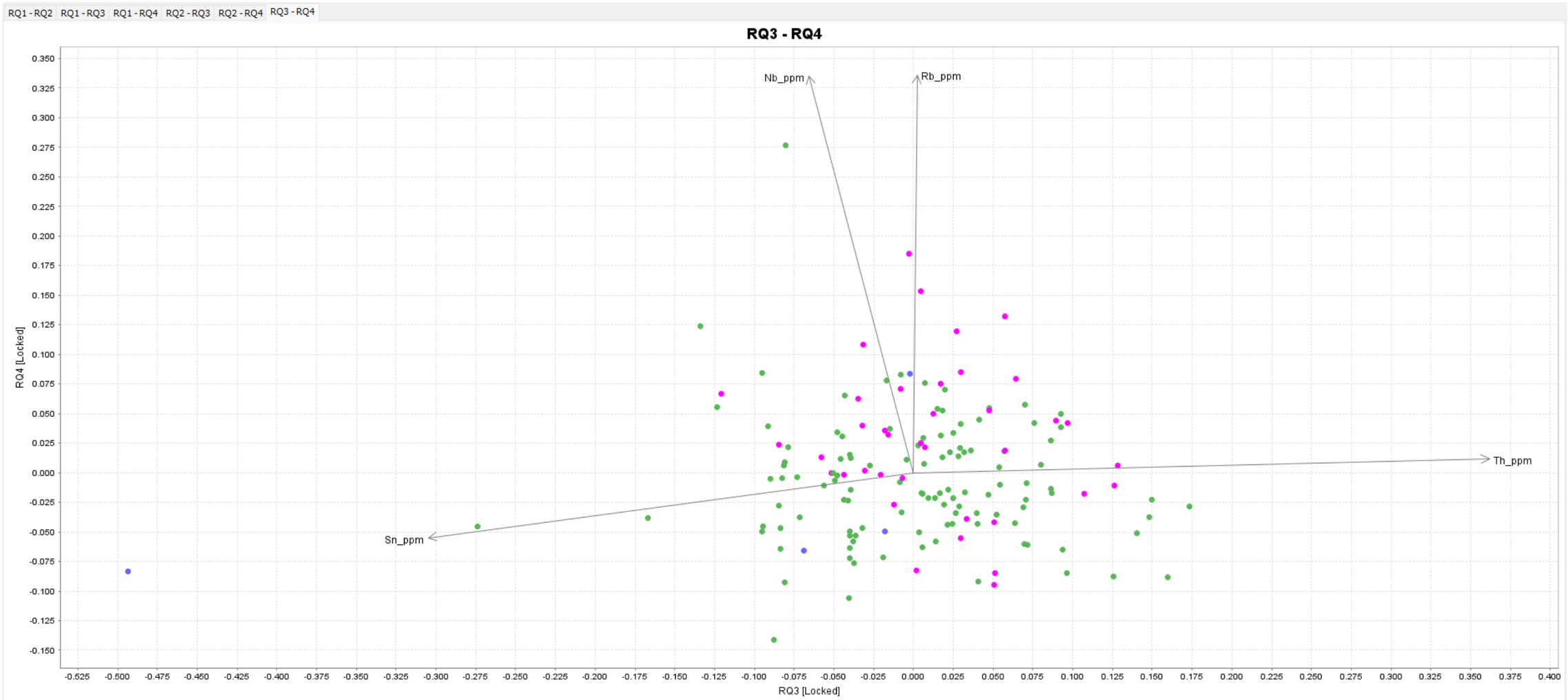


Figure D17. Biplot projecting components RQ3 and RQ4; PCA of group "PATH2".

Table D3. PCA of Al, K, Mn, Rb, Nb, Sn and Th (group “PATH3”): Eigenvector and eigenvalues matrix.

	PC1	PC2	PC3	PC4	PC5	PC6	PC7
Al	0.3338	0.636	0.03226	0.078	0.0808	0.2874	0.6227
K	0.5129	0.1698	0.3039	0.2493	0.04655	-0.7234	-0.1676
Mn	-0.3712	0.3684	0.2157	0.2765	-0.7678	-0.013	-0.1175
Rb	0.5619	-0.1007	0.1484	0.1775	-0.1501	0.6013	-0.4863
Nb	-0.3622	0.5113	0.2075	0.05564	0.5692	0.1158	-0.4731
Sn	-0.0055	-0.0882	0.7703	-0.6156	-0.0631	0.05685	0.1122
Th	-0.2019	-0.3893	0.449	0.6646	0.2265	0.1254	0.312
Eigenvalues	2.281	1.476	1.071	0.9126	0.6138	0.3677	0.2774
Accounted variance	32.59	21.09	15.3	13.04	8.768	5.253	3.963
Cumulativevariance	32.59	53.68	68.98	82.02	90.78	96.04	100

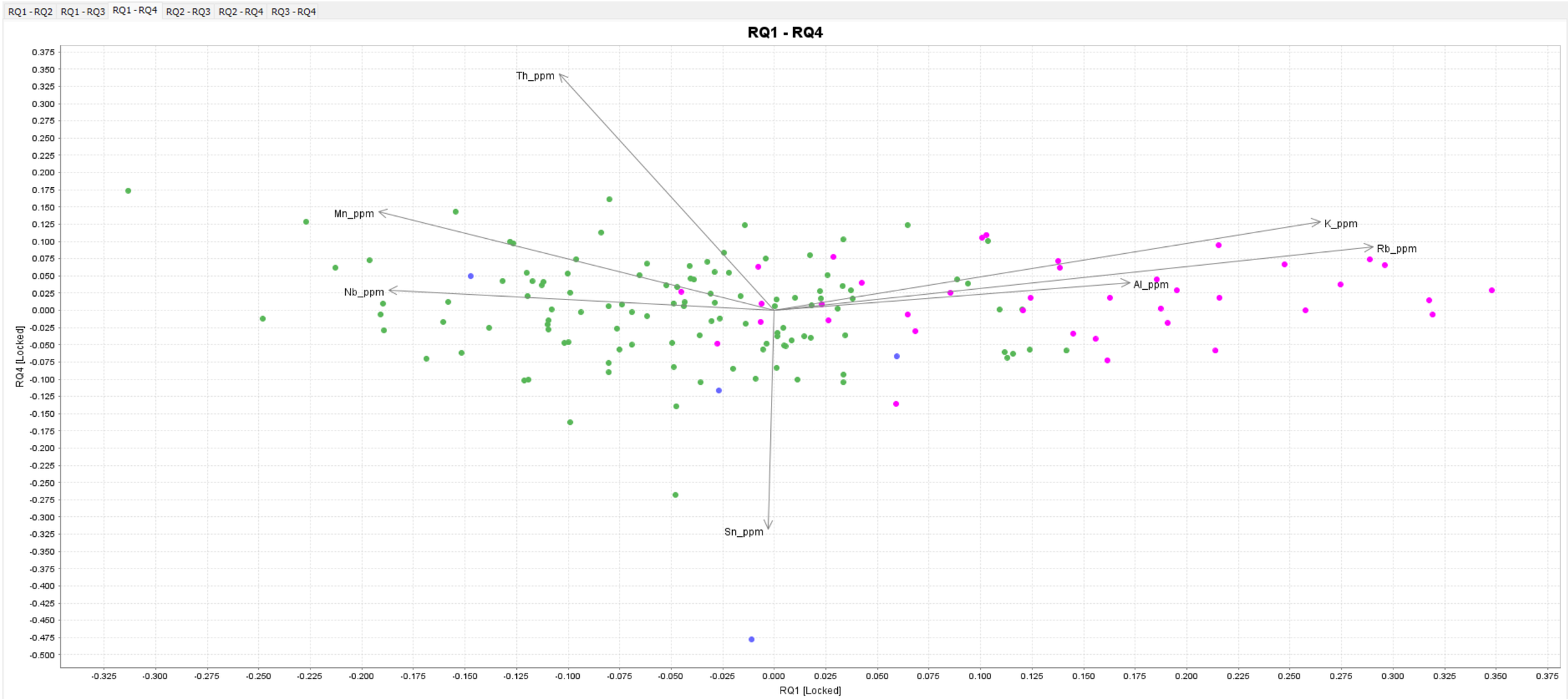


Figure D18. Biplot projecting components RQ1 and RQ4; PCA of group "PATH3".

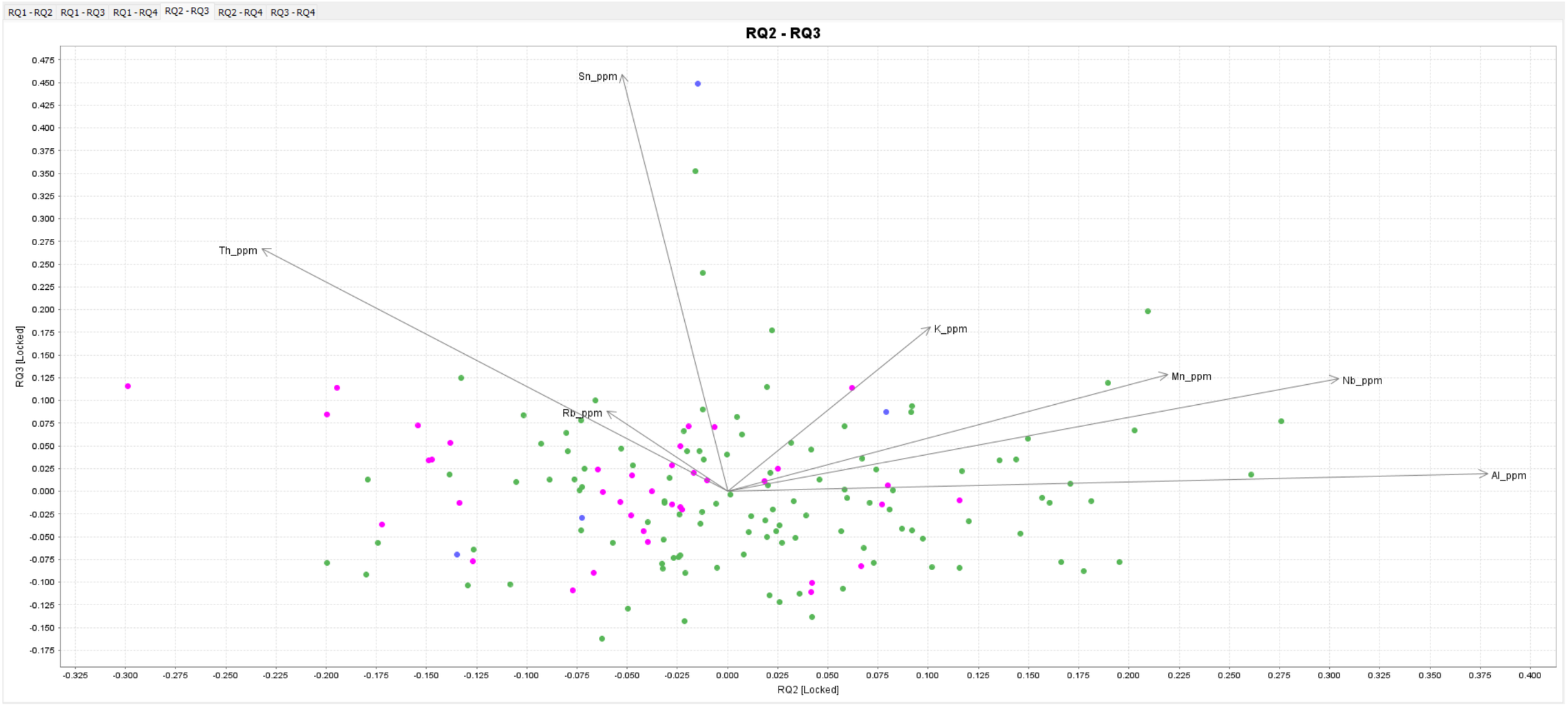


Figure D19. Biplot projecting components RQ2 and RQ3; PCA of group "PATH3".

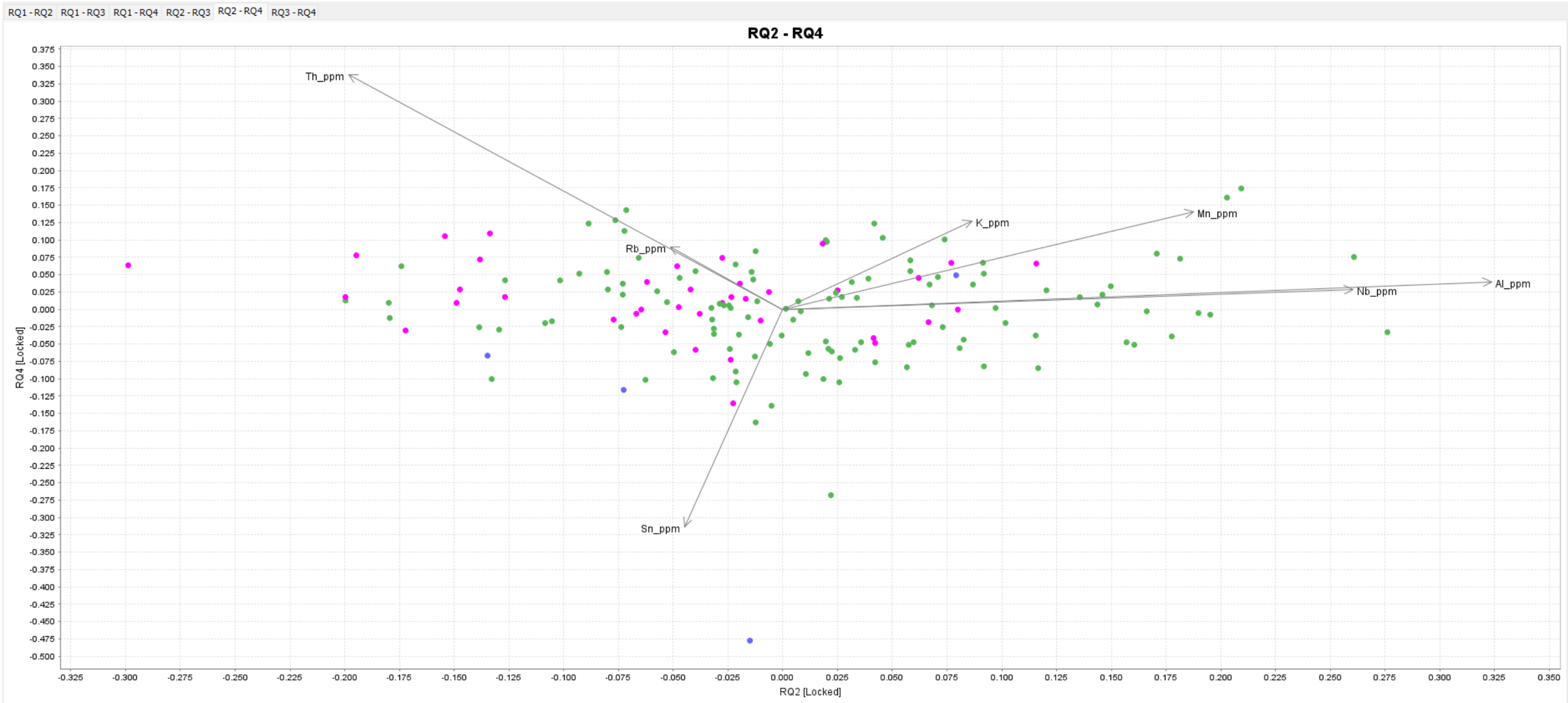


Figure D20. Biplot projecting components RQ2 and RQ4; PCA of group "PATH3".

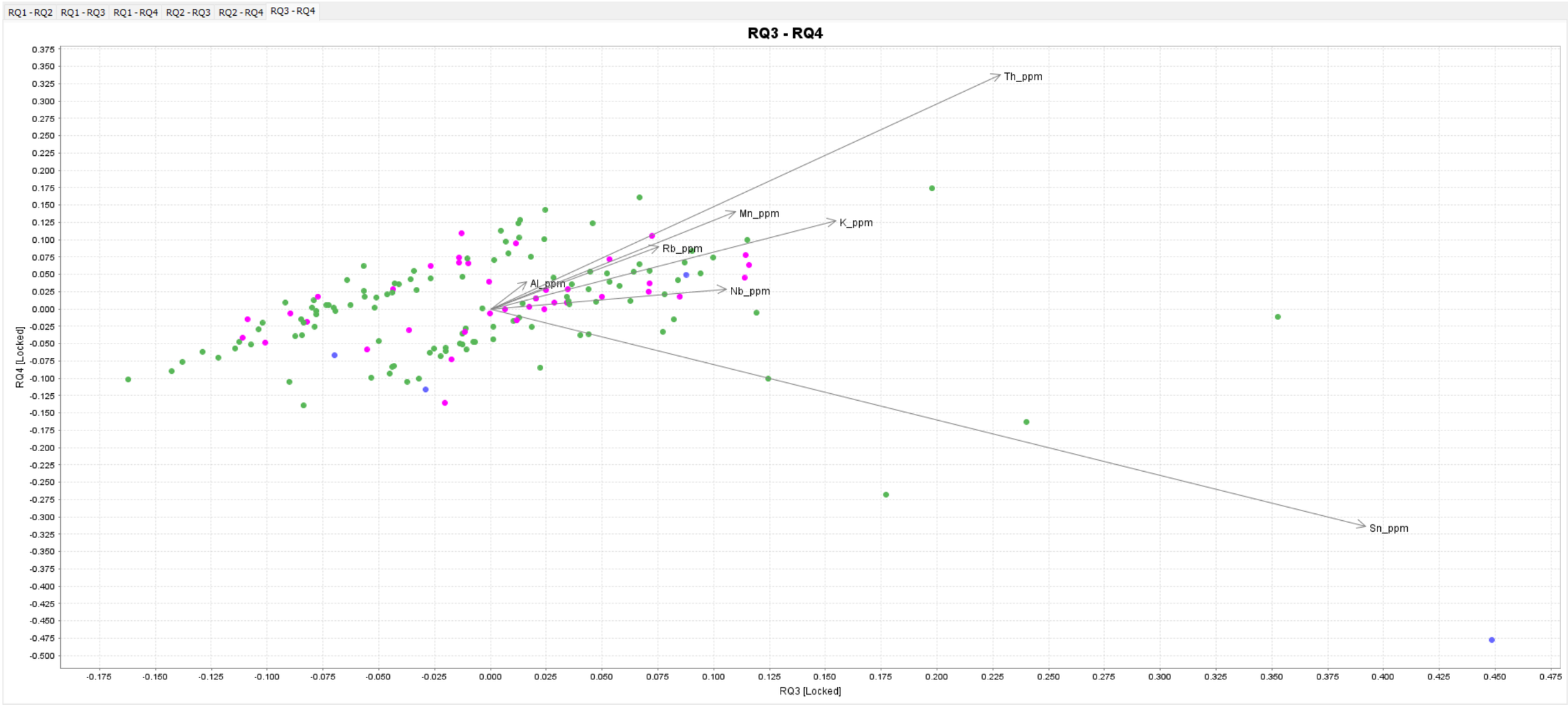


Figure D21. Biplot projecting components RQ3 and RQ4; PCA of group "PATH3".

Table D4. PCA of Al, K, Mn, Rb, Nb and Sn (group “PATH4”): Eigenvector and eigenvalues matrix.

	PC1	PC2	PC3	PC4	PC5	PC6
Al	0.2903	0.6718	0.1055	0.1623	0.526	0.3877
K	0.523	0.3146	-0.1041	-0.09354	-0.7621	0.1647
Mn	-0.3862	0.4061	-0.04103	-0.8254	-0.00231	-0.0547
Rb	0.5842	0.008666	-0.03676	-0.2197	0.2789	-0.7289
Nb	-0.3896	0.5329	-0.09083	0.4845	-0.2083	-0.5271
Sn	0.006068	-0.02768	-0.9832	0.02522	0.146	0.1024
Eigenvalues	2.23	1.387	1.021	0.6398	0.391	0.3315
Accountedvariance	37.17	23.11	17.01	10.66	6.516	5.525
Cumulativevariance	37.17	60.29	77.3	87.96	94.48	100

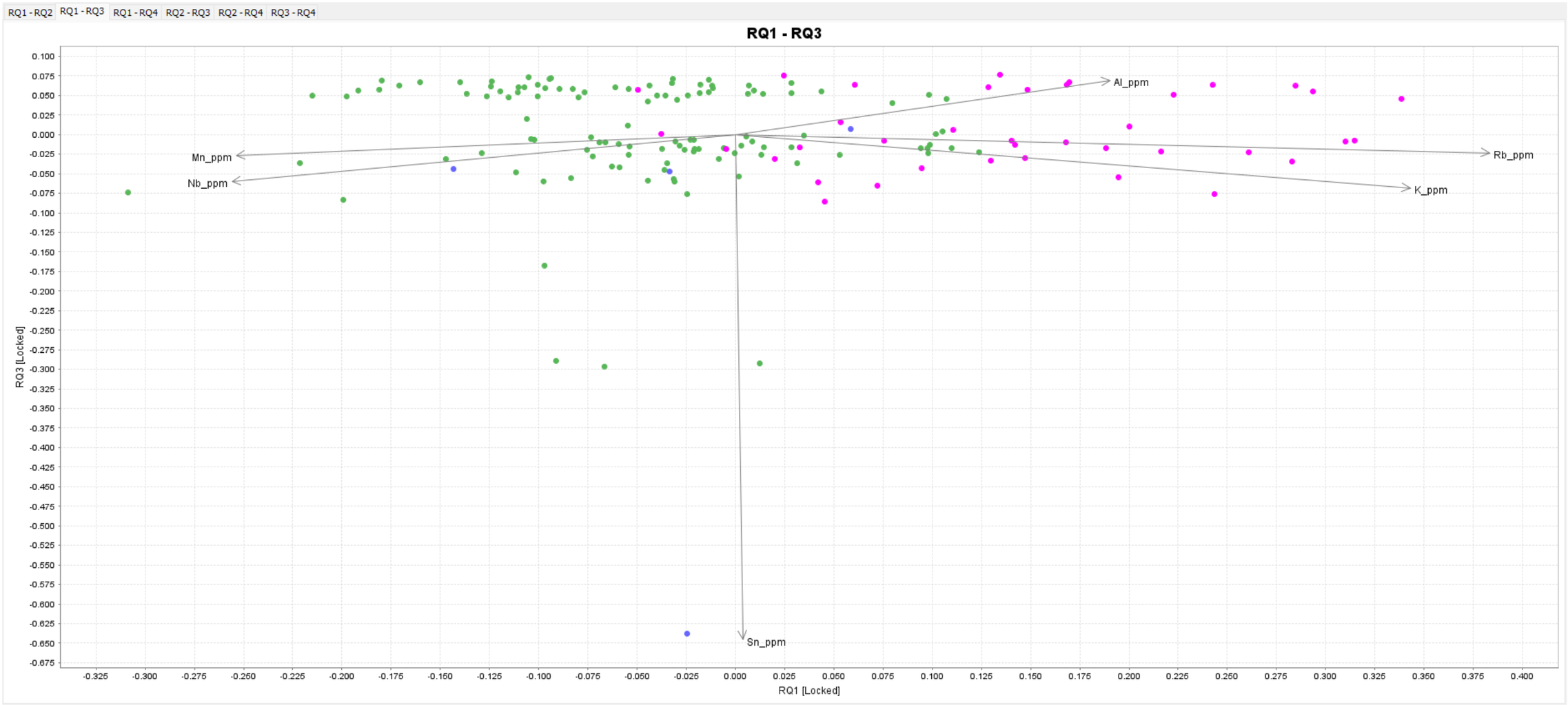


Figure D22. Biplot projecting components RQ1 and RQ3; PCA of group "PATH4".

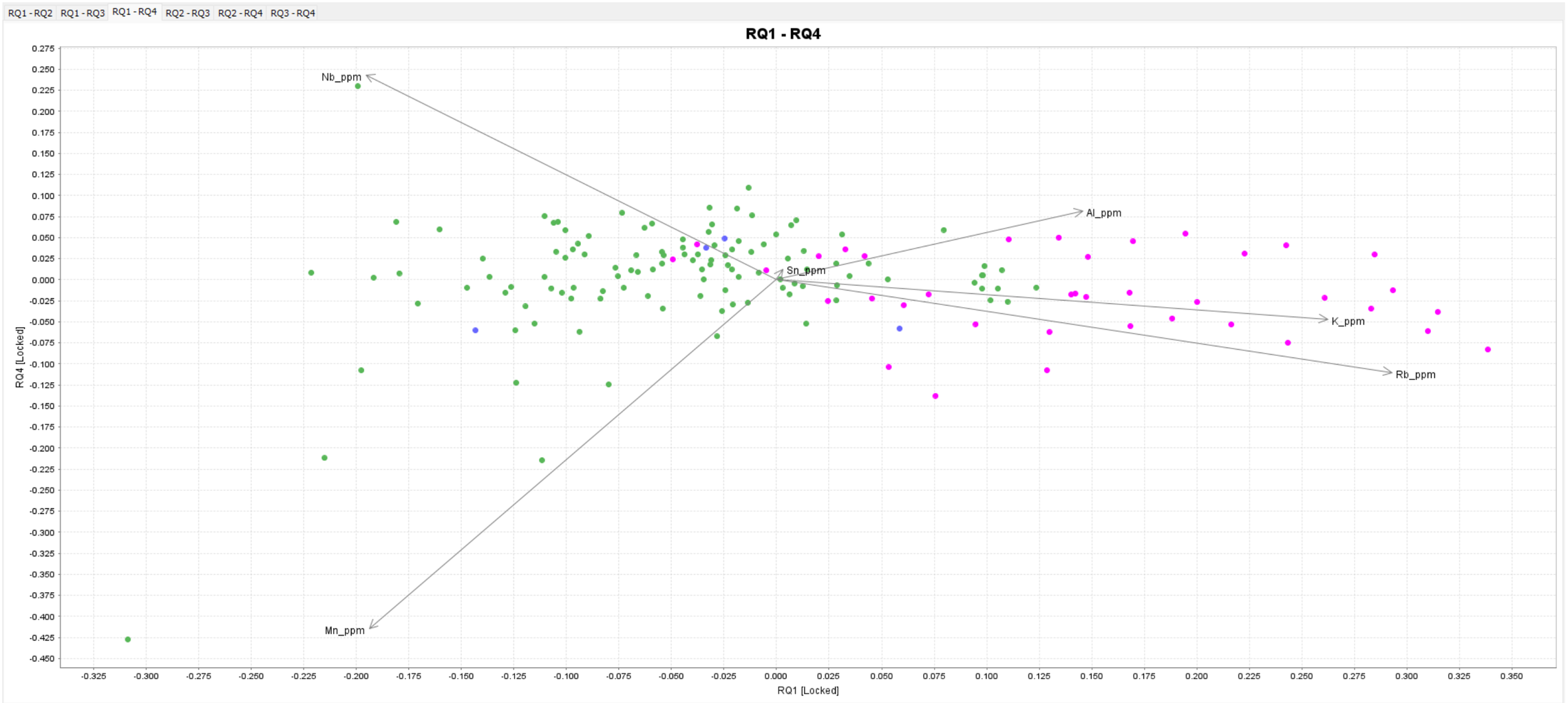


Figure D23. Biplot projecting components RQ1 and RQ4; PCA of group "PATH4".

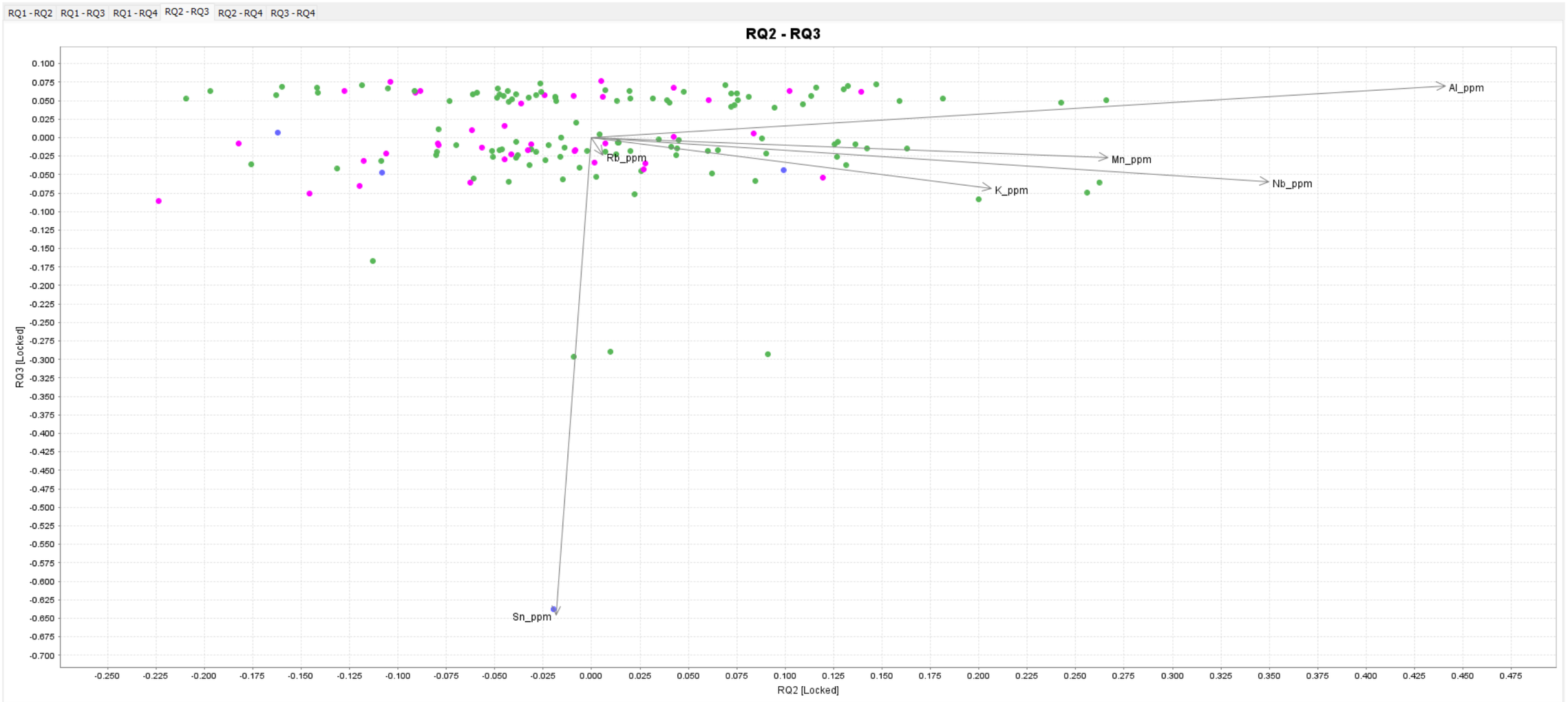


Figure D24. Biplot projecting components RQ2 and RQ3; PCA of group "PATH4".

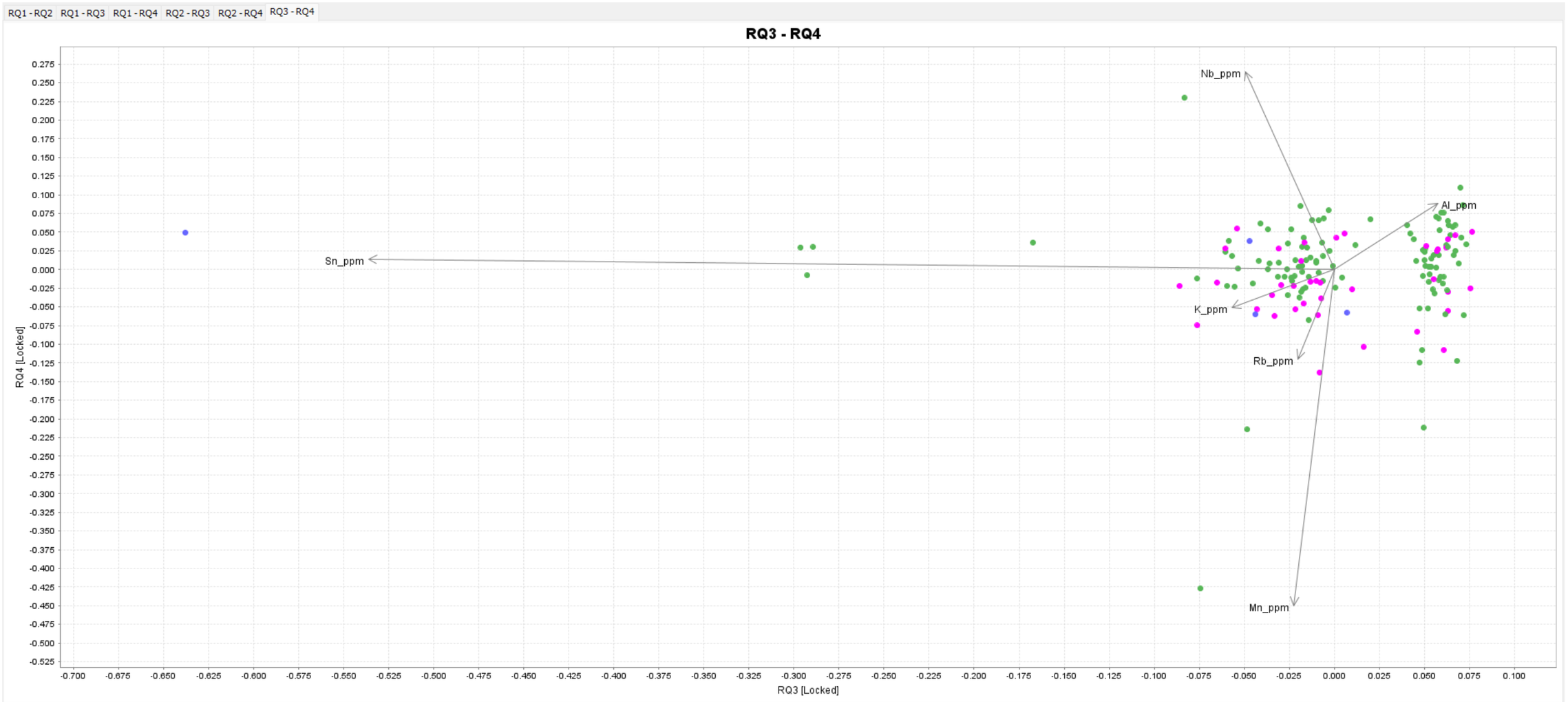


Figure D25. Biplot projecting components RQ3 and RQ4; PCA of group "PATH4".

Appendix E – Pearson correlation matrices for the stream sediment samples

Correlation	Mg_ppm	Al_ppm	Si_ppm	P_ppm	S_ppm	K_ppm	Ca_ppm	Ti_ppm	Cr_ppm	Mn_ppm	Fe_ppm	Ni_ppm	Cu_ppm	Zn_ppm	As_ppm	Rb_ppm	Sr_ppm	Y_ppm	Zr_ppm	Nb_ppm	Sn_ppm	Ba_ppm	La_ppm	Ce_ppm	Nd_ppm	W_ppm	Pb_ppm	Bi_ppm	Th_ppm	LE_ppm
Mg_ppm	1																												
Al_ppm	0.32	1																											
Si_ppm	-0.08	0.36	1																										
P_ppm	-0.36	0.17	0.08	1																									
S_ppm	-0.11	-0.11	-0.29	0.35	1																								
K_ppm	-0.30	0.48	0.53	0.30	-0.07	1																							
Ca_ppm	0.01	0.08	-0.26	0.45	0.33	-0.13	1																						
Ti_ppm	0.53	0.16	-0.30	-0.62	-0.19	-0.31	-0.12	1																					
Cr_ppm	0.65	0.15	-0.06	-0.67	-0.14	-0.23	-0.27	0.73	1																				
Mn_ppm	0.28	0.03	-0.27	-0.19	-0.08	-0.22	-0.04	0.41	0.42	1																			
Fe_ppm	0.60	0.19	-0.38	-0.51	-0.10	-0.29	-0.09	0.83	0.76	0.68	1																		
Ni_ppm	0.64	0.09	-0.43	-0.56	0.01	-0.37	-0.15	0.76	0.77	0.62	0.92	1																	
Cu_ppm	0.64	0.02	-0.54	-0.42	0.13	-0.38	0.01	0.63	0.63	0.46	0.79	0.87	1																
Zn_ppm	0.40	0.26	-0.61	-0.02	0.13	-0.26	0.18	0.43	0.27	0.39	0.60	0.60	0.68	1															
As_ppm	0.19	-0.01	-0.06	-0.20	-0.16	-0.08	-0.10	0.23	0.27	0.34	0.35	0.32	0.26	0.18	1														
Rb_ppm	-0.55	0.32	0.23	0.70	0.07	0.58	0.30	-0.62	-0.71	-0.37	-0.63	-0.72	-0.64	-0.14	-0.22	1													
Sr_ppm	-0.29	0.14	-0.08	0.32	0.01	0.18	0.69	-0.12	-0.32	-0.04	-0.14	-0.30	-0.25	0.00	-0.05	0.51	1												
Y_ppm	0.60	0.08	-0.42	-0.60	-0.08	-0.42	0.00	0.82	0.73	0.49	0.86	0.87	0.77	0.54	0.31	-0.70	-0.079	1											
Zr_ppm	0.22	0.00	-0.30	-0.56	-0.21	-0.31	-0.13	0.78	0.50	0.35	0.57	0.56	0.38	0.25	0.19	-0.51	-0.06	0.70	1										
Nb_ppm	0.37	0.17	-0.27	-0.46	-0.12	-0.21	-0.21	0.76	0.58	0.39	0.70	0.64	0.49	0.45	0.21	-0.46	-0.22	0.67	0.66	1									
Sn_ppm	-0.06	-0.08	0.10	0.03	-0.14	0.06	-0.01	-0.01	-0.02	0.01	0.00	-0.07	-0.04	-0.04	0.31	0.03	0.03	-0.05	-0.09	0.043	1								
Ba_ppm	0.42	0.41	0.43	-0.48	-0.28	0.16	-0.29	0.51	0.67	0.26	0.44	0.37	0.14	-0.13	0.18	-0.34	-0.12	0.38	0.36	0.44	0.04	1							
La_ppm	0.19	0.27	0.13	0.01	-0.12	0.06	0.11	0.12	0.18	0.13	0.14	0.09	0.03	0.06	0.08	0.02	0.16	0.18	0.08	0.17	0.12	0.26	1						
Ce_ppm	0.43	0.41	0.07	-0.21	-0.14	-0.03	-0.01	0.49	0.44	0.24	0.49	0.40	0.28	0.24	0.21	-0.23	0.03	0.44	0.33	0.41	0.11	0.49	0.36	1					
Nd_ppm	-0.02	0.16	0.08	-0.08	-0.02	0.13	-0.05	0.09	0.09	0.01	0.09	0.08	0.02	0.01	0.06	-0.01	-0.05	0.04	0.10	0.16	0.03	0.17	0.04	0.19	1				
W_ppm	0.15	-0.02	0.05	-0.19	-0.03	-0.14	-0.05	0.07	0.18	0.04	0.11	0.12	0.15	0.08	0.40	-0.12	-0.04	0.13	0.00	0.03	0.21	0.09	0.10	0.14	-0.03	1			
Pb_ppm	-0.07	0.13	-0.39	0.37	0.21	0.12	0.50	-0.18	-0.31	0.02	-0.06	-0.06	0.11	0.41	-0.06	0.40	0.52	0.03	-0.11	-0.18	-0.03	-0.41	0.04	-0.05	-0.06	-0.13	1		
Bi_ppm	0.20	0.26	0.43	-0.05	-0.08	0.02	-0.17	-0.04	0.23	-0.10	-0.07	-0.03	-0.14	-0.23	0.04	-0.08	-0.23	-0.06	-0.12	0.09	0.11	0.46	0.17	0.10	0.05	0.00	-0.34	1	
Th_ppm	-0.16	-0.38	-0.56	-0.05	0.12	-0.08	0.16	0.14	-0.14	0.11	0.18	0.17	0.26	0.28	0.20	-0.06	0.19	0.17	0.12	0.05	0.05	-0.40	-0.12	-0.15	-0.10	-0.03	0.28	-0.48	1
LE_ppm	-0.26	-0.75	-0.84	0.00	0.29	-0.57	0.18	-0.05	-0.22	0.02	-0.04	0.06	0.20	0.22	-0.05	-0.15	0.03	0.07	0.10	-0.03	-0.05	-0.64	-0.26	-0.36	-0.15	-0.06	0.25	-0.42	0.54	1

Figure E1. Pearson correlation for all the lithologies (green rectangle represents the correlation value for LE-Th).

Correlation	Mg_ppm	Al_ppm	Si_ppm	P_ppm	S_ppm	K_ppm	Ca_ppm	Ti_ppm	Cr_ppm	Mn_ppm	Fe_ppm	Ni_ppm	Cu_ppm	Zn_ppm	As_ppm	Rb_ppm	Sr_ppm	Y_ppm	Zr_ppm	Nb_ppm	Sn_ppm	Ba_ppm	La_ppm	Ce_ppm	Nd_ppm	W_ppm	Pb_ppm	Bi_ppm	Th_ppm	LE_ppm
Mg_ppm	1																												
Al_ppm	0.36	1																											
Si_ppm	-0.095	0.21	1																										
P_ppm	-0.41	0.06	0.059	1																									
S_ppm	-0.28	-0.37	-0.21	0.4	1																								
K_ppm	-0.55	0.13	0.66	0.24	0.039	1																							
Ca_ppm	0.45	-0.15	-0.43	-0.026	0.087	-0.53	1																						
Ti_ppm	0.69	0.15	-0.48	-0.56	-0.21	-0.67	0.48	1																					
Cr_ppm	0.58	-0.041	0.17	-0.56	-0.096	-0.32	0.13	0.54	1																				
Mn_ppm	0.51	-0.16	-0.27	-0.22	-0.072	-0.54	0.29	0.43	0.3	1																			
Fe_ppm	0.71	0.15	-0.45	-0.52	-0.17	-0.71	0.42	0.94	0.54	0.56	1																		
Ni_ppm	0.5	0.034	-0.35	-0.47	-0.12	-0.58	0.18	0.72	0.5	0.55	0.83	1																	
Cu_ppm	0.27	-0.2	-0.45	-0.39	0.11	-0.49	0.19	0.63	0.41	0.39	0.69	0.64	1																
Zn_ppm	0.26	0.48	-0.62	-0.019	-0.098	-0.46	0.076	0.49	-0.083	0.049	0.53	0.39	0.33	1															
As_ppm	0.3	-0.0061	-0.064	-0.33	0.028	-0.28	-0.061	0.4	0.35	0.32	0.56	0.54	0.67	0.2	1														
Rb_ppm	-0.36	0.55	0.16	0.46	-0.17	0.51	-0.35	-0.49	-0.65	-0.47	-0.52	-0.55	-0.65	0.23	-0.42	1													
Sr_ppm	0.43	-0.19	-0.17	-0.48	-0.25	-0.31	0.72	0.47	0.27	0.25	0.34	0.12	0.098	-0.15	-0.066	-0.36	1												
Y_ppm	0.71	0.0059	-0.4	-0.52	-0.17	-0.73	0.57	0.9	0.58	0.47	0.91	0.72	0.61	0.34	0.44	-0.62	0.5	1											
Zr_ppm	0.68	0.24	-0.48	-0.47	-0.27	-0.63	0.4	0.92	0.45	0.33	0.87	0.69	0.5	0.56	0.27	-0.38	0.32	0.83	1										
Nb_ppm	0.39	0.32	-0.56	-0.079	-0.08	-0.52	0.32	0.67	0.16	0.17	0.72	0.48	0.49	0.77	0.32	-0.066	0.0046	0.6	0.72	1									
Sn_ppm	-0.16	-0.37	-0.22	-0.026	0.059	-0.053	0.07	-0.025	-0.031	0.12	0.024	0.058	0.12	0.022	0.14	-0.06	0.092	0.036	-0.12	0.038	1								
Ba_ppm	0.6	0.037	0.4	-0.6	-0.17	-0.081	0.11	0.39	0.75	0.32	0.41	0.41	0.29	-0.31	0.36	-0.6	0.36	0.47	0.33	-0.059	-0.21	1							
La_ppm	0.32	0.34	0.16	-0.025	-0.13	0.028	0.27	0.27	0.25	-0.11	0.24	0.12	0.065	0.16	0.14	0.058	0.12	0.27	0.27	0.23	0.15	0.24	1						
Ce_ppm	0.42	0.37	0.018	-0.23	-0.11	-0.14	0.11	0.41	0.25	-0.011	0.4	0.22	0.2	0.28	0.32	-0.0017	0.12	0.32	0.39	0.39	-0.063	0.29	0.27	1					
Nd_ppm	-0.026	0.37	0.22	0.23	-0.17	0.28	-0.03	-0.097	-0.26	-0.27	-0.14	-0.25	-0.23	0.063	-0.11	0.27	-0.062	-0.16	-0.014	-0.049	-0.29	-0.051	0.2	0.027	1				
W_ppm	0.27	0.027	0.026	-0.26	0.11	-0.19	-0.2	0.23	0.39	0.16	0.4	0.4	0.53	0.2	0.88	-0.3	-0.17	0.26	0.14	0.2	0.17	0.3	0.14	0.31	-0.16	1			
Pb_ppm	-0.28	-0.11	-0.17	-0.095	-0.0073	0.19	0.14	-0.09	-0.35	-0.24	-0.19	-0.35	-0.22	-0.0079	-0.35	0.22	0.4	-0.065	-0.14	-0.17	0.2	-0.23	-0.16	-0.12	0.23	-0.36	1		
Bi_ppm	-0.027	0.12	0.17	0.19	0.071	-0.11	-0.17	-0.19	0.15	-0.16	-0.13	-0.058	-0.085	0.057	-0.17	-0.025	-0.36	-0.063	-0.09	-0.024	-0.27	0.013	-0.0017	-0.35	0.1	-0.1	-0.13	1	
Th_ppm	-0.2	-0.48	-0.42	-0.079	0.083	-0.093	0.34	0.11	-0.3	0.1	0.065	-0.067	0.28	-0.06	0.046	-0.16	0.35	0.11	-0.0031	0.076	0.37	-0.26	-0.03	-0.21	-0.2	-0.15	0.28	-0.36	1
LE_ppm	-0.24	-0.67	-0.84	0.025	0.36	-0.51	0.31	0.14	-0.23	0.2	0.1	0.12	0.33	0.2	-0.046	-0.29	0.14	0.14	0.11	0.17	0.34	-0.44	-0.37	-0.28	-0.34	-0.1	0.21	-0.13	0.55

Figure E2. Pearson correlation for granite (green rectangle represents the correlation value for LE-Th).

Correlation	Mg_ppm	Al_ppm	Si_ppm	P_ppm	S_ppm	K_ppm	Ca_ppm	Ti_ppm	Cr_ppm	Mn_ppm	Fe_ppm	Ni_ppm	Cu_ppm	Zn_ppm	As_ppm	Rb_ppm	Sr_ppm	Y_ppm	Zr_ppm	Nb_ppm	Sn_ppm	Ba_ppm	La_ppm	Ce_ppm	Nd_ppm	W_ppm	Pb_ppm	Bi_ppm	Th_ppm	LE_ppm
Mg_ppm	1																												
Al_ppm	0.56	1																											
Si_ppm	0.09	0.6	1																										
P_ppm	-0.67	0.17	0.63	1																									
S_ppm	-0.31	-0.96	-0.58	-0.39	1																								
K_ppm	0.78	0.95	0.42	-0.14	-0.83	1																							
Ca_ppm	-0.96	-0.31	0.057	0.81	0.028	-0.57	1																						
Ti_ppm	0.78	0.22	-0.53	-0.89	-0.049	0.49	-0.78	1																					
Cr_ppm	0.75	0.11	-0.58	-0.93	0.068	0.4	-0.8	0.99	1																				
Mn_ppm	0.35	0.3	-0.57	-0.45	-0.33	0.43	-0.24	0.77	0.71	1																			
Fe_ppm	0.68	0.5	-0.37	-0.59	-0.43	0.68	-0.56	0.9	0.84	0.93	1																		
Ni_ppm	0.58	0.23	-0.62	-0.74	-0.15	0.44	-0.54	0.94	0.92	0.93	0.96	1																	
Cu_ppm	0.35	0.032	-0.78	-0.67	-0.018	0.22	-0.33	0.85	0.83	0.95	0.87	0.96	1																
Zn_ppm	0.1	0.049	-0.73	-0.41	-0.13	0.15	-0.04	0.65	0.62	0.96	0.79	0.86	0.95	1															
As_ppm	0.75	0.87	0.15	-0.27	-0.78	0.95	-0.55	0.65	0.56	0.68	0.86	0.67	0.5	0.45	1														
Rb_ppm	-0.97	-0.47	-0.19	0.64	0.19	-0.69	0.97	-0.65	-0.65	-0.12	-0.48	-0.4	-0.15	0.12	-0.6	1													
Sr_ppm	0.25	0.11	-0.72	-0.52	-0.14	0.25	-0.19	0.76	0.72	0.98	0.86	0.93	0.98	0.99	0.53	-0.033	1												
Y_ppm	0.65	0.21	-0.61	-0.81	-0.098	0.45	-0.63	0.98	0.96	0.88	0.94	0.99	0.94	0.8	0.66	-0.49	0.88	1											
Zr_ppm	0.39	-0.1	-0.84	-0.79	0.16	0.13	-0.43	0.88	0.89	0.86	0.81	0.95	0.98	0.88	0.4	-0.22	0.92	0.94	1										
Nb_ppm	0.81	0.59	-0.23	-0.62	-0.47	0.78	-0.69	0.9	0.85	0.83	0.98	0.9	0.76	0.64	0.91	-0.64	0.74	0.91	0.72										
Sn_ppm	0.42	0.88	0.9	0.39	-0.82	0.77	-0.21	-0.15	-0.23	-0.19	0.057	-0.23	-0.44	-0.43	0.56	-0.44	-0.38	-0.22	-0.53	0.2	1								
Ba_ppm	0.82	0.93	0.41	-0.19	-0.8	1	-0.63	0.52	0.44	0.41	0.68	0.46	0.23	0.13	0.95	-0.73	0.24	0.47	0.15	0.79	0.76	1							
La_ppm	0.57	0.58	-0.3	-0.42	-0.55	0.7	-0.41	0.79	0.72	0.94	0.98	0.9	0.83	0.81	0.88	-0.35	0.87	0.87	0.74	0.94	0.12	0.69	1						
Ce_ppm	0.68	0.99	0.52	0.023	-0.91	0.99	-0.44	0.35	0.25	0.37	0.59	0.33	0.13	0.1	0.92	-0.58	0.18	0.33	0.011	0.69	0.84	0.97	0.64	1					
Nd_ppm	0.28	-0.51	-0.14	-0.56	0.73	-0.32	-0.53	0.15	0.25	-0.48	-0.29	-0.14	-0.21	-0.47	-0.42	-0.46	-0.39	-0.03	8.20E-17	-0.19	-0.28	-0.25	-0.48	-0.42	1				
W_ppm	0.61	0.41	0.68	-0.1	-0.18	0.47	-0.62	0.0071	0.013	-0.51	-0.14	-0.28	-0.52	-0.72	0.21	-0.76	-0.61	-0.19	-0.45	0.068	0.68	0.5	-0.22	0.44	0.51	1			
Pb_ppm	-0.38	-0.14	-0.66	0.0062	-0.06	-0.17	0.45	0.21	0.17	0.73	0.42	0.51	0.7	0.88	0.11	0.58	0.79	0.41	0.59	0.22	-0.52	-0.21	0.51	-0.16	-0.65	-0.95	1		
Bi_ppm	0.57	0.36	0.69	-0.077	-0.14	0.42	-0.58	-0.038	-0.027	-0.55	-0.2	-0.33	-0.56	-0.76	0.15	-0.73	-0.65	-0.24	-0.48	0.012	0.66	0.45	-0.28	0.39	0.54	1	-0.97	1	
Th_ppm	0.053	-0.29	-0.93	-0.6	0.25	-0.12	-0.1	0.67	0.68	0.82	0.65	0.82	0.94	0.93	0.18	0.12	0.92	0.79	0.94	0.5	-0.71	-0.12	0.61	-0.21	-0.14	-0.72	0.8	-0.74	1
LE_ppm	-0.36	-0.83	-0.94	-0.45	0.78	-0.71	0.16	0.23	0.31	0.27	0.031	0.31	0.52	0.5	-0.48	0.4	0.46	0.31	0.6	-0.12	-1	-0.7	-0.037	-0.78	0.25	-0.7	0.56	-0.68	0.77

Figure E3. Pearson correlation for granite+schist (green rectangle represents the correlation value for LE-Th, and red rectangles represent the correlation values for LE-S, LE-Cu, LE-Zn, LE-Zr).

Correlation	Mg_ppm	Al_ppm	Si_ppm	P_ppm	S_ppm	K_ppm	Ca_ppm	Ti_ppm	Cr_ppm	Mn_ppm	Fe_ppm	Ni_ppm	Cu_ppm	Zn_ppm	As_ppm	Rb_ppm	Sr_ppm	Y_ppm	Zr_ppm	Nb_ppm	Sn_ppm	Ba_ppm	La_ppm	Ce_ppm	Nd_ppm	W_ppm	Pb_ppm	Bi_ppm	Th_ppm	LE_ppm
Mg_ppm	1																												
Al_ppm	0.47	1																											
Si_ppm	-0.039	0.41	1																										
P_ppm	0.1	0.14	-0.022	1																									
S_ppm	0.049	-0.015	-0.35	0.26	1																								
K_ppm	-0.11	0.61	0.52	-0.012	-0.25	1																							
Ca_ppm	0.27	0.11	-0.33	0.38	0.41	-0.21	1																						
Ti_ppm	0.29	0.4	-0.26	-0.072	-0.015	0.14	0.095	1																					
Cr_ppm	0.56	0.62	-0.064	0.01	0.065	0.22	0.081	0.49	1																				
Mn_ppm	0.093	0.14	-0.25	0.36	0.024	-0.042	0.17	0.18	0.22	1																			
Fe_ppm	0.41	0.44	-0.43	0.21	0.14	0.097	0.27	0.63	0.59	0.61	1																		
Ni_ppm	0.51	0.34	-0.56	0.12	0.36	-0.12	0.36	0.54	0.6	0.51	0.87	1																	
Cu_ppm	0.57	0.2	-0.62	0.13	0.38	-0.22	0.45	0.41	0.44	0.28	0.69	0.83	1																
Zn_ppm	0.42	0.21	-0.6	0.22	0.3	-0.14	0.38	0.44	0.43	0.42	0.73	0.82	0.83	1															
As_ppm	0.077	0.031	-0.047	0.043	-0.16	0.042	0.041	0.061	0.12	0.28	0.23	0.18	0.11	0.16	1														
Rb_ppm	-0.36	0.3	0.35	0.1	-0.16	0.65	-0.031	-0.12	-0.074	-0.021	-0.11	-0.31	-0.39	-0.19	0.032	1													
Sr_ppm	-0.18	0.2	-0.11	0.18	-0.034	0.18	0.55	0.22	-0.04	0.18	0.27	0.095	-0.0037	0.15	0.12	0.42	1												
Y_ppm	0.42	0.31	-0.51	-0.038	0.18	-0.098	0.39	0.59	0.46	0.31	0.72	0.79	0.68	0.68	0.18	-0.29	0.33	1											
Zr_ppm	-0.16	0.03	-0.24	-0.21	-0.08	-0.0081	0.036	0.59	0.089	0.14	0.2	0.22	0.044	0.098	0.047	-0.1	0.26	0.47	1										
Nb_ppm	0.11	0.29	-0.19	-0.13	0.032	0.16	-0.074	0.62	0.43	0.23	0.46	0.4	0.22	0.33	0.056	-0.01	0.084	0.45	0.45	1									
Sn_ppm	-0.053	-0.036	0.028	-0.037	-0.18	0.14	-0.047	0.016	0.0055	0.026	0.027	-0.082	-0.039	-0.034	0.44	0.14	0.033	-0.071	-0.065	0.068	1								
Ba_ppm	0.2	0.7	0.57	-0.072	-0.23	0.53	-0.17	0.3	0.51	0.054	0.14	-0.012	-0.24	-0.21	0.036	0.36	0.12	0.0091	0.11	0.32	0.038	1							
La_ppm	0.18	0.27	0.13	0.11	-0.11	0.11	0.1	0.061	0.21	0.14	0.12	0.071	-0.026	0.022	0.068	0.12	0.21	0.18	0.015	0.16	0.09	0.28	1						
Ce_ppm	0.35	0.51	0.11	0.12	-0.069	0.15	0.15	0.44	0.44	0.18	0.43	0.32	0.16	0.2	0.14	-0.0071	0.24	0.37	0.18	0.29	0.11	0.45	0.38	1					
Nd_ppm	-0.13	0.12	0.079	-0.038	0.067	0.15	0.041	0.034	0.09	-0.017	0.043	0.016	-0.033	-0.023	0.047	0.19	0.085	-0.034	0.049	0.16	0.2	0.16	0.02	0.21	1				
W_ppm	0.11	0.0036	0.047	-0.18	-0.071	-0.072	0.086	-0.072	0.065	-0.0075	-0.012	0.021	0.045	0.043	0.36	0.019	0.062	0.047	-0.11	-0.11	0.15	4.90E-04	0.065	0.051	0.0078	1			
Pb_ppm	0.23	0.12	-0.53	0.16	0.2	-0.11	0.48	0.22	0.15	0.28	0.43	0.54	0.57	0.65	0.087	0.0087	0.37	0.61	0.21	0.14	0.018	-0.26	0.1	0.15	-0.033	-0.022	1		
Bi_ppm	0.18	0.35	0.5	0.035	-0.11	0.14	-0.089	-0.16	0.21	-0.16	-0.24	-0.2	-0.29	-0.33	0.028	0.13	-0.12	-0.24	-0.25	0.023	0.094	0.54	0.21	0.18	0.004	-0.022	-0.32	1	
Th_ppm	-0.18	-0.36	-0.59	-0.082	0.14	-0.095	0.1	0.21	-0.17	0.12	0.28	0.3	0.32	0.38	0.24	-0.094	0.18	0.25	0.17	0.041	0.12	-0.51	-0.14	-0.13	-0.077	0.042	0.31	-0.51	1
LE_ppm	-0.27	-0.81	-0.85	-0.089	0.26	-0.69	0.14	-0.094	-0.32	0.014	-0.046	0.12	0.25	0.23	-0.03	-0.37	-0.041	0.12	0.15	-0.059	-0.024	-0.75	-0.24	-0.38	-0.11	-0.038	0.27	-0.48	0.54	1

Figure E4. Pearson correlation for schist (dark green rectangle represents the correlation value for LE-Th).

Appendix F – Tukey values (Anomaly Assessment Tool for the stream sediment samples)

Lithology	Sample ID	Mg_Tuke	Al_Tukey	Si_Tukey	P_Tukey	S_Tukey	K_Tukey	Ca_Tuke	Ti_Tukey	Cr_Tuke	Mn_Tuke	Fe_Tuke	Ni_Tukey	Cu_Tuke	Zn_Tuke	As_Tuke	Rb_Tuke	Sr_Tuke	Y_Tukey	Zr_Tukey	Nb_Tuke	Sn_Tuke	Ba_Tuke	La_Tuke	Ce_Tuke	Nd_Tuke	W_Tukey	Pb_Tuke	Bi_Tukey	Th_Tuke	LE_Tuke
granite	PT001042	0	0	0	0	0	0	0	0	0	0	0	0	0	0	0	0	0	0	0	0	0	0	0	0	0	0	0	0	0	0
granite	PT001043	0	0	0	0	0	0	0	0	0	0	0	0	0	0	0	0	0	0	0	1	0	1	0	0	0	0	0	0	0	0
granite	PT001044	0	0	0	0	0	0	0	0	0	0	0	0	0	0	0	0	0	0	0	0	0	0	0	0	0	0	0	0	0	0
granite	PT001045	0	0	0	0	0	0	0	0	0	0	0	0	0	0	0	0	0	0	0	0	0	0	0	0	0	0	0	0	0	0
granite	PT001046	0	0	0	0	0	0	0	0	0	0	0	0	0	0	0	0	0	0	0	1	0	0	1	0	0	0	0	0	0	0
granite	PT001047	0	0	0	0	0	0	0	0	0	0	0	0	0	0	0	0	0	0	0	0	0	1	0	0	0	0	0	0	0	0
granite	PT001048	0	0	0	0	0	0	0	0	0	0	0	0	0	0	0	0	0	0	0	0	0	0	0	0	0	0	0	0	0	0
granite	PT001049	0	0	0	0	0	0	0	0	0	0	0	0	0	0	0	0	0	0	0	0	0	0	0	0	0	0	0	0	0	0
granite	PT001061	0	0	0	0	0	0	0	0	0	0	0	0	0	0	0	0	0	0	0	0	0	0	0	0	0	0	0	0	0	0
granite	PT001062	0	0	0	0	0	0	0	0	0	0	0	0	0	0	1	0	0	0	0	0	0	0	0	0	0	0	0	0	0	0
granite	PT001063	0	0	0	0	0	0	0	0	0	0	0	0	0	0	2	0	0	0	0	2	0	0	0	0	0	0	0	0	0	0
granite	PT001064	0	0	0	0	0	0	0	0	0	0	0	0	0	0	2	0	0	0	0	0	0	0	0	0	0	0	0	0	0	0
granite	PT001065	0	0	0	0	0	0	0	0	0	0	0	0	0	0	0	0	0	0	0	0	0	0	0	0	0	0	0	0	0	0
granite	PT001066	0	0	0	0	0	0	0	0	0	0	0	0	0	0	0	0	0	0	0	0	0	0	0	0	0	0	0	0	0	0
granite	PT001067	0	0	0	0	0	0	0	0	0	0	0	0	0	0	0	0	0	0	0	0	0	0	0	0	0	0	0	0	0	0
granite	PT001068	0	0	0	0	0	0	0	0	0	0	0	0	0	0	0	0	0	0	0	0	0	0	0	0	0	0	0	0	0	0
granite	PT001069	0	0	0	0	0	0	0	0	0	0	0	0	0	0	0	0	0	0	0	0	0	0	0	0	0	0	0	0	0	0
granite	PT001070	0	0	0	0	0	0	0	0	0	0	0	0	0	0	0	0	0	0	0	0	0	1	0	0	0	0	0	0	0	0
granite	PT001071	0	0	0	0	0	0	0	0	0	0	0	0	0	0	0	0	0	0	0	0	0	0	0	0	0	0	0	0	0	0
granite	PT001072	1	0	0	0	0	0	0	0	0	0	0	0	0	0	0	0	0	0	0	0	0	0	0	0	0	0	0	0	0	0
granite	PT001073	0	0	0	0	0	0	0	0	0	0	0	0	0	0	0	0	0	0	0	0	0	2	0	0	0	0	0	0	0	0
granite	PT001074	1	0	0	0	0	0	0	0	0	0	0	0	0	0	2	0	0	0	0	0	0	0	0	0	0	2	0	0	0	0
granite	PT001075	1	0	0	0	0	0	0	0	0	0	0	0	0	0	2	0	0	0	0	0	0	0	0	0	0	0	0	0	0	0
granite	PT001076	0	0	0	0	0	0	0	0	0	0	0	0	0	0	2	0	0	0	0	0	0	0	0	0	0	0	0	0	0	0
granite	PT001077	0	0	0	0	0	0	0	0	0	0	0	0	0	0	0	0	0	0	0	0	0	0	0	0	0	0	0	0	0	0
granite	PT001078	0	0	0	0	0	0	0	0	0	0	0	0	0	0	0	0	0	0	0	0	0	0	0	0	0	0	0	0	0	0
granite	PT001079	0	0	0	0	0	0	0	0	0	0	0	0	0	0	0	0	0	0	0	0	0	0	0	0	0	0	0	0	0	0
granite	PT001080	0	0	0	0	0	0	0	0	0	0	0	0	0	0	0	0	0	0	0	0	0	0	0	0	0	0	0	0	0	0
granite	PT001081	0	0	0	0	0	0	0	0	0	0	0	0	0	0	0	0	0	0	0	0	0	0	0	0	1	0	0	0	0	0
granite	PT001082	0	0	0	0	0	0	0	0	0	0	0	0	0	0	0	0	0	0	0	0	0	0	0	0	0	0	0	0	0	0
granite	PT001083	0	0	0	0	0	0	0	0	0	0	0	0	0	0	0	0	0	0	0	0	0	2	0	0	0	0	0	0	0	0
granite	PT001084	0	0	1	0	0	1	0	0	0	0	0	0	0	0	0	0	0	0	0	1	0	0	0	0	0	0	0	0	0	0
granite	PT001085	0	0	1	0	0	1	0	1	0	0	0	0	0	0	0	0	0	0	0	0	0	0	1	0	0	0	0	0	0	0
granite	PT001087	0	0	0	0	0	0	0	0	1	0	0	0	0	0	0	0	0	0	0	0	0	0	0	0	0	0	0	0	0	0
granite	PT001088	0	0	0	0	0	0	0	0	0	0	0	0	0	0	0	0	0	0	0	0	0	1	0	0	0	0	0	0	0	0
granite	PT001089	0	0	0	0	0	0	0	0	1	0	0	0	0	0	0	0	0	0	0	0	0	0	0	0	0	0	0	0	0	0
granite	PT001091	0	0	0	0	0	0	0	0	1	0	0	0	0	0	0	0	0	0	0	1	0	0	1	0	0	0	0	0	0	0
granite	PT001092	0	0	0	0	0	0	0	0	1	0	0	0	0	0	0	0	0	0	0	0	0	0	0	1	0	0	0	0	0	0
granite+schi	PT001093	0	0	0	1	0	0	0	0	0	0	0	0	0	0	0	0	0	0	0	0	0	0	0	0	0	0	0	0	0	0
granite+schi	PT001094	0	0	0	0	0	0	0	0	0	0	0	0	0	0	0	0	0	0	1	0	0	0	0	1	0	0	0	0	0	0
granite+schi	PT001095	0	0	0	0	0	0	0	0	0	0	0	0	0	0	0	0	0	0	1	0	0	0	0	0	0	0	0	0	0	0
granite+schi	PT001096	0	0	0	0	0	0	0	0	0	0	0	0	0	0	1	0	0	0	0	0	0	2	0	0	0	0	0	0	0	0
schist	PT001097	0	0	0	0	0	0	0	0	0	0	0	0	0	0	0	0	0	0	0	0	0	0	0	0	0	0	0	0	0	0
schist	PT001098	0	0	0	0	0	0	0	0	0	0	0	0	0	0	0	0	0	0	0	0	0	0	0	0	0	0	0	0	0	0
schist	PT001099	0	1	1	0	0	0	0	0	0	0	0	0	0	0	0	0	0	0	0	0	0	0	0	0	0	0	0	0	0	1
schist	PT001100	0	0	0	0	0	0	0	0	0	0	0	0	0	0	0	0	0	0	0	0	0	0	0	0	0	0	0	0	0	0
schist	PT001101	0	1	0	0	0	0	0	0	0	0	0	0	0	0	0	0	0	0	0	0	0	1	0	0	0	0	0	0	0	0
schist	PT001102	0	0	0	0	0	0	0	0	0	0	0	0	0	0	0	0	0	0	0	0	0	0	0	0	0	0	0	0	0	0
schist	PT001103	0	0	0	0	0	0	0	0	0	0	0	0	0	0	0	0	0	0	0	0	0	0	0	0	0	0	0	0	0	0
schist	PT001104	0	0	0	0	0	0	0	0	0	0	0	0	0	0	0	0	0	0	0	0	0	1	0	0	0	0	0	0	0	0
schist	PT001105	0	0	0	0	0	0	0	0	0	0	0	0	0	0	0	0	0	0	0	0	0	0	0	0	0	0	0	0	0	0
schist	PT001106	0	0	0	0	0	0	0	0	0	0	0	0	0	0	0	0	0	0	0	0	0	0	0	0	0	0	0	0	0	0
schist	PT001107	0	0	0	0	0	0	0	0	0	0	0	0	0	0	0	0	0	0	0	0	0	0	0	0	0	0	0	0	0	0
schist	PT001108	0	0	0	0	0	0	0	0	1	0	0	0	0	0	0	0	0	0	0	0	0	0	0	0	0	0	0	0	0	0

Lithology	Sample ID	Mg_Tuke	Al_Tukey	Si_Tukey	P_Tukey	S_Tukey	K_Tukey	Ca_Tuke	Ti_Tukey	Cr_Tukey	Mn_Tuke	Fe_Tuke	Ni_Tukey	Cu_Tuke	Zn_Tuke	As_Tuke	Rb_Tuke	Sr_Tukey	Y_Tukey	Zr_Tukey	Nb_Tuke	Sn_Tuke	Ba_Tuke	La_Tuke	Ce_Tuke	Nd_Tuke	W_Tukey	Pb_Tuke	Bi_Tukey	Th_Tuke	LE_Tuke
schist	PT001166	0	0	0	0	0	0	1	0	0	0	0	0	0	0	0	0	1	0	0	0	0	0	0	0	0	0	0	0	0	0
schist	PT001167	0	0	0	0	0	0	0	0	0	0	0	0	0	0	0	0	0	0	0	0	0	0	0	0	0	0	0	0	0	0
schist	PT001168	0	0	0	0	0	0	0	0	0	0	0	0	0	0	0	0	0	0	0	0	0	0	0	0	0	0	0	0	0	0
schist	PT001169	0	0	0	0	0	0	0	0	0	0	0	0	0	0	0	0	0	0	0	0	0	0	0	0	0	0	0	0	0	0
schist	PT001170	0	0	0	0	0	0	0	0	0	0	0	0	0	0	0	0	0	0	0	0	0	0	1	0	0	0	0	0	0	0
schist	PT001171	0	0	0	0	0	0	0	0	0	2	1	0	0	0	2	0	0	0	0	0	0	0	0	0	0	0	0	0	0	0
schist	PT001172	0	0	0	0	0	0	0	0	0	0	0	0	0	0	0	0	0	0	0	0	0	0	0	0	0	0	0	0	0	0
schist	PT001173	0	0	0	0	0	0	0	0	0	0	0	0	0	0	0	0	0	0	1	0	0	0	0	0	0	0	0	0	0	0
schist	PT001174	0	0	0	0	0	0	0	0	0	0	0	0	0	0	1	0	0	0	0	0	0	0	1	0	0	0	0	0	0	0
schist	PT001175	0	0	0	0	0	0	0	0	0	0	0	0	0	0	0	0	0	0	0	0	0	0	1	0	0	0	0	0	0	0
schist	PT001176	0	0	0	0	0	0	0	0	0	0	0	0	0	0	0	0	0	0	0	0	0	0	0	0	0	0	0	0	0	0
schist	PT001177	0	0	0	0	0	0	0	0	0	0	0	0	0	0	0	0	0	0	0	0	0	1	0	0	0	0	0	0	0	0
schist	PT001178	0	0	0	0	0	0	0	0	0	0	0	0	0	0	0	0	0	0	0	0	0	0	0	0	0	0	0	0	0	0
schist	PT001179	0	0	0	0	0	0	0	0	0	0	0	0	0	0	0	0	0	0	0	0	0	0	0	0	0	0	0	0	0	0
schist	PT001180	0	0	0	0	0	0	0	0	0	0	0	0	0	0	0	0	0	0	0	0	0	0	0	0	0	0	0	0	0	0
schist	PT001181	0	0	0	0	0	0	0	0	0	0	0	0	0	0	0	0	0	0	0	0	0	1	1	0	0	0	0	0	0	0
schist	PT001182	0	0	0	0	0	0	0	0	0	0	0	0	0	0	0	0	0	0	0	0	0	0	0	0	0	0	0	0	0	0
schist	PT001183	0	0	0	0	0	0	0	0	0	0	0	0	0	0	0	0	0	0	0	0	0	0	0	0	0	0	0	0	0	0
schist	PT001184	0	0	0	0	0	0	0	0	0	0	0	0	0	0	0	0	0	0	0	0	0	0	0	1	0	0	0	0	0	0
schist	PT001185	0	0	0	0	0	0	0	0	0	0	0	0	0	0	0	0	0	0	0	0	0	0	0	0	0	0	0	0	0	0
schist	PT001186	0	0	0	0	0	0	0	0	0	0	0	0	0	0	1	0	0	0	0	0	0	0	0	0	0	0	0	0	0	0
schist	PT001187	0	0	0	0	0	0	0	0	0	0	0	0	0	0	0	0	0	0	0	0	0	0	1	0	0	0	0	0	0	0
schist	PT001188	0	0	0	0	0	0	0	0	0	0	0	0	0	0	0	0	0	0	0	0	0	0	0	0	0	0	0	0	0	0
schist	PT001189	0	0	0	0	0	0	0	0	0	0	0	0	0	0	2	0	0	0	0	0	0	0	0	0	0	2	0	0	0	0
schist	PT001190	0	0	0	0	0	0	0	0	0	1	0	0	0	0	0	0	0	0	0	0	0	0	0	0	0	0	0	0	0	0
schist	PT001191	0	0	0	0	0	0	0	0	0	0	0	0	0	0	0	0	0	0	0	0	0	0	1	0	0	0	0	0	0	0
schist	PT001192	0	0	0	0	0	0	0	0	0	0	0	0	0	0	0	0	0	0	0	0	0	0	0	0	0	0	0	0	0	0
schist	PT001193	0	0	0	0	0	0	0	0	0	0	0	0	0	0	0	0	0	0	0	0	0	0	0	0	0	0	0	0	0	0
schist	PT001194	0	0	0	0	0	0	0	0	0	0	0	0	0	0	0	0	0	0	0	0	0	0	0	0	0	0	0	0	0	0
schist	PT001197	0	0	0	0	0	0	0	0	0	0	0	0	0	0	0	0	0	0	0	0	0	0	0	0	0	0	0	0	0	0
schist	PT001198	0	0	0	0	0	0	0	0	0	0	0	0	0	0	0	0	0	0	0	0	0	0	0	0	0	0	0	0	0	0
schist	PT001199	0	0	0	0	0	0	0	0	0	0	0	0	0	0	0	0	0	0	0	0	0	0	0	0	0	0	0	0	0	0
schist	PT001200	0	0	0	0	0	0	0	0	0	0	0	0	0	0	0	0	0	0	0	0	0	0	0	0	0	0	0	0	0	0
schist	PT001201	0	0	0	0	0	0	0	0	0	0	0	0	0	0	0	0	0	0	0	0	0	0	1	0	0	0	0	0	0	0
schist	PT001202	0	0	0	0	0	0	0	0	0	0	0	0	0	0	0	0	0	0	0	0	0	0	0	0	0	0	0	0	0	0
schist	PT001203	0	0	0	0	0	0	0	0	0	0	0	0	0	0	0	0	0	0	0	0	0	0	0	0	0	0	0	0	0	0
schist	PT001204	0	0	0	0	0	0	0	0	0	0	0	0	0	0	0	0	0	0	0	0	0	0	1	0	0	0	0	0	0	0
schist	PT001205	0	0	0	0	0	0	0	0	0	0	0	0	0	0	0	0	0	0	0	0	0	0	0	0	0	0	0	0	0	0
schist	PT001206	0	0	0	0	0	0	0	0	0	2	0	0	0	0	0	0	0	0	0	0	0	0	0	0	0	0	0	0	0	0
schist	PT001207	0	0	0	0	0	0	0	0	0	0	0	0	0	0	0	0	0	0	0	0	0	0	0	0	0	0	0	0	0	0
schist	PT001208	0	0	0	0	0	0	0	0	1	0	0	0	0	0	0	0	0	0	0	0	0	0	0	0	0	0	0	0	0	0
schist	PT001209	0	0	0	0	0	0	0	0	0	0	0	0	0	0	0	0	0	0	0	0	0	0	0	0	0	1	0	0	0	0
schist	PT001210	0	0	0	0	0	0	0	0	0	0	0	0	0	0	0	0	0	0	0	0	0	0	0	0	0	0	0	0	0	0
schist	PT001211	0	0	0	0	0	0	0	0	1	0	0	0	0	0	0	0	0	0	0	0	0	0	1	0	0	0	0	0	0	0
schist	PT001212	0	0	0	0	1	1	0	0	0	0	0	0	0	0	0	0	0	0	0	0	0	0	0	0	0	0	0	0	0	0
schist	PT001213	0	0	0	0	0	0	0	0	0	0	0	0	0	0	0	0	0	0	0	0	0	0	0	0	0	0	0	0	0	0
schist	PT001214	0	0	0	0	0	0	0	0	0	0	0	0	0	0	0	0	0	0	0	0	0	0	0	0	0	0	0	0	0	0
schist	PT001215	0	0	0	0	0	0	0	0	0	0	0	0	0	0	0	0	0	0	0	0	0	0	0	0	0	0	0	0	0	0
schist	PT001216	0	0	0	0	0	0	0	0	0	0	0	0	0	0	0	0	0	0	0	0	0	0	0	0	0	0	0	0	0	0
schist	PT001217	0	0	0	0	0	0	0	0	0	0	0	0	0	0	0	0	0	0	0	0	0	0	0	0	0	0	0	0	0	0
schist	PT001153	0	1	0	1	0	0	0	0	1	0	0	0	0	0	0	1	0	0	0	0	0	0	0	0	0	0	0	0	0	0
schist	PT001154	0	0	0	0	0	0	1	0	0	0	0	0	0	0	0	0	0	0	0	0	0	0	0	0	0	0	0	0	0	0
schist	PT001155	0	0	0	0	0	0	0	0	0	0	0	0	0	0	0	0	0	0	0	0	0	0	0	0	0	0	0	0	0	0
schist	PT001156	0	0	0	1	1	0	0	0	1	0	0	0	0	0	0	0	0	0	0	0	0	0	0	0	0	0	0	0	0	0
schist	PT001157	0	0	0	1	0	0	0	0	1	0	0	0	0	0	0	0	0	0	0	0	0	0	0	0	0	0	0	0	0	0
schist	PT001158	0	0	0	0	0	0	0	0	1	0	0	0	0	0	0	0	0	0	0	0	0	0	0	0	0	0	0	0	0	0
schist	PT001159	0	0	0	0	0	0	0	0	1	0	0	0	0	0	0	0	0	0	0	0	0	0	0	0	0	0	0	0	0	0
schist	PT001160	0	0	0	0	0	0	0	0	0	0	0	0	0	0	0	0	0	0	0	0	0	0	0	0	0	0	0	0	0	0
schist	PT001162	0	0	0	0	0	0	1	0	0	0	0	0	0	0	0	0	1	0	0	0	0	0	0	0	0	0	0	0	0	0
schist	PT001163	0	0	0	0	0	0	0	0	0	0	0	0	0	0	0	0	0	0	0	0	0	0	0	0	0	0	0	0	0	0
schist	PT001164	0	0	0	0	0	0	1	0	0	0	0	0	0	0	0	0	1	0	0	0	0	0	0	0	0	0	0	0	0	0
schist	PT001165	0	0	0	0	0	0	0	0	0	0	0	0	0	0	0	0	0	0	0	0	0	0	0	0	0	0	0	0	0	0

Appendix G – Standardized Tukey values for stream sediment anomaly definition

[Colour]	Sample ID	Mg_Z	Al_Z	Si_Z	P_Z	S_Z	K_Z	Ca_Z	Ti_Z	Cr_Z	Mn_Z	Fe_Z	Ni_Z	Cu_Z	Zn_Z	As_Z	Rb_Z	Sr_Z	Y_Z	Zr_Z	Nb_Z	Sn_Z	Ba_Z	La_Z	Ce_Z	Nd_Z	W_Z	Pb_Z	Bi_Z	Th_Z	LE_Z
schist	PT001042	-2.3	-1.25	-0.11	-2.28	-2.43	-0.68	-3.06	-2.71	-1.93	-2.257	-2.81	-3	-3.147	-2.722	-2.654	-1.006	-2.89	-3.29	-2.89	-2.358	-2.5	-1.868	-3.73	-2.966	-2.5	-2.5	-2.75	-1.05	-2.5	-3.15
schist	PT001043	-1.6	-0.24	-1.64	-2.98	-2.34	-1.34	-2.577	-0.92	-0.69	-0.353	-1.18	-1.39	-1.882	-1.965	-2.423	-1.153	-1.07	-1.5	-1.61	0.3584	-1.1	0.5372	-1.42	-0.958	-1.428	-2.5	-1.889	-0.85	-2.5	-2.77
schist	PT001044	-2.2	-1.5	-0.57	-1.32	-2.15	-0.75	-2.725	-2.36	-1.46	-2.29	-2.64	-2.67	-2.736	-2.288	-2.692	-0.624	-2.44	-2.96	-2.62	-2.217	-1.645	-1.202	-1.7	-2.042	-1.621	-1.35	-2.223	-1.64	-1.755	-2.87
schist	PT001045	-2.3	-2.52	-1.62	-1.22	-1.5	-1.52	-2.152	-2.14	-2.09	-2.15	-2.59	-3.03	-2.882	-2.621	-2.474	-1.006	-2.3	-3.13	-2.75	-2.788	-1.645	-2.209	-2.33	-2.534	-2.5	-2.5	-2.306	-2.5	-2.181	-1.97
schist	PT001046	-1.5	-2.88	-1.97	-1.73	-2.37	-2.56	-2.229	-2.17	-2.14	-2.576	-2.12	-2.5	-2.353	-2.318	-2.705	-3.053	-2.44	-2.25	-2.62	-2.646	0.5	-2.722	-0.34	0.2627	-1.448	-2.5	-2.862	-1.31	-1.287	-1.71
schist	PT001047	-1.7	-1.14	-0.78	-2.04	-2.41	-0.21	-3.04	-1.94	-2.11	-2.186	-1.41	-2.19	-2.647	-2.156	-2.449	-1.288	-2.28	-2.58	-2.78	-2.071	-2.5	-0.691	-4.8	-1.229	-1.225	-2.5	-2.667	-2.5	-1.67	-3.06
schist	PT001048	-2.5	-3.09	-2.46	-1.5	-1.2	-1.93	-0.855	-1.66	-2.5	-1.555	-2.25	-1.86	-1.647	-2.167	-2.32	-2.388	-1.11	-1.88	-1.2	-2.217	-1.173	-2.994	-2.57	-2.703	-2.5	-2.5	-2.112	-2.5	-1.074	-1.39
schist	PT001049	-2.2	-1.82	-1.57	-1.3	-1.97	-1.3	-2.719	-2.89	-0.43	-2.035	-1.62	-2.33	-2.323	-2.247	-2.462	-1.606	-2.48	-2.33	-2.93	-2.5	-2.5	-1.476	-2.19	-2.364	-1.261	-2.5	-2.612	-2.5	-2.138	-2.3
schist	PT001061	-2.2	-2.32	-0.09	-1.93	-2.73	-1.58	-2.512	-2.92	-3	-1.858	-2.73	-2.81	-3.089	-2.621	-0.82	-2.223	-1.99	-2.58	-2.72	-2.929	-2.5	-1.661	-1.24	-1.5	-1.69	-1.35	-2.695	-1.5	-1.628	-2.86
schist	PT001062	-1.5	-1.63	-0.63	-1.54	-2.7	-1.74	-2.435	-1.22	-2.09	-0.686	-1.35	-2.64	-0.852	-2.368	-0.064	-1.93	-2.03	-2.25	-2.69	-2.646	-1.555	-1.115	-1.73	-1.746	-1.025	-1.25	-2.612	-2.5	-2.5	-2.95
schist	PT001063	-2.0	-1.52	-1.52	-1.68	-2.44	-1.16	-2.036	-1.94	-1.5	-1.218	-1.41	-1.81	-1.97	-1.712	16.654	-1.235	-0.91	-1.88	-2.14	-1.5	1.9425	-1.476	-1.81	-1.438	-1.418	-0.83	-2.112	-1.03	-0.649	-2.48
schist	PT001064	-1.7	-0.59	-1.74	-1.69	-1.91	-1.21	-1.5	-1.08	-0.97	-0.689	-0.83	-0.67	-2.059	-1.53	3.2819	-1.429	-0.5	-0.5	-0.95	-1.212	-2.5	-0.578	-1.5	-0.997	-1.582	-2.5	-1.333	-1.69	-1.926	-2.69
schist	PT001065	-2.1	-1.32	-1.76	-2.69	-2.59	-1.82	-2.024	-1.88	-2.21	-2.147	-1.86	-2.11	-2.03	-1.652	-2.192	-2.141	-1.21	-1.33	-1.38	-2.071	-2.5	-2.014	-1.31	-1.59	-1.625	-2.5	-0.195	-2.5	-2.096	-2.27
schist	PT001066	-2.5	-1.45	-2.8	-2.82	-2.15	-2.08	-2.199	-2.04	-1.48	-2.846	-1.08	-1.08	-1.353	-0.975	-2.141	-1.459	-0.75	-1.33	-2.44	-1.929	-2.5	-2.434	-1.88	-1.373	-1.89	-1.01	-1.083	-2.5	-1.869	-1.7
schist	PT001067	-2.1	-1.77	-1.5	-1.36	-0.97	-1.6	0.2806	-2.55	-2.47	-1.407	-2.19	-1.5	-1.617	-2.04	-2.394	-2.354	-1	-1.84	-1.62	-2.68	-1.5	-2.404	-2.06	-1.805	-1.5	-1.57	-1.035	-2.5	-1.181	-2.32
schist	PT001068	-1.7	-1.58	-1.45	-1.52	-0.8	-2.1	-1.482	-2.81	-1.43	-2.541	-2.02	-1.92	-2.03	-1.985	-2.603	-2.071	-1.44	-1.42	-2.15	-2.217	-2.5	-1.923	-1.72	-2.373	-2.5	-2.5	-1.583	-1.69	-2.5	-2.37
schist	PT001069	-1.8	-0.89	-1.07	-0.63	-1.1	-1.31	-0.645	-2.65	-2.05	-1.781	-1.57	-1.5	-1.441	-1.783	-1.295	-1.877	-1.4	-1.88	-1.78	-2.358	-1.682	-1.743	-2	-1.37	-1.68	-2.5	-1.5	-1.69	-1.67	-2.88
schist	PT001070	-2.8	-3.24	-2.05	-2.28	-2.06	-2.74	-1.744	-2.66	-1.95	-2.201	-2.98	-2.56	-2.264	-2.227	-2.346	-2.812	-2.66	-2.58	-1.62	-3.075	-2.5	-2.9	-4.8	-2.788	-2.5	-2.5	-2.167	-2.5	-1.883	-1.38
schist	PT001071	-0.3	-1.35	-2.26	-0.8	-1.96	-1.81	0.0512	-1.33	-1.13	-0.988	-0.84	-0.67	-0.647	-0.692	-2.205	-2.782	-1.93	-1.38	-1.93	-2.071	-2.5	-2.425	-1.01	-1.593	-2.5	-2.5	-1.667	-2.5	-1.94	-2.25
schist	PT001072	0.0	-0.91	-2.59	-2.35	-2.62	-1.22	-1.896	-1.03	-0.95	-2.357	-0.88	-0.72	-0.499	-0.672	-2.077	-2.371	-2.3	-0.75	-2.17	-1.358	-2.5	-1.931	-1.36	-1.946	-2.5	-2.5	-1.445	-1.64	-2.032	-2.2
schist	PT001073	-1.7	-2.29	-3.06	-2.18	-2.3	-2.01	-1.708	-1.5	-1.65	-1.619	-1.01	-1.28	-1.029	-1.177	-2.141	-2.541	-2.54	-1.63	-2.02	-1.358	1.9545	-2.861	-2.34	-2.568	-1.323	-2.5	-0.445	-2.5	-1.642	-1.42
schist	PT001074	0.0	-2.02	-2.55	-2.09	-2.31	-2.41	-1.144	-1.71	-1.13	-1.097	-1.17	-0.97	-0.794	-1.167	4.5	-2.494	-2.15	-1.5	-2.24	-1.929	-1.645	-2.475	-2.17	-2.5	-2.5	4.5	-1.556	-2.5	-1.202	-1.83
schist	PT001075	0.4	-1.2	-2.41	-2.04	-2.41	-1.72	-0.49	-1.55	-1.01	-0.387	-0.26	0.167	-0.264	-0.955	3.4488	-1.853	-1.81	-0.33	-1.71	-1.358	-1.464	-1.974	-1.79	-1.492	-1.67	-2.5	-1.139	-2.5	-1.415	-2.32
schist	PT001076	-1.2	-2.89	-2.96	-2.3	-2.32	-2.81	-1.657	-2.11	-2.16	-1.528	-1.5	-1.69	-0.97	-1.54	2.0896	-2.612	-2.36	-2.08	-2.63	-2.358	-1.427	-2.824	-1.24	-1.695	-2.5	-2.5	-1.667	-2.5	-1.606	-1.23
schist	PT001077	-0.8	-2.42	-2.39	-2.11	-2.73	-2.08	-2.429	-2.5	-1.77	-1.802	-1.85	-2.19	-1.706	-2.035	-1.68	-2.629	-2.75	-2.5	-2.53	-2.217	-1.518	-2.604	-2.29	-1.653	-1.53	-2.5	-2.583	-2.5	-2.053	-1.69
schist	PT001078	-2.1	-2.33	-2.81	-1.78	-2.31	-1.94	-2.294	-1.76	-2.19	-0.373	-1.45	-1.67	-1.205	-1.47	-1.5	-2.612	-2.58	-1.38	-2.06	-1.642	-2.5	-2.998	-2.01	-2.246	-2.5	-2.5	-1.139	-2.5	-1.386	-1.48
schist	PT001079	-1.1	-2.04	-2.12	-1.49	-2	-1.73	-1.523	-2.05	-1.7	-2.179	-1.92	-2.08	-1.647	-1.702	-1.32	-2.671	-2.15	-2.04	-1.95	-2.5	-0.991	-2.5	-3.13	-2.59	-2.5	-2.5	-2.195	-2.5	-1.713	-1.95
schist	PT001080	-1.4	-2.43	-1.81	-1.11	-2.75	-2.43	-2.713	-2.56	-1.78	-1.603	-1.91	-2.19	-2.471	-2.126	-1.769	-2.647	-2.91	-2.33	-2.27	-2.358	-2.5	-1.979	-1.97	-2.602	-1.523	-1.57	-2.723	-2.5	-2.5	-1.94
schist	PT001081	-1.7	-1.26	-2.02	-2.41	-2.65	-1.65	-1.409	-2.05	-1.14	-2.142	-1.69	-1.86	-1.588	-2.045	-1.103	-2.071	-1.05	-1.25	-2.08	-1.788	-1.5	-2.033	-1.59	-1.551	-1.556	0.722	-1.973	-1.5	-2.181	-2.2
granite+schis	PT001082	-2.807	-2.5	-2.09	-1.45	-1.78	-2.58	-1.257	-2.62	-2.6	-2.404	-2.57	-2.57	-2.44	-2.189	-2.562	-1.26	-2.37	-2.58	-2.41	-2.617	-2.509	-2.604	-2.51	-2.542	-2.5	-2.52	-1.702	-2.5	-2.095	-1.57
granite+schis	PT001083	-1.492	-1.35	-1.3	-1.66	-2.63	-1.41	-2.23	-2.15	-2.21	-2.264	-2	-2.28	-2.52	-2.463	-1.514	-2.448	-2.49	-2.25	-2.53	-1.851	-1.197	-1.414	-1.96	-1.379	-2.5	-1.47	-2.399	-1.48	-2.615	-2.79
granite	PT001084	-2.93	-2.1	0.176	-2.02	-2.5	-0.38	-2.877	-3.07	-1.67	-2.418	-2.95	-3.63	-2.5	-2.868	-2.5	-1.533	-2.14	-3.38	-3.05	-3.167	-2.5	-1.285	-1.23	-0.506	-1.417	#DIV/0!	-1.864	-2.5	-3.038	-3.9
granite	PT001085	-2.749	-2.26	0.068	-1.56	-2.53	-0.51	-2.628	-3.35	-1.72	-2.441	-3.07	-2.93	-3.864	-2.936	-2.712	-1.497	-2	-2.76	-3.04	-2.753	-1.911	-1.348	-2.02	-5.405	-1.352	#DIV/0!	-1.552	-1.21	-3.038	-3.68
granite	PT001087	-1.997	-2.04	-2.9	-1.93	-2.44	-2.1	-1.741	-1.44	-2.5	-2.563	-1.85	-2.36	-1.227	-0.799	-2.03	-1.733	-1.87	-2.05	-0.98	-1.65	-2.5	-2.529	-2.37	-2.392	-1.633	#DIV/0!	-2.331	-2.5	-1.727	-1.14
granite	PT001088	-1.871	-2.61	-3.02	-2.29	-2.2	-2.87	-2.492	-2.23	-1.75	-1.472	-2.06	-2.36	-2.773	-1.515	-1.935	-1.865	-2.74	-2.28	-1.69	-1.926	-2.5	-2.586	-5.3	-2.899	-2.5	#DIV/0!	-2.746	-1.16	-2.467	-0.41
granite	PT001089	-2.527	-1.97	-2.07	-2.22	-2.9	-1.38	-2.703	-2.33	-2.5	-2.746	-2.78	-3.63	-2.5	-2.005	-2.712	-1.247	-2.52	-2.52	-1.87	-2.477	-1.609	-2.275	-2.19	-1.65	-1.278	#DIV/0!	-1.343	-2.5	-2.287	-1.75
granite	PT001091	-2.792	-3.49	-2.4	-1.41	-2.14	-2.43	-2.778	-2.65	-2.5	-0.62	-2.46	-0.18	-1.682	-2.495	-1.935	-2.488	-2.49	-2.49	-2.76	-3.167	-1.72	-2.501	-5.3	-2.924	-2.5	#DIV/0!	-2.487	-2.5	-2.265	-0.45
granite	PT001092	-2.027	-2.58	-2.46	-1.15	-0.9	-2.21	-1.891	-2.4	-2.5	-0.814	-2.18	-2.38	-2.227	-2.172	-2.712	-1.91	-2.33	-2.52	-2.34	-2.753	-2.5	-2.377	-2.16	-5.405	-1.924	#DIV/0!	-2.071	-1.68	-1.122	-1.11
granite	PT001093	-1.962	-1.08	-1.79	-0.77	-1.15	-2.03	-1.886	-1.65	-1.77	-2.556	-2.06	-2.82	-1.955	-1.593	-2.712	-1.988	-2.33	-2.05	-1.77	-1.65	-2.5	-2.038	-1.45	-1.641	-1.521	#DIV/0!	-2.487	-1.32	-3.038	-2.65
granite	PT001094	-2.943	-2.42	-1.3	-2.1	-2.64	-1.38	-2.642	-2.45	-1.46	-2.51	-2.69	-2.15	-1.349	-2.534	-2.5	-2.537	-2.56	-2.11	-2.62	-3.167	-1.561	-2.113	-2.1	-5.405	-2.5	#DIV/0!	-2.227	-1.53	-1.491	-2.2
schist	PT001095	-2.7	-3.09	-2.34	-3.17	-2.62	-2.37	-2.956	-1.21	-2.95	-2.219	-2.46	-2.31	-2.412	-2.258	-1.077	-2.312	-2.48	-1.88	0.559	-1.788	-2.5	-2.551	-1.73	-2.41	-2.5	-2.5	-1.806	-2.5	-1.529	-1.32
schist	PT001096	-1.9	-2.1	-2.17	-2.71	-2.85	-2.26	-2.1	-2.46	-2.32	-1.888	-2.47	-2.11	-1.97	-2.52	0.5385	-2.094	-2.13	-1.71	-1.23	-1.788	2.1364	-1.502	-2.08	-1.805	-2.5	-1.43	-1.417	-1.64	-2.5	-1.74
schist	PT001097	-2.8	-3.7	-3.42	-2.01	-2.45	-2.68	-2.675	-2.43	-2.62	-1.61	-1.73	-1.58	-1.617	-1.571	-1.551	-2.294	-2.66	-2.17	-2.25	-1.788	-1.5	-2.916	-2.57	-2.212	-1.852	-2.5	-1.917	-2.5	-1.571	-0.65
schist	PT001098	-1.8	-2.41	-2.14	-2.35	-1.9	-1.87	-1.64	-2.49	-1.7	-2.008	-2.04	-1.64	-1.677	-2.227	-1.026	-2	-1.62	-1.58	-1.5	-2.358	-1.318	-1.911	-2.78	-2.206	-1.68	-0.87	-1.667	-1.59	-1.457	-1.74
schist	PT001099	-2.1	-4.42	-3.93	-3.58	-2.73	-3.53	-2.544	-2.75	-2.68	-1.79	-2.5	-1.86	-1.853	-1.53	-0.513	-2.477	-1.81	-1.5	-1.31	-1.5	-1.427	-3.51	-3.01	-2.958	-2.5	-2.5	0.3333	-2.5	-1.202	-0.01
schist	PT001100	-0.2	-0.83	-1.3	-2.09	-2.73	-1.55	-2.59	-1.82	-0.41	-1.32	-1.56	-1.58	-1.647	-1.197	-1.115	-2.271	-2.48	-1.13	-1.88	-1.5	-1.645	-0.642	-1.3	-1.85	-2.5	-2.5	-1.639	-1.33	-2.5	-2.81
schist	PT001101	-3.1	-4.2	-3.27	-3.97	-2.29	-3.02	-2.44	-2.9	-2.18	-2.585	-2.98	-2.53	-2.5	-2.722	-0.859	-2.523	-2.36	-2.42	-0.98	-2.788	-2.5	-3.119	-4.8	-2.992	-1.91	-2.5	-2	-2.5	-1.415	-0.35
schist	PT001102	-1.3	-2.49	-2.62	-2.42	-2.85	-2.48	-2.541	-1.86	-1.65	-1.013	-1.82	-1.36	-1.677	-1.177	-1.743	-2.547	-2.48	-1.67	-2.3	-2.071	-2.5	-2.476	-1.73	-2.11	-2.5	-2.5	-0.973	-2.5	-0.691	-1.49
granite+schis	PT001103	-1.579	-2.5	-2.16	-2.49	-1.41	-2.25	-2.553	-1.89	-1.81	-2.532	-2.28	-2.2	-2.312	-2.512	-2.314	-2.517	-2.5	-2.08	-2.08	-2.149	-2.41	-2.187	-2.46	-2.373	-1.167	-1.58	-2.534	-1.55	-2.156	-1.64
schist	PT001104	-2.2	-2.45	-1.81	-2.45	-1.94	-2.62	-2.157	-2.58	-2.24	-2.646	-2.78	-2.75	-2.441	-2.358	-2.243	-1.935	-1.85	-2.33	-1.91	-2.5	-1.827	-1.538	-4.8	-1.924	-1.631	-1.57	-2.362	-1.39	-2.5	-1.77
schist	PT001105	-2.2	-3.32	-1.8	-3.33	-2.41	-2.35	-2.15	-2.45	-2.75	-2.626	-3.07	-3.36	-2.617	-2.561	-2.09	-1.888	-1.56	-2.63	-2.52	-2.646	-1.264	-2.5	-2.9	-2.576	-2.5	-0.56	-2.556	-2.5	-1.5	-1.5
schist	PT001106	-2.1	-1.71	-0.63	-3.06	-2.24	-1.88	-2.058	-2.46	-1.73	-2.69	-2.61	-2.94	-2.353	-2.581	-2.257	-1.835	-1.5	-2.83	-2.51	-2.646	-1.33	-1.203	-0.8	-1.203	-2.5	-1.43	-2.278	-1.69	-2.5	-2.71
schist	PT001107	-1.5	-2.06	-2.19	-2.21	-2.7	-1.38	-2.653	-2.06	-1.89	-1.386	-1.85	-2.25	-1.735	-1.712	-2.18	-2.547	-2.5	-2.13	-2.39	-2.217	-1.245	-2.041	-2.34	-2.415	-1.621	-2.5	-1.389	-2.5	-1.606	-1.91
granite	PT001108	-2.006	-0.74	-2.82	-1.77	-2.89	-2.02	-2.418	-1.48	-2.5	-2.08	-1.24	-1.06	-2.015	-0.22	-1.512	-0.642	-2.37	-1.63	-1.12	-0.822	-1.211	-2.72	-1.21	-2.055	-2.5	#DIV/0!	-2.175	-2.5	-1.503	-2

schist	PT001109	-2.4	-2.59	-0.49	0.692	-2.06	-1.95	-2.52	-3.14	-2.69	-1.916	-2.78	-3.14	-2.882	-2.621	-2.013	-2.2	-2.26	-3	-3.49	-3.358	-1.476	-2.083	-1.43	-2.398	-2.5	-2.5	-2.945	-1.64	-2.5	-2.52
granite	PT001110	-2.315	-2.62	-1.58	-3.53	-2.43	-1.71	-2.026	-2.27	-1.77	-2.349	-2.31	-2.31	-2.136	-2.848	-1.935	-2.887	0.096	-2.23	-2.45	-3.167	-2.5	-0.996	-5.3	-2.696	-1.489	#DIV/0!	-0.876	-2.5	-2.198	-1.97
schist	PT001111	-2.7	-2.51	-2.2	-2.1	-1.83	-1.7	-2.5	-0.5	-1.89	-2.273	-1.69	-2.47	-2.412	-1.833	-2.526	-2.071	-2.44	-1.92	-1.33	4.221	-1.27	-2.026	-1.95	-1.477	-1.464	-2.5	-2.612	-2.5	-1.812	-1.74
schist	PT001112	-2.8	-2.46	-2.86	-2.94	-1.92	-2.15	-1.206	-1.52	-2.29	-2.508	-0.71	-0.92	-1.205	-0.823	-1.872	-1.841	-1.01	-1.54	-2.19	-2.217	-1.536	-2.743	-4.8	-1.924	-1.703	-1.13	-1.556	-2.5	-1.032	-1.43
granite	PT001113	-1.142	-2.14	-2.61	-2.85	-3.07	-2.69	-0.571	-0.97	-1.51	-1.649	-1.13	-1.63	-1.409	-1.887	-1.512	-2.433	0.883	0.026	-0.87	-1.098	-1.625	-1.635	-1.83	-2.198	-2.5	#DIV/0!	-2.123	-2.5	-1.592	-1.55
granite	PT001114	-1.761	-3.01	-3	-3.62	-2.54	-2.83	-0.644	-0.35	-1.11	-2.282	-0.9	-0.12	-1.5	-1.75	-1.794	-2.724	1.091	0.026	-0.44	-1.65	-1.455	-1.869	-0.46	-1.228	-2.5	#DIV/0!	-1.811	-2.5	-1.032	-0.73
schist	PT001115	-4.0	-2.43	-2.5	-2.16	-2.31	-1.42	-2.123	-2.71	-2.84	-1.737	-2.52	-2.42	-2	-2.268	-2.077	-1.706	-1.66	-2.04	-2.48	-3.217	-2.5	-3.058	-2.78	-2.89	-2.5	-2.5	-1.75	-2.5	-1.06	-1.38
schist	PT001116	-2.2	-1.72	-1.63	-2.15	-1.82	-1.79	-1.517	-1.99	-2.38	-2.033	-2.3	-2.78	-2.264	-2.116	-1.077	-1.859	-1.75	-2.54	-2.5	-2.646	-1.003	-1.978	-4.8	-1.822	-1.334	-0.71	-2.278	-2.5	-1.84	-2.2
schist	PT001117	-3.0	-2.48	-2.7	0.487	-2.62	-2.32	-1.389	-1.86	-2.72	2.0446	-1.78	-2.08	-1.765	0.5909	-0.192	-0.394	-0.87	-2.17	-0.74	-2.071	-1.318	-3.012	-2.41	-2.251	-1.756	-2.5	-0.389	-2.5	-1.316	-1.41
schist	PT001118	-1.9	-1.96	-0.29	-2.65	-2.83	-1.68	-2.693	-2.43	-2.34	-2.512	-2.24	-2.56	-2.941	-2.5	-0.077	-2.006	-1.97	-2.67	-3.11	-2.929	-1.5	-1.189	-1.36	-1.636	-2.5	-1.35	-2.667	-1.43	-2.5	-2.9
schist	PT001119	-2.2	-2.01	-0.42	-2.63	-2.19	-1.87	-2.464	-2.78	-2.28	-2.252	-2.68	-2.42	-2.853	-2.48	0.8462	-1.947	-2.07	-2.5	-3.01	-2.646	-1.318	-1.073	-1.87	-1.356	-1.087	-1.28	-2.473	-1.69	-2.5	-2.74
schist	PT001120	-2.6	-1.71	-1.21	-1.78	-2.61	-1.29	-2.21	-2.89	-2.49	-2.452	-2.14	-2.94	-2.853	-2.752	-1.923	-0.5	-0.64	-2.63	-2.28	-3.358	-1.743	-1.494	-1.94	-2.15	-2.5	-1.5	-1.667	-2.5	-1.543	-2.45
schist	PT001123	-3.2	-1.5	-2.15	-3.4	-2.66	-0.36	-2.28	-0.5	-2.05	-2.713	-1.88	-2.42	-2.588	-2.652	-2.667	-1.388	1.676	-0.83	0.648	-1.358	-2.5	-1.734	-1.79	-1.941	-2.5	-2.5	-1.667	-2.5	-1.316	-2.06
schist	PT001124	-2.7	-1.64	-1.52	-1.83	-2.32	-1.45	-1.128	-2.47	-2.66	-2.484	-2.67	-3.39	-2.706	-2.086	-1.449	0.2351	0.853	-3	-2.37	-2.788	-1.827	-1.986	-1.29	-1.703	-1.52	-0.12	-1.556	-2.5	-2.053	-2.23
schist	PT001125	0.7	-0.03	-2.07	-0.69	-1.99	-1.07	-1.05	-0.51	-0.72	-0.556	0.014	0.111	-0.029	-0.368	-2.564	-2.024	-1.74	-0.17	-1.57	-0.071	-2.5	-1.304	-1.08	-0.856	-2.5	-2.5	-0.306	-1.36	-2.053	-2.9
schist	PT001126	0.0	-0.27	-0.81	-2.4	-2.31	-1.84	-2.811	-0.97	-1.9	-2.636	-1.98	-1.83	-1.529	-1.995	-2.82	-2.694	-2.75	-2.17	-2.06	-1.212	-2.5	-1.322	-1.36	-1.119	-2.5	-2.5	-2.778	-1.36	-2.5	-3.16
schist	PT001127	-2.3	-2.79	-0.99	-2.35	-2.95	-3.35	-2.794	-1.09	-3.04	-2.561	-2.99	-2.67	-2.294	-2.853	-1.897	-3.265	-3.52	-2.67	-0.99	-2.071	-2.5	-2.79	-4.8	-2.534	-1.595	-2.5	-2.583	-1.73	-2.096	-2.06
schist	PT001128	-0.3	-1.66	-2.19	-3.45	-0.21	-3.01	-1.495	-2.06	-1.54	-2.349	-1.91	-0.83	-0.794	-0.641	-2.218	-2.741	-2.5	-0.67	-1.98	-1.788	-1.827	-2.176	-2.1	-0.831	-1.559	-0.86	-1.083	-2.5	-1.904	-1.96
schist	PT001129	0.1	-0.81	-1.51	-2.77	0.145	-2.29	-1.126	-1.66	-1.23	-2.605	-2.02	-0.69	-0.676	-0.631	-1.91	-2.4	-2.19	-1.04	-1.97	-1.642	-2.5	-1.558	-1.83	-1.246	-2.5	-0.29	-1.056	-1.69	-2.181	-2.63
schist	PT001130	0.0	-0.55	-2.28	-3	-2.21	-2.01	-1.876	-0.91	-0.78	-1.797	-0.16	-0.14	-1.147	-0.783	-1.859	-2.147	-1.99	-0.29	-1.9	-1.212	-2.5	-1.714	-1.99	-1.5	-2.5	-0.91	-0.973	-2.5	-2.053	-2.49
schist	PT001131	-0.2	-0.43	-2.16	-0.19	-0.87	-2.52	-0.877	-1.46	-0.78	0.2444	-0.75	-0.33	-0.97	-1.5	-2.218	-2.4	-1.95	-1.63	-2.08	-1.929	-2.5	-1.547	-1.87	-0.72	-1.362	-2.5	0.555	-1.59	-2.5	-2.5
schist	PT001132	0.0	-0.96	-2.44	-0.98	-0.32	-2.57	0.2897	-1.88	-0.98	1.0435	-0.21	0.194	-0.823	-1.49	-2.372	-2.547	-1.6	-1.08	-2.22	-2.358	-2.5	-1.78	-1.24	-1.223	-1.146	-2.5	-1.528	-1.64	-2.5	-2.3
schist	PT001133	-2.2	-2.74	-2.65	-1.75	-1.09	-2.45	-0.994	-2.08	-1.95	-1.233	-2	-1.81	-1.647	-1.429	-2.346	-2.306	-1.77	-2.33	-2	-1.5	-2.5	-2.578	-4.8	-2.737	-1.841	-2.5	-1.889	-2.5	-1.649	-1.37
schist	PT001134	-2.2	-2.09	-2.09	-2.05	-1.24	-1.68	-2.497	-1.61	-2.41	-2.963	-2.13	-2.47	-2.353	-2.247	-2.487	-1.971	-2.13	-2.21	-1.16	-1.358	-1.591	-2.026	-2.3	-2.517	-1.444	-2.5	-2.056	-2.5	-1.521	-1.83
schist	PT001135	-2.4	-2.82	-2.7	-2.47	-1.4	-2.21	-1.071	-2.08	-2.64	-1.349	-2.23	-1.81	-1.588	-1.783	-2.308	-2.312	-1.87	-1.92	-1.58	-2.071	-1.064	-2.698	-0.76	-2.573	-1.543	-2.5	-1.389	-2.5	-1.216	-1.3
schist	PT001136	-1.4	-2.27	-2.31	-2.45	-1.97	-2.77	-2.411	-1.6	-1.57	-2.542	-1.71	-1.69	-1.5	-1.268	-2.397	-2.582	-2.32	-1.17	-2.29	-1.642	-1.609	-2.186	-2.17	-1.749	-1.651	-2.5	-1.889	-2.5	-1.628	-1.71
schist	PT001137	-1.7	-3.23	-3.04	-2.5	-2.33	-2.83	-1.885	-2.27	-2.16	0.3604	-1.63	-0.83	-1.205	-0.591	-1.808	-2.741	-2.44	-1.79	-2.49	-2.071	-2.5	-2.84	-2.64	-2.602	-2.5	-0.76	-1.223	-2.5	-0.904	-1.06
schist	PT001138	-2.6	-2.39	-1.62	-2.25	-1.88	-2.14	-2.235	-1.98	-2	-1.891	-2.53	-2.42	-2.529	-2.449	-2.038	-2.4	-2.15	-2	-1.33	-1.929	-2.5	-2.041	-2.42	-2.314	-2.5	-2.5	-1.945	-2.5	-2.053	-1.95
schist	PT001139	-2.4	-3.69	-3.52	-2.57	0.861	-3.47	-0.951	-2.6	-3.1	-2.871	-2.88	-1.64	-1.235	-1.692	-2.526	-2.953	-2.07	-1.5	-2.25	-1.788	-2.5	-3.48	-4.8	-4.653	-1.854	-1.57	-1.75	-2.5	-1.684	-0.44
schist	PT001140	-1.7	-2.52	-2.61	-1.69	-1.42	-2.81	-1.645	-2.33	-2	-2.758	-2.27	-1.69	-1.323	-1.399	-2.385	-2.653	-2.3	-1.71	-2.17	-1.642	-2.5	-2.322	-1.73	-1.771	-1.664	-2.5	-1.583	-0.71	-1.84	-1.39
schist	PT001141	-1.2	-2.58	-2.54	-1.52	-1.34	-2.55	-1.848	-1.99	-2.59	-2.594	-2.01	-1.75	-1.059	-1.288	-2.257	-2.482	-2.26	-1.67	-1.83	-1.929	-2.5	-2.616	-4.8	-1.72	-2.5	-2.5	-1.5	-2.5	-1.543	-1.44
schist	PT001142	-1.7	-3.06	-2.28	-2.1	-2.8	-3.51	-0.178	-3.82	-2.66	-2.44	-2.9	-2.72	-2.03	-2.53	-2.68	-2.5	-0.19	-2.38	-2.87	-2.573	-2.5	-2.236	-2.06	-2.805	-1.136	-1.57	-2.556	-1.31	-2.5	-1.31
granite	PT001143	-1.95	-2.22	-3.74	-2.08	-1.47	-3.16	-2.001	-1.93	-1.63	-1.968	-1.72	-1.21	-1.531	-0.064	-1.794	-1.883	-2.43	-1.1	-1.81	-1.465	-1.02	-2.5	-2.38	-2.418	-2.5	#DIV/0!	-0.825	-1.37	-3.038	-0.06
granite	PT001144	-3.027	-3.15	-1.02	-2.3	-2.29	-1.13	-2.668	-3.09	-2.5	-2.577	-2.95	-2.46	-3.864	-2.799	-2.712	-1.883	-2.06	-3.11	-2.97	-3.167	-1.084	-2.243	-2.22	-2.519	-2.5	#DIV/0!	-1.708	-2.5	-1.424	-2.05
granite	PT001145	-3.756	-5.06	-3.51	0.235	1.64	-1.69	-1.193	-2.93	-2.5	-2.438	-2.95	-3.63	-1.227	-2.534	-2.076	-3.015	-2.04	-2.46	-2.86	-1.926	-1.211	-2.967	-3.63	-3.392	-2.5	#DIV/0!	-1.241	-2.5	-0.247	1.266
granite	PT001146	-3.756	-3.71	-3.38	-2.61	-1.26	-1.99	-1.435	-2.17	-2.5	-1.899	-1.94	-1.79	-0.56	-1.877	-1.324	-2.278	-1.5	-2.11	-2.53	-1.65	-1.306	-2.621	-2.63	-3.228	-2.5	#DIV/0!	-1.241	-2.5	-0.404	0.331
schist	PT001148	-2.7	-2.44	-3.76	-0.51	0.723	-2.65	-0.733	-1.66	-2.02	-1.645	-0.91	-0.31	-0.617	-0.752	-1.115	-1.388	-0.38	-1.46	-2.49	-2.071	-1.391	-3.145	-2.78	-2.712	-1.372	-2.5	-1.028	-2.5	-1.018	-0.9
schist	PT001149	-2.6	-0.62	-3.01	0.328	-0.13	-1.44	-0.995	-1.95	-1.2	1.693	0.375	0.5	-0.382	0.5	-1.603	-1.688	0.01	-1.29	-2.52	-0.929	-2.5	-2.416	-1.59	-1.647	-1.674	-2.5	-1.083	-2.5	-1.471	-2.06
schist	PT001150	-2.6	-1.64	-2.52	-0.72	0.193	-1.34	-0.91	-1.44	-1.71	-1.436	-0.23	-0.69	-0.647	-1.015	-1.526	-1.735	-1.19	-1.25	-1.81	-1.212	-1.609	-2.009	-4.8	-0.788	-1.67	-2.5	-1.306	-2.5	-1.5	-2.02
schist	PT001151	-2.6	-2.5	-2.88	-2.04	-1.44	-2.02	-2.406	-1.56	-1.67	-2.417	-0.54	-1.47	-1.323	-0.611	-1.885	-1.8	-0.7	-1.67	-2.58	-1.071	-1.355	-2.938	-2.35	-2.941	-1.608	-2.5	-1.5	-2.5	-0.819	-1.4
granite	PT001152	-1.866	-1.26	-2.05	-1.92	-2.29	-1.14	-1.986	-2.18	-2.5	-2.189	-2.36	-2.31	-2.591	-2.005	-2.076	-1.369	-1.5	-2.49	-1.56	-2.477	-1.434	-1.543	-0.79	-1.751	-0.958	#DIV/0!	-0.72	-2.5	-1.883	-2.33
granite	PT001153	-2.346	-0.21	-1.79	-0.94	-2.44	-1.48	-2.243	-2.54	-2.5	-2.352	-2.29	-2.2	-2.864	-1.387	-1.558	-0.533	-3.45	-2.23	-1.9	-1.465	-2.5	-2.727	-2.09	-1.139	-2.5	#DIV/0!	-2.539	-2.5	-2.489	-3.04
granite	PT001154	-0.531	-1.83	-3.07	-3.02	-2.11	-2.98	-0.864	0.239	-1.51	-0.822	0.58	0.447	-0.56	-0.779	3.1011	-2.951	-0.17	2.158	0.242	-0.637	-1.8	-1.549	-1.88	-0.578	-1.439	#DIV/0!	-0.408	-2.5	-1.458	-1.72
granite	PT001155	-1.126	-1.69	-2.16	-2.48	-2.46	-2.14	-1.735	-1.51	-1.48	-0.444	-1.47	-2.05	-1.5	-2.034	-0.711	-2.351	-1.21	-1.28	-1.86	-1.834	-1.306	-1.714	-2.66	-2.299	-1.67	#DIV/0!	-2.071	-2.5	-1.626	-2.16
granite	PT001156	-2.491	-1.87	-1.31	0.402	-0.4	-2.07	-1.22	-3.12	-2.5	-2.404	-2.66	-2.77	-3.045	-2.309	-2.076	-1.501	-3.57	-2.58	-3	-2.568	-1.848	-2.657	-2.1	-2.215	-1.523	#DIV/0!	-3.057	-1.3	-3.038	-2.5
granite	PT001157	-2.286	-1.41	-2.35	-0.63	-2.51	-1.51	-2.056	-2.26	-2.5	-2.497	-2.38	-2.46	-2.5	-1.593	-2.712	-1.11	-2.95	-2.31	-2.04	-1.374	-2.5	-2.824	-2.46	-2	-1.504	#DIV/0!	-2.746	-2.5	-1.772	-1.91
granite	PT001158	-2.343	-0.57	-2.16	-1.93	-2.67	-1.64	-2.124	-2.13	-2.5	-2.522	-1.96	-1.58	-1.531	-0.917	-1.183	-1.133	-2.23	-2.11	-2.21	-1.512	-2.5	-2.038	-1.61	-2.165	-1.451	#DIV/0!	-1.241	-1.16	-2.198	-2.57
granite	PT001159	-2.579	-2	-2.37	-1.93	-1.86	-2.16	-2.388	-2.32	-2.5	-0.696	-2.05	-2.31	-2.318	-1.515	-2.03	-1.419	-2.56	-2.52	-2.3	-1.834	-1.476	-2.373	-3.04	-2.494	-2.5	#DIV/0!	-2.123	-2.5	-1.962	-1.42
granite	PT001160	-1.516	-1.19	-2.02	-1.25	-2.35	-2.17	-1.459	-1.64	-1.77	-1.725	-1.51	-1.27	-2.196	-1.083	-1.889	-2.01	-1.89	-1.93	-1.51	-0.96	-1.879	-1.895	-2.08	-1.203	-1.528	#DIV/0!	-2.85	-2.5	-2.399	-2.53
granite	PT001162	-0.308	-2.16	-2.23	-1.92	-2.27	-2.52	-0.113	-1.47	-1.55	0.0526	-1.36	-0.83	-1.713	-2.142	-1.653	-2.765	1.34	-0.69	-1.59	-2.477	-1.911	-0.71	-1.56	-1.987	-2.5	#DIV/0!	-2.487	-2.5	-1.626	-1.97
granite	PT001163	-1.935	-2.62	-1.11	-2.42	-2.62	-1.88	-2.276	-2.42	-1.72	-2.209	-2.4	-3.63	-1.591	-2.515	-2.359	-2.269	-1.58	-1.93	-2.49	-2.201	-1.784	-1.444	-2.63	-1.405	-2.5	#DIV/0!	-1.967	-1.42	-0.449	-2.32
schist	PT001164	-1.2	-1.86	-1.82	-0.72	-2.51	-2.47	1.8269	-1.78	-2.51	-2.791	-2.48	-3.5	-2.941	-2.54	-2.718	-0.5	3.363	-2.13	-2.05	-2.788	-2.5	-1.403	-1.1	-1.573	-2.5	-2.5	-1.333	-1.55	-1.968	-2.09
schist	PT001165	-2.1	-1.37	-2.04	0.9	-2.62	-2.06	-0.844	-0.86	-2.84	-2.164	-1.59	-2.19	-2.206	-1.904	-2.41	-1.224	0.755	-1.21	-0.54	-2.071	-1.645	-1.92	-1.57	-1.229	-2.5	-2.5	-1.223	-2.5	-1.642	-2.15
granite	PT001166	-0.732	-2.35	-2.1	-3.12	-2.19	-3.05	-0.677	-1.18	-1.43	-1.509	-1.43	-2.05	-2.409	-2.534	-1.465	-2.997	0.531	0.262	-1.36	-2.339	-2.5	-0.6	-1.23	-1.717	-2.5	#DIV/0!	-1.864	-2.5	-2.265	-1.8
schist	PT001167	-2.4	-2.64	-0.09	-2.82	-2.66	-2.66	-2.918	-3.66	-3.16	-2.848	-3.76	-3.58	-3.03	-3.389	-2.788	-3.118	-3.44	-3.31	-1.98	-2.358	-2.5	-2.269	-1.71	-2.178	-1.549	-1.72	-3.223	-1.64	-2.5	-2.53

schist	PT001168	-2.7	-2.34	-1.12	-2.1	-1.42	-2.59	-2.072	-3.63	-3.08	-0.685	-2.84	-2.97	-3.074	-3.065	-2.423	-2.876	-2.66	-2.63	-1.59	-2.646	-2.5	-2.249	-2.2	-2.347	-1.71	-2.5	-2.528	-1.34	-2.5	-2.16
schist	PT001169	-2.2	-1.23	-1.56	-2.13	-2.1	-1.16	-2.61	-1.4	-1.6	-1.097	-1.54	-2.06	-2.353	-2.055	-2.103	-1.106	-2.54	-2.17	-1.37	-1.071	-1.791	-0.744	-1.74	-1.777	-1.293	-2.5	-2.583	-1.69	-2.138	-2.5
schist	PT001170	-2.5	-1.95	-1.79	-2.86	-1.64	-1.73	-2.508	-1.59	-2.16	-1.847	-1.9	-1.97	-2.059	-2.197	-2.385	-1.935	-2.64	-1.83	-0.67	-1.5	-2.5	-1.569	-4.8	-2.475	-2.5	-2.5	-2.333	-2.5	-1.798	-2.08
schist	PT001171	-2.6	-2.3	-2.58	-0.92	-2.63	-2.27	-1.936	-1.78	-2.14	7.4017	1.364	-0.28	-2.5	-1.672	2.4488	-1.665	0.814	-1.13	-1.38	-0.783	-1.209	-1.819	-1.81	-1.138	-2.5	-1.35	-1.889	-2.5	-1.386	-1.96
schist	PT001172	-2.7	-1.86	-1.79	-3.01	-2.87	-1.44	-2.044	-0.59	-3.29	-1.896	-1.33	-1.5	-2.264	-2.015	-1.487	-1.747	-0.09	-0.79	-0.29	-0.929	-2.5	-1.772	-1.13	-2.461	-1.697	-2.5	-1.806	-2.5	-1.656	-2.2
schist	PT001173	-2.5	-2	-1.6	-2.53	-2.58	-1.54	-1.947	-0.67	-1.52	-1.891	-1.63	-1.67	-2.383	-2.086	-2.243	-1.676	-0.74	-0.58	0.692	-0.642	-2.5	-1.5	-2.02	-0.534	-1.428	-2.5	-1.667	-2.5	-1.869	-2.24
schist	PT001174	-2.0	-1.77	-0.91	-2.26	-2.78	-1.83	-1.807	-1.32	-1.58	-2.301	-2.44	-2.42	-2.677	-2.52	-0.257	-2.165	-1.72	-2.25	-2.41	-2.071	-1.645	-1.369	-4.8	-2.014	-2.5	-1.13	-2.75	-0.94	-2.5	-2.58
schist	PT001175	-1.6	-1.42	-1.54	-2.98	-2.34	-2.49	-1.648	-0.98	-1.67	-2.262	-0.89	-1.64	-1.911	-1.955	-2.436	-1.947	-0.95	-1.13	-2.22	-1.358	-1.5	-0.979	0.756	-1.031	-2.5	-1.57	-2.167	-1.34	-2.011	-2.49
schist	PT001176	-2.6	-2.18	-0.56	0.051	-2.47	-1.27	-0.821	-3.66	-3.58	-2.702	-3.55	-3.94	-3.235	-2.762	-2.615	-0.171	0.676	-3.08	-3.31	-3.002	-1.518	-1.66	-2	-2	-1.474	-2.5	-0.917	-1.57	-2.5	-2.54
schist	PT001177	-1.5	-1.27	-1.52	-2.4	-2.11	-1.65	-2.183	-0.9	-0.49	-1.837	-1.74	-1.86	-2.264	-2.076	-2.231	-1.441	-2.32	-2.17	-1.46	-0.354	-1.755	0.2476	-1.43	-1.822	-1.444	-2.5	-2.473	-1.22	-2.5	-2.5
schist	PT001178	-2.4	-2.67	-2.34	-1.21	-1.2	-1.5	-2.367	-3.05	-3.25	-2.613	-2.89	-2.94	-2.736	-2.833	-2.526	-0.177	-2.5	-3.08	-3.19	-2.358	-1.573	-2.662	-2.38	-1.381	-1.418	-2.5	-1.833	-1.73	-1.543	-1.48
schist	PT001179	-2.2	-1.17	-1.64	-3.19	-1.42	-1.01	-2.059	-0.52	-1.05	-2.025	-1.84	-1.56	-2.471	-1.965	-2.641	-1.159	-1.79	-2.33	-0.92	-0.783	-1.427	-0.24	-1.03	-1.602	-1.408	-1.43	-2.389	-1.29	-1.543	-2.46
schist	PT001180	-2.5	-1.51	-0.46	-2.12	-2.12	-1	-2.5	-3.24	-1.86	-2.587	-3.48	-3.25	-3.294	-3.187	-2.615	-0.347	-2.6	-3.17	-3.33	-3.075	-1.482	-1.821	-0.59	-1.924	-1.516	-1.57	-2.5	-1.39	-2.5	-2.78
schist	PT001181	-2.3	-1.81	-0.38	-2.23	-2.42	-1.23	-2.738	-4.02	-2.88	-2.558	-3.26	-3.69	-2.765	-2.965	-2.654	-0.377	-2.91	-3.42	-3.2	-2.788	-1.573	-1.972	-4.8	-4.653	-2.5	-2.5	-2.612	-1.19	-2.5	-2.75
schist	PT001182	-2.5	-1.92	-0.26	-2.6	-2.5	-1.26	-2.844	-4.32	-2.73	-2.915	-3.61	-3.44	-3.235	-3.177	-2.757	-0.235	-2.91	-3.33	-3.7	-2.646	-1.645	-2.15	-1.73	-2.22	-1.31	-1.69	-2.667	-1.55	-2.5	-2.72
schist	PT001183	-3.0	-3.81	-3.66	-2.43	-0.75	-3.6	-1.42	-3.49	-3.08	-1.895	-2.83	-2.25	-2.147	-2.358	-2.551	-2.671	-2.58	-1.79	-2.41	-3.075	-2.5	-2.71	-1.36	-2.763	-2.5	-1.28	-2.278	-1.73	-1.415	-0.28
schist	PT001184	-2.9	-2.36	-0.16	-2.21	-2.22	-1.02	-2.673	-4.86	-3.26	-2.643	-3.82	-3.72	-3.03	-3.258	-2.718	-0.188	-2.79	-3.67	-3.6	-3.217	-1.645	-2.204	-1.62	-4.653	-2.5	-2.5	-2.583	-1.59	-2.5	-2.65
schist	PT001185	-2.0	-1.65	-1.6	-2.55	-2.04	-1.8	-1.652	-0.61	-0.46	-1.633	-1.72	-1.67	-2.118	-2.126	-2.474	-1.5	-2.07	-2.5	-1.2	-0.783	-1.1	-0.684	-1.71	-1.472	-1.225	-2.5	-2.333	-1.29	-2.5	-2.34
schist	PT001186	-2.1	-2.86	-2.3	0.353	-1.89	-3.29	-2.174	-2.88	-1.36	-1.153	-2.14	-1.89	-2.323	-1.975	0.4873	-2.671	-2.7	-2.17	-1.74	-1.358	-2.5	-1.832	-1.06	-1.347	-2.5	-0.81	-2.083	-1.03	-2.5	-1.45
schist	PT001187	-0.8	-2.25	-3.49	-2.48	-2.12	-2.19	-1.997	-1.21	-1.3	-2.169	-0.5	0.111	-0.176	-0.732	-2.743	-2.2	-2.17	-1.96	-2.4	-2.217	-2.5	-2.618	-4.8	-2.364	-1.697	-2.5	-1.833	-2.5	-0.904	-1.22
schist	PT001188	-2.8	-2.45	-2.36	-1.39	-1.41	-2.1	-2.968	-1.72	-2.4	-1.862	-2.18	-2.39	-2.559	-2.631	-1.577	-2.082	-2.52	-2.67	-0.82	-1.929	-1.682	-2.248	-1.41	-2.085	-2.5	-1.43	-2.389	-2.5	-1.614	-1.52
granite	PT001189	-1.327	-2.21	-1.83	-3.37	-1.51	-2.49	-2.698	-1	-1.05	-1.034	-0.3	0.914	1.1964	-1.456	16.749	-3.556	-2.93	-0.21	-1.47	-1.374	-1.593	-0.523	-1.52	-0.57	-2.5	#DIV/0!	-3.992	-2.5	-1.929	-2.39
granite+schis	PT001190	-1.525	-1.96	-2.61	-2.5	-2.1	-1.77	-2.34	-1.37	-1.4	-1.245	-1.33	-1.27	-1.229	-1.27	-1.495	-2.221	-1.21	-1.31	-1.31	-1.383	-2.474	-1.758	-1.35	-1.862	-2.5	-2.45	-1.433	-2.5	-1.302	-1.48
schist	PT001191	-1.6	-0.97	-1.39	-2.5	-2.56	-1.24	-2.747	-1.06	-1.52	-0.977	-1.27	-1.67	-2.235	-2.106	-2.5	-1.506	-2.54	-2.46	-1.79	-1.358	-1.645	-0.35	-4.8	-1.653	-2.5	-2.5	-2.5	-1.17	-2.138	-2.72
schist	PT001192	-2.0	-1.17	-1.61	-2.12	-1.88	-1.3	-2.324	-1.94	-1.67	-2.066	-1.81	-2	-1.794	-2.197	-2.513	-1.253	-2.19	-2.38	-2.15	-1.929	-2.5	-1.132	-2.06	-1.941	-2.5	-2.5	-2.417	-1.38	-1.415	-2.44
schist	PT001193	-1.9	-0.98	-1.66	-2.63	-2.15	-1.72	-2.059	-1.26	-0.86	-0.977	-1.42	-1.14	-2.147	-2.177	-2.295	-1.641	0.166	-1.46	-0.78	-0.354	-1.645	-0.829	-1.2	-0.941	-1.162	-2.5	-1.973	-1.59	-1.798	-2.5
schist	PT001194	-2.3	-2.5	-2.1	-2.5	-2.19	-2.52	-2.173	-1.92	-1.87	-1.663	-1.93	-2.19	-1.853	-2.389	-2.026	-2.076	-2.03	-2.29	-1.65	-2.358	-2.5	-1.598	-1.27	-0.686	-2.5	-2.5	-2.25	-2.5	-1.926	-1.72
schist	PT001197	-2.1	-1.85	-2.06	-0.77	-1.3	-1.91	-1.825	-2.08	-1.48	-1.751	-1.95	-1.89	-2.147	-2.207	-2.397	-1.235	-1.97	-2.17	-1.99	-1.788	-2.5	-1.073	-1.63	-2.037	-1.526	-2.5	-1.945	-1.48	-2.5	-1.97
schist	PT001198	-1.6	-1.19	-0.62	-2.17	-2.4	-1.62	-2.959	-2.9	-1.08	-2.564	-2.36	-2.33	-2.853	-2.611	-2.603	-2.394	-2.46	-2.38	-2.39	-1.5	-2.5	-0.681	-1.69	-1.98	-2.5	-2.5	-2.862	-0.94	-2.5	-2.9
schist	PT001199	-2.3	-2.17	-2.04	-2.11	-1.97	-1.93	-2.138	-1.34	-2.11	-1.874	-2.13	-2.22	-2	-2.197	-2.513	-1.435	-1.93	-2.13	-0.64	-1.642	-2.5	-1.702	-2.36	-2.305	-1.457	-1.43	-2.306	-2.5	-1.968	-1.86
schist	PT001200	-0.8	-1.76	-2.42	-0.1	-0.75	-3	-0.587	-1.97	-1.38	-2.078	-1.74	-1.17	-1.059	-1.449	-2.577	-2.894	-2.5	-1.88	-2.64	-2.358	-2.5	-2.304	-1.74	-1.794	-2.5	-2.5	-1.945	-1.58	-2.5	-1.82
schist	PT001201	-0.4	-1.75	-1.15	-0.34	-2.16	-2.82	-2.49	-1.82	-1.89	-2.29	-2.05	-2.36	-2.206	-2.419	-2.154	-3.2	-3.36	-2.54	-3.11	-3.504	-1.318	-1.99	-4.8	-1.686	-2.5	-2.5	-2.945	-1.27	-2.5	-2.5
schist	PT001202	-1.3	-2.58	-2.86	-1.79	-0.88	-2.98	-1.509	-2.08	-2.09	-2.862	-2.28	-1.83	-1.5	-1.853	-2.615	-2.947	-2.54	-1.71	-2.35	-2.929	-2.5	-2.844	-2.47	-2.568	-2.5	-2.5	-2.139	-1.55	-1.16	-1.25
schist	PT001203	-1.0	-3.25	-2.76	-1.35	-0.75	-3.7	-2.349	-2.25	-2.79	-2.105	-2.02	-1.83	-2.059	-2.187	-2.692	-3.159	-2.83	-2.63	-2.95	-2.788	-2.5	-2.962	-2.15	-2.847	-2.5	-2.5	-2.362	-2.5	-0.862	-1.06
schist	PT001204	-3.0	-2.13	-2	-2.57	-2.09	-2.29	-2.323	-2.08	-2.63	-2.5	-2.57	-2.61	-2.5	-2.762	-2.346	-2.282	-2.07	-2.38	-1.08	-2.5	-2.5	-2.266	-4.8	-2.709	-1.146	-2.5	-2.5	-2.5	-1.84	-1.75
schist	PT001205	-2.2	-1.82	-1.64	-2.31	-1.98	-2.21	-2.301	-1.97	-1.62	-2.294	-2.49	-2.56	-2.853	-2.662	-2.128	-2.047	-2.09	-2.25	-1.16	-0.783	-1.755	-1.016	-1.22	-1.915	-1.303	-2.5	-2.639	-1.22	-2.5	-2.1
schist	PT001206	-1.2	-1.68	-2.67	-0.49	-1.61	-2.63	-1.621	-1.86	-1.39	3.1718	-0.77	-0.36	-0.852	-0.712	-1.243	-2.271	-2.19	-1.42	-2.14	-1.358	-2.5	-1.528	-1.6	-2.441	-2.5	-2.5	-1.556	-2.5	-2.124	-1.83
schist	PT001207	-2.8	-2.76	-2.14	-1.68	-1.33	-2.5	-2.202	-1.95	-2.78	-1.712	-2.54	-2.39	-2.824	-2.54	-2.115	-2.424	-2.28	-2.58	-1.64	-1.929	-2.5	-2.401	-2.5	-2.681	-2.5	-2.5	-2.473	-2.5	-1.926	-1.5
granite	PT001208	-2.042	-2.42	-2.04	-1.4	-2.15	-2.09	-1.616	-2.5	-2.5	-2.421	-2.48	-2.46	-2.5	-1.917	-0.146	-1.506	-1.56	-1.93	-2.48	-2.201	-1.72	-2.13	-0.76	-2.418	-1.367	#DIV/0!	-2.487	-2.5	-0.92	-1.53
granite	PT001209	-1.439	-2.25	-1.34	-1.88	-2.42	-1.97	-2.525	-2.32	-1.31	-1.915	-1.99	-1.92	-1.955	-2.113	0.7008	-1.951	-2.33	-2.23	-2.12	-2.063	-1.508	-1.602	-2.22	-1.532	-2.5	#DIV/0!	-3.213	-2.5	-3.038	-2.48
granite	PT001210	-1.86	-1.11	-1.82	-1.7	-1.4	-2.54	-2.239	-1.95	-1.61	-2.681	-1.87	-1.63	-1.955	-1.123	-2.147	-2.169	-2.29	-1.57	-1.48	-1.834	-2.5	-1.789	-1.3	-1.692	-1.466	#DIV/0!	-2.434	-1.21	-3.038	-2.51
granite	PT001211	-2.332	-1.51	-1.83	-2.46	-0.96	-1.12	-2.529	-2.39	-2.5	-2.834	-2.56	-2.62	-2.591	-1.966	-2.712	-1.165	-1.62	-2.58	-2.32	-2.386	-2.5	-1.819	-5.3	-1.818	-2.5	#DIV/0!	-0.929	-2.5	-2.097	-2.3
granite	PT001212	-1.65	-1.46	-1.52	-2.55	0.041	-0.78	-2.362	-2.5	-1.42	-2.575	-2.56	-2.46	-2.5	-2.162	-2.5	-1.528	-2.41	-2.94	-2.74	-2.753	-1.784	-1.535	-0.82	-1.354	-2.5	#DIV/0!	-2.539	-2.5	-2.534	-2.8
schist	PT001213	-2.2	-2.01	-1.27	-2.47	-2.32	-1.29	-2.964	-1.61	-1.89	-2.41	-2.17	-2.36	-2.441	-2.571	-2.692	-1.577	-2.56	-3	-2.85	-1.212	-1.609	-1.314	-2.19	-2.89	-2.5	-2.5	-2.556	-1.2	-1.074	-2.36
granite	PT001214	-1.001	-2.47	-2.02	-3.34	-1.63	-2.55	-2.287	-0.61	-0.52	-0.964	-0.45	1.849	-0.318	-1.956	-0.477	-4.024	-3.43	0.44	0.211	-1.098	-2.5	0.2318	-1.87	-1.975	-2.5	#DIV/0!	-4.304	-1.42	-3.038	-2.08
schist	PT001215	-2.3	-2	-1.48	-2.49	-2.56	-1.84	-2.401	-1.35	-1.67	-1.5	-1.81	-1.67	-2.353	-1.843	-0.423	-1.382	-1.74	-1.63	-0.64	-1.929	-0.821	-1.646	-1.87	-1.895	-0.918	-0.73	-2.417	-2.5	-1.67	-2.27
granite	PT001216	-1.453	-2.25	-1.14	-1.64	-2.37	-1.99	-1.514	-2.73	-1.84	-2.075	-2.42	-2.62	-2.318	-2.73	-2.218	-2.237	-1.67	-1.75	-2.45	-2.201	-1.667	-1.348	-1.75	-1.886	-2.5	#DIV/0!	-2.02	-1.53	-2.467	-2.58
granite	PT001217	-2.428	-2.23	-1.44	-1.53	-1.57	-1.64	-2.208	-1.66	-1.4	-1.725	-2.04	-2.31	-2.318	-2.338	-1.935	-1.597	-1.46	-1.99	-2.27	-2.201	-1.704	-1.519	-2.03	-1.329	-2.5	#DIV/0!	-1.604	-2.5	-2.332	-2.42

Figure G1. Standardized (Z) values for each samples considering the upper outlier threshold based on the Tukey plots for each lithological subset.